Niloofar Hamzelui

Investigation of active materials and polymeric binders in silicon-based negative electrodes for lithium-ion batteries

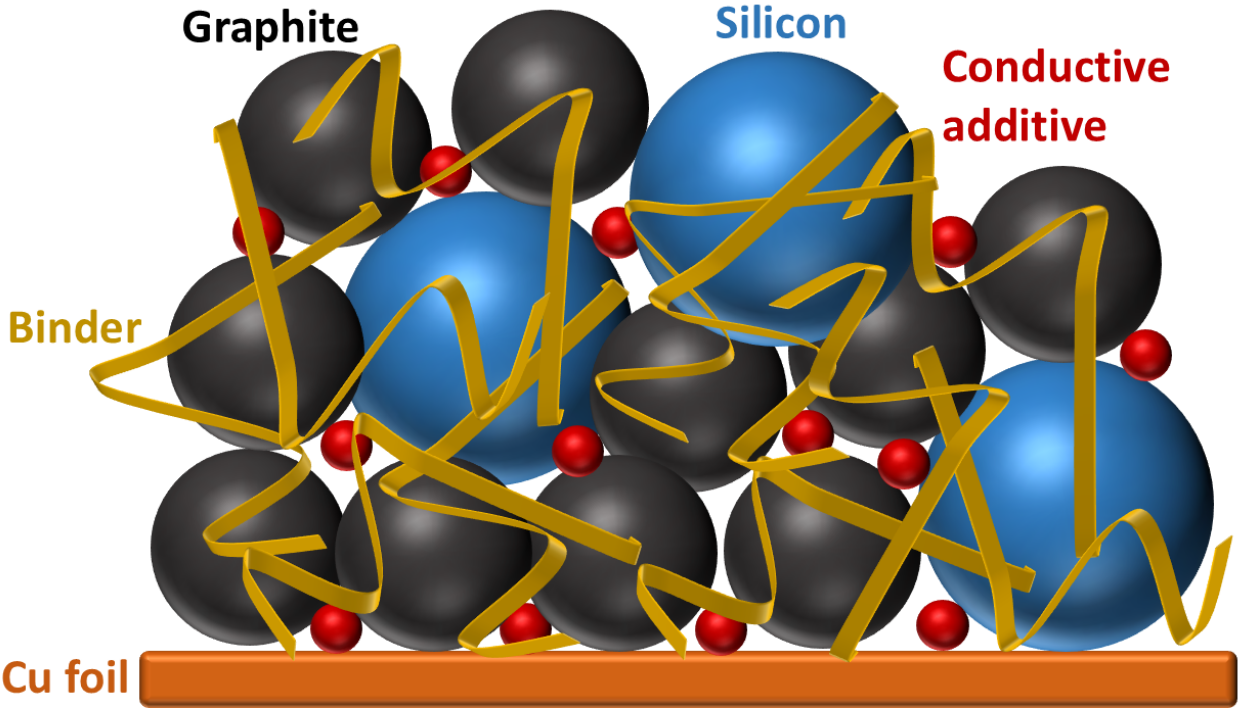

Aachener Beiträge des ISEA Band 191

Investigation of active materials and polymeric binders in silicon-based negative electrodes for lithium-ion batteries

Von der Fakultät für Elektrotechnik und Informationstechnik der Rheinisch-Westfälischen Technischen Hochschule Aachen zur Erlangung des akademischen Grades einer Doktorin der Naturwissenschaften genehmigte Dissertation

vorgelegt von
Niloofar Hamzelui, MSc.
aus Teheran

Berichter:
Univ.-Prof. Dr. rer. nat. Egbert Figgemeier
Univ.-Prof. Dr. rer. nat. Hans-Dieter Wiemhöfer

Tag der mündlichen Prüfung: 16. Dezember 2024

AACHENER BEITRÄGE DES ISEA
Vol. 191

Editor:
Univ.-Prof. Dr. ir. Dr. h. c. Rik W. De Doncker
Director of the Institute for Power Electronics and Electrical Drives (ISEA)
RWTH Aachen University

ISSN 1437-675X

Institute for Power Electronics and Electrical Drives (ISEA)
Campus-Boulevard 89 • 52074 Aachen • Germany
Tel: +49 (0)241 80-96920
post@isea.rwth-aachen.de

Acknowledgements

This dissertation was written during my work as a research associate at the Institute for Power Electronics and Electrical Drives (ISEA) at RWTH Aachen University.

I would like to extend my sincere thanks to all those whose support, guidance, and contributions have been essential to the completion and success of this work. First and foremost, I would like to sincerely thank Prof. Egbert Figgemeier for giving me the opportunity to carry out my PhD in his group. I am truly grateful for his support, encouragement, and valuable guidance throughout the course of this work. I would also like to thank my second advisor, Prof. Hans-Dieter Wiemhöfer, as well as Prof. Uwe Rau and Prof. Johannes Stegmaier, for generously accepting to be members of my examination committee.
I would like to thank all my colleagues at ISEA, especially the ALB-HIMS group. A special thanks to Kidan, Felix W., Sehriban, Hyunsang, Leyla, Hannes, Shiho, Sherran, Laura, Nicha, Martin, Sascha, and Benedikt for your insightful discussions, valuable feedback, and encouragement. Thanks to Viviane, Kevin, and Adrian for all the SEM/EDX measurements and the insightful discussions.
A special thanks to Rita for always supporting me in the lab and for encouraging me to speak German, I appreciate it more than you know. Many thanks to Luke and Felix A. for welcoming me to the group when I first started and for all their support and the engaging discussions we had in the office. Thanks to my students, Gabriela and Julian, for their dedication and hard work in the lab.
I would like to thank my project partners from the GrEEn Project, Ruijie and Max, for the wonderful collaborations that we had together. I also want to extend my thanks to Tsveti and Sasha, from IEK-5 (FZJ), for our collaboration. It was truly a pleasure working with you.
A special thanks to my partner, Aidin, for standing by my side throughout this journey, especially during the challenging moments. Your kindness, encouragement, and support mean the world to me.
Most importantly, I want to thank my parents for their unconditional love and support in every step of my life. Thanks for letting me follow my dreams and always standing by my side, none of this would have been possible without your support.

Niloofar Hamzelui
Aachen, December 2024

Abstract

Silicon (Si) is one of the most promising anode active materials for the next-generation high-energy-density lithium-ion batteries (LIBs), due to its high theoretical capacity compared to state-of-the-art graphite (Gr) anode material. However, the utilization of Si-based anodes in LIBs is limited due to the excessive volumetric changes of Si particles upon lithiation and delithiation. These volume changes lead to particle pulverization, resulting in mechanical degradation, unstable solid electrolyte interphase (SEI), and short cycle life of the battery. To improve the performance of Si-based electrodes, different strategies have been applied. The co-utilization of Si and Gr active materials (Si/Gr composite electrodes) and the development of polymeric binder systems with unique chemistries are two of the most effective strategies to enhance the performance of Si-based anodes.

This thesis focuses on the development of Si-based anodes by optimizing the electrode formulations to achieve better mechanical and electrochemical performance. In the first part of this work, a systematic investigation of Si and Gr active material content in the anode, ranging from pure Gr to pure Si, has been conducted using a dual binder system of lithium poly(acrylic acid) (LiPAA) and carboxymethyl cellulose (CMC). The ratio of binders (LiPAA:CMC) was optimized according to the ratio of active materials (Si:Gr). The electrochemical performance of the electrodes was investigated versus lithium (Li) metal and nickel manganese cobalt oxide (NMC622). Post-mortem scanning electron microscopy (SEM) with energy dispersive X-ray analysis (EDX) was performed on the optimized Si/Gr after lithiation/delithiation at different cycle numbers and C-rates to investigate the changes in morphology and Si particle degradation. The electrochemical performance of the high-capacity Si/Gr and NMC622 cell was investigated and optimized at high temperatures to integrate the cell into a PV-battery system.

In the second part of this work, the optimized Si/Gr anode was further studied using sustainable and environmentally friendly natural polymeric binders. Chitosan biopolymers with different degrees of acetylation (DA) and polymerization (DP) were utilized as binders in the Si/Gr anode. After further fine-tuning of the anode formulation with chitosan binders, cross-linking of chitosan with citric acid monohydrate, combined with the development of a free-standing electrode, resulted in improved electrochemical performance of the cell. The electrochemically cycled Si/Gr anodes were analyzed using X-ray photoelectron spectroscopy (XPS) to study the surface chemistry of electrodes with and without chitosan binder. Moreover, the effect of various parameters of the binder solution, such as pH, was investigated for the state-of-the-art LiPAA binder. The mechanical and electrochemical performance of the Si/Gr anodes, as well as the cross-linking of LiPAA

with CMC, sodium alginate (SA), and tragacanth gum (TG), was studied. All binders were characterized by Fourier transform infrared spectroscopy (FTIR) and thermogravimetric analysis (TGA), and the mechanical properties of the electrodes were measured by a 90-degree peel test. Based on the electrochemical and mechanical properties of the Si/Gr anodes, the LiPAA binder with a neutral pH exhibited superior performance, especially at higher C-rates. Overall, this work indicates the importance of the anode's chemistry and formulation and its direct effect on the electrochemical performance of the LIBs.

Contents

1 Introduction and Motivation

The overconsumption of limited natural resources, notably fossil fuels, leads to environmental issues such as resource depletion and climate change. The increase in global energy demand results in excessive use of petrol and diesel in the transportation sector and other applications, increasing the emission of greenhouse gases, such as carbon dioxide (CO_2). Therefore, it is essential to reduce the dependency on fossil fuels by increasing the use of renewable energy sources, such as solar photovoltaics and wind. However, the intermittency of renewable sources can lead to a mismatch between demand and supply. Energy storage systems play a key role in overcoming these intermittencies and balancing energy supply and demand. Among the various energy storage systems, lithium-ion battery (LIB) technology is highly promising for the integration of renewable energy sources and large-scale applications in electric vehicles and smart grid or utility storage devices. Therefore, much research has been conducted to improve the properties of LIBs, such as energy density, cycle life, operating temperature range, and safety [1]–[5].

The state-of-the-art LIBs are based on graphite (Gr) as an anode active material, due to its abundance, low cost, long cycle life, and low operating voltage ($\sim$0.2 V vs. Li/Li^+). However, the low theoretical capacity of Gr (372 mAh g^{-1}, based on LiC_6) limits its application for high-energy battery technologies. Therefore, anode materials need to be studied and developed that can hold more Li-ions during lithiation. Silicon (Si) is a promising anode active material with a high gravimetric capacity (3590 mAh g^{-1}, based on $Li_{15}Si_4$ at room temperature), high abundance, and suitable operating potential ($\sim$ 0.2–0.4 V vs. Li/Li^+). Therefore, the utilization of Si-based anode materials is of high interest in research and industry. Nonetheless, the main disadvantage of Si is that it undergoes massive volume changes ($\sim$ 200–400% vs. 8–12% for Gr), leading to mechanical instability of the electrode, unstable solid electrolyte interphase (SEI), loss of contact with the current collector, irreversible capacity loss, and short cycle life. Various methods have been investigated to overcome these challenges and enhance the electrochemical and mechanical performance of Si-based anodes. The two most promising strategies are the use of Si/Gr composite electrodes and suitable polymeric binder materials. The Si/Gr composite electrode merges the benefits of both anode active materials, showing less volume change compared to the pure Si electrode and higher specific capacity and electrical conductivity compared to the pure Gr electrode [6], [7]. The optimization of the composite electrode formulation is of high importance in obtaining desirable electrochemical performance. Binders play a major role in the mechanical stability of the electrodes, which has a direct impact on the irreversible capacity loss and cycle life of the battery. Utilizing suitable binder material(s) can accommodate the volume change of Si particles

upon lithiation/delithiation. Binders can be processed in aqueous or non-aqueous solvents. Some of the non-aqueous solvents are toxic and hazardous to the environment and human health, and are more expensive compared to water. The drying process of these toxic non-aqueous solvents is more complicated and time-consuming, and it requires more energy and cost to collect solvent vapors. Therefore, water-based electrode manufacturing utilizing natural polymeric binders is beneficial and more environmentally friendly, not only at the electrode production stage but also for the recycling of the battery [8], [9].

The main goals of this thesis are as follows:

- Develop a high-performance Si/Gr composite negative electrode for LIBs with enhanced specific capacity, coulombic efficiency, and cycle life.

- Investigate the influence of certain parameters and changes in the Si/Gr negative electrode, such as electrode formulation, production process, active materials, and binder chemistry, on the overall performance of the negative electrode and the battery cell.

- Identify and optimize natural and abundant biopolymeric binders suitable for Si/Gr-based systems, while maintaining mechanical integrity during the charge/discharge process. This includes achieving environmental benefits such as water-based processing methods, elimination of hazardous wastes, cost reduction, and contribution to sustainable electrode and battery technologies.

To fulfill the aims of this study, the following investigations were performed. The Si/Gr anode formulation was systematically investigated, and the ratio of active materials (Si:Gr) was optimized to minimize irreversible capacity losses and maintain a stable capacity (close to the theoretical capacity value) and coulombic efficiency over long-term charge/discharge. Abundant, sustainable, and water-soluble biopolymeric binders were investigated in this work to ensure the mechanical stability of the Si/Gr anodes and accommodate the volume change of Si particles upon lithiation/delithiation. The Si/Gr anode formulation was further optimized according to the different binder chemistries. The effect of binders on the electrode/electrolyte interface and the battery cell's overall performance was also investigated. The capability of Si/Gr-based cells for application in an integrated PV-battery system was investigated in solar charging experiments with a perovskite solar cell. The sustainable processing and optimization of the Si/Gr anodes, and the development of natural biopolymeric binders, can contribute to enhanced electrochemical performance of the Si/Gr-based anodes for cost-effective commercial LIBs and reducing the environmental impacts.

2 Lithium ion batteries

In this section, a summary of the history and development of lithium-ion batteries (LIBs) is provided, followed by a detailed explanation of LIBs working principles. In the following chapters, different components of LIBs, such as anode, cathode, binder, and electrolyte, are reviewed and explained in detail.

2.1 History

In 1936, several clay jars, containing cylindrical copper and an iron rod, were found near Baghdad, which dates back to more than 2000 years ago (during the Parthian period in the Persian Empire). It was suggested by a German archaeologist, Wilhelm König, that these pots are similar to galvanic cells and can produce a voltage of 1–2 V. These were the very first concept of batteries and are named Parthian or Baghdad batteries. Later in 1800, the electric battery was invented by Alessandro Volta, followed by the invention of the Daniell cell by John Frederic Daniell in 1836. The batteries mentioned so far were primary batteries, which can only be discharged. In 1859 lead-acid battery was invented by Gaston Planté, which is a secondary battery and is rechargeable. Nickel-cadmium and nickel-metal hydride are also among the secondary batteries [10], [11].

Lithium (Li) has a low atomic weight of 6.938 g mol^{-1} (atomic number of 3), low density (0.534 g cm^{-1}), high specific capacity of 3860 mAh g^{-1}, and low redox potential of -3.04 V vs. standard hydrogen electrode (SHE). Lithium-metal primary battery ($Li\|MnO_2$) was commercialized by Sanyo in 1975. Secondary lithium-ion batteries (LIBs) were commercialized by Sony in 1991, in which carbon-based materials have been commonly used as anode active material. In 2005, Nexelion LIB was developed by Sony, which replaced the graphite with a tin-based anode (Sn–Co–C), which increased the overall battery capacity and thus suggested the use of high-capacity alloy anode materials, such as silicon [12], [13]. Silicon is one of the most promising candidates for replacing state-of-the-art graphite-based anodes due to its high capacity (3590 mAh g^{-1}, $Li_{3.75}Si$, at RT), abundance, eco-friendliness, and low operating voltage (ca. 0.2–0.4 V vs Li/Li^+). However, large volume changes during charge/discharge (approx. 280%) limit its usage and require further electrode optimization [14], which will be discussed in more detail in the following chapters.

2.2 Working principles

Batteries are electrochemical cells that store chemical energy and convert it to electrical energy. In secondary batteries, the conversion between electrical and chemical energy is reversible. A lithium-ion battery is a rechargeable (secondary) battery that contains a negative electrode and a positive electrode. These electrodes are separated by an electrolyte, which is typically a lithium salt dissolved in organic solvent(s). The electrolyte allows the Li ions to transfer from the positive to the negative electrode and vice versa. A separator is used to prevent the physical contact between the negative and positive electrodes, which could otherwise result in a short circuit. The porous structure of the separator is an electron insulator but allows the Li ions to pass through it. The positive and negative active materials are coated on current collectors, which are aluminum for the positive and copper for the negative side. The current collectors are ionically insulating, electrically conductive, and electrochemically stable within the voltage range of the battery.

Figure 2.1 shows a schematic overview of a LIB in a discharging process. Upon discharge, the chemical energy is converted to electrical energy via electrochemical reactions at the electrodes. Oxidation (loss of electron(s)) happens at the negative electrode, while reduction (gain of electron(s)) takes place at the positive electrode. Therefore, in battery science, the negative and positive electrodes are referred to as the anode and cathode, respectively. The oxidation-reduction reactions are known as redox reactions in electrochemistry. Electrons (e^-) travel from the negative to the positive electrode via the current collectors through an external circuit. Meanwhile, lithium ions (Li^+) move from the negative electrode to the positive electrode through the electrolyte. Upon charge, the reverse process occurs. A potential difference is applied between the two electrodes, leading to the oxidation of the positive electrode and the reduction of the negative electrode. The lithium ions travel from the positive electrode, through the electrolyte, to the negative electrode (lithiation of the negative electrode and delithiation of the positive electrode). The electrons travel via the current collectors through an external circuit [10], [15].

A state-of-the-art LIB with a graphite negative electrode and a layered transition metal oxide positive electrode, such as lithium cobalt oxide ($LiCoO_2$), undergoes the following reactions during the charge/discharge process [16]:

$$\text{Negative electrode} : x\text{Li}^+ + 6\text{C} + x\text{e}^- \rightleftharpoons \text{Li}_\text{x}\text{C}_6 \tag{2.1}$$

$$\text{Positive electrode} : \text{LiCoO}_2 \rightleftharpoons \text{Li}_{1-\text{x}}\text{CoO}_2 + x\text{Li}^+ + x\text{e}^- \tag{2.2}$$

In the battery community, the terms “cycling”or “electrochemical cycling” refer to continuous charge and discharge of the battery. One cycle is defined as one complete charge

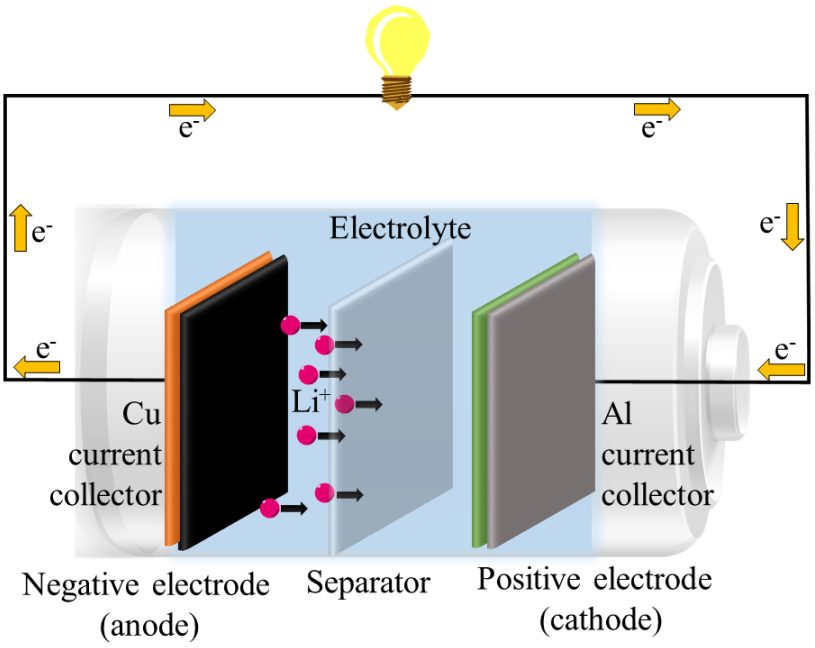

Figure 2.1: Schematic illustration of the operation principles of a lithium-ion battery during discharge.

and discharge process.

Voltage

The electrochemical potential difference between the anode and cathode is the voltage of the battery cell and is the driving force of the electrochemical reactions occurring in the LIB. If the cell is disconnected from any circuit and no current is applied, the cell voltage is referred to as the open circuit voltage (OCV). The potential difference can be described as the difference in Gibbs free energy (ΔG). In an electrochemical cell, under equilibrium conditions, the Gibbs free energy and potential are given by Equation 2.3 [10], [15]:

$$\Delta G^{\circ}_{\text{cell}} = -z \cdot F \cdot E^{\circ}_{\text{cell}} \tag{2.3}$$

where z is the number of electrons or ionic species involved in the reaction, F is the Faraday constant (96485 C mol^{-1}), and E_{cell} is the potential (voltage) difference between the electrodes. The standard Gibbs free energy and the equilibrium constant (K) are related by the following equation [10]:

$$\Delta G^{\circ}_{\text{cell}} = -RT \ln K \tag{2.4}$$

where R is the gas constant (8.31432 J.K^{-1}.mol^{-1}) and T is temperature (in kelvin).

Therefore:

$$-z.F.E^{\circ}_{\text{cell}} = -RT\ln K \rightarrow E^{\circ}_{\text{cell}} = \frac{RT}{zF}\ln K \tag{2.5}$$

Since:

$$\Delta G = \Delta G^{\circ} + RT\ln Q \tag{2.6}$$

where Q is the reaction quotient. Therefore:

$$-z{\cdot}F{\cdot}E_{\text{cell}} = -z{\cdot}F{\cdot}E^{\circ}_{\text{cell}} + RT\ln Q \tag{2.7}$$

$$E_{\text{cell}} = E^{\circ}_{\text{cell}} - \frac{RT}{zF}\ln Q = E^{\circ}_{\text{cell}} - \frac{RT}{zF}\ln\frac{C_{\text{Red}}}{C_{\text{Ox}}} \tag{2.8}$$

Equation 2.8 is known as the Nernst equation, where C_{Red} and C_{Ox} are the concentrations of reduced and oxidized species, respectively. When an electrode is not inan equilibrium condition, an overpotential ($E - E^{\circ}$) arises. The Nernst equation shows that the overpotential of the cell is related to the activity of lithium ions in the positive and negative electrodes, reflecting the concentration gradient. Under non-equilibrium conditions, the concentration gradient results in the movement of lithium ions through the electrolyte and within the electrodes. These diffusion processes are described by Fick's second law of diffusion:

$$\frac{\delta C}{\delta t} = D{\cdot}\frac{\delta^2 C}{\delta x^2} \tag{2.9}$$

where C is the concentration, D is the diffusion coefficient, x is the distance, and t is time. The reaction kinetics within an electrochemical cell is described by the Arrhenius equation:

$$k = Ae^{\frac{-E_a}{RT}} \tag{2.10}$$

where k is the reaction rate, A is a frequency factor or pre-exponential factor, E_a is the activation energy, R is the gas constant, and T is the temperature .

Capacity

The term "capacity"is defined as the available electric charge (Q) in an electrode (anode or cathode), a cell, or a battery. The capacity is usually reported as gravimetric capacity (Ah kg^{-1} or mAh g^{-1}) or volumetric capacity (Ah L^{-1}). The theoretical capacity (Q_{theo}) of an active material can be calculated by Faraday's law of electrolysis (Equation 2.11). Where m is mass (g), I is current (A), t is time (s), M is the molar mass (g mol^{-1}), F is the Faraday's constant (96485 C mol^{-1}), and z is the number of electrons involved in the redox reaction process.

$$m = \frac{It}{Fz}M \tag{2.11}$$

Since electric charge is the current multiplied by time ($Q = It$), the Q_{theo} (in Ah or C) is defined as below:

$$Q_{\text{theo}} = \frac{m{\cdot}z{\cdot}F}{M} = n{\cdot}z{\cdot}F \tag{2.12}$$

where n is the amount of substance (mol).

Specific capacity (also known as gravimetric capacity) is defined as the amount of electrical charge delivered per unit mass, typically expressed in mAh g^{-1}. The terms charge capacity and discharge capacity refer to the amount of charge that is stored during charging and discharging of LIB, respectively. The Coulombic efficiency (CE) of LIBs is defined as the discharge capacity (Q_{dis}) divided by the charge capacity (Q_{ch}), as shown in Equation 2.13:

$$\text{CE} = \frac{Q_{\text{dis}}}{Q_{\text{ch}}}{\cdot}100[\%] \tag{2.13}$$

A CE lower than 100% indicates that a portion of the charge is irreversibly lost, resulting in a higher irreversible capacity (Q_{irr}) in that cycle. Q_{irr} is the difference between the charge and discharge capacity within a single cycle ($Q_{\text{irr}} = Q_{\text{ch}} - Q_{\text{dis}}$), implying that the charge capacity cannot be fully recovered in the discharge process due to parasitic side reactions such as electrolyte decomposition [17].

The current rate, or C-rate is described as the current required to fully charge or discharge a battery over a specific period of time. For example, when a current of 0.1 A is applied to a 1 Ah battery, the C-rate is C/10, meaning that the battery would be fully charged or discharged in 10 hours.

In commercial LIBs, negative electrodes are usually based on graphite active material, and positive electrodes are based on lithium transition metal oxides (the electrode materials will be fully discussed in the following sub-chapters). Due to the difference between the reversible specific capacity of the active materials in the negative and positive electrodes, it is necessary to balance the active mass of negative (N) and positive (P) electrodes. This ensures that both electrodes have similar discharge capacity (Q_{dis}) during battery operation. A general mass balancing calculation, based on the assumption of an equal Q_{dis} for the negative and positive electrodes, is shown in Equation 2.14 [18].

$$Q_{\mathrm{dis}} = q_{\mathrm{N}} \cdot m_{\mathrm{N}} = q_{\mathrm{P}} \cdot m_{\mathrm{P}} \tag{2.14}$$

where Q_{dis} is in mAh, q (reversible specific capacity) in mAh g^{-1}, and m (active mass) in g. Lithium plating is a major safety and aging concern in LIBs, leading to irreversible capacity loss, and can be prevented by slightly oversizing the capacity of the negative electrode. The negative to positive capacity ratio (N/P ratio) can influence the long-term electrochemical performance, energy density, safety, and cost of the battery. If the N / P ratio is less than 1, there are not enough active sites available on the anode to accommodate all the lithium ions removed from the cathode, leading to lithium plating on the anode surface. On the other hand, excessive oversizing of the anode increase the overall mass and volume in the cell, including inactive masses, and results in reducing the specific energy of the battery. Therefore, a trade-off between safety (N/P $>$ 1) and optimizing specific capacity (N/P = 1) is required. In commercial applications, an N/P ratio of approximately 1.1–1.2 is considered optimal [18]–[20].

Energy density

The gravimetric (specific energy) and volumetric energy density of a LIB are defined as the energy that can be stored per unit weight (Wh kg^{-1}) and unit volume (Wh L^{-1}), respectively, as shown in Equations 2.15 and 2.16 [21]:

$$\text{Gravimetric energy density (Wh kg}^{-1}) = \frac{\text{Capacity (Ah)} \times \text{Voltage (V)}}{\text{Weight (kg)}} \tag{2.15}$$

$$\text{Volumetric energy density (Wh L}^{-1}) = \frac{\text{Capacity (Ah)} \times \text{Voltage (V)}}{\text{Volume (L)}} \tag{2.16}$$

2.3 Graphite negative electrode

Graphite (Gr) is a state-of-the-art anode active material due to its long cycle life, high Coulombic efficiency, low working potential ($\sim$ 0.2 V vs. Li/Li^+), low cost, high abundance, and low volume change (8–12 %) during charge/discharge. Graphite was developed as a negative electrode active material for LIBs in 1983 by Yazami and Touzian[22], using a polymer electrolyte. In 1990, Dahn et al. [23] reported that reversible lithium intercalation happens in graphite anodes using liquid electrolytes, containing ethylene carbonate (EC) as a co-solvent, due to the formation of a solid electrolyte interphase (SEI) layer (discussed further in Chapter 2.3.2).

2.3.1 Structural change of graphite upon lithiation and delithiation

Graphite has a layered structure, consisting of stacked graphene layers that are linked by weak van der Waals forces and π-π interactions. The graphene layers are arranged in either an ABAB sequence (hexagonal symmetry), which is thermodynamically favored, or in an ABCABC sequence (rhombohedral symmetry). Graphite has two different types of surfaces in its layered morphology; basal planes and edge (prismatic) planes, as shown in Figure 2.2 [24]–[26].

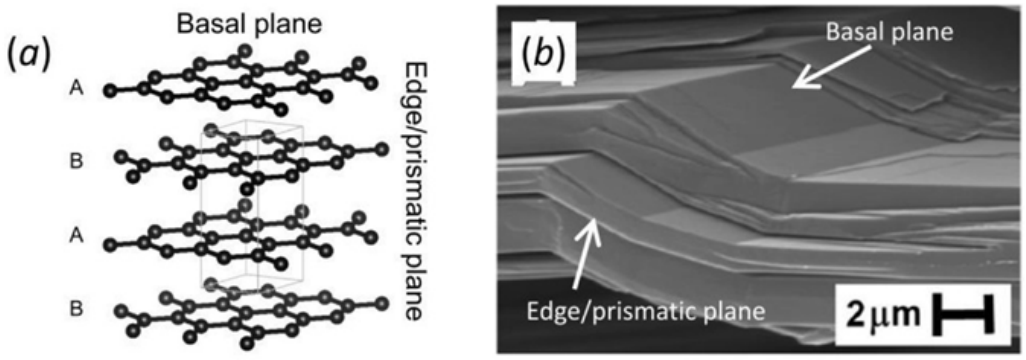

Figure 2.2: (a) A schematic view of graphite's layered morphology, basal and edge planes. (b) SEM image of basal and edge planes in graphite (Reproduced from Ref. [24] with permission from Wiley Online Library. Copyright 2021 and Ref. [25] with permission from Elsevier. Copyright 2014)

The weak van der Waals forces between graphene sheets allow expansion in the distance between the layers, enabling Li ions to intercalate through the edge planes into the graphite structure during battery charging. The intercalation mechanism in graphite is explained by the staging mechanism, which was investigated by Rüdorff and Hofmann in 1938 [27]. According to this model, stage n is defined as the sequence of intercalated ions within the graphene layers, where n is the number of graphene layers in between two adjacent intercalated layers. This concept is schematically shown in Figure 2.3. One

limitation of this model is that the transition from stage 3 to stage 2 cannot be explained since it requires the complete deintercalation of Li ions from one layer and their intercalation into the next available layer. To overcome this limitation, Daumas and Herold [28] modified this model as depicted in Figure 2.3. Based on the Daumas and Herold model in stages 2, 3, and 4, the graphene layers are flexible and can deform around the intercalated Li ions. This structural flexibility allows the transfer from stage 3 to stage 2, as Li ions can diffuse within the same intercalation layer.

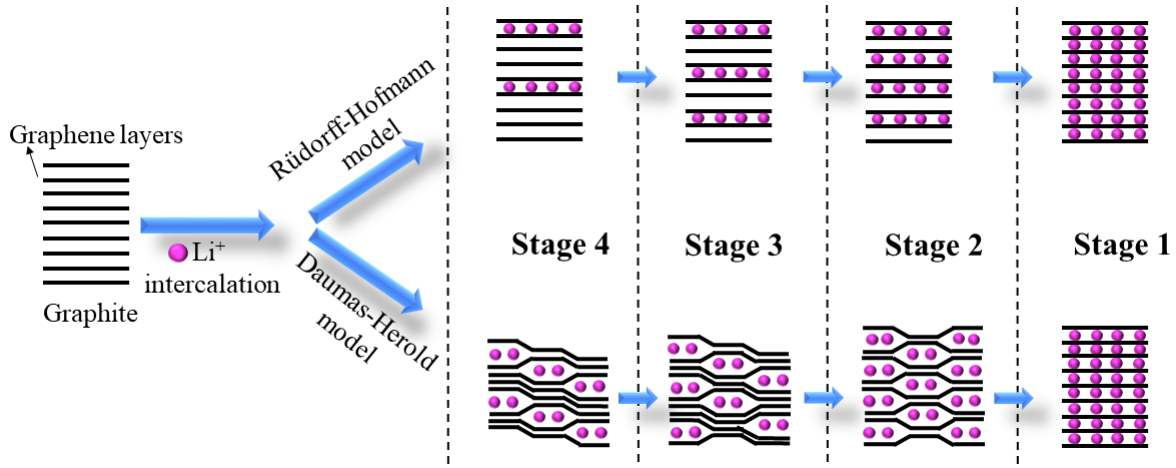

Figure 2.3: Schematic illustration of intercalation mechanism of Li ions in graphite active material, based on Rüdorff-Hofmann and Daumas-Herold models (Inspired and redrawn from Ref. [26] with permission from Royal Society of Chemistry. Copyright 2020)

Graphite has a theoretical specific and volumetric capacity of 372 mAh g^{-1} and 850 mAh cm^{-3}, respectively. The theoretical capacity of graphite is calculated according to Faraday's law of electrolysis (equation 2.12). With z =1/6, LiC_6 representing the fully lithiated state, and M =12.011 u, the atomic mass of carbon. Figure 2.4 shows the electrochemical performance of a graphite anode versus Li metal and the respective stages for Li ion (de-)intercalation. By increasing the content of intercalated Li ions, the graphite anode goes through stages 1L, 4, 3, 2L, 2, and 1, respectively. Stage 1 is the formation of LiC_6 (fully lithiated state), which provides the highest capacity. "L"refers to stages in which Li ions are not organized within the graphene layers. The potential plateaus in Figure 2.4 indicate the stage transitions [26], [29].

2.3.2 Solid electrolyte interphase (SEI)

During the first few charge/discharge cycles, the low reduction potential of the graphite anode results in electrolyte decomposition and formation of a passivation layer on the anode surface, leading to a significant irreversible capacity loss in the initial cycles. The passivation layer, known as the solid electrolyte interphase (SEI) layer, plays an essential

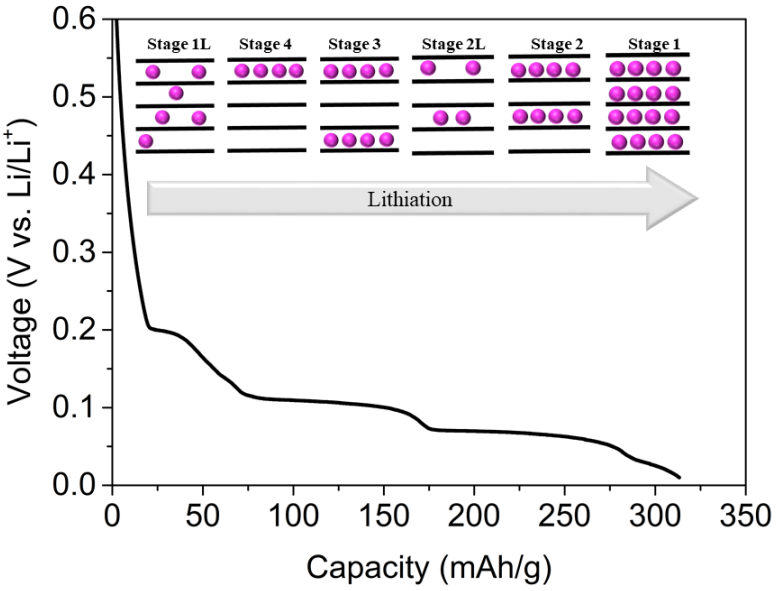

Figure 2.4: Electrochemical performance of graphite anode half cell and different stages of Li ion intercalation during lithiation. Inspired and redrawn from Ref. [26] with permission from Royal Society of Chemistry. Copyright 2020)

role in the subsequent charging/discharging processes. The SEI layer prevents further electrolyte decomposition, allows Li ions to pass through, and acts as an electrical insulator. Therefore, SEI is necessary for the reversible intercalation of Li ions [30], [31]. The SEI layer consists of organic and inorganic species. Inorganic species, such as Li_2O and LiF, form a thin and dense layer close to the graphite surface due to the reduction of electrolyte salt anions. A layer of porous organic species, such as ROLi, $ROCO_2Li$ (R = low-molecular alkyl group), semicarbonates, and polymers, is formed on top of the inorganic layer as a result of electrolyte solvents decomposition [32]. A schematic illustration of the mosaic model of the SEI layer on the graphite anode is shown in Figure 2.5 [33]. According to Shi et al. [34], Li ion diffusion is faster in the porous organic SEI layer compared to the inorganic layer. In Gr anodes, the SEI layer formed on basal planes ($\sim$ 7 nm) is thinner and contains fewer inorganic species compared to the SEI on edge planes ($\sim$ 35 nm). This difference can be due to higher Li ions intercalation through the edge planes, where Li salt anions can decompose and contribute to the formation of inorganic SEI species [26], [35]. Optimizing the electrolyte formulation, particularly through the use of electrolyte additives, can improve the stability of the SEI layer, thereby improving the overall battery performance [26], [36].

Despite many advantageous properties of graphite, its low theoretical capacity (372 mAh g^{-1}) limits its usage in high-energy battery applications. Therefore, anode active materials that store and release Li ions by electrochemical (de-)alloying mechanism have been investigated as promising candidates for high-energy-density LIBs.

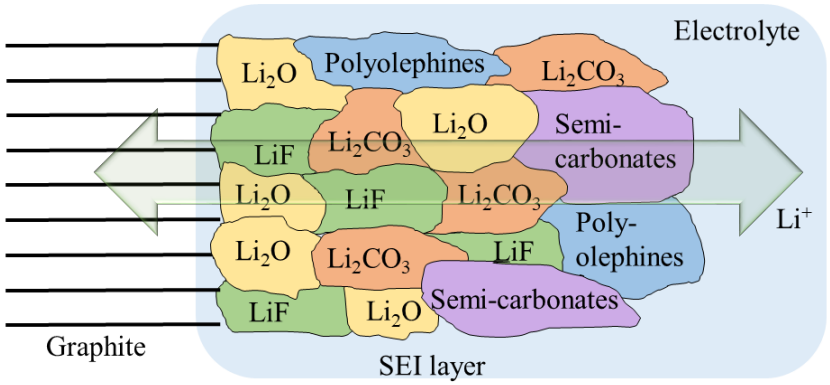

Figure 2.5: Schematic illustration of SEI layer on graphite anode (Inspired and redrawn from Ref. [33] with permission from IOP Publishing. Copyright 1997)

2.4 Silicon negative electrode

Alloy anode active materials are among the most promising candidates for the next-generation LIBs because of their high energy density. Among these materials, silicon (Si) has beneficial properties, such as a suitable operating potential of 0.2–0.4 V vs. Li/Li^+, high abundance, and low cost. During lithiation/delithiation, Si undergoes reversible alloying/de-alloying with Li ions, forming $Li_{4.4}Si$ at 415°C and $Li_{3.75}Si$ at room temperature (RT) in fully lithiated state, according to the Li-Si phase diagram (Figure 2.10). These lithiated stated result in capacities of approximately 4200 mAh g^{-1} and 3590 mAh g^{-1} at elevated temperature and room temperature, respectively [37], [38]. Si-based anodes enhance the capacity and energy density of LIBs, since each Si atom can accommodate up to 3.75 Li ions at room temperature, whereas Gr can intercalate one Li ion per six carbon atoms (LiC_6). However, despite these advantages, Si has a low electronic conductivity and an enormous volume change of 200–400% (vs. 8–12% for graphite) during lithiation and delithiation. This large volume change upon electrochemical cycling (Figure 2.6) leads to Si particle cracking and pulverization, causing mechanical instability of the electrode film, loss of contact with the Cu current collector, irreversible capacity loss, short cycle life, and unstable SEI layer. To overcome these issues, several studies have been performed to improve the performance of Si-based anodes, such as using Si nanostructures [39]–[41], Si nanowires [42], silicon/carbon (Si/C) composite electrodes[43], [44], etc. Additional strategies include the usage of electrolyte additives [3], [31], [45]–[47], and suitable polymeric binders [3], [48]–[50], which have been widely investigated to improve the electrochemical performance and stability of Si anodes[51].

As mentioned above, an effective strategy to enhance the performance of Si anodes is to combine Si and Gr active materials in a so-called Si/Gr composite (blend) anode, which results in the synergistic effects of both active materials. The Si/Gr anode is expected to show a longer cycle life, higher electrical conductivity, a more stable SEI layer, and reduced volume change compared to pure Si anodes. Moreover, the presence of Si increases

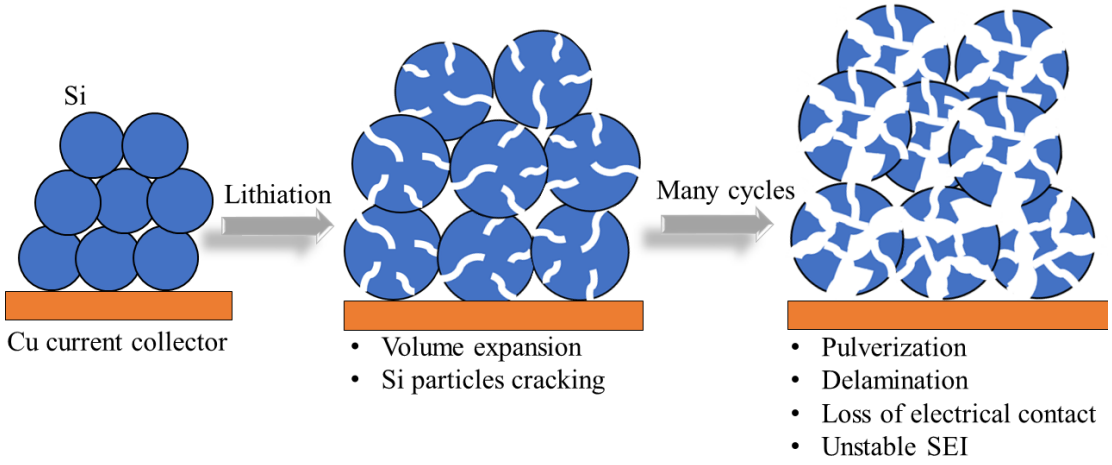

Figure 2.6: Schematic illustration of Si particles volume expansion upon lithiation

the overall capacity of the electrode compared to pure Gr anodes. An overview of the synergistic effect of using both Si and Gr active materials in the negative electrode is shown in Figure 2.7. It should be noted that the preparation process of the Si/Gr anode and the slurry formulation and optimization are of high importance and have a significant impact on the capacity and cycling stability of the anode. These aspects will be discussed in detail in Chapter 4.

Another method to mitigate the large volume change of Si is the use of suitable binders for Si-based anodes. These binders form a strong network that can accommodate mechanical stresses due to the volume change of Si particles during electrochemical cycling. Although binders are considered electrochemically inactive components of LIBs, they play a major role in the mechanical stability of the electrodes, irreversible capacity losses, and stabilizing the cycling performance. The effect of binders will be fully discussed in Chapters 2.5, 4, and 5.

2.4.1 Surface chemistry of silicon

Si powder (nm–µm scale) is used for preparing Si-based anodes in LIBs. Once Si particles get in contact with oxygen and moister at room temperature native oxide film (amorphous SiO_x) will form on the Si surface (Equations 2.17 and 2.18), containing Si–O–Si (siloxane) and Si–OH (silanol) functional groups [8], [52], [53]. Therefore, hydroxyl (–OH) terminations exist on the surface of the Si particles, forming thermodynamically stable SEI species such as LiOH and Li_2O. The SEI layer of Si-based anodes contains Li_xSiO_y due to the reactions of the native oxide layer [54].

$$Si + O_2 \rightarrow SiO_2 \tag{2.17}$$

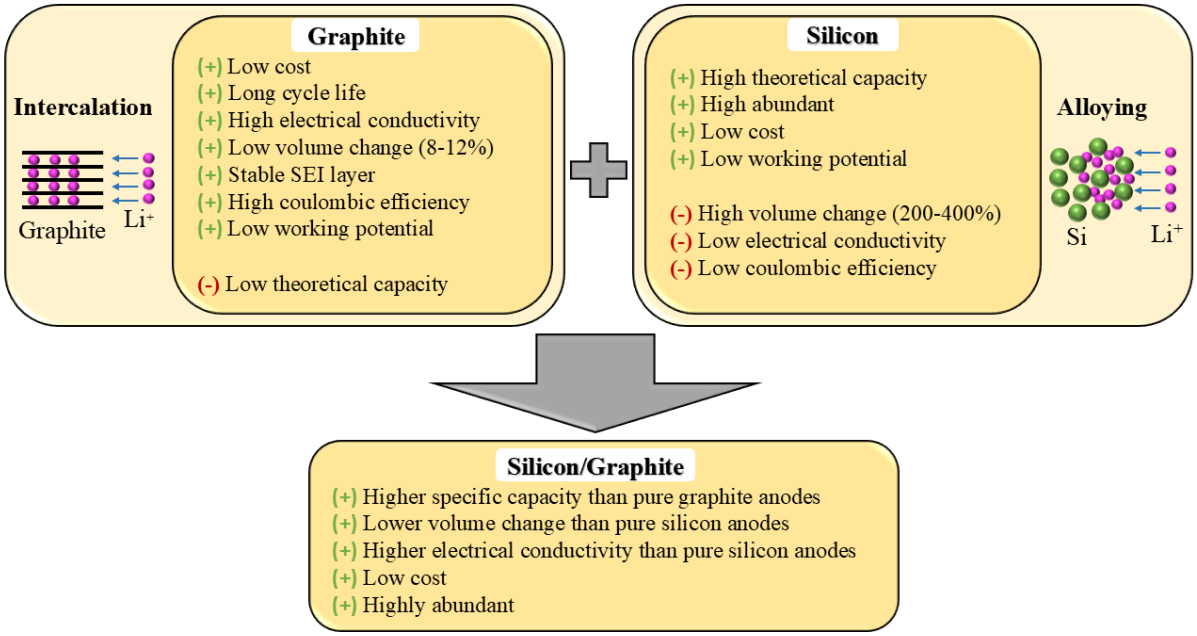

Figure 2.7: Overview of the synergistic effect of using silicon/graphite blend anodes in LIBs (Inspired by Ref. [7])

$$2Si + 2H_2O \rightarrow SiO_2 + 2H_2 \tag{2.18}$$

Si is more hydrophilic compared to Gr and therefore, Si oxidation can happen during slurry formation, in the presence of water, leading to the generation of gas (production of H_2) in the slurry, especially in large production scales. Contact of Si particles with the solvent (water) and carbon black (CB), as well as the reaction of O_2 with the defects on the Si surface (caused by mechanically grinding the Si particles), can lead to Si oxidation during slurry preparation [52]. The Li salts in the electrolyte, such as $LiPF_6$, decompose during electrochemical charge/discharge (Equations 2.19 and 2.20), which can react with the Si oxide native film.

$$LiPF_6 \rightarrow LiF + PF_5 \tag{2.19}$$

$$PF_5 + H_2O \rightarrow POF_3 + 2HF \tag{2.20}$$

The Si oxide native film and Si surface go through chemical and electrochemical reactions shown in Equations 2.21 to 2.24, leading to the formation of the SEI layer on the surface of the anode [3], [55], [56].

$$SiO_2 + 4Li^+ + 4e^- \rightarrow Si + 2Li_2O \tag{2.21}$$

$$Si + xLi^+ + xe^- \rightarrow Li_xSi \tag{2.22}$$

$$ySiO_2 + xLi^+ + xe^- \rightarrow (y-1)Si + Li_xSiO_{2y} \tag{2.23}$$

$$SiO_2 + HF \rightarrow SiO_xF_y + H_2O \tag{2.24}$$

Figure 2.8 shows the differential capacity (dQ/dV) vs. voltage analysis (explained in Chapter 2.8.1) for the Si half-cell at the first cycle. Fears et al. [55], [57] investigated the SEI layer formation of Si anodes via X-ray photoelectron spectroscopy (XPS) and showed that above 0.6 V SEI layer formation starts and continues to grow during SiO_2 (0.4 V) and Si (0.2 V) lithiation, forming products such as Li_2CO_3, LiF, and Li_4SiO_4 or $Li_2Si_2O_5$. These lithiation products strongly affect the properties of the SEI layer. For example, Li_4SiO_4 has low ionic conductivity and reduces the Li-ion diffusion in the SEI [58]. The SEI layer formed on Si electrodes at the lithiated state is thicker compared to graphite [59].

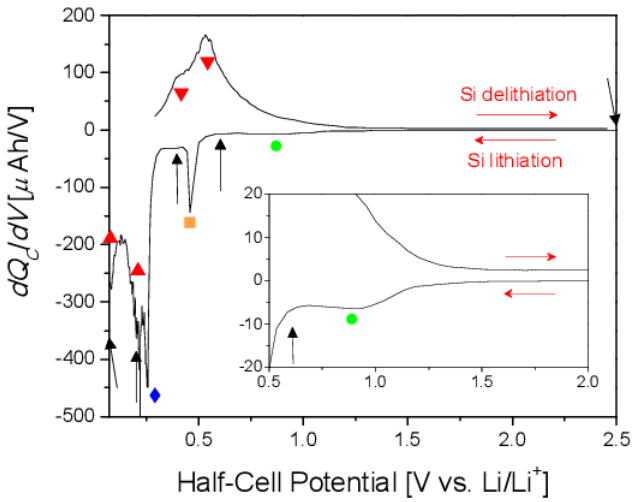

Figure 2.8: Differential capacity (dQ/dV) vs. voltage curve for a thin film Si half-cell at the first cycle. Shape marks show the electrochemical reactions: SEI layer formation (green circle), SiO_2 lithiation (orange square), irreversible lithiation (blue square), Si lithiation/delithiation (red triangle) (Reproduced from Ref. [57] with permission from Royal Society of Chemistry. Copyright 2016)

Cao et al. [56] studied the potential dependence of the SEI layer formation on the native oxide surface on the Si anodes. Figure 2.9 shows a schematic illustration of the SEI layer formation on the Si anode at different voltages upon lithiation. Based on the XPS measurements performed by Cao et al. [56], at open circuit voltage (OCV), the native oxide film is covering the surface of the Si electrode. At 0.8 V, the organic SEI layer and a small amount of electrolyte decomposition products are formed, but the native oxide layer is not reacted. At 0.7 V, the native oxide layer starts to lithiate and form Li_xSiO_y. The lithiation of the native Si oxide film will also result in the formation of Si and lithium silicide (Li_xSi). At 0.6 V, the top inorganic SEI layer starts to form due to electrolyte decomposition, which mostly contains LiF. The bottom SEI continues to grow up to 0.3 V by further reduction of the native oxide to Li_xSiO_y, and the formation of Li_2O starts. At 0.2 V, Li_2O is formed in the bottom inorganic SEI layer [56], [60]–[62].

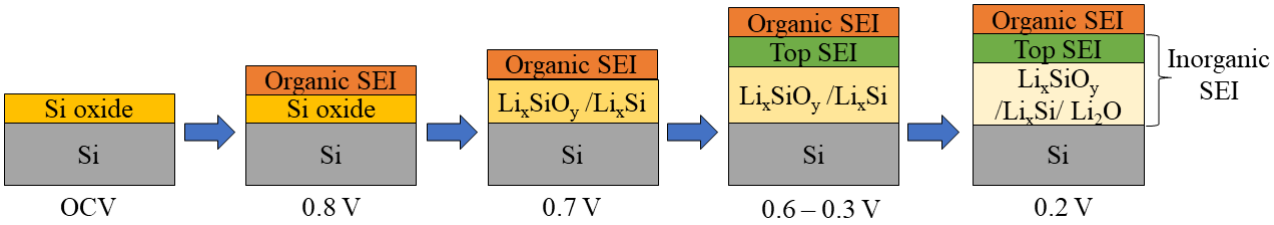

Figure 2.9: Schematic illustration of SEI layer formation on Si native oxide film in a Si anode at different voltages (Adapted and redrawn from Ref. [56] with permission from Elsevier. Copyright 2019)

The functional groups present on the surface of Si can chemically react with binders containing functional groups such as carboxyl (–COOH) by forming hydrogen bonding and/or ion-dipole interactions, which will be fully discussed in Chapter 2.5.

2.4.2 Electrochemical lithiation/delithiation of silicon

The reaction between Li and a metal or an alloy compound is generally divided into two different types: (1) solid-solution reactions and (2) addition reactions. In both types, Li-ions are added to the reactant phase without removing the reactant's components (Equation 2.25) [63], where M is the reactant, which can be a compound or an element.

$$\mathrm{Li} + x\mathrm{M} \leftrightarrow \mathrm{LiM}_x \tag{2.25}$$

In solid-solution reactions, the lithiated LiM_x has the same phase or structure as M. In addition reactions, the phase of the LiM_x product is different from the phase of the M reactant. Lithiation/delithiation of crystalline Si is an addition reaction, in which an amorphous Li_xSi_y phase forms. The amorphous lithiated Si phase can accommodate a high amount ($x = 3.4 \pm 0.2$) of Li per Si atom, therefore, high capacity and volume change

are observed. Based on the Gibbs phase rule, in a closed system, the degree of freedom (f) is defined as $f = C - P$, where C is the number of components and P is the number of phases. In a binary Li-M system with a solid-solution reaction, $C = 2$ and $P = 1$, the electrical potential is a degree of freedom and a function of Li concentration, which is represented as a slope in the voltage profile. Whereas, in an addition reaction, $C = 2$ and $P = 2$, $f = 0$, and the electrical potential is under equilibrium and does not depend on the composition. Therefore, a plateau in the voltage profile is observed in the regions where two phases co-exist [63], [64].

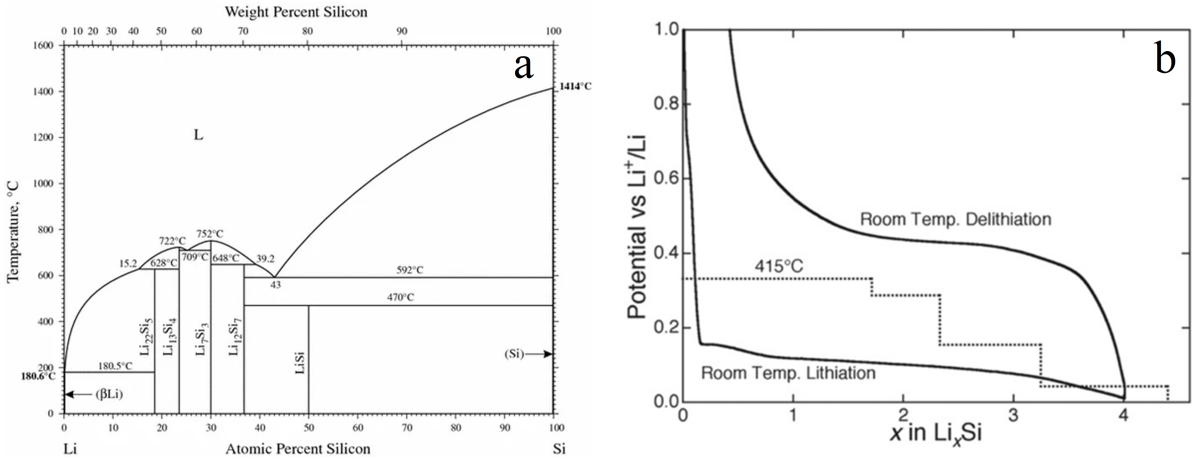

Figure 2.10: a) Si-Li phase diagram (Reproduced from Ref. [65] with permission from Springer. Copyright 2009), b) Voltage profile of crystalline Si upon lithiation/delithiation at 415°C (dotted line) and room temperature (solid line) (Reproduced from Ref. [66] with permission from Wiley Online Library. Copyright 2013). High temperature data are from Ref [38].

Wen and Huggins [38] showed that based on the Li-Si phase diagram (Figure 2.10a) at 415°C, Li and Si electrochemically react and produce $Li_{12}Si_7$, Li_7Si_3, $Li_{13}Si_4$, and $Li_{22}Si_5$ at 332, 288, 158, and 44 mV respectively. This results in a stepped galvanostatic voltage profile, according to the coulometric titration measurement [38], which is shown in Figure 2.10b (dotted line). Elevated temperatures enhance the formation of crystallized equilibrium intermetallic phases, however, this process is different at room temperature (RT), as it is also shown in Figure 2.10b (solid line) and depends largely on the Si particle size and depth of lithiation. The voltage profile for charge/discharge of crystalline Si at RT shows a flat plateau at ~0.1 V vs. Li/Li^+, which is because of the existence of two phases: lithiated amorphous Li_xSi_y and non-lithiated crystalline Si. The difference between the voltage profile at room temperature and the equilibrium voltage profile at high temperature is due to the electrochemical solid-state amorphization, which happens at room temperature. This leads to the formation of metastable a-Li_xSi_y, since the formation of the equilibrium intermetallic Li_xSi_y phase is kinetically not favorable at room temperature (due to higher Gibbs free energy). Figure 2.11 shows the four different possibilities that a metal electrode can get lithiated electrochemically. Figure 2.11a shows the plating of Li

metal on the surface of the electrode, which can happen when alloying is thermodynamically not favored or when Li ions travel at a high rate and the alloying reaction cannot take place. In Figure 2.11b, the supersaturation of the alloy has happened. Figure 2.11c shows the conventional alloying, leading to the formation of solid solutions or crystalline compounds based on the equilibrium phase diagram. However, if the crystalline Li-M phase is not kinetically favored and the amorphous phase with lower Gibbs free energy can form, amorphization happens according to Figure 2.11d [67], [68].

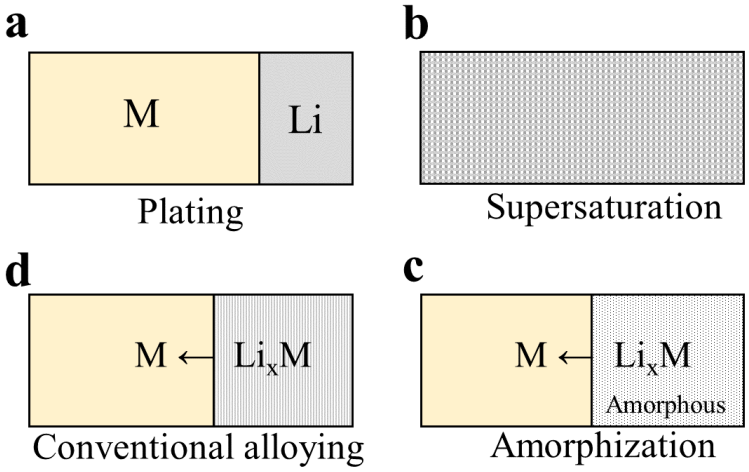

Figure 2.11: Electrochemical lithiation of a metal (M) electrode: a) Li plating, b) Supersaturation, c) Alloy formation (equilibrium), d) Solid state amorphization (Adapted and redrawn from Ref. [67] with permission from Elsevier. Copyright 2003)

2.5 Binders

Binders have a remarkable impact on the mechanical stability of the electrodes, leading to less irreversible capacity loss and stable cycling performance of the battery. Binders are divided into two groups: aqueous (water-based) and non-aqueous. Poly (vinylidene difluoride) (PVDF) is a conventional non-aqueous binder used for both anodes and cathodes. It is soluble in N-methyl-2-pyrrolidone (NMP), which is a toxic, not environmentally friendly, and expensive solvent (compared to water). In addition to health hazards, NMP has a boiling point of 203 °C; therefore, the drying process of NMP-containing electrodes requires higher temperatures, longer processing times, and specialized equipment for collecting and disposing of the toxic vapors. On the other hand, aqueous binders enable environmentally friendly and cost-effective slurry processing and electrode fabrication. Therefore, many investigations have been carried out to replace non-aqueous binder systems with aqueous binders. Aqueous binders derived from natural and organic sources are known as natural binders, such as carboxymethyl cellulose (CMC), chitosan, alginate, etc. [50], [69], [70]. These binders are introduced in this chapter and discussed in more detail in Chapters 4 and 5.

2.5.1 Enabling characteristics of polymer binders for silicon-based electrodes

As discussed in Chapter 2.4, binders used in Si-based electrodes play a critical role in maintaining the mechanical stability of the electrode upon volume changes associated with lithiation and delithiation, which greatly impacts the electrochemical performance of Si-based anodes in high-performance LIBs. The enormous volume change of Si particles upon electrochemical cycling can lead to particle pulverization and repeated destruction and reconstruction of the SEI layer, resulting in high electrolyte consumption, SEI layer thickening, and irreversible capacity loss. In this thesis, the term "accommodate"describes the function of binders that exhibit mechanical elasticity, stretchability, and ductility upon Si volume change, while remaining attached to the surface of Si particles and the current collector (Figure 2.12). Binders that accommodate the volume change of Si particles enhance the interfacial adhesion strength between the binder and active material and maintain the mechanical integrity and electrical conductivity of the electrode [49], [71], [72]. This reduces stress and damage to the anode film, as well as the capacity loss of the battery.

Extensive research has been conducted on polymeric and bio-derived water-based binders for Si-based anodes. For example, Choi et al. [73] developed a spider silk binder that can accommodate the massive volume change of Si and enhance the cycling stability of the battery cell. Other investigations have developed multi-component binder systems (containing more than one type of binder) to better accommodate the volume changes of Si particles. For instance, Kang et al. [74] developed a binder system containing poly-

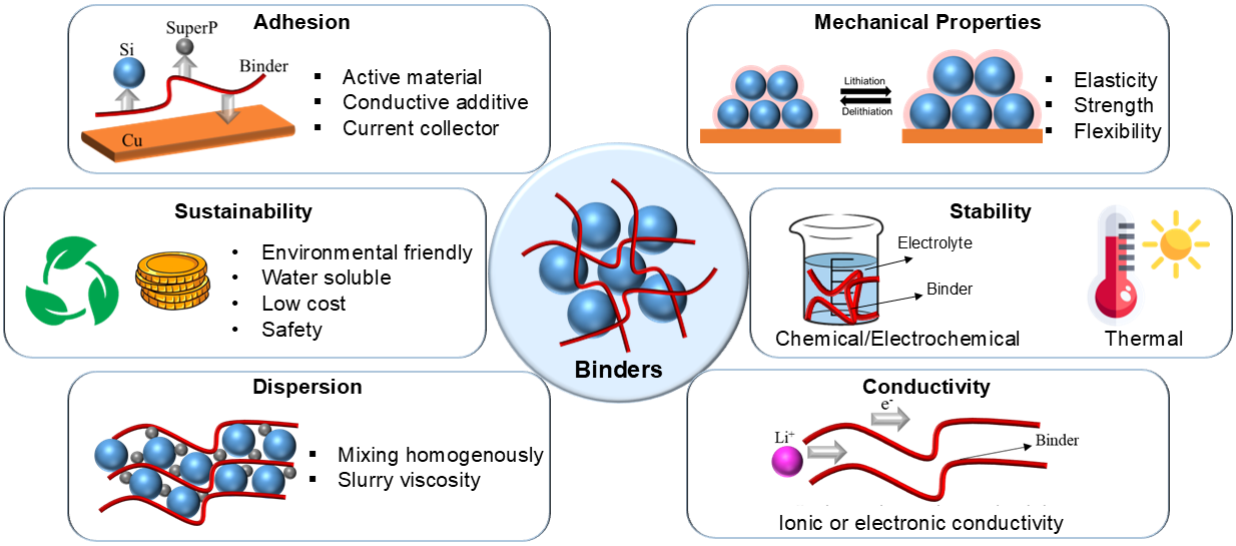

Figure 2.12: Schematic illustration of the key properties of a suitable binder for Si-based electrodes.

acrylamide (PAM), CMC, styrene butadiene rubber (SBR), and poly(tetrafluoroethylene) (PTFE), which enhanced cycling performance and reduced electrolyte consumption compared to anodes with a single binder. Figure 2.12 shows the key properties of an ideal binder material, particularly for Si-based electrodes. As mentioned earlier, adhesion and elasticity of the binder are highly important parameters for binder performance. Furthermore, the chemical structure and functional groups of the binders significantly influence the physical and chemical properties of the binder, as well as its compatibility with Si active material [75], [76]. The binder solution also impacts the dispersion of active and conductive materials within the slurry, as well as the slurry viscosity. Binders need to be chemically stable in contact with the electrolyte and have electrochemical and thermal stability within the operating voltage and temperature ranges of the battery. Moreover, the ionic and electronic conductivity of the binder also impacts the electrode's performance upon lithiation and delithiation [77], [78]. Other factors, such as sustainability, abundance, and cost, are highly important in the selection of binder materials for specific applications [79].

2.5.2 Molecular level functionality of bio-derived polymer binders for silicon-based electrodes

The interaction of the functional groups of the polymeric binders and Si active material can affect the mechanical and electrochemical stability of the anode films by allowing better accommodation of the Si volume change upon the charge and discharge process. Therefore, it is crucial to study the functional groups of the polymeric binders.

Carboxyl (–COOH) and hydroxyl (–OH) functional groups are important binding sites commonly found in polymeric binders. Carboxyl groups, consisting of carbonyl (C=O) and hydroxyl groups attached to a C atom, are polar and water-soluble. However, longer carbon chains increase the hydrophobicity of the molecule. Carboxylic groups can accept and donate hydrogen bonds due to their carbonyl and hydroxyl groups, respectively. Binders containing carboxylic or hydroxyl groups form polar hydrogen bonds with the native SiO_x surface layer, thereby enhancing the adhesion. Carboxymethyl cellulose (CMC) [80]–[82], sodium alginate (SA) [83], [84], and polyacrylic acid (PAA) [85]–[90] are among the commonly used binders in Si-based electrodes, due to their abundance of carboxyl and hydroxyl functional groups. Carboxyl groups of the binders can also improve the electrolyte absorption in battery electrode[91]. Amino ($–NH_2$) functional groups in polymeric binders can interact with the surface of Si particles. These groups can also be cross-linked with PAA, citric acid, or glutaraldehyde, to form a 3D binder network that can improve the mechanical and electrochemical performance of Si-based anodes [8], [92]–[94]. The catechol functional group ($C_6H_6O_2$) results in excellent wetness-resistant adhesion [95], [96]. Ryou et al. [96] conjugated mussel-inspired adhesive catechol groups to PAA and alginate backbones in Si nanoparticle (NP)-based and Si/Gr anodes. Catecholic adhesion and hydrogen bonds improved the cycling performance and capacity retention of the anodes. Moreover, the catecholic interaction with the surface of Si NP allows more Si NP to actively participate in the lithiation/delithiation process, thus increasing the capacity of the anode.

Carboxymethyl cellulose (CMC)
CMC is a semiflexible linear polymer derived from cellulose and is one of the most abundant biopolymers on Earth. In CMC, some of the hydroxyl groups are substituted with carboxymethyl groups ($–CH_2COOH$) (Figure 2.13a). The degree of substitution (DS) in CMC is defined as the number of substituted hydroxyl groups in one monomer. The highest DS is three because of the three hydroxyl groups per carbon ring [80], [97], [98]. In a study by Wang et al. [99], it was shown that DS influences the specific capacity and cycle life of Si-based anodes using nano-silicon. A DS of 0.55 was identified as the optimum value in their research.

Polyacrylic acid (PAA)
PAA contains carboxyl groups and is a high-performing binder for Si-based anodes, enhancing the Coulombic efficiency and cycle life of the cell [86], [88]. Carboxylic groups

in PAA can dissociate in water with the addition of alkaline hydroxides such as LiOH, NaOH, or KOH. The neutralization degree can be adjusted by the amount of alkaline hydroxides (AOH) in the binder solution, as shown in Equation 2.26 [100]:

$$\begin{aligned} -[CH_2 - CH(COOH)]_n - + xAOH \rightarrow \\ -[CH_2 - CH(COOH)]_{n-x} - [CH_2 - CH(COOA)]_x + H_2O \end{aligned} \tag{2.26}$$

The pH of the binder solution can be controlled by adjusting the degree of neutralization. The addition of AOH increases the pH of the PAA solution from acidic to basic [100]. PAA is commonly used as lithium polyacrylic acid (LiPAA) or sodium polyacrylic acid (NaPAA). The chemical structure of LiPAA is shown in Figure 2.13b. The addition of alkaline hydroxides and the pH adjustment can directly influence the physical and chemical properties of the slurry and the electrode [86], [100].

Sodium alginate (SA)
Alginate is a linear natural polysaccharide derived from algae, commonly used in the form of its sodium (Na), Sodium alginate (SA) ($NaC_6H_7O_6$) [101], as shown in Figure 2.13c. SA is water-soluble and contains a high number of hydroxyl and carboxylic groups, which can form hydrogen bonds and ion-dipole interactions with Si particles [101], [102].

Tragacanth gum (TG)
Tragacanth gum (TG) is one of the most abundant polysaccharides and is biocompatible, biodegradable, and rich in carboxyl and hydroxyl groups. TG is a natural gum that is used as a stabilizer, thickener, emulsifier, moisturizer, and water-soluble binding agent in the textile, pharmaceutical, and food industries [103]–[106]. TG has been studied as a binder for graphite anodes [107], carbon-based materials for electrochemical capacitors [108], and high-voltage lithium nickel manganese oxide (LNMO) cathode [109]. The chemical structure of TG is shown in Figure 2.13d.

Chitosan
Chitosan biopolymer is produced by the partial deacetylation of chitin (poly(β-(1→4)-N-acetyl-D-glucosamine)) according to Figure 2.14. Chitin is one of the most naturally abundant polysaccharides after cellulose and the most abundant nitrogen-containing organic compound in nature [110], [111]. Chitin is lightweight, and due to its superior mechanical properties, such as high strength and toughness, it is one of the major load-bearing components in the stiff tissues of the exoskeleton of diatoms, sponges, corals, and mainly arthropod cuticles and shells of crustaceans (such as shrimps, crabs, and lobsters). In these structures, chitin fibers are within a protein network, along with calcium carbonate and silica [110]. Chitin's structure is similar to cellulose, in which the hydroxyl groups are replaced by acetamide groups (–$NHCOCH_3$), and it is not soluble in water [112], [113].

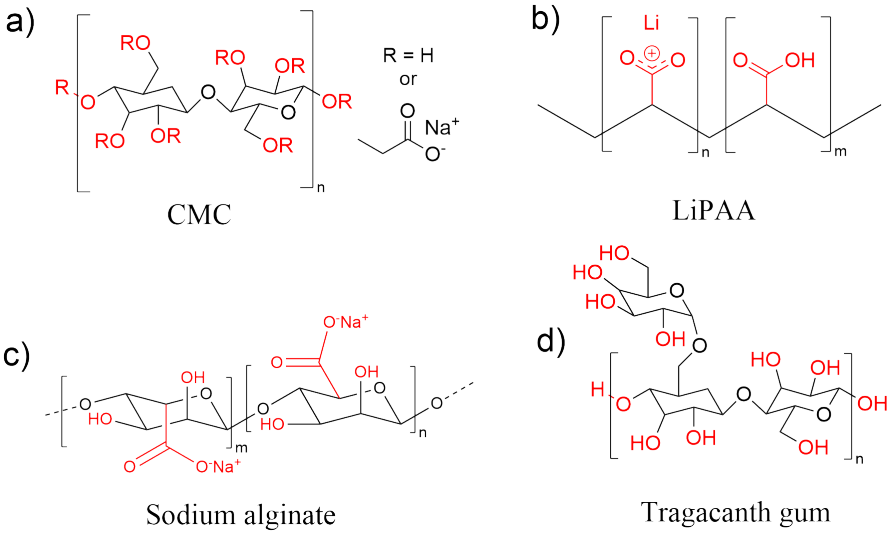

Figure 2.13: Chemical structure of a) Carboxymethyl cellulose (CMC), b) Lithium polyacrylic acid (LiPAA), depending on the degree of neutralization/pH, number of carboxyl groups or Li substituted carboxyl groups may vary, c) Sodium alginate (SA) and, d) Tragacanth gum (TG)

To extract chitin, acid and alkaline treatments are performed to remove calcium carbonate and proteins, respectively. The (partial) deacetylation of chitin under alkaline conditions (concentrated NaOH) or enzymatic hydrolysis results in the production of chitosan, which is the most important derivative of chitin [111]. Due to the hydrophobicity of acetyl groups (CH_3CO) chitin does not dissolve in aqueous solutions, however, chitosan can be dissolved in dilute aqueous acid solutions, such as acetic acid, by converting the glucosamine unit ($R–NH_2$) into its protonated form ($R–NH_3^+$) [93], [111], [114]. Chitosan biopolymer consists of acetylated (N-acetyl-D-glucosamine (GlcNAc)) and deacetylated units (β-(1,4)-linked D-glucosamine (GlcN)) (Figure 2.14). The degree of acetylation (DA) is described as the percentage of monomeric acetylated units (Equation 2.27). DA determines the chemical and physical properties of the chitosan biopolymer [50], [110], [115]. Acetyl groups and the DA can affect the mechanical properties of chitin and chitosan. Acetyl groups can contribute to the hydrogen bond formation and stabilization of the hydrogen bond network, which enhances the fracture resistance of the biopolymer [110]. Acetyl, hydroxyl, and amino groups in chitosan form hydrogen bonds and dipole-dipole interactions with the surface of the active material and the Cu current collector, thereby improving the mechanical and electrochemical performance of the anodes [92], [116], [117].

$$\mathrm{DA} = \frac{n(\mathrm{GlcNAc})}{n(\mathrm{GlcNAc}) + n(\mathrm{GlcN})} \cdot 100\% \tag{2.27}$$

The degree of polymerization (DP) refers to the number of monomeric units in the chi-

tosan biopolymer (Equation 2.28) and is correlated with its molecular weight (M_W). The mechanical properties of polymers, such as tensile strength, are directly influenced by DA, DP, and M_W. The research conducted in this thesis on chitosan biopolymeric binder is fully described in Chapter 5.1.

$$DP = n + 2 \tag{2.28}$$

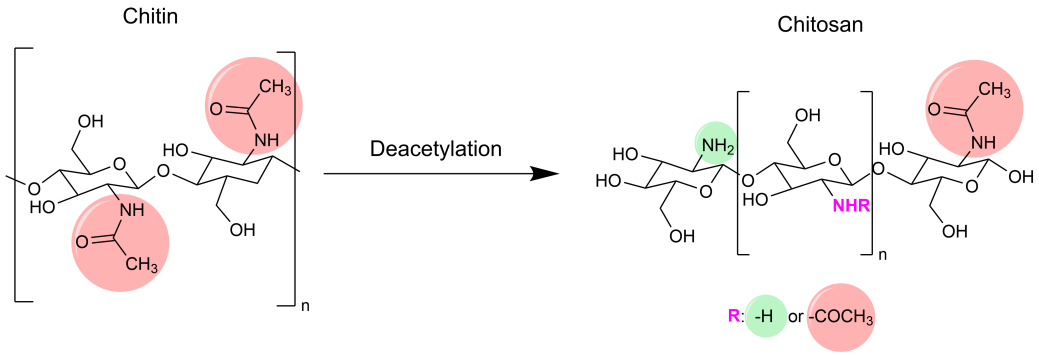

Figure 2.14: Partial deacetylation of chitin to chitosan. (Reproduced from Ref. [50] (Hamzelui et al.) with permission from Wiley Online Library. Copyright 2022)

2.5.3 Interactions between active materials and polymeric binders

The chemistry of polymeric binders directly influences the adhesion strength between the binder and electrode, and the cohesion of the electrode film [69]. Covalent bonds form when two atoms share an electron pair. The Si–O and Si–OH on the surface of Si particles covalently bond with the polymeric binders by chemically reacting with their functional groups. During the electrode drying process at elevated temperatures, esterification may occur between OH groups on the Si surface and COOH groups of the binders, such as CMC with a neutral pH [118]. In an investigation by Mazouzi et al. [119], it is suggested that the esterification reaction is enhanced at ∼pH 3. Decreasing the pH neutralizes SiO^- and COO^- groups to SiOH and COOH, respectively, and therefore, favors the esterification [119]. PAA binder covalently bonds with OH groups on the Si oxide surface layer [120]. Another example is glyoxalated polyacrylamide (GxPAAm) binder, which forms a covalent bond with Si under acidic conditions (pH ∼4) [121]. Polysaccharides containing carboxylic groups in their side chains, such as CMC and pectin, can form covalent bonds with the oxide layer on the Si surface. Yoon et al. [122] investigated pectin as a binder for Si-based anodes, and suggested that due to its elastic nature and strong covalent bond with Si, pectin accommodates the volume change of Si particles during charge/discharge. However, despite the strong adhesion provided by covalent bonds, these bonds are irreversible and cannot be recovered upon breaking. In contrast, dynamic covalent bonds

can form between the polymer binder and Si active material with the help of external factors such as catalysts, heat, or pH [21], offering partial self-healing capability. Otherwise, mechanical stress caused by the large Si volume change upon charge/discharge leads to a plastic rupture of covalent bonds. Hence, binders that form covalent bonds are not always ideal for the Si-based anodes. Alternatively, supramolecular interactions are reversible, dynamic, and recover once broken (self-healing), however, these interactions are weaker compared to covalent bonds. The recovery of supramolecular interactions depends on the strength of the interactions. Figure 2.15 illustrates the chemical bonds and supramolecular interactions and their adhesion properties in Si-based anodes [69].

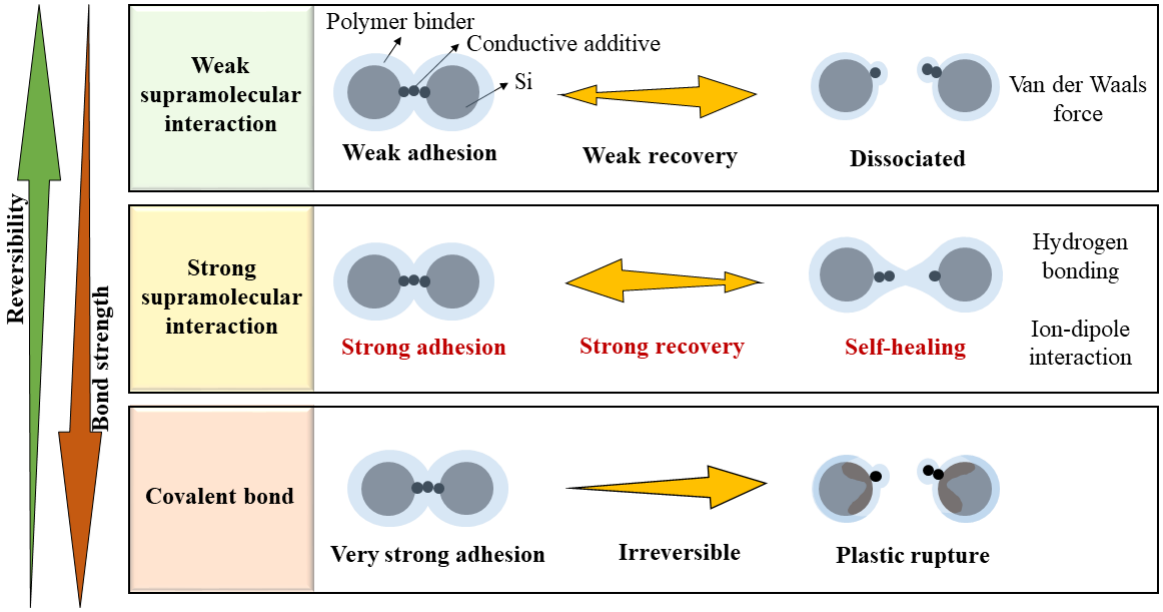

Figure 2.15: Chemical bonds and supramolecular interactions and their adhesion properties in Si-based anodes. (Inspired and redrawn from Ref. [69], with permission from Royal Society of Chemistry. Copyright 2018)

Van der Waals force is among the weakest supramolecular interactions that occur upon temporarily induced dipoles in two molecules, which can dissociate under small mechanical stress. These weak bonds result in low reversibility and show a low driving force to recover [69]. For example, the state-of-the-art PVDF binder; the weak Van der Waals force between the binder and active material cannot maintain the stability of Si-based anodes upon high volume change of Si particles during charge/discharge [123].

Dipole-dipole bonding occurs between molecules with permanent dipoles. Biomaterials and biopolymers usually contain functional groups containing oxygen and nitrogen, which can form dipole-dipole bonds with the oxides on the Si surface. Therefore, biomaterials such as proteins and amino acids can be suitable binders for Si-based anodes due to their polar functional groups [124]. Another example is the chitosan binder, with hydroxyl and amine polar groups that form a dipole-dipole interaction with the surface of the Si active material [116].

Hydrogen bonding is a strong and reversible supramolecular interaction and is among the favorable bonds between the polymeric binders and Si active material, due to strong adhesion, strong recovery, and self-healing properties [69]. Biopolymers and natural polysaccharide binders with –COOH and –OH groups can form hydrogen bonds with the native Si oxide film [117]. Hydrogen bonds can form along the polymer backbone, such as carboxymethyl fenugreek gum (CFG) binder, which was developed for Si-based anodes by Qiu et al. [125]. CFG contains carboxyl and hydroxyl groups on its backbone chain, which form strong hydrogen bonds with the Si surface, resulting in homogeneous anode films. In polymeric binders with longer chains, hydrogen bonds form between the functional groups at the side-chain of the binder and the surface of Si. The hydrogen bond at the side-chain provides strong physical adhesion to the Si particles in the form of single, double, or quadruple hydrogen bonding [21].

Ion-dipole interaction is a strong supramolecular interaction that provides strong adhesion and self-healing ability [126]. CMC and sodium alginate, which contain hydroxyl and carboxylate groups, can form ion-dipole bonds as well as hydrogen bonds with the silanol groups on the oxide layer of Si particle surfaces [69].

2.6 Positive electrode

The positive electrode is the main source of lithium in LIBs, in which Li ions are extracted and inserted during the charge and discharge processes. Minimal structural changes should occur to the cathode host structure during electrochemical cycling to ensure stable performance. Therefore, the majority of commercial cathode materials are intercalation-type, which are classified into three categories based on their structure and dimensionality of Li ion transport: (1) layered, (2) spinel, and (3) olivine. The crystal structures of these three groups are shown in Figure 2.16 [127].

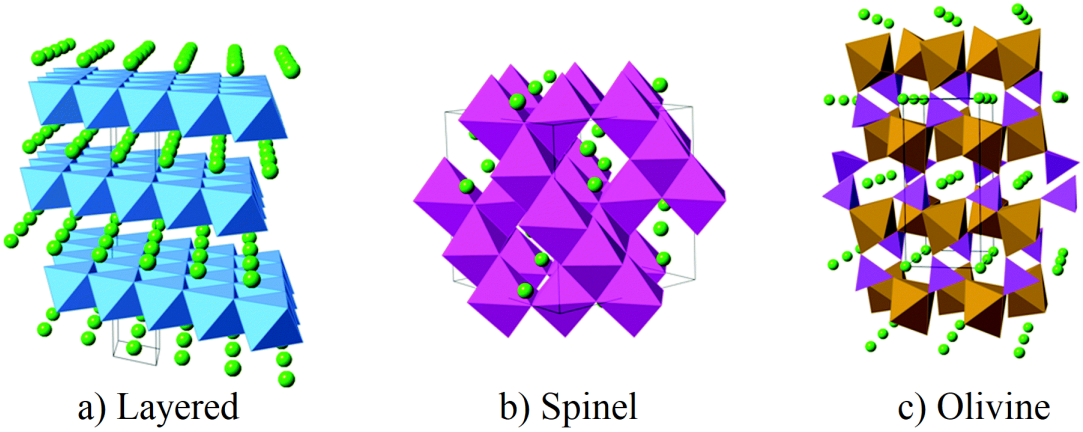

Figure 2.16: Schematic structure of different cathode materials: a) Layered, b) Spinel, and c) Olivine. (Reproduced from Ref. [127] with permission from the Royal Society of Chemistry. Copyright 2014.)

Layered oxide cathodes are mostly used in high-energy battery applications. Lithium cobalt oxide ($LiCoO_2$, LCO), with a high theoretical specific capacity of 274 mAh g^{-1} and operating potential of ~4 V vs. Li/Li^+, was the first investigated commercial oxide cathode with a stable electrochemical performance. However, its high costs, thermal safety issues, and limited practical capacity of ~140 mAh g^{-1} have led to the development of substitutional cathode oxides such as lithium nickel cobalt manganese oxide ($LiNi_{1-y-z}Mn_yCo_zO_2$) (NMC). NMC contains less cobalt, has lower costs, and a higher capacity of ~160-200 mAh g^{-1} compared to LCO. NMC can have different stoichiometries and therefore, different properties depending on the ratio of Ni, Mn, and Co. Ni increases the capacity but lowers the capacity retention and thermal stability, and safety. Co improves the electronic conductivity and rate capability, but increases the costs. Mn enhances safety, lowers costs, and improves rate capability. Different stoichiometries of NMC materials such as NMC111 ($LiNi_{0.33}Mn_{0.33}Co_{0.33}O_2$), NMC532 ($LiNi_{0.5}Mn_{0.3}Co_{0.2}O_2$), NMC622 ($LiNi_{0.6}Mn_{0.2}Co_{0.2}O_2$), and NMC811 ($LiNi_{0.8}Mn_{0.1}Co_{0.1}O_2$) have been investigated to move toward Ni-rich cathodes and reduce the content of Co [128], [129].

Spinel oxide cathodes, such as lithium manganese oxide ($LiMn_2O_4$, LMO), have a three-

dimensional structure that facilitates Li ion movement, improves electrical conductivity, and enhances capacity retention compared to LCO. An advantage of using Mn is its lower cost relative to Co. However, cathode degradation and Mn dissolution can happen during the charge/discharge of the battery, which can lead to the migration of Mn to the anode and blocking the path of Li ion intercalation into the graphite anode, therefore, reducing the cycle life. It was suggested that substituting a small amount of Li (∼5 at%) with Mn leads to Mn-Mn interactions and reduces the Mn dissolution [129]–[131].

Olivine cathodes, such as lithium iron phosphate ($LiFePO_4$, LFP), are another type of cathode material. LFP has an operating voltage of ∼3.5 V vs. Li/Li^+, specific capacity of ∼170 mAh g^{-1}, low cost, and good sustainability. It also shows a long cycle life and shelf life due to the stability of the polyanionic phosphate network, however, this comes at the cost of lower gravimetric and volumetric energy density [132]–[134].

2.7 Electrolyte

The electrolyte is a medium that enables the movement of Li ions between the electrodes, therefore, it should be ionically conductive and electronically isolating. Commercial liquid electrolytes usually consist of lithium salt, organic solvent, and additives. A suitable electrolyte should be stable in the operating electrochemical and temperature windows and be chemically and electrochemically stable against the other battery components (such as anode, cathode, and separator). The negative and positive electrodes have different electrochemical potentials, which are shown in Figure 2.17 as μ_A and μ_C, respectively. A suitable electrolyte should have a wide electrochemical stability window (E_g), in which no oxidation or reduction takes place, resulting in large output voltages as it is depicted in Figure 2.17 [135], [136]. Oxidation and reduction reactions between the electrodes and electrolyte lead to the formation of interphases, such as the SEI layer, which is explained in Chapter 2.3.2. Due to the significant volume change of Si particles and chemical reactivity of Li_xSi phases with the electrolyte [137], the SEI layer on Si-based anodes is of high importance to prevent further electrolyte degradation, therefore, enhancing the capacity retention and cycle life of the battery. As a result, many investigations have focused on improving the electrolyte formulation in Si-based LIBs.

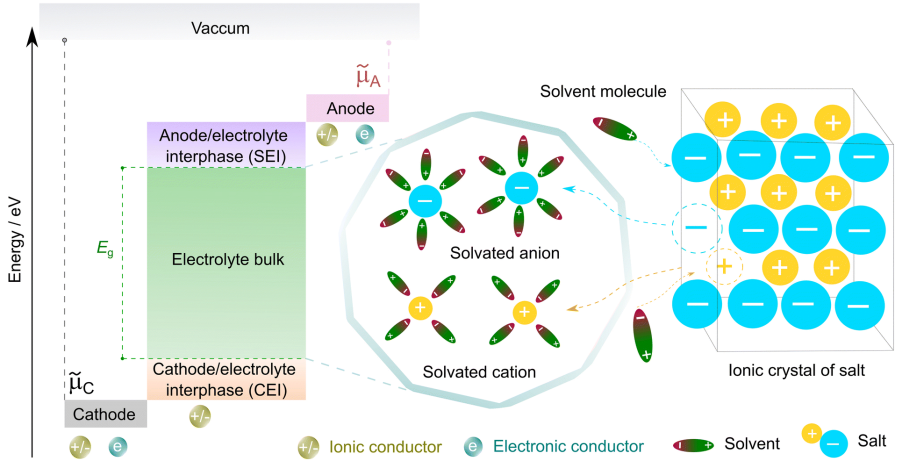

Figure 2.17: Schematic illustration of electrolytes in LIBs. E_g is the thermodynamic stability window of the electrolyte. μ_A and μ_C are the electrochemical potentials of the anode and cathode. (Reproduced from Ref. [135] with permission from the Royal Society of Chemistry. Copyright 2023.)

A mixture of two or more solvents is typically used in electrolytes. These solvents should remain in a liquid state within the operating temperature range, exhibit chemical stability against other battery components, have low viscosity (to facilitate ion transport), a high dielectric constant, and be able to dissolve suitable concentrations of lithium salt. As shown in Figure 2.17 [135], [136], salt-solvent interactions (ion-dipole) lead to the dissolution of the salt into anions and cations. In commercial cells, the electrolyte solvent system is usually a mixture of cyclic, such as ethylene carbonate (EC), and linear car-

bonates, such as ethyl methyl carbonate (EMC), dimethyl carbonate (DMC), and diethyl carbonate (DEC) [45].

The lithium salt used in most commercial LIBs is lithium hexafluorophosphate ($LiPF_6$). However, $LiPF_6$ is very sensitive to traces of moisture and temperatures above 70 °C, which limits its usage due to safety and degradation issues. Other lithium salts such as lithium bis(fluorosulfonyl)imide (LiFSI) and lithium bis(oxalate)borate (LiBOB) are being investigated as alternatives or additions to $LiPF_6$ salt [45].

The addition of small amounts of additives to the electrolyte can enhance different properties of LIBs, such as cycle life, thermal stability, safety, and cost, depending on the application. Additives have a significant impact on the properties of the SEI, especially in Si-based anodes. Suitable additives should be low-cost, environmentally friendly (green chemistry), and ionically conductive [3], [46]. Vinylene carbonate (VC) and fluoroethylene carbonate (FEC) are among the most widely used electrolyte additives. VC has been reported to improve the cycle life and thermal stability of Si-based anodes. Studies have shown that VC undergoes electrochemical polymerization, forming a poly(VC) on the surface of Si-based anodes, which makes the SEI layer denser and mechanically flexible [138]–[140]. FEC enhances the composition and structure of the SEI layer, leading to improved electrochemical performance. Figure 2.18 shows the chemical structures of solvents and additives in LIB electrolytes.

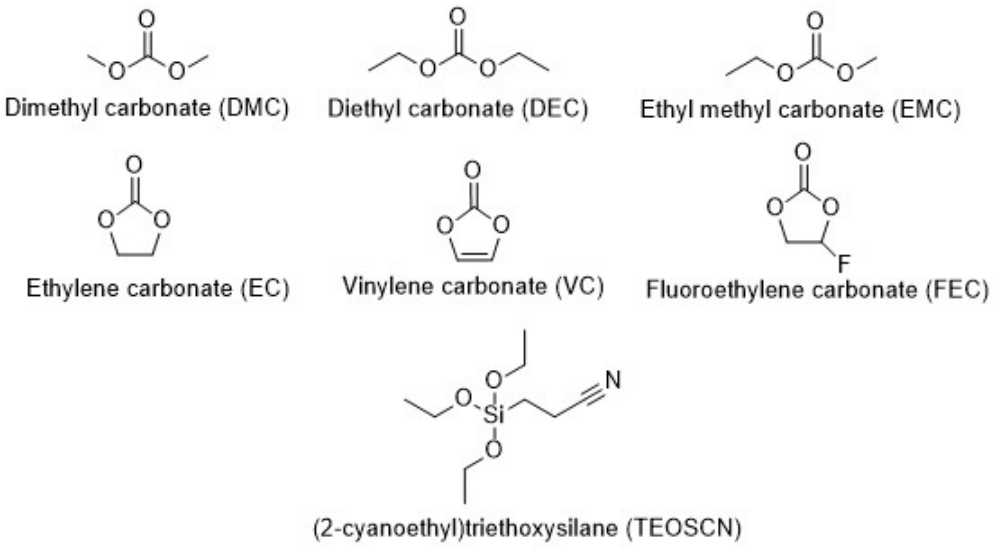

Figure 2.18: Chemical structures of cyclic carbonate (EC), linear carbonates (DMC, DEC, and EMC), and additives (VC, FEC, and TEOSCN) used in LIB's electrolytes.

2.8 Characterization methods

2.8.1 Electrochemical characterization

Electrochemical characterization involves measuring the potential, charge, or current to evaluate the electrochemical behavior of the battery and its components under different conditions. In a two-electrode setup, the cell consists of a working and counter electrode, and the potential measured across these two electrodes is referred to as the cell voltage. In full-cell configurations, these electrodes correspond to the battery's negative and positive electrodes. To measure the electrochemical properties of negative and positive electrodes individually, the electrodes are measured against Li metal, known as the half-cell configuration. The setups for both half-cell and full-cell configurations are schematically illustrated in Figure 3.5.

Galvanostatic charge/discharge measurement provides information about the material's durability and the stability of the cell. The test is carried out at constant current density (mA cm^{-2}) within a defined voltage range and is repeated over multiple cycles. The charge and discharge currents are expressed as C-rate (Chapter 2.2), which influences the measured capacity and performance of the electrochemical cell [141]. To evaluate the electrochemical stability and rate performance of the electrode components, rate capability measurements are conducted by performing galvanostatic charge/discharge at different C-rates for a specific number of cycles. In the final step, the capacity is re-evaluated at the initial C-rate to calculate the capacity recovery of the cell.

Understanding the degradation mechanisms of LIBs is of high importance, as they correlate with the capacity loss within the cell. The measurement of capacity vs. voltage helps to better understand the degradation mechanisms of the electrodes. One method involves using a three-electrode setup, with a Li metal reference electrode. However, adding a reference electrode to LIBs interferes with the cell's performance, and a Li metal electrode may not deliver a constant potential as required for a reference electrode. Other methods that do not require the addition of a reference electrode are differential capacity (dQ/dV) or differential voltage (dV/dQ) analysis [142]. The voltage vs. capacity curve in full-cells carries thermodynamic information of both negative and positive electrodes. The peaks from the dV/dQ and dQ/dV curves show the phase transitions and phase equilibria, respectively [143]. The intensity, shape, and integrated area of the peaks in dQ/dV vs. V plot can provide information about the different redox reactions during charge/discharge. For example, Figure 2.19 shows the dQ/dV plot of a Si-alloy (3M material used in this work) anode half-cell at cycles 5 and 50. In Si-based anodes at the first cycle, crystalline Si (c-Si) transforms to amorphous Si (a-Si), therefore, the peaks for the first cycle are different than the rest of the cycles (depicted in Figure 2.8). Figure 2.19 shows that the first (at 0.2–0.3 V) and second (at 0.08–0.10 V) lithiation peaks result in the formation of a-$Li_{2.0}Si$ and a-$Li_{3.5}Si$, respectively. Loveridge et al. [144] suggest that if the formation of c-$Li_{3.75}Si$ phase happened during lithiation, it would delithiate at ∼0.45–0.5 V. The

reverse processes happen in delithiation by conversion of $Li_{3.5}Si$ to $Li_{2.0}Si$ at ∼0.25 V and delithiation of $Li_{2.0}Si$ and $Li_{3.75}Si$ at ∼0.45–0.5 V [144], [145].

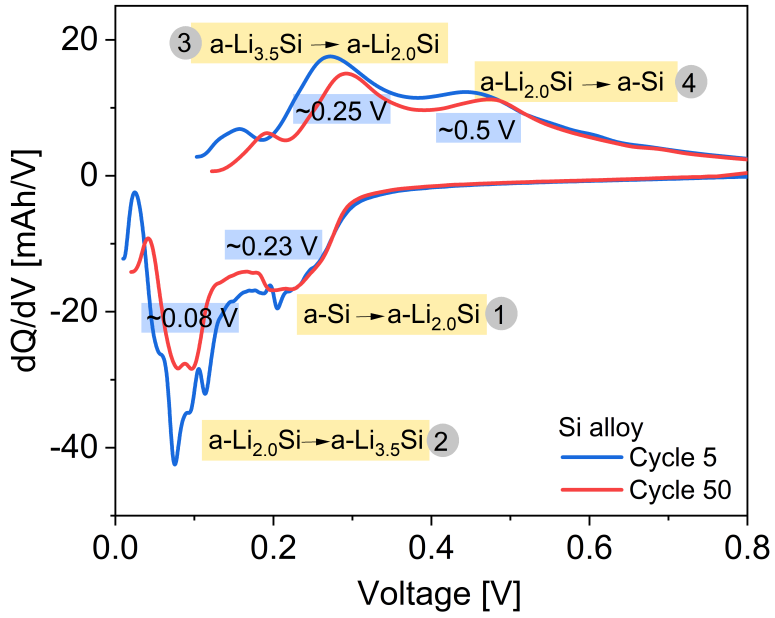

Figure 2.19: Differential capacity analysis (dQ/dV) vs. voltage (V) for Si-alloy (3M material which was used in this work) anode half-cell at cycles 5 and 50. The structural and phase transformations at different voltages are depicted.

2.8.2 Thermogravimetric analysis (TGA) and differential scanning calorimetry (DSC)

Thermogravimetric analysis (TGA) measures mass changes as a function of temperature or time under different gas atmospheres, such as argon (Ar), nitrogen (N_2), or air. When samples are exposed to isotherm or dynamic temperature changes, mass loss can occur during decomposition, desorption, and phase transformation of the material, while an increase in mass indicates oxidation or reaction of the material with the atmosphere. TGA is useful for investigating the thermal stability, moisture content, and the temperature required for the removal of residual water from battery binders and electrodes. Derivative thermogravimetry (DTG) is the first derivative of the TGA curve and helps to determine distinct weight loss regions and identify the temperature at which thermal processes, such as decomposition, occur. Differential scanning calorimetry (DSC) is often measured in parallel with TGA and determines the heat flow as a function of temperature. DSC can identify endothermic (heat absorbed by the sample) and exothermic (heat released to the atmosphere) processes. TGA/DSC technique is useful for investigating battery materials such as polymeric binders and active materials in terms of thermal properties, safety, and solvent interactions [87], [146].

The TGA, DSC, and DTG curves of CMC polymeric binder are shown in Figure 2.20 a, b, and c, respectively. The TGA curve shows a residual mass of 39.48% at 500 °C, similar to literature values[147]. The first weight loss region, below 110 °C, is attributed to the loss of free adsorbed water. The second weight loss region has two main steps, as indicated by the DTG curve: 1) loss of adsorbed water and 2) thermal decomposition and degradation of CMC (exothermic). The water loss in the second step is related to water trapped in the internal layers and attached to the polymer chain, which requires more energy and time to evaporate [148].

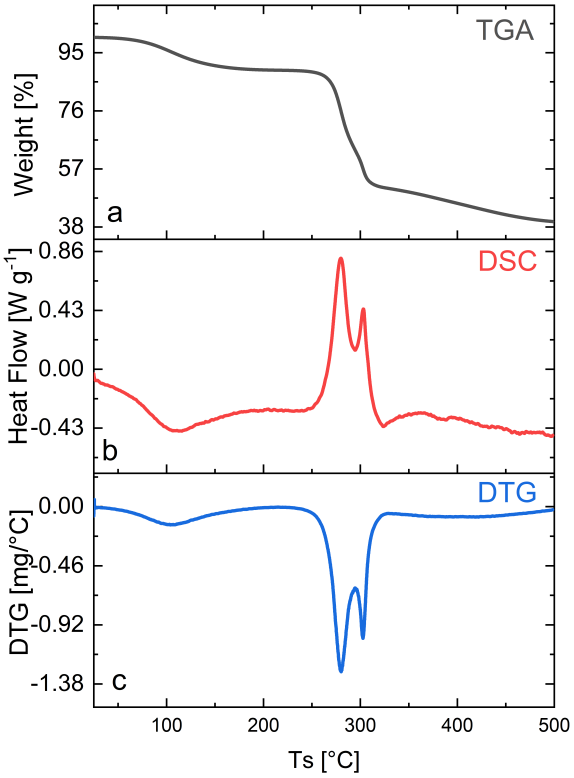

Figure 2.20: a) TGA, b) DSC, and c) DTG of CMC polymeric binder

2.8.3 Fourier transform infrared spectroscopy (FTIR)

Fourier transform infrared (FTIR) spectroscopy is a technique used for characterizing materials by identifying their functional groups. When infrared (IR) light is absorbed by molecules, it causes molecular bond vibration depending on the energy level. This results in a unique spectrum, which is the material's fingerprint. FTIR collects the spectra of all wavelengths in one measurement, and the raw signal is mathematically processed using Fourier transform (FT) to present the intensity as a function of wavenumber. Attenuated total reflectance (ATR) is a standard mode for measuring FTIR spectra. In ATR-FTIR, the sample is placed on an ATR crystal with a high refractive index, such as diamond, germanium, or zinc selenide. The IR light passes through the crystal and is partially

absorbed on the sample's surface (a few microns). The reflected light is then detected to generate the spectrum. The transition energies required for changing the vibrational energy state of functional groups are typically in the mid-IR range (4000–400 cm^{-1}). Changes in chemical structure can be observed as variations in peak intensity or shifts in peak position.

Figure 2.21 shows the different regions of an FTIR spectrum of a CMC polymer binder. Higher wavenumbers (2500–4000 cm^{-1}) correspond to single bonds. Triple and double bonds can be observed in lower regions of 2000-2500 cm^{-1} and 1500–2000 cm^{-1}, respectively. Signals at lower wavenumbers (650–1500 cm^{-1}) are due to the molecular vibrations, which can be used for the overall characterization and identification of the molecule [149], [150].

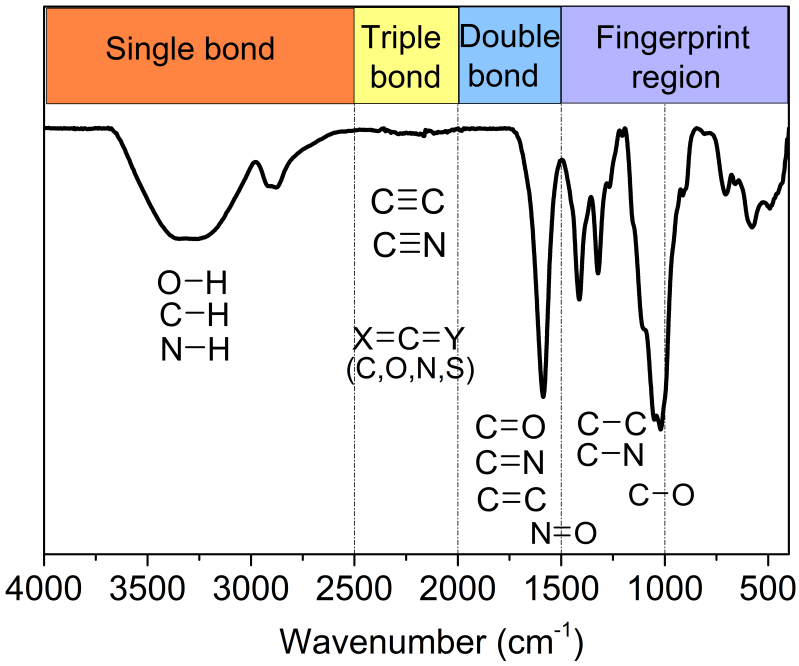

Figure 2.21: FTIR spectrum of CMC polymeric binder used in this work. The various common types of bonds and the approximate regions are marked. (Inspired and redrawn from Ref. [149] with permission from Elsevier. Copyright 2017.)

2.8.4 Scanning electron microscopy (SEM) and energy dispersive X-ray spectroscopy (EDX)

In scanning electron microscopy (SEM), a focused electron beam scans the sample's surface and results in the generation of different signals that are collected by the detector.

Secondary electrons and backscattered electrons are among the common SEM imaging modes. Secondary electrons originate from atoms near the sample's surface and provide information about the sample's morphology and surface topography. Backscattered electrons result from the elastic interactions of the electron beam with the sample, originatng from deeper regions of the sample. Backscattered electrons are sensitive to the atomic number of the sample. In samples with higher atomic numbers, more backscattered electrons are detected and therefore, the image appears brighter compared to lower atomic numbers.
When the electron beam strikes the sample, it can remove an electron from the sample's inner shell, creating a vacancy. This vacancy is filled by an outer shell electron with a higher energy level, releasing the excess energy as a characteristic X-ray photon. The energy of the X-ray photon is characteristic of a particular element. These energies are detected by energy dispersive X-ray spectroscopy (EDX), to investigate the elemental composition of the sample [151], [152]. SEM and EDX are powerful tools for investigating battery electrodes in both pristine state and in post-mortem analysis after lithiation/delithiation. SEM/EDX analysis of surface and cross-section of the sample enables deeper understanding of the morphological changes and potential chemical reactions within the electrodes [153].

2.8.5 X-Ray photoelectron spectroscopy (XPS)

X-Ray photoelectron spectroscopy (XPS) is a non-destructive and surface-sensitive (depth of ∼10 nm) characterization method that investigates the elemental composition and chemical state of elements. The sample is subjected to a low-energy X-ray under ultra-high vacuum conditions (10^{-9}–10^{-8} Pa), leading to the emission of electrons from the sample's atoms. The number of electrons and their energy provide information about the elements, their concentrations (number of emitted electrons), as well as the chemical bonds and valence state of the atoms. The results are presented in the XPS spectrum with binding energy on the x-axis and the count of electrons on the y-axis [154], [155]. XPS can be used in LIB research for a deeper investigation of the SEI layer and to understand the influence of different battery components, such as binders and electrolytes, on SEI formation and composition[46], [156]. The XPS results form this work are presented in Chapter 5.1.4.

3 Experimental section

3.1 Negative electrode preparation

In this section, the process of preparing the Si/Gr anodes is explained, and different binders and slurry formulations have been investigated and optimized. The different steps of the anode manufacturing process are schematically shown in Figure 3.1. All the chemicals and materials used in this work are listed in Table A.1, in the Appendix section.

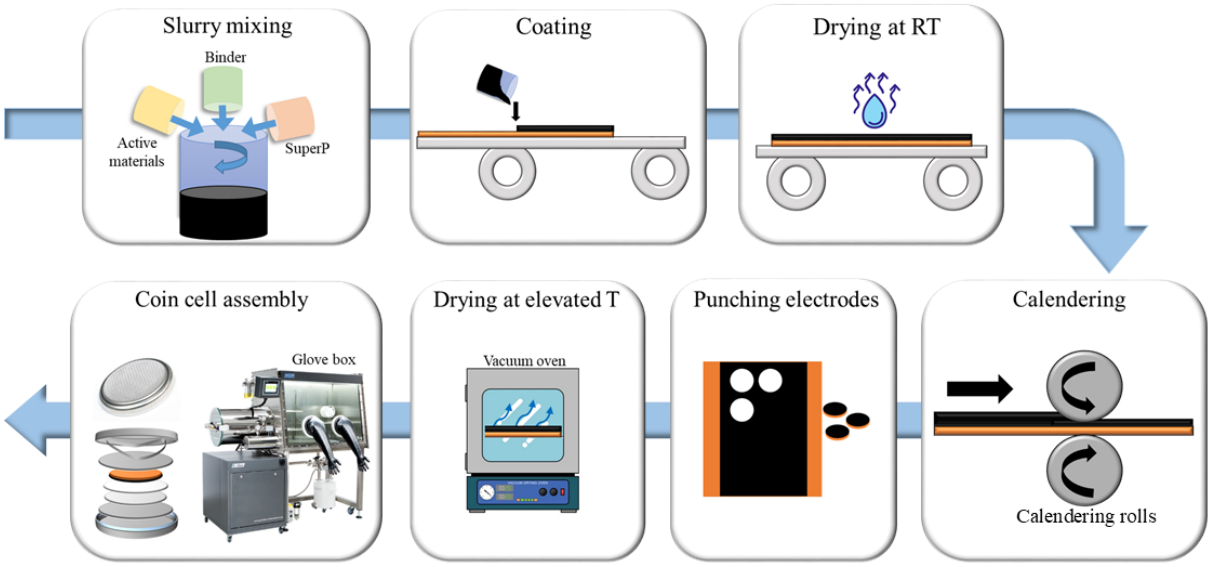

Figure 3.1: Anode manufacturing process, from slurry to coin cell preparation.

3.1.1 Binder preparation

The first step prior to slurry preparation, is producing the binder solutions. Different binders such as lithium polyacrylic acid (LiPAA), carboxymethyl cellulose (CMC), chitosan, sodium alginate (SA), and tragacanth gum (TG) were used in this work. The preparation of different binder solutions is explained below.

Lithium Poly(acrylic acid)(LiPAA)

LiPAA binder was prepared by firstly diluting poly(acrylic acid) (PAA, 25 wt% solution in water, M_W=240,000, Acros) in deionized (DI) water. Afterwards, 80% of the stoichiometric value of lithium hydroxide monohydrate ($LiOH.H_2O$, battery grade, Alfa Aesar) was added step by step, and the solution was stirred at < 60 °C, until obtaining 10 wt% LiPAA with a neutral pH value between 7 and 8.

Different pH values of LiPAA were investigated in this work, such as pH 4, 6, 8, and 9. The molar ratio of $LiOH.H_2O$ to PAA was adjusted to synthesize LiPAA with different neutralization degrees (x in $PAAH_{1-x}Li_x$). The pH of the LiPAA solution was measured at different $LiOH.H_2O$ to PAA molar ratios, as depicted in Figure 3.2.

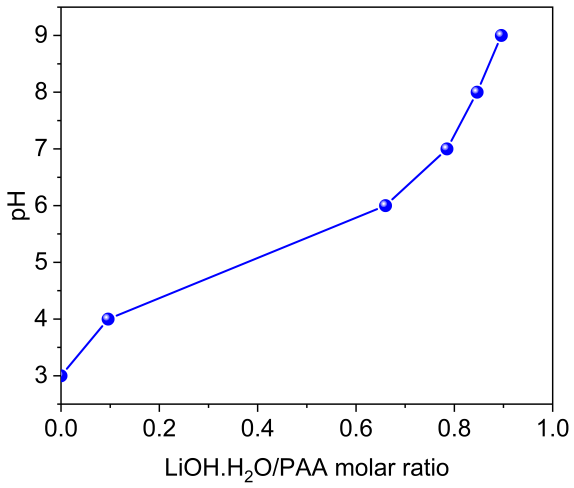

Figure 3.2: The pH of the LiPAA binder solutions measured at different $LiOH.H_2O$ to PAA molar ratios

Carboxymethyl cellulose (CMC), Sodium alginate (SA), Tragacanth gum (TG)

CMC (M_W: 400,000, DS = 0.85–0.9, MTI), SA (Sigma-Aldrich), and TG (Sigma-Aldrich) were prepared by dissolving the polymeric binder in DI water to achieve a 2.5 wt% or 4.5 wt% solution.

CMC, SA, and TG were cross-linked with LiPAA with neutral (between 7 and 8) and acid pH (pH4). For preparing anodes with the cross-linked binders the Si/Gr-20 and Si/Gr-60 formulations (Figure 3.3) were used. The ratio of LiPAA to CMC, SA, or TG was the same as the Si to Gr ratio. The anodes with LiPAA/CMC (Chapter 3.1.3) and pure LiPAA were also measured for comparison. The anodes were dried under vacuum at 150 °C for two hours to enhance the thermal cross-linking of the binders by forming

covalent ester bonds between free carboxylic acid groups of binders and the OH group on the Si surface [157]. Afterwards, the samples were dried overnight at 80 °C under vacuum (Buchi, Glass oven B-585).

Chitosan

In collaboration with the Institute of Biology and Biotechnology of Plants (IBBP) at the University of Münster, five different chitosan samples were received. These samples were prepared from a chitosan sample with DP=1618 and DA=1.7 (Chitosan 134, Mahtani Chitosan Pvt. Ltd., Veraval, Gujarat, India) by washing, nitric acid depolymerization, and acetic anhydride re-N-acetylation protocols, which are described in ref [115]. Different chitosan modifications used in this work are summarized in Table 3.1.

Table 3.1: Different chitosan samples investigated in this work.

Sample	Degree of acetylation(DA) [%]	Degree of polymerization(DP)	Molecular weight(M_W) [kDa]
DA50	47.8	1618	293.0
DA30	28.8	1618	293.0
DA0-1	1.7	1154	183.6
DA0-2	1.7	147	24.2
DA0-3	1.7	189	30.4

Chitosan binder solutions were prepared by dissolving chitosan in 0.5 wt% acetic acid (Rotipuran 100%, p.a, Carl Roth) solution to achieve a 2 wt% chitosan binder solution. Five different chitosan samples were used in this work (Table 3.1) with degrees of acetylation (DA) of 0% (DA0), 30% (DA30), and 50% (DA50). Chitosan with DA0 was produced with three different DPs (DA0-1, DA0-2, and DA0-3).

Chitosan binder (DA50) was further investigated by cross-linking with citric acid (CA) (Sigma-Aldrich). CA was added to the 2wt% DA50 binder solution at DA50:CA mass ratios of 9:1, 8:2, 7:3, and 6:4. After preparing the Si/Gr anodes with DA50/CA binder, thermal cross-linking was attempted by drying the anodes overnight at 80 °C under vacuum.

3.1.2 Slurry preparation and coating process

Si/Gr anodes were prepared by using Si-alloy ($Si_xFe_yC_z$, 1200 mAh g^{-1}, with a density of 3.17 g/cc and surface area of 12 m^2/g) (G7, 3M Germany), hereafter referred to as Si, and graphite (MagE3, Hitachi, Japan) as active materials. Polymeric binders (Chapter 3.1.1) and SuperP carbon black (Imerys Graphite & Carbon), as conductive additive, were mixed with the active materials to form the slurry. The slurries were mixed in three steps, each for 20 minutes at 800 rpm, using a planetary micro mill (Pulverisette 7, Fritsch), where the

materials were mixed in a plastic jar without using milling media. First, binder solution(s) and SuperP were mixed followed by the addition of active material(s) in the next steps. After the slurries were prepared, they were tape cast on a copper (Cu) current collector (10 μm, 8.12 g/cc, Schlenk) using a coating unit (CUF 5, SUMET, Germany) which pulls the draw bar at 5.0 mm/s. Different draw-bar gaps (125, 250, 300, 350 μm) were used for achieving different thicknesses of the electrode film. Anodes were dried at room temperature for 24 hours after coating and afterward calendered (SUMET, Germany), using 8.0 N/mm at 1.0 m/s. The electrodes were punched with a high-precision electrode cutter (EL-CELL) in 14 mm and 16 mm diameters for preparing half-cells and full-cells, respectively. The punched electrodes were dried overnight at 80 °C under vacuum (Buchi, Glass oven B-585). Different slurry formulations are described in the next sections. Figure 3.1 schematically shows the electrode manufacturing process.

3.1.3 Si/Gr anodes with different Si to Gr ratios

For optimizing the Si to Gr ratio, electrodes with different Si and Gr contents (from pure Gr (Gr-90) to pure Si (Si-88)) were prepared. The LiPAA and CMC binders were used as a dual polymeric binder system, and the LiPAA:CMC ratio was the same as Si:Gr ratio. Based on the Si percentage by weight (wt%) in the electrodes, the anodes were named Si/Gr-10 (10 wt%S i), Si/Gr-20 (20 wt% Si), Si/Gr-40 (40 wt% Si), Si/Gr-60 (60 wt% Si), and Si/Gr-70 (70 wt% Si). The Si/Gr and pure Si anodes consist of 88 wt% active material(s), 2 wt% conductive additive, and 10 wt% binder(s). The pure Gr electrode consists of 90 wt% active material (Gr), 5 wt% binder (CMC), and 5 wt% conductive additive. The detailed electrode formulations are depicted in Figure 3.3. The results from this section are further explained in Chapter 4.

3.1.4 Si/Gr anodes with chitosan binder

Initially, the same formulation as Si/Gr-20 (Chapter 3.1.3) was used for anodes with different chitosan binders (Table 3.1). Although the films with this slurry formulation exhibited sufficient cohesion, their adhesion to the Cu foil was not sufficient and the films did not fully adhere to the current collector. Therefore, the binder amount was gradually reduced from 10 wt% to 4 wt%. Binder concentrations of 9, 8, 7, 6, and 5 wt% binders were also tested, with 4 wt% resulting in the most suitable adhesion to the Cu foil. Hence, anodes with a chitosan binder were produced with the following formulation: 21.36% Si (G7, 3M Germany) and 72.64% Gr as active materials, 2 wt% SuperP as a conductive additive, and 4 wt% binder (2 wt% chitosan in 0.5 wt% acetic acid solution). Si/Gr anodes with chitosan binder were further investigated as free-standing electrodes by coating the slurry onto a separator (Whatman GF/C). In the absence of the Cu current collector, the initial anode formulation with 10 wt% binder was used. Si/Gr anode has a loading

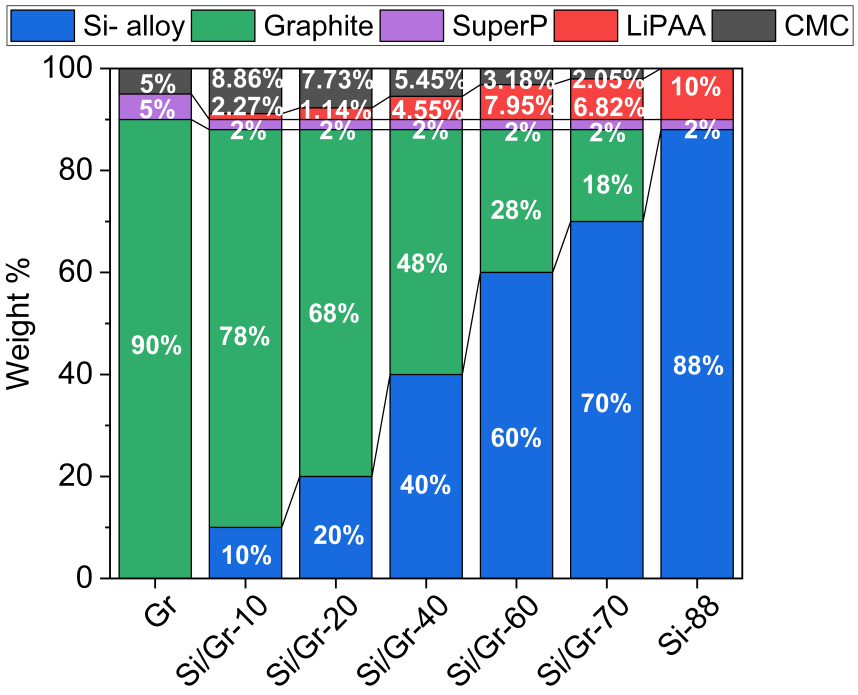

Figure 3.3: Different compositions (in wt%) of Si/Gr anodes used in this work, the results are explained in Chapter 4 (Reproduced from Ref. [44] (Hamzelui et. al) with permission from Elsevier. Copyright 2021)

and areal capacity in the range of 2.2–2.9 mg cm^{-2} and 1.2–1.4 mAh cm^{-2}, respectively. Figure 3.4 shows the anode formulations with and without Cu current collector.

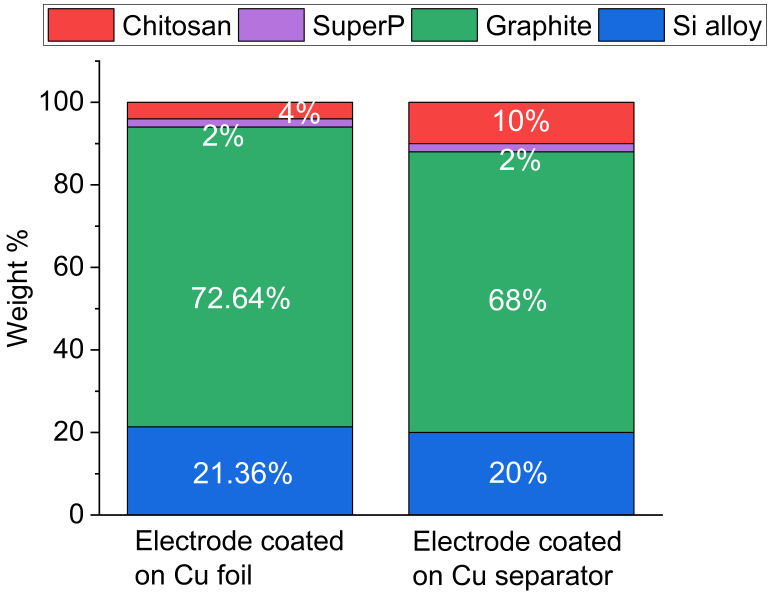

Figure 3.4: Si/Gr electrode formulation with chitosan binder coated on Cu foil and glass microfiber sheet separator (free-standing electrode). The results are shown in Chapter 5.1. (Reproduced from Ref. [50] (Hamzelui et. al) with permission from Wiley Online Library. Copyright 2022)

3.2 Electrolyte mixing and coin cell assembly

In this work, an electrolyte formulation of 1.2 M lithium hexafluorophosphate ($LiPF_6$) in ethylene carbonate (EC):ethyl methyl carbonate (EMC) (3:7, w/w) with 10 wt% fluoroethylene carbonate (FEC) additive was used. For optimizing the performance of the cells at high temperature, 1M $LiPF_6$ in EC:diethyl carbonate (DEC) (1:1, w/w) with 5 wt% FEC, 2 wt% vinylene carbonate (VC), and 1 wt% (2-cyanoethyl)triethoxysilane (TEOSCN) was used [46].

Coin cells (type 2032 (20 mm diameter and 3.2 mm thickness)) were assembled in an argon-filled glovebox (O_2 and $H_2O < 0.5$ ppm), and 90 μl electrolyte was used in each coin cell. Half-cells were built by using the Si/Gr electrode vs. Li metal counter electrode (Si/Gr‖Li metal), and full-cells were produced using Si/Gr negative electrode (anode) and NMC622 positive electrode (cathode) (NMC622‖Si/Gr). Figure 3.5 shows the construction of half-cells and full-cells. Two different types of NMC622 cathode were used in this work, one type with a loading of 6.4 mg cm^{-2} and an areal capacity of 1 mAh cm^{-2} (Custom Cells, Germany) and another type, used in the full-cells with the chitosan containing anodes, (Chapter 5.1) with a loading of 6.7 mg cm^{-2} and an areal capacity of 1.15 mAh cm^{-2} (MEET, Germany).

The electrochemical performance of the coin cells was measured galvanostatically using

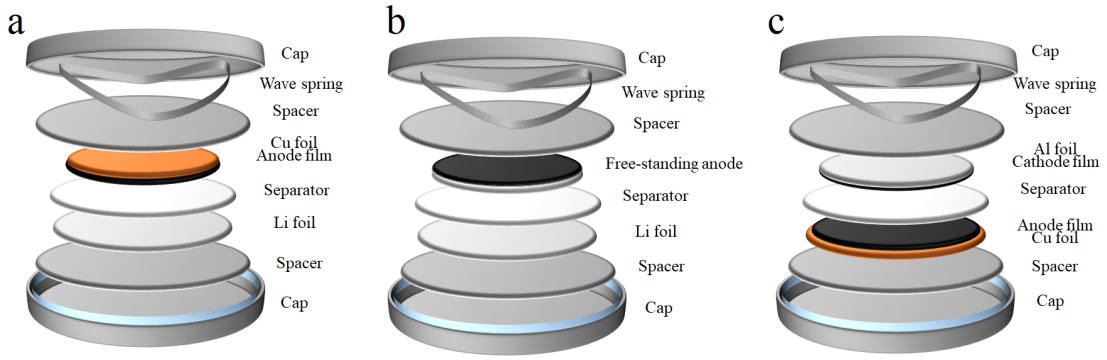

Figure 3.5: Schematic illustration of the construction of coin cells. a, b) Half-cells with anode coatings on Cu foil and separator, respectively, c) Full-cell

a Neware BTS4000-5V10mA. The potential window was set to 0.9–0.01 V vs. Li/Li^+ for half-cells. In full-cells, two different potential windows of 2.5–4.35 and 2.8–4.35 V were tested in Chapters 4 and 5, respectively. All cells were subjected to an open circuit potential (OCV) for 24 hours prior to the measurements. Formation cycles were performed at 0.05C for 5 cycles. The long-term electrochemical performance was measured at 0.1C or 0.2C. Rate capability measurements were performed in C-rates ranging from 0.05C to 5C. Measurements at various temperatures were performed, such as room temperature (RT), 45 °C, and 60 °C. For all the electrochemical measurements 3–5 coin cells were cycled, and the average result is shown in the results sections (Chapters 4 and 5).

3.3 SEM/EDX measurements

The SEM/EDX measurements were performed at two different institutes and with different devices. Part of the measurements were done at the Center for Ageing, Reliability and Lifetime Prediction of Electrochemical and Power Electronic Systems (CARL) and the other part was carried out at the Central Facility for Electron Microscopy (GFE) at RWTH Aachen University.

At CARL, surface scanning electron microscopy (SEM) measurements were performed using a Supra 55 system (Carl Zeiss Microscopy), and an accelerating voltage of 5 or 10 kV. Samples were prepared according to their atmosphere sensitivity. Pristine electrodes were cut to the desired pin stub size without further precautions, while lithiated electrodes were prepared in an Ar-filled glovebox and transferred to the SEM using a transfer shuttle (Kammrath & Weiss). Energy-dispersive X-ray spectroscopy (EDX) measurements were performed using an Ultim Extreme (Oxford Instruments). For cross-section SEM/EDX analysis, a Zeiss Crossbeam 350 (Carl Zeiss Microscopy) was used and cross-section samples were prepared with a next generation focused ion beam (FIB). The SEM resolution goes down to 0.9 nm at 15 kV, and the FIB resolution is 3 nm in depth at 30 kV. An

EDX Oxford Ultim Max 100 detector was used for chemical composition analysis.

At GFE, the surface and cross-section morphology of Si/Gr electrodes were studied before and after lithiation/delithiation by scanning electron microscopy (SEM) using a Gemini SEM 300 (Carl Zeiss Microscopy). For imaging and analysis, the SEM was operated at 15kV, and secondary electron (SE) and backscattered electron (BSE) images were collected. For cross-section measurements, samples were prepared by Ar-ion polishing using a SM-09010 cross-section polisher by JEOL. EDX measurements were performed using an UltimMax 65 SDD-detector and Aztec (V. 6.0) software (Oxford Instruments).

3.4 TGA/DSC measurements

Thermal properties of the binders were investigated by TGA measurements using a Mettler Toledo TGA/DSC 1. The measurements were performed in a temperature range of 25 to 500 °C at 5 °C/min under a nitrogen atmosphere. Aluminum crucibles and lids (40 μl, Mettler Toledo) were used for the measurement. Three blank measurements were performed prior to the actual measurements, and the blank curve was automatically substracted from the measurement curve. The data were evaluated using STARe software (Mettler Toledo).

3.5 FTIR measurements

FTIR analysis was performed on different polymeric binder materials using a Bruker Vertex 70 in attenuated total reflection (ATR) mode in an argon-filled glovebox (O_2 and $H_2O < 0.5$ ppm) and under dry room conditions (dew point < 55 °C, room temperature ~22 °C). The measurements were performed in the wavenumber range of $4000 - 400$ cm^{-1} at a resolution of 4 cm^{-1} for 50 scans. The data were evaluated using OPUS software.

3.6 Adhesion measurements

An adhesion or peel test was performed on Si/Gr electrodes with different binders to evaluate the adhesion of the coating to the current collector and cohesion within the coating film. The adhesion test can be a good indicator of binder's adhesive properties [158]. The measurement was done at a 90° angle as schematically shown in Figure 3.6. The tests were performed on the electrodes using a Mark-10 ESM303 instrument using a double-sided tape (3M VHB). The electrodes were dried at 80 °C and cut into 1 cm width before the measurements, and the length of the measurement tape was 10 cm.

The electrodes were pulled at a speed of 10 cm/min, and the load (N) versus time was measured using MESURgauge software.

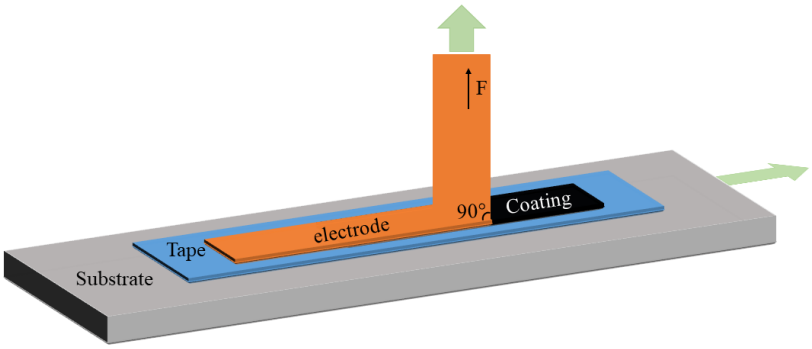

Figure 3.6: Schematic illustration of adhesion test measurements with 90° angle used in this work.

3.7 Inductively coupled plasma atomic emission spectroscopy (ICP-OES)

Inductively coupled plasma atomic emission spectroscopy (ICP-OES) measurements were performed on LiPAA binders with different pH using an iCAP PRO ICP-OES system and QTEGRA software (Thermo Fisher Scientific). An automated dilution system based on ASX-560 SDX autosampler was used. LiPAA binders with different pH values were coated on a Cu current collector and dried at room temperature. The binders were then separated from the Cu foil and investigated using ICP-OES measurements to analyze the Cu content in the samples.

3.8 XPS measurements

XPS measurements were carried out at Münster Electrochemical Energy Technology (MEET), University of Münster, to investigate the surface chemistry of cycled Si/Gr anodes with chitosan DA50 and LiPAA/CMC binders after 3 cycles at 0.05C (results are explained in Chapter 5.1.4). The XPS instrument (Axis Ultra DLD, Kratos, U.K.) was used, and samples were transferred into the device using a sealed transfer system. Al Kα radiation energy of 1486.3 eV with an emission angle of 0° relative to the surface normal was used. Core-level spectra were recorded using a pass energy of 20 eV, with a filament current of 10 mA and a voltage of 12 kV. A neutralizer was used for compensation of charging. Casa XPS software (Version 2.3.16 PR 1.6, Casa Software Ltd., U.K.) was used for fitting the XPS spectra. Gaussian/Lorentzian lineshapes (GL(30) in CasaXPS, product of Lorentz and Gaussian function with 30% Lorentz component) were used for fitting

XPS data. An exception was the graphite sp2 peaks in the C spectrum, which we fitted with an asymmetric lineshape (in CasaXPS LF lineshape) due to the asymmetric peak shape. The asymmetry parameters were based on pure graphite reference measurements. For calibrating the binding energy of the spectra, the C 1s C-C peak (i.e., 284.5 eV) was used as an internal reference.

4 Customizing and optimization of silicon/graphite negative electrode

4.1 Optimization of the anode formulation

This chapter is based on the results of the publication entitled *"Customizing Active Materials and Polymeric Binders: Stern Requirements to Realize Silicon-Graphite Anode Based Lithium-Ion Batteries"*, which was published during this thesis by Hamzelui et al. [44]. The contents and figures of this chapter are reproduced and modified from Ref. [44] with the permission of Elsevier, copyright 2021.

Enhancing the electrode's formulation and manufacturing process are among the main factors in reducing the costs of LIBs and increasing their volumetric energy density. The cost of materials, especially anode and cathode active materials, plays a major role in the overall manufacturing costs of LIBs. Therefore, it is highly important to use abundant and environmentally friendly materials in both the anode and cathode coatings to reduce environmental impacts and costs [159]. Slurry mixing, coating, drying, and calendering contribute to ∼28% of the entire manufacturing costs [160]. Therefore, improving the formulation and production process is important for cost reduction and enhancing cell performance. The development of next-generation batteries, with advanced and sustainable chemistries, begins at the laboratory scale, where the material properties and composition are investigated and optimized.

As discussed in Chapter 2.4, the use of Si/Gr composite (or blend) anodes in combination with suitable polymeric binders is highly promising for improving the performance of Si-based anodes. The addition of Si, with its high theoretical capacity, to the Gr active material increases the energy density of LIB compared to pure Gr anodes. The co-utilization of Si and Gr combines the advantages of both anode active materials, as depicted in Figure 2.7. In Si/Gr electrodes, Si particles are homogeneously distributed within a graphite matrix, which maintains the electrical contact between the Si particles and accommodates the volume change, resulting in enhanced electrochemical performance of the anode. Berckmans et al. investigated the cost calculations for NMC622‖Gr and NMC622‖Si/Gr cells and reported that using Si can increase the energy density from 155 Wh/kg to 205 Wh/kg. The total cost breakdown indicates that the negative electrode cost decreases from 24% to 19% by using Si-based anodes [161].

This work investigates the effect of the Si to Gr ratio on the electrochemical performance of the Si/Gr anode half-cells (Si/Gr‖Li) (Chapter 4.1.1). A dual binder system consisting of LiPAA and CMC is used in these electrodes, as Si and Gr chemistry require different polymeric binder materials due to their different physical and chemical properties. Therefore, an optimal binder for Gr electrodes may not be an ideal binder for Si-containing anodes. CMC and LiPAA are commonly used binders for Gr and Si, respectively. The optimized Si/Gr anode formulation is further investigated by fine-tuning the ratio of LiPAA to CMC in Chapter 4.1.2. Finally, the performance of the optimized Si/Gr anode was evaluated in a full-cell using NMC622 cathode (NMC622‖Si/Gr) in Chapter 4.8. All electrochemical measurements in this chapter use 1.2 M $LiPF_6$ EC:EMC (3:7) + 10 wt% FEC electrolyte. The formulations of the anodes used in this chapter are summarized in Table 4.1.

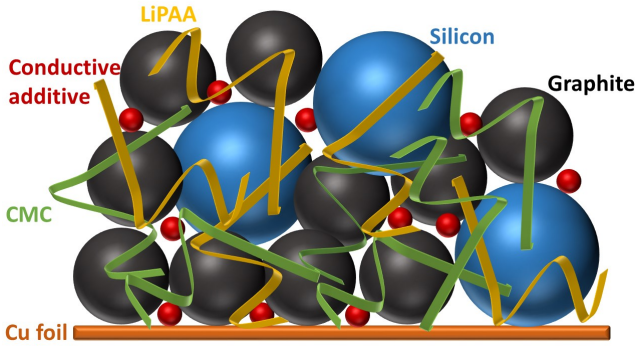

Figure 4.1: Schematic illustration of Si/Gr blend anode and LiPAA/CMC binder system.

Table 4.1: Different anode formulations used in this chapter.

Anode	Si (wt%)	Graphite (wt%)	LiPAA (wt%)	CMC (wt%)	SuperP (wt%)
Gr-90	0	90	0	5	5
Si/Gr-10	10	78	8.86	1.14	2
Si/Gr-20	20	68	7.73	2.27	2
Si/Gr-40	40	48	5.45	4.55	2
Si/Gr-60	60	28	3.18	6.82	2
Si/Gr-70	70	18	7.95	2.05	2
Si-88	88	0	10	0	2

4.1.1 Optimization of the active materials

Different Si to Gr ratios (from pure Gr to pure Si) (Table 4.1) were investigated, and the slurry preparation and coating procedure are explained in Chapter 3.1.3. The theoretical total capacity (Q_{tot}) of each anode formulation is calculated based on Equation 4.1. Where Q_{Gr} and Q_{Si} are the theoretical specific capacities of Gr and Si, respectively. $Gr_{wt\%}$ and $Si_{wt\%}$ are the weight percentages of Gr and Si within the active material, respectively.

$$Q_{\text{tot}} = Q_{\text{Gr}} \cdot \text{Gr}_{\text{wt\%}} + Q_{\text{Si}} \cdot \text{Si}_{\text{wt\%}} \tag{4.1}$$

Figure 4.2a shows the capacity and coulombic efficiency (CE) vs. cycle number for Si/Gr anode half-cells with 10, 20, 40, 60, and 70 wt% Si. Based on Equation 4.1, anodes with 10, 20, 40, 60, and 70 wt% Si show 89.47, 97.19, 86.39, 81.43, and 77.83% of their Q_{tot} in the first cycle. The Si/Gr-20 anode half-cell (Si/Gr-20‖Li) has the closest value to its theoretical capacity, which can be due to the uniform distribution of Si particles within the coating and slightly limited volume change in the Si/Gr blend anode. Localization of Si particles, non-uniform coatings, and large volume change of Si particles (especially at higher Si contents) can result in limited silicon utilization, higher difference from the theoretical capacity, decrease in cycle life, and electrochemical instability of the Si/Gr‖Li cells. After 500 cycles, the order of capacity retention (with respect to the 2^{nd} cycle) is Si/Gr-10 (98.32%) > Si/Gr-20 (85.95%) ≫ Si/Gr-40 (39.19%) ≈ Si/Gr-60 (39.47%) ≫ Si/Gr-70 (4.15%), which almost decreases with increasing the Si content. The Si/Gr-20‖Li cell shows a capacity retention of 80.06% after 900 cycles. Anodes with more than 40 wt% Si show a rapid capacity loss at ∼ 200 cycles. It should be noted that the results are highly dependent on the type of active materials and binders as well as the formulation, slurry preparation, and coating methods. Small changes in the electrode production procedure can result in changes in the electrochemical and mechanical properties of the anode.

To investigate the reversibility and long-term cycling performance of the Si/Gr‖Li cells, the Coulombic efficiency (CE) of the cells was calculated. Minimal changes in CE can result in a significant capacity loss, which can also be related to rapid electrolyte consumption. Usually, a capacity retention of 80% and CE of 99.96% after 500 cycles is required for commercial applications, such as the electric vehicle (EV) industry [162]. The initial CE of the anode half-cells with 10, 20, 40, 60, and 70 wt% Si are 87.17%, 86.06%, 85.08%, 84.90%, and 84.95%, respectively. The CE of the first cycle of Si-based anodes is reported to be in the range of 65–85%, which is lower compared to graphite electrodes (90–94%) [163]. This is due to the significant loss of active Li^+ in the first cycle for SEI layer formation. The Si/Gr‖Li cells in this work show CEs higher or in the upper range of the reported values. For industry applications, an initial CE higher than 85% is usually accepted for carbon and Si anode [164], which can be seen for Si/Gr-10‖Li and Si/Gr-20‖Li cells. After initial cycles and stabilization of the SEI layer, the CE increases to 99.73% at the 900^{th} cycle for Si/Gr-20. This can be due to the volume change of Si particles, which leads to pulverization and loss of electrical contact. The expansion of the electrode also leads to the compression of the separator, pore shrinkage, and limitation of Li^+ transport [165].

Irreversible capacity (Q_{irr}) helps to better investigate the parasitic side reactions in each cycle and is defined as the difference between lithiation and delithiation capacity in one cycle (Equation 4.2). The value of Q_{irr} is predominantly related to SEI layer (re)formation, especially during the initial cycles, as well as irreversible Li metal plating and Li trapping. A lower Q_{irr} shows that fewer side reactions and charge loss are occurring, which is

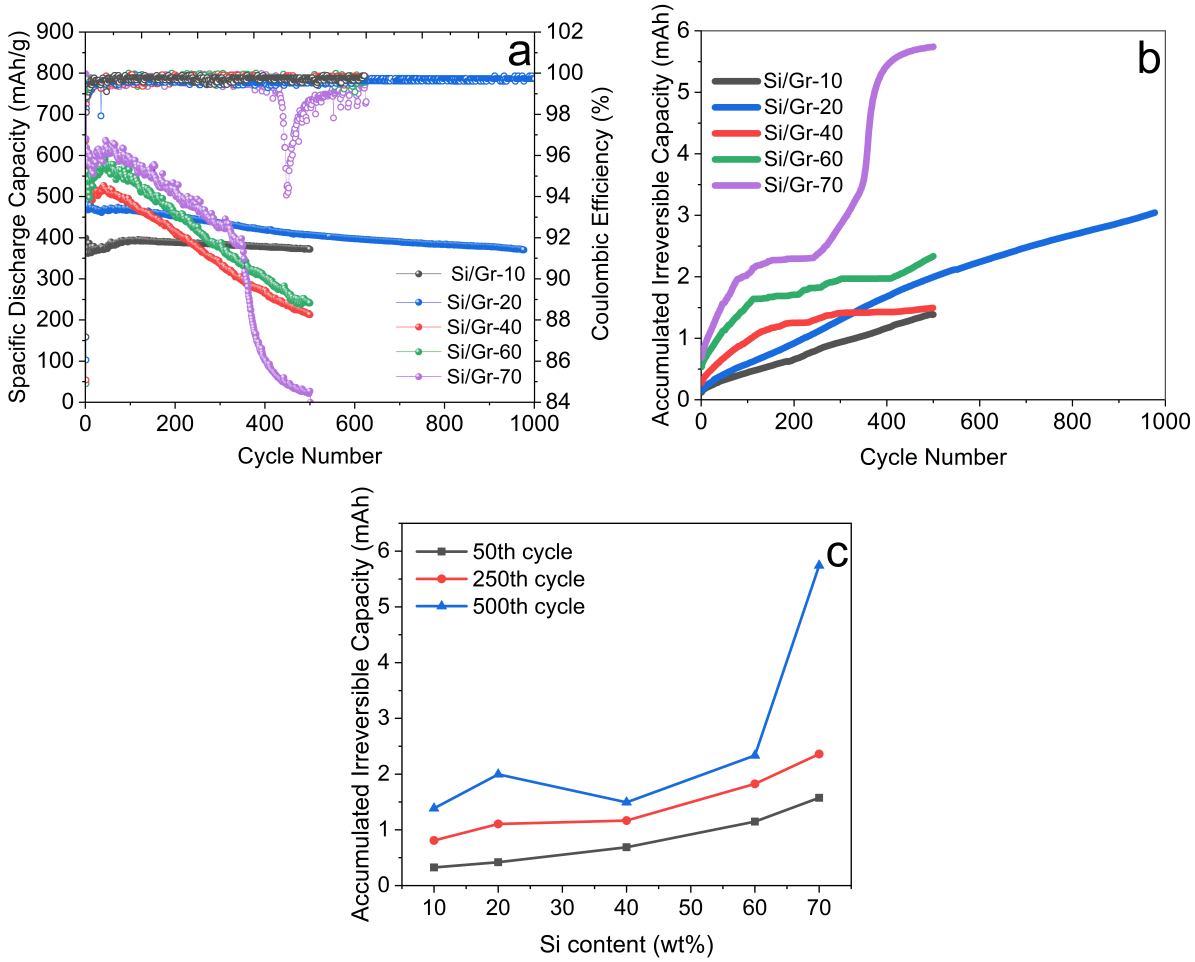

Figure 4.2: a) Capacity and Coulombic efficiency vs. cycle number, b) Accumulated irreversible capacity vs. cycle number, and c) Accumulated irreversible capacity vs. Si content of the electrodes at different cycle numbers, for Si/Gr anode half-cells with different Si to Gr ratio at 0.1C

desirable for a practical battery cell [17]. Accumulated irreversible capacity (Q_{AIC}) is the sum of Q_{irr} during a specific number of lithiation/delithiation (n), as shown in Equation 4.3, which indicates the active lithium loss due to irreversible Li ion consumption. A lower Q_{AIC} indicates better electrochemical performance and CE, among other factors. However, it should be noted that the active lithium loss is not always directly equal to or proportional to Q_{AIC}. Some parasitic reactions do not result in loss of active lithium in the cell, but increase the Q_{AIC}. Reactions such as SEI formation, lithium metal plating, loss of active material, and lithium trapping consume active lithium. On the other hand, redox shuttle mechanism, metal dissolution deposition, and H_2 formation are among the parasitic reactions that do not contribute to the active lithium loss [17], [166].

$$\mathrm{Q_{irr}} = \mathrm{Q_{Lithiation}} - \mathrm{Q_{Delithiation}}[\mathrm{mAh}] \tag{4.2}$$

$$Q_{\mathrm{AIC}} = \Sigma_1^n Q_{\mathrm{irr}}(n)[\mathrm{mAh}] \tag{4.3}$$

Figure 4.2b shows the Q_{AIC} over the cycle numbers for the Si/Gr‖Li cells with different Si to Gr ratios. The Q_{AIC} curve for anode half-cells with 10 and 20 wt% Si shows a linear behavior, while for Si contents higher than 40 wt%, a sigmoidal shape is observed. The initial slopes of Si/Gr-10 and Si/Gr-20 are very similar, while for higher Si contents, a higher slope is observed. The initial Q_{AIC} increases from 0.121 mAh for Si/Gr-10 to 0.685 mAh for Si/Gr-70, indicating a higher capacity loss in the first cycle for anodes with a higher amount of Si. The increase in the initial slope and Q_{AIC} at higher Si contents is due to ongoing SEI formation. In Si/Gr-20 the Q_{AIC} is 1.996 mAh at the 500$^{\mathrm{th}}$ cycle (∼13.77 times higher than the initial Q_{AIC}) and 3.546 mAh at the 900$^{\mathrm{th}}$ cycle (∼24.46 times higher than the initial Q_{AIC}). For Si/Gr-70, the slope of the curve decreases after ∼70 cycles, indicating fewer decomposition reactions. After ∼240 cycles, a sharp increase in the slope is observed, which is related to the severe capacity loss of this cell (Figure 4.2a). Figure 4.2c shows the Q_{AIC} vs. Si content for three different cycle numbers of 50, 250, and 500. A linear behavior is observed for cycles 50 and 250, meaning that with the increase in Si content, the Q_{AIC} increases. At the 500$^{\mathrm{th}}$ cycle Si/Gr-20 electrode shows a higher Q_{AIC} compared to Si/Gr-40, which is also observed in Figure 4.2b. However, based on the electrochemical cycling results in Figure 4.2a it is observed that Si/Gr-20 shows higher capacity at the 500th cycle, which is 74.94% of the theoretical capacity value. This value is reduced to 28.92% for the Si/Gr-40. Based on the sigmoidal shape of Si/Gr-70 in Figure 4.2b, it can be predicted that a sharp increase in Q_{AIC} is observed with rapid capacity loss in Figure 4.2a. The same trend can be expected from other electrodes, during their rapid capacity loss. Therefore, Si/Gr-40 at 500$^{\mathrm{th}}$ might have a similar flat stage as Si/Gr-70 between cycles 100–250, and at higher cycle numbers rapid increase in Q_{AIC} can be expected. Therefore, based on the capacity and Q_{AIC} results in Figure 4.2, Si/Gr-20 shows a more stable electrochemical performance.

The kinetics and potentials of lithiation and delithiation are different for Si and Gr active materials. The differential capacity (dQ/dV) analysis provides information on the electrochemical activity and degradation phenomena of the electrodes. The characteristics of the dQ/dV peaks, such as intensity, shape, position, and integrated area, can indicate different redox reactions and phase transformations related to (de)alloying of Si and (de)intercalation of Gr.

Figure 4.3a shows the normalized (dQ/dV)/Q vs. V for Si/Gr‖Li cells with different Si:Gr ratios, as well as pure Gr (Gr-90) and pure Si (Si-88) electrodes. To compare the samples with different Si-content, dQ/dV was normalized for each charge and discharge process (based on the measured capacity), to clearly present the changes in electrode potential. The (dQ/dV)/Q vs. V is plotted at the 50$^{\mathrm{th}}$ cycle, to ensure the stability of the SEI layer due to limited electrolyte degradation and regulated volume change after a certain number of (de)lithiation. The lithiation of Si-88‖Li cells shows peaks at ∼0.23 V and ∼0.08 V, corresponding to the conversion of a-Si to a-Li_2Si and a-Li_2Si to a-$Li_{3.5}Si$,

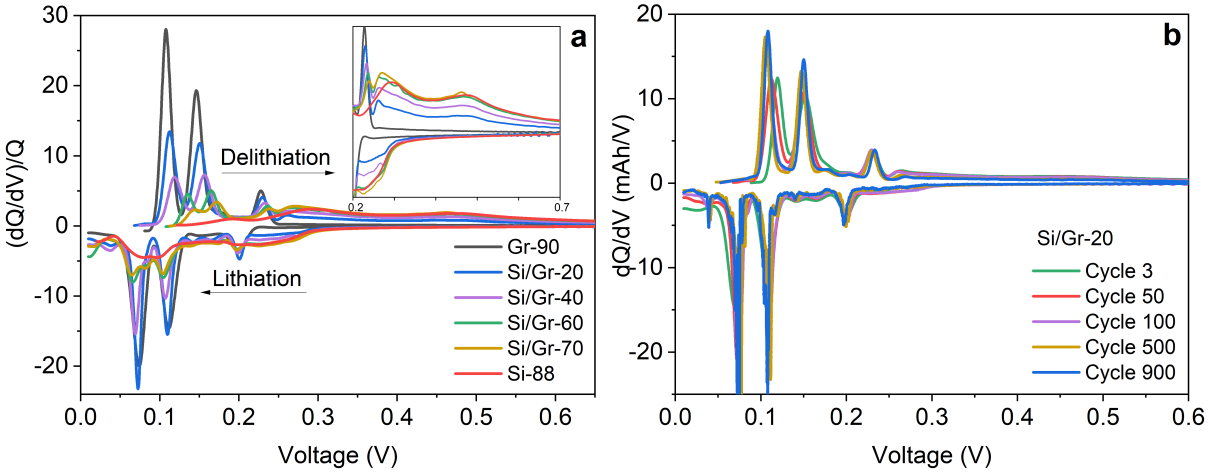

Figure 4.3: Normalized differential capacity (dQ/dV)/Q vs. V for a) Different Si to Gr ratios at the 50^{th} cycle, and b) Si/Gr-20 at cycle numbers 3, 50, 100, 500, and 900^{th} cycle

respectively. Upon delithiation, Li ions are extracted at higher potentials of ∼0.28 V and ∼0.47 V, leading to the phase transitions of a-$Li_{3.5}Si$ to a-Li_2Si and a-Li_2Si to a-Si, respectively, as described in Chapter 2.8.1. The broad signals in the Si-88 peaks indicate low (de)lithiation kinetics. The Gr-90‖Li cell shows peaks in the range of 0.2–0.07 V and 0.11–0.23 V for Li intercalation and de-intercalation ($C_6 + xLi^+ + xe^- \rightleftharpoons Li_xC_6$), respectively [144], [167], [168]. It is observed that the characteristic peaks of Si become more pronounced with increasing Si content in the Si/Gr anode.

Si/Gr-20‖Li cell exhibits a long cycle life of more than 900 cycles. To verify that the electrochemical activity of active materials is maintained after long-term cycling, the dQ/dV plot for Si/Gr-20‖Li at different cycles is shown in Figure 4.3b. The peaks related to Gr and Si active materials are clearly observed after 900 cycles, confirming that the obtained capacity is due to (de)lithiation of active materials and not due to Li plating and stripping.

Figure 4.4a shows the discharge capacity and CE of Si/Gr-20‖Li, Si-88‖Li, and Gr-90‖Li cells. The Si/Gr-20‖Li cell exhibits enhanced electrochemical performance, such as better cycle life, cycling stability, and CE, compared to Si-88‖Li, and higher capacity compared to Gr-90‖Li. This confirms the contribution of both active materials to the overall electrochemical performance and the synergistic benefits of Si and Gr chemistry. The Si-88‖Li cell shows stable performance up to ∼140 cycles, followed by a rapid loss of capacity. The long-term cycling and rapid capacity loss of Si-88‖Li after ∼140 cycles is shown in Figure A.1 in the Appendix. Figure 4.4b shows the accumulated irreversible capacity of Si/Gr-20‖Li, Gr-90‖Li, and Si-88‖Li cells. It can be observed that Gr-90 and Si/Gr-20 show linear behavior with a similar slope. The Si-88‖Li cell demonstrates a Q_{AIC} similar to Si/Gr-70 (Figure 4.2b). It exhibits a high initial slope, followed by a lower slope region (stabilization) between 60 and 120 cycles, and an increase in Q_{AIC} with a steep slope after

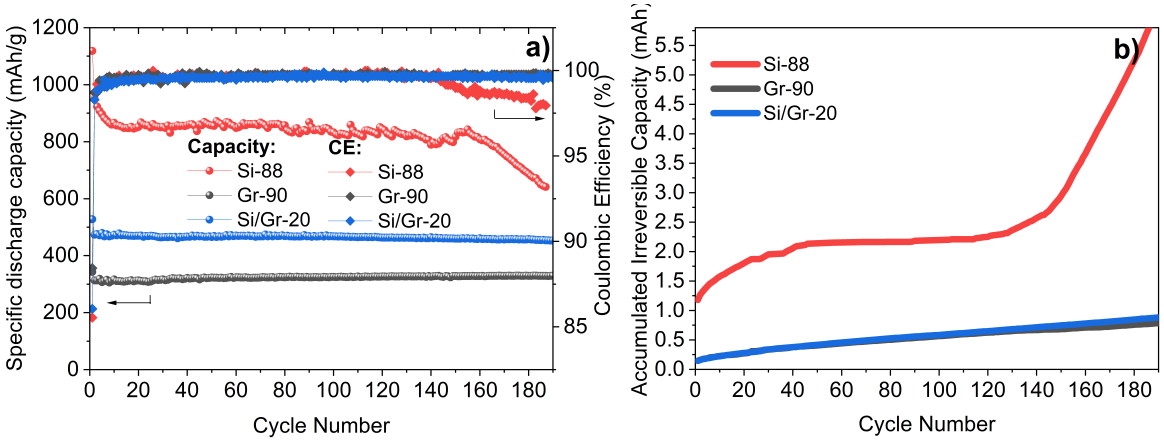

Figure 4.4: a) Discharge capacity and Coulombic efficiency vs. cycle number and b) Accumulated irreversible capacity of Si/Gr-20, Gr-90, and Si-88 anode half-cells

∼140 cycles. This is in agreement with the results in Figure 4.2a, which show a rapid loss of capacity and CE for Si-88‖Li after ∼140 cycles.

The Q_{AIC} in the first cycle for Gr-90‖Li, Si/Gr-20‖Li, and Si-88‖Li is 0.149, 0.145, and 1.18 mAh, respectively, implying that the initial Q_{AIC} of Si-88‖Li is almost 8 times higher than the initial Q_{AIC} of Si/Gr-20‖Li. There are different sources for Q_{AIC}, some of which are related to active lithium loss. The amount of Q_{AIC} can depend on temperature, electrode potential, electrode surface area, and electrolyte consumption, which can lead to electrolyte drying, increased impedance, and decreased rate capability of the cell [17], [169].

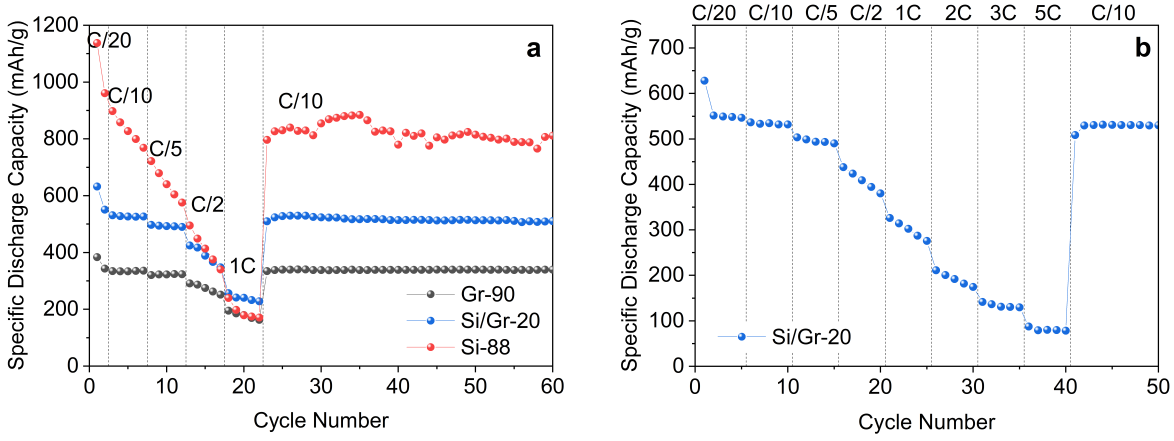

Figure 4.5: Rate capability of a) Gr-90, Si/Gr-20, and Si-88 half-cells at C/20 to 1C and b) Si/Gr-20 half-cell at C/20 to 5C

Figure 4.5a shows the rate capability of Gr-90‖Li, Si/Gr-20‖Li, and Si-88‖Li cells at

different C-rates from C/20 to 1C. The Si/Gr-20‖Li and Gr-90‖Li cells exhibit stable electrochemical performance at different C-rates, while the Si-88‖Li cell shows a rapid capacity decay and unstable performance at different C-rates. After cycling at 1C, the cells were cycled again at C/10 to investigate capacity recovery after deep (de)lithiation at 1C. For Si/Gr-20, the rate capability was measured by further charging/discharging the cell up to 5C (Figure 4.5b). The capacity recovery of Si/Gr-20‖Li cell is 99.37% and 98.67% at C/10 after deep charge/discharge at 1C and 5C, respectively.

All results of the electrochemical performance of the Si/Gr‖Li cells suggest that Si/Gr-20 is the optimized Si/Gr anode formulation, with a high initial capacity (compared to its theoretical capacity), high CE, stable Q_{AIC}, and very stable long-term cycling for more than 900 cycles at a high capacity retention value (>80%).

4.1.2 Optimization of the binders content

Investigating composite electrodes with two or more active materials chemistries requires optimization of the polymeric binders. Due to the difference in physical and chemical nature of Si and Gr, the use of a blended polymeric binder system or a single binder with synergistic effects is required. Therefore, a suitable binder for Gr may not necessarily be the optimal choice for Si. The surface reactivity and chemistry of Si require supramolecular polymeric binders with abundant polar functional groups such as –OH, COO^-, NH_2, etc., as described in Chapter 2.5. LiPAA and CMC were reported to be suitable binders for Si and Gr, respectively [8], [90], [170], [171]. PAA contains a larger number of –COOH/COO^- moieties compared to CMC, which can form stronger H-bonding with the surface of Si [90], [172]. The mixture of LiPAA and CMC in an optimized ratio can meet the distinct requirements of both Si and Gr active materials.

Figure 4.6 shows the chemical structure of LiPAA and CMC, as well as the LiPAA to CMC ratios used in this work for Si/Gr-20 anode, for further optimizing the binder formulation. The investigated LiPAA to CMC ratios are the following: 2.27:7.73 (same as Si to Gr), 1:1, 7.73:2.27 (same as Gr to Si), 1:0 (only LiPAA), and 0:1 (only CMC).

Figure 4.7a shows the long-term cycling performance of Si/Gr-20‖Li cells with different LiPAA to CMC ratios. It is observed that the electrode using LiPAA to CMC ratio of 2.27:7.73 (same as Si to Gr ratio) exhibits better cycling stability with a high capacity retention of 97.85% after 120 cycles and CE of 86.05% and 99.67% at the 1^{st} and 120^{th} cycle, respectively.

Figure 4.7b shows the rate capability of Si/Gr-20‖Li cells with different LiPAA to CMC ratios at C/20 to 1C. The initial capacities are in the order of: $Q_{\mathrm{LiPAA/CMC(2.27:7.73)}} > Q_{\mathrm{LiPAA}} > Q_{\mathrm{CMC}} > Q_{\mathrm{LiPAA/CMC(1:1)}} > Q_{\mathrm{LiPAA/CMC(7.73:2.27)}}$, linked to the active material, especially Si, utilization. The better performance of LiPAA/CMC(2.27:7.73) can be explained by better adhesion properties and wettability of the electrode compared to the

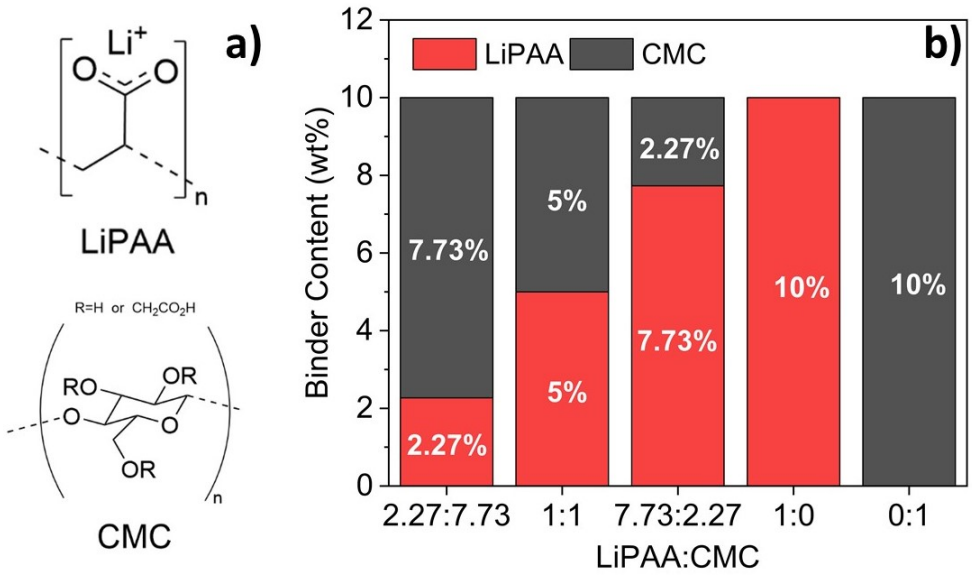

Figure 4.6: a) Chemical structures of LiPAA and CMC, b) LiPAA to CMC ratio (in wt%) for Si/Gr-20 anode

other electrodes with single or dual binder system. LiPAA/CMC(2.27:7.73) exhibits stable rate capability up to 1C and superior capacity recovery of 99.71% at C/10. It is also observed that LiPAA as a single binder system shows a better performance than a single CMC binder at different C-rates. The results confirm that the optimized amount of LiPAA and CMC binder follows the ratio of Si and Gr active material in the Si/Gr blend electrode.

In summary, Si/Gr blend electrodes with different Si to Gr and LiPAA to CMC ratios have been investigated. The electrochemical performance of Si/Gr‖Li cells showed that 20 wt% Si (Si/Gr-20) and LiPAA to CMC ratio of 2.27:7.73 are the optimal values for active materials and binders, respectively. These findings highlight the importance of slurry formulation and optimization of both active materials and binder systems in a Si-based anode.

4.1.3 Validation of the optimized anode in full-cell configuration

Although the study of Si/Gr‖Li cells provides important information on the stability and cycling performance of the anode, optimized parameters need to be further studied in a full-cell configuration (NMC622‖Si/Gr). The development of high-energy-density rechargeable batteries requires high-capacity and/or low-potential anodes coupled with a high-capacity and/or high-voltage cathode. Therefore, a high-capacity anode does not necessarily increase the overall capacity of the full-cell (Equation 4.4) [2], [163], [173].

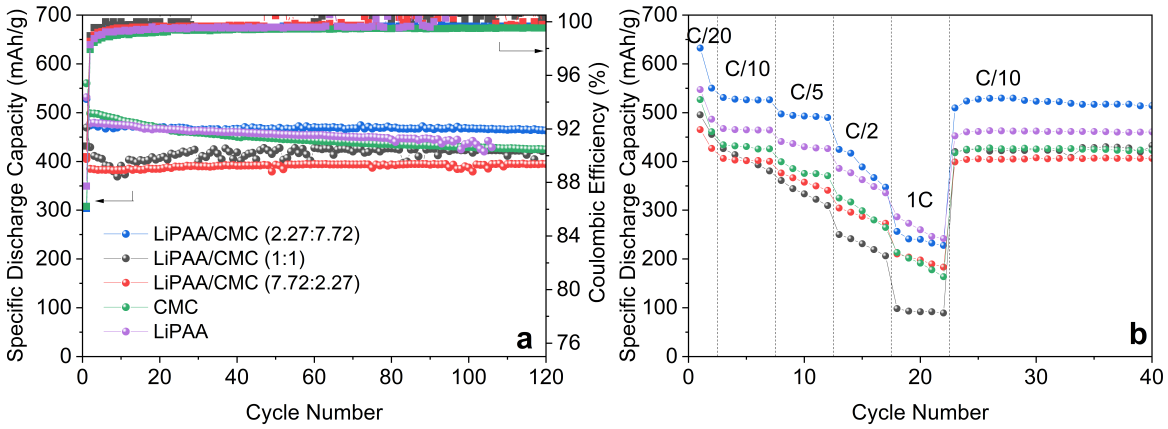

Figure 4.7: a) Long-term electrochemical cycling performance and Coulombic efficiency at C/10 and b) Rate capability of Si/Gr-20 anode half-cell with different LiPAA to CMC ratios

$$\frac{1}{Q_{\text{Cell}}} = \frac{1}{Q_{\text{A}}} + \frac{1}{Q_{\text{C}}} \tag{4.4}$$

where Q_{A} and Q_{C} are the capacity of the anode and cathode respectively.

In this work, a high-capacity Si-based anode and high-energy NMC622 cathode were assembled and examined in a full-cell as a promising development towards next-generation high-energy-density LIBs [174], [175].

For full-cell investigations the optimized anode (Chapters 4.1.1 and 4.1.2) was assembled in a coin cell configuration with an NMC622 cathode (NMC622‖Si/Gr-20). The cells were initially charged/discharged at C/20 for five cycles using a 1.2 M $LiPF_6$ in EC:EMC (3:7) + 10 wt% FEC electrolyte to build up a stable SEI layer, followed by charge/discharge at C/5 in the potential range of 2.5–4.35 V to investigate the long-term performance of the cells. The rate capability was measured at different C-rates ranging from C/10 to 5C.

Figure 4.8a shows the voltage vs. capacity curve obtained during galvanostatic charge and discharge from cycles 2 to 300. In order to better understand the degradation phenomena and electrochemical performance, the dQ/dV vs. V curve is shown in Figure 4.8b. It is difficult to directly indicate the contribution of both electrodes in the full-cell from the dQ/dV plot. According to Ohm's law (V = I.R), the shift of the peak position to higher voltages indicates an increase in the internal resistance. The widening of the peaks is related to the chemical changes in the electrodes, and the changes in peak intensity are related to the electrochemical changes within the cell [174], [176], [177]. It is observed in Figure 4.8b that the peaks are shifted to higher potentials, widened, and have lower intensity with increasing cycle number, implying an increase in resistance and lower elec-

trochemical performance at higher cycle numbers. At the initial charging, a sharp peak is observed at 3.7 V, which may be attributed to the electrode/electrolyte interphase and gas formation. The intensity of this peak decreases with increasing cycle number.

Figure 4.8c shows the capacity, Coulombic efficiency, and accumulated irreversible capacity of the NMC622||Si/Gr-20 cell. Capacity retention of 99.04% and 74.30% is observed in the 2nd and 50th cycle, respectively. The Coulombic efficiency in the 1^{st} and 2^{nd} cycles are 96.59% and 98.38%, respectively, and increases to 99.79% and 99.57% at the 300^{th} and 500^{th} cycle, respectively. The low initial Coulombic efficiencies in full-cells are linked to the anode's SEI layer formation and ongoing parasitic reactions on the cathode side. The accumulated irreversible capacity shows a higher slope up to 40 cycles, which can be related to the electrode/electrolyte interphase formation. Afterwards, the slope decreases and stays steady, indicating fewer parasitic reactions and irreversible active lithium loss. Figure 4.8d shows the rate capability measurement at C-rates ranging from C/10 to 5C of the NMC622||Si/Gr-20 cell, which exhibits 81.93% capacity recovery after deep charge/discharge at 5C.

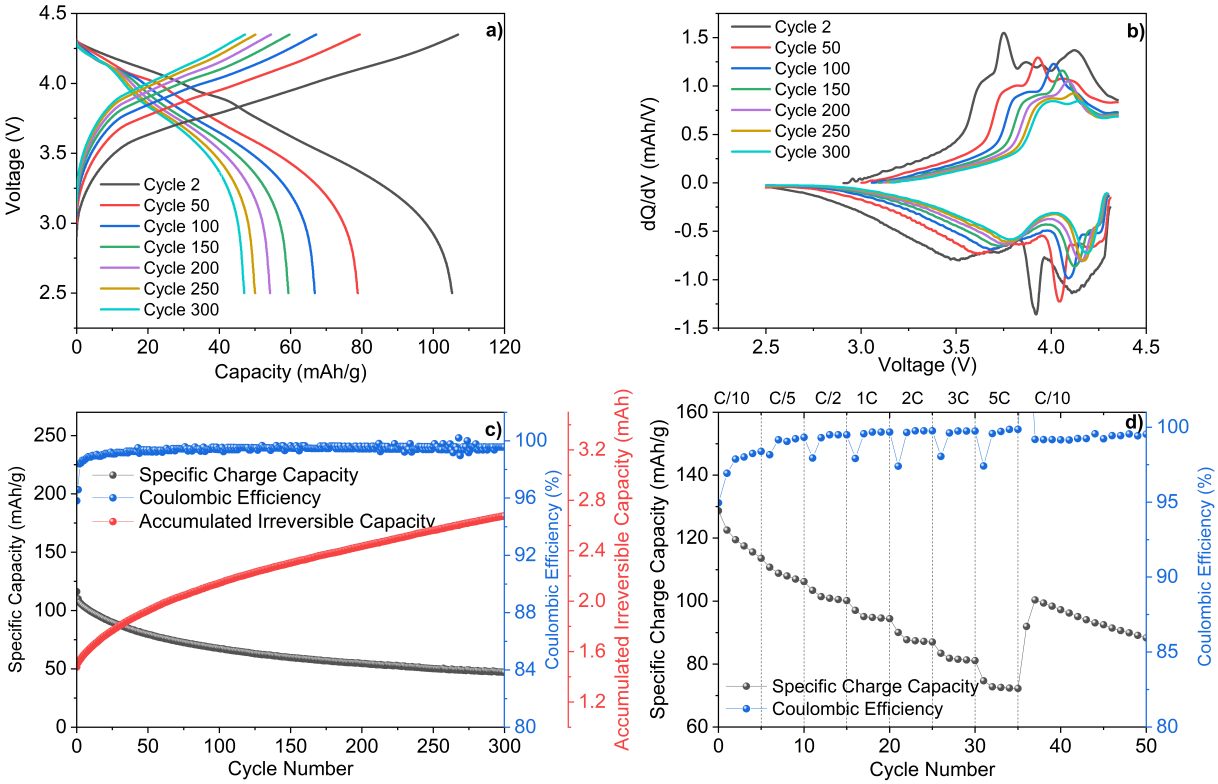

Figure 4.8: a) Charge-discharge profile and b) dQ/dV vs. V plot at different cycles, c) Cycling performance, Coulombic efficiency and accumulated irreversible capacity, and d) Rate capability at C/20, C/10, C/5, C/2, 1C, 2C, 3C and, 5C for NMC622||Si/Gr-20 full cells.

Voltage efficiency (VE) is defined as the ratio of average discharge voltage ($\overline{V_{\mathrm{d}}}$) to average

charge voltage ($\overline{V_c}$) and energy efficiency (EE) is defined as the ratio of discharge energy density ($\overline{E_d}$) to charge energy density ($\overline{E_c}$) as shown in equations 4.5 and 4.6.

$$VE = \frac{\overline{V_d}}{\overline{V_c}} \times 100[\%] \tag{4.5}$$

$$EE = \frac{\int_0^{t_d} V_d I_d \, dt}{\int_0^{t_c} V_c I_c \, dt} \times 100[\%] \tag{4.6}$$

At a constant current equation 4.6 could be simplified as below:

$$EE = CE \frac{\frac{\int_0^{t_d} V_d \, dt}{t_d}}{\frac{\int_0^{t_c} V_c \, dt}{t_c}} = CE \frac{\overline{V_d}}{\overline{V_c}} = CE \cdot VE[\%] \tag{4.7}$$

Therefore, both VE and CE have a direct impact on the value of EE. CE depends on the properties of the electrode, such as particle size, porosity, specific surface area, and mechanical stability, which can impact the formation of SEI and cathode electrolyte interphase (CEI) as well as their stability. The operating parameters (temperature, voltage range, C-rate) and electrolyte properties also affect the CE. VE depends on different parameters such as lithium storage mechanism (intercalation vs. alloying materials), active materials properties (particle size, specific surface area), material stability (structural or phase changes), electrode properties (formulation, thickness, porosity, etc.), electrolyte formulation, and operating parameters (temperature, C-rate) [178].

Figure 4.9 shows the VE and EE for selected cycle numbers in the NMC622‖Si/Gr-20 full-cell. In the 2^{nd} cycle, VE shows a value of 94.78% and it slightly decreases to 93.41% at the 300^{th} cycle. The obtained EE is higher than 93% after 300 cycles, and CE at the 2^{nd} cycle is 98.38%, which increases to 99.65% and 99.79% after 150 and 300 cycles, respectively. EE values are higher than the values reported for different anode/cathode materials [179], as well as the values reported for Si/Gr electrodes (∼89%) [178], confirming the enhanced results of this work.

4.1.4 Summary

In summary, the performance of the negative electrode was improved by optimizing the anode formulation, active materials (Si/Gr), and polymeric binders (LiPAA/CMC) ratios. The electrochemical performance of the Si/Gr anodes was investigated in Si/Gr‖Li and NMC622‖Si/Gr cells. The results prove the importance of optimizing Si to Gr and LiPAA to CMC ratios. Based on the initial discharge capacity, capacity retention, and CE

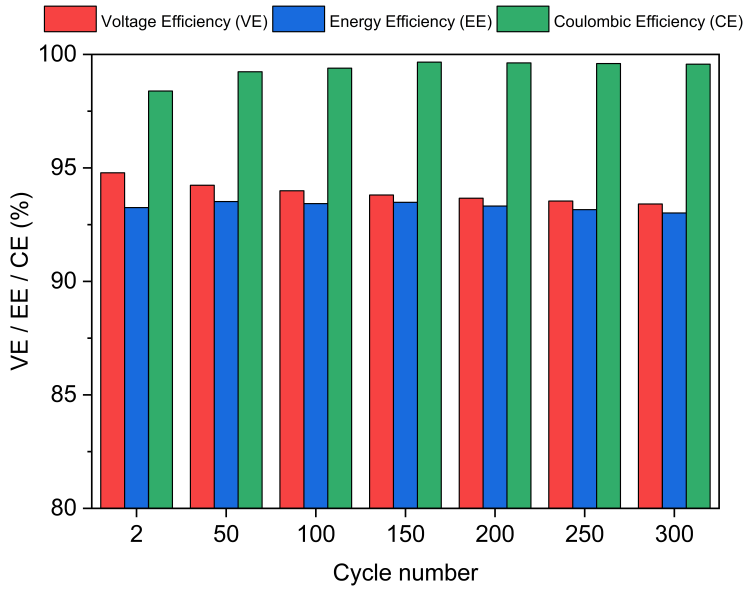

Figure 4.9: Voltage efficiency (VE), energy efficiency (EE), and Coulombic efficiency (CE) of the NMC622‖Si/Gr-20 full cell at selected cycle numbers.

of Si/Gr‖Li with different Si to Gr ratios, the configuration with 20 wt% Si (Si/Gr-20) and LiPAA/CMC ratio of 2.27:7.73 was identified as the optimal combination of materials and binders. The Si/Gr-20‖Li cell exhibits stable electrochemical performance with over 900 cycles at C/10, achieving a capacity retention of 80.06%. The rate capability measurements showed a capacity recovery of 98.67% after deep charge/discharge at 5C.

The electrochemical performance of NMC622‖Si/Gr-20 was investigated in long-term cycling and rate capability measurements. The Key electrochemical efficiencies, such as CE, VE, and EE, were investigated. After 300 cycles the cells show VE and EE higher than 93%, which are higher than the reported values in the literature. However, the full-cell configurations in this study were not fully optimized, particularly on the cathode side. The performance gap between Si/Gr‖Li and NMC622‖Si/Gr cells suggests that Li loss governs the degradation mechanism and significantly contributes to aging. Further cathode optimization is expected to improve the overall cell performance.

4.2 SEM/EDX analysis of silicon/graphite anodes

The optimized Si/Gr anode (Si/Gr-20, described in Chapter 4.1.1) was analyzed with SEM and EDX before electrochemical cycling (pristine electrode) to investigate the morphology and the distribution of the particles after coating the electrode. After electrochemically cycling the Si/Gr anodes, the coin cells were disassembled, and SEM/EDX measurements were conducted on the cycled anode to study the changes in morphology after lithiation/delithiation (Figure 4.10). In both cases, surface and cross-section SEM/EDX analysis was performed. Cross-section imaging can provide further information about particle size, porosity, and thickness of the electrodes.

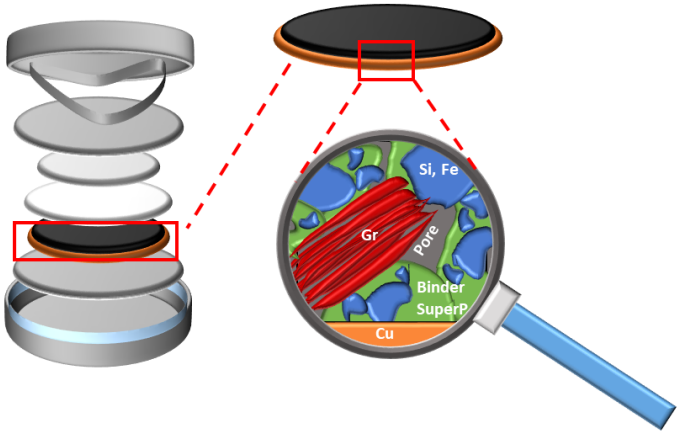

Figure 4.10: Schematic illustration of postmortem SEM analysis on the Si/Gr anodes

4.2.1 Pristine anode

Figure 4.11 shows SEM images from the surface of the Si/Gr-20 pristine anode after calendering. Measurements were conducted in secondary electron (SE) and backscattered electron (BSE) modes at two different magnifications. SE imaging captures the electrons originating from the near surface regions (a few nm) and provides information about the surface morphology. As observed in Figure 4.11 a and c, the slurry is distributed homogeneously and covers the surface of the current collector. This homogenous distribution of the slurry is also observed in the panorama cross-section SEM image in Figure 4.12a. Pores are visible in both surface and cross-section SEM images in Figure 4.11 and 4.12, but no cracks are observed in these films. It should be noted that SEM measurements were performed on 2–3 samples, and several areas were investigated per sample, which consistently showed similar morphology and particle distribution. BSE imaging captures electrons from deeper below the surface (a few μm) and contains information about the composition of the sample, but has a lower image resolution. In BSE images, a contrast between the elements with different atomic numbers is observed. More BSEs are detected

in the elements with higher atomic numbers, and therefore, the image is brighter compared to the lower atomic numbers. Figure 4.11 b and d, as well as Figure 4.12b, show the SEM images in BSE mode from the surface and cross-section of Si/Gr-20 samples, respectively. The contrast between Si (atomic number 14) and Gr (carbon, atomic number 6) active material is observed, appearing as light and dark grey particles, respectively, which is also confirmed by the EDX layered mapping in Figure 4.12c.

For a better understanding of the Si material (Si-alloy, 3M), electrodes were prepared with only Si active material, (Si-88 in section 4.1), and the electrode morphology and particle distribution are investigated by SEM/EDX, as depicted in Figure 4.13. EDX mapping in Figure 4.13 b and c confirms the presence of Si-Fe alloy and carbon in the Si-alloy material ($Si_xFe_yC_z$), which is consistent with the observations from Figure 4.12c. Based on the cross-section SEM/EDX investigations, the Si-Fe alloy particle size ranges from $\sim$ 0.35 to 10 μm.

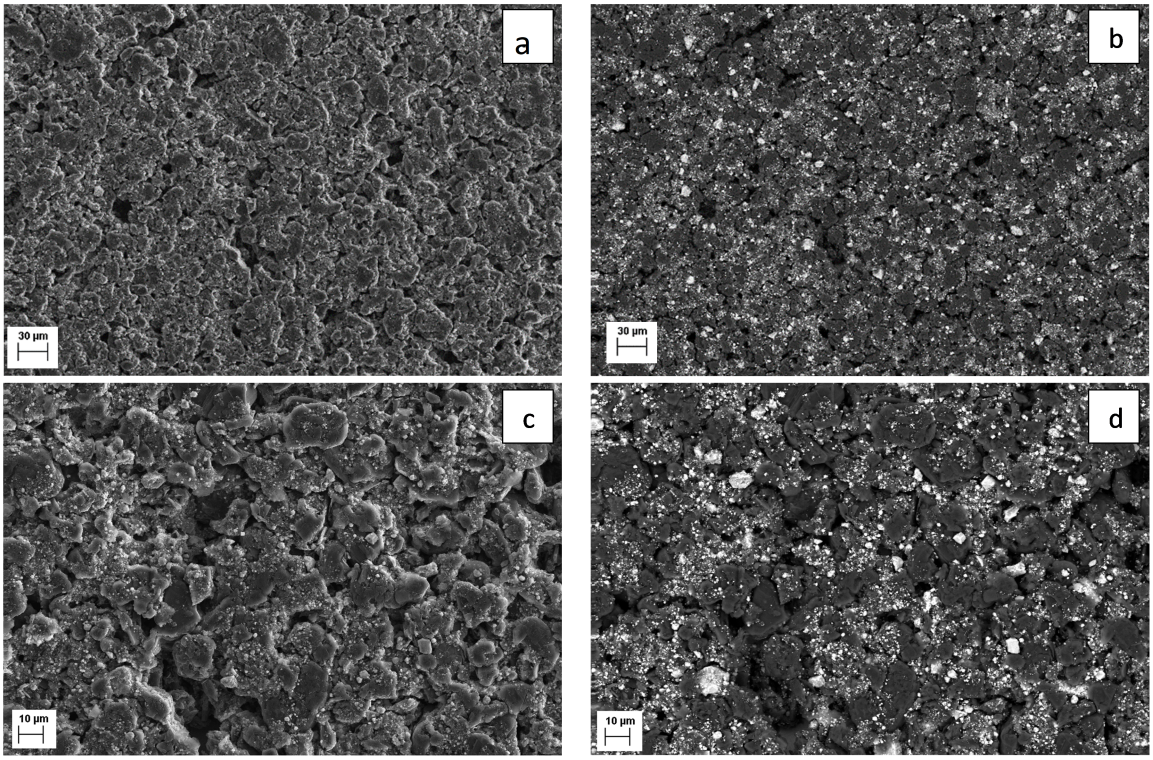

Figure 4.11: SEM images of the surface of pristine Si/Gr-20 anode, captured in a,c) secondary electron (SE) mode, and b,d) backscattered electron mode (BSE) at different magnifications

To study the effect of calendering on the morphology of Si/Gr anodes, the electrode surfaces were investigated using SEM. Based on Figure 4.14, calendered electrodes exhibit more closely packed particles and a flatter surface. Calendering is commonly applied on commercial electrodes to enhance the volumetric energy density (Wh L^{-1}) by compacting more active material in the unit volume [180]. The Si active material undergoes a large

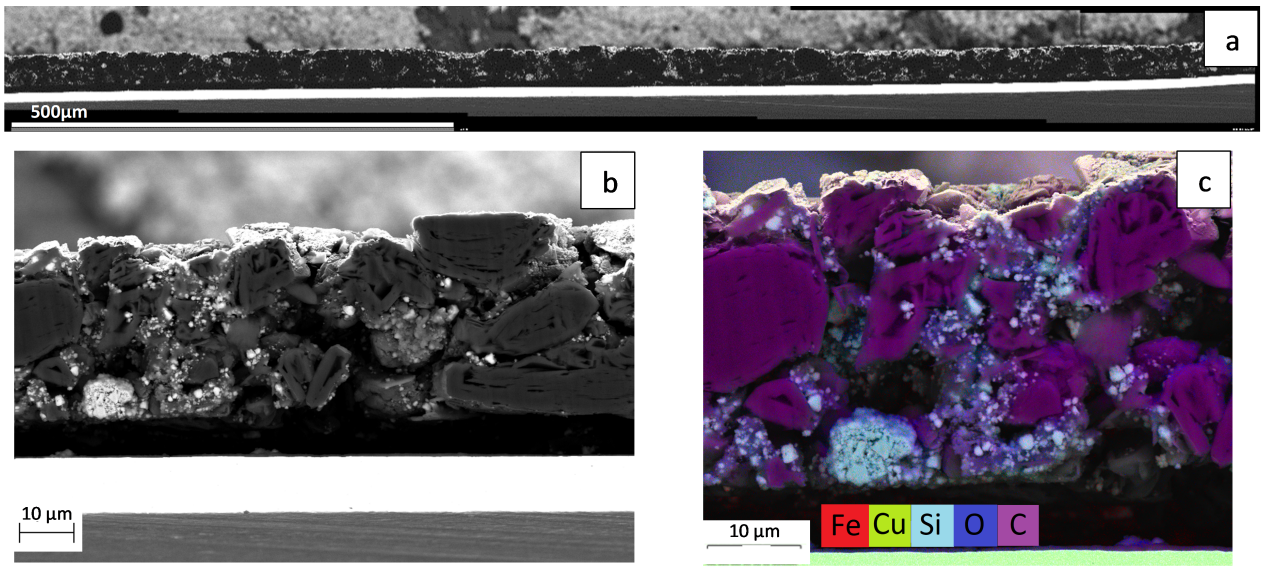

Figure 4.12: Pristine Si/Gr-20 anode a) panorama SEM cross-section image, b) SEM cross-section image, c) EDX layered mapping, indicating iron (Fe), copper (Cu), silicon (Si), oxygen (O), and carbon (C)

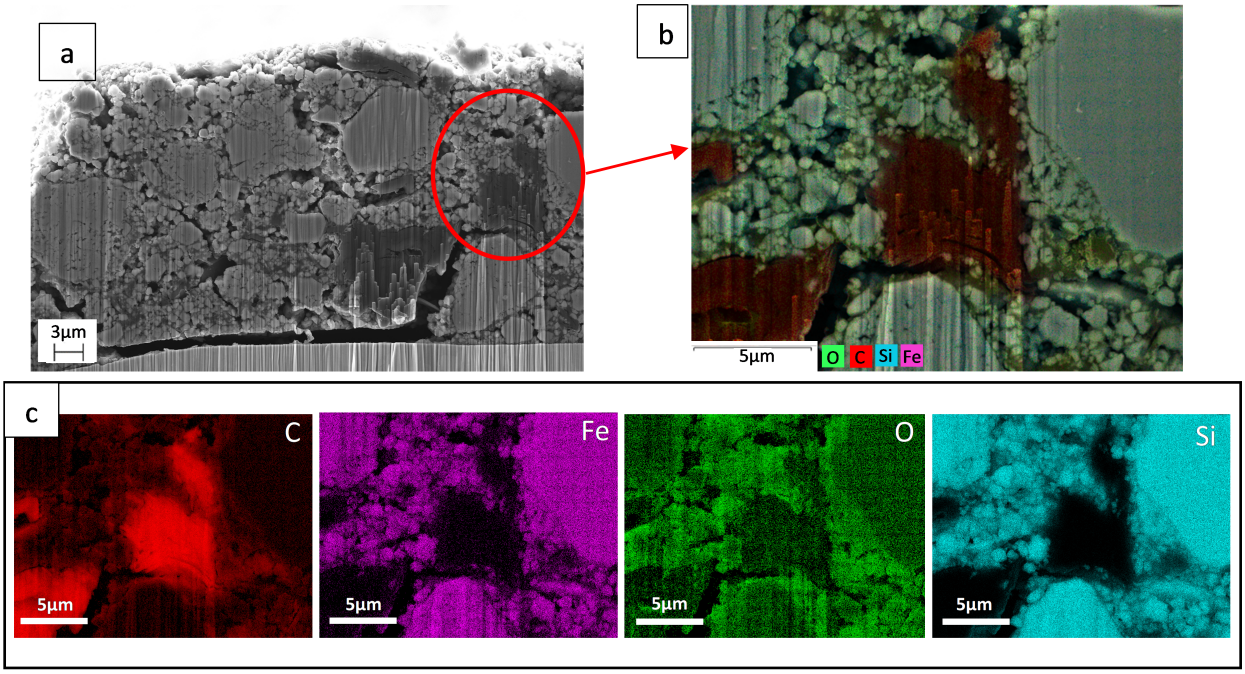

Figure 4.13: Pristine Si(Si-alloy, 3M) material used in this work: a) Cross-section SEM image, b) EDX layered mapping image, c) EDX elemental mapping for carbon (C), iron (Fe), oxygen (O), and silicon (Si)

volume change during lithiation and delithiation, and the presence of a certain amount of porosity within the electrodes is essential. On the other hand, high porosity can reduce the contact area of the active particles, which reduces the stability of the anode. Therefore, it is highly important to optimize the porosity of the electrode and balance the energy density and cycling performance.

Figure 4.14 a and b show the BSE and SE SEM images of Si/Gr anodes before and after calendering, respectively. Different areas on the surface of the electrodes were analyzed using EDX, confirming that the light and dark grey particles in BSE images are Si and Gr, respectively. The EDX results are depicted in Figure A.2 (Appendix). Figure 4.14 c and d provide magnified SEM images of the anode surface before and after calendering. The morphology of Si and Gr particles, including basal and prismatic planes, is clearly visible before calendering (Figure 4.14c). It is observed that after calendering, the electrodes have flatter and smoother surfaces and particles are more densely packed compared to the uncalendered samples.

4.2.2 Post-mortem analysis

To better understand the structural change of the Si particles after electrochemical cycling, surface and cross-section SEM/EDX of the Si/Gr electrodes were investigated after lithiation and delithiation. Figure 4.15 shows the electrochemical performance of Si/Gr‖Li cells at C/10 for up to 1200 cycles, and at C/5 and C/2 for up to 100 cycles. Red marks indicate cycles 20, 500, and 1200 at C/10, corresponding to the anodes investigated by SEM/EDX in this research.

Figure 4.16a shows the EDX surface mapping of the pristine Si/Gr-20 anode and the distribution of Si, C, O, and Fe. Si particles are uniformly distributed across the surface. The Si/Gr electrodes were analyzed with SEM/EDX after electrochemical cycling (Si/Gr-20‖Li cells at C/10). The Si/Gr-20‖Li cells were disassembled at the lithiated state after 20 and 500 cycles, and SEM/EDX mapping was performed on the lithiated anodes (2–3 samples were prepared for each SEM/EDX measurement). The EDX mappings of the Si/Gr anodes after 20 and 500 cycles are observed in Figure 4.16 b and c, respectively. The intensity of the oxygen signal is increased after lithiation, as shown in Figure 4.16b and c. The surface oxygen can originate from the oxygen-containing species on the surface of the lithiated electrode and the SEI layer, such as Li_2O. The growth of oxygen-rich domains can be related to the ongoing reformation and growth of decomposition products. A fluorine (F)-rich layer is also observed on the surface of lithiated Si/Gr anode in Figure 4.16 b and c, which can be due to $LiPF_6$ decomposition products and the inorganic SEI species, such as LiF and $LiPF_xO_y$. An increased distribution of O and F over the surface area is observed at higher cycle numbers, as depicted in Figure 4.16d. The presence of phosphorus (P) on the surface could be due to residual $LiPF_6$ salt or its P–F containing decomposition species. The higher magnification of the SEM images and EDX mapping of Figure 4.16 is provided in the Appendix (Figure A.3).

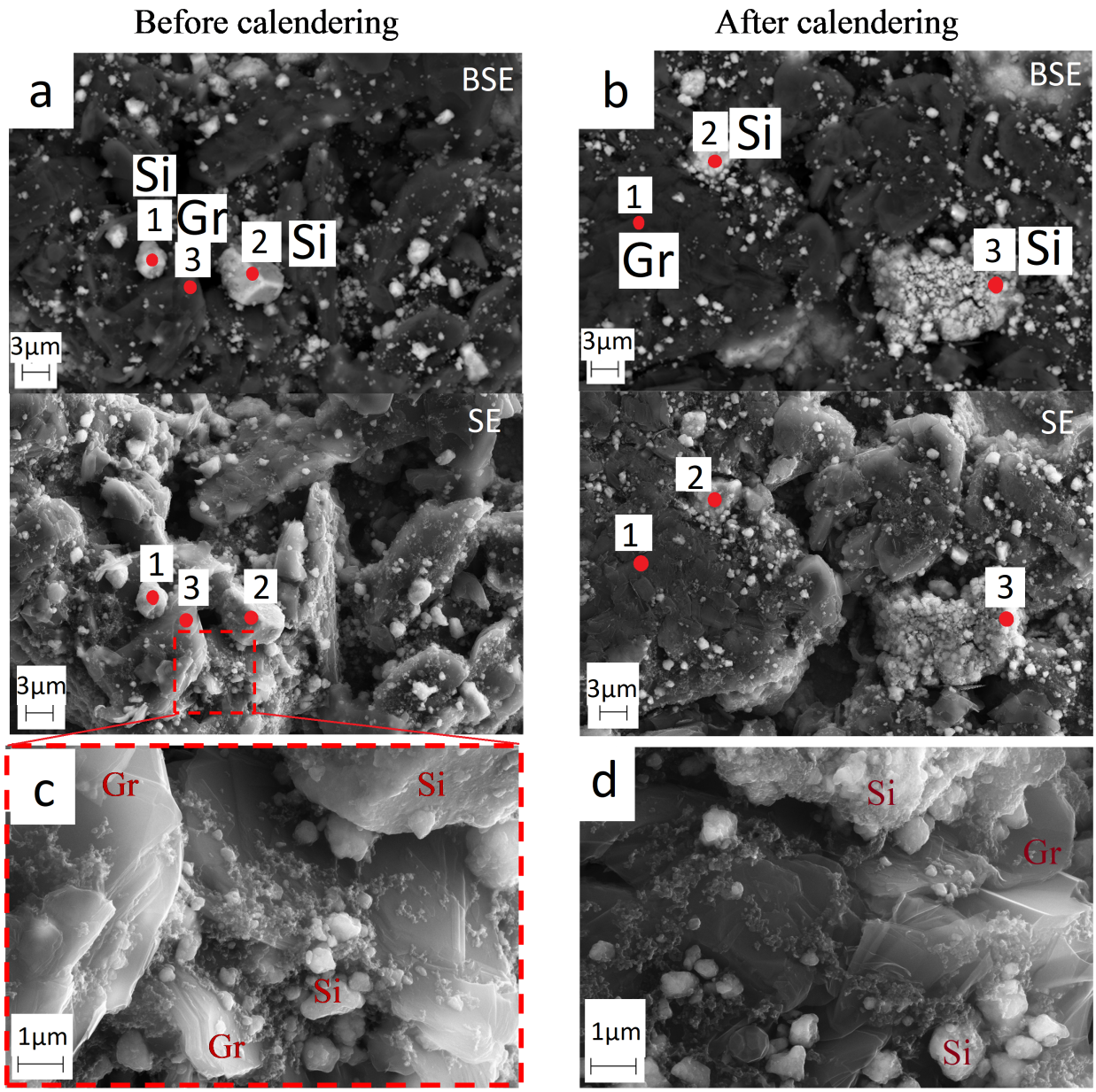

Figure 4.14: Surface SEM images of pristine Si/Gr-20 anode a,c) before calendering the electrode and b,c) after calendering the electrode, EDX analysis of the pristine Si/Gr anode before and after calendering is depicted in the Appendix (Figure A.2)

To investigate structural changes in Si/Gr electrodes after long-term cycling, the cross-section SEM and EDX analysis were performed after 1200 cycles, as shown in Figure 4.17. Significant morphological changes and gradual loss of Si volume fraction are observed in these images. Similar morphologies and degradation patterns have been reported by Vorauer et al. [181] and Kumar et al. [182], studying the 3M Si-alloy materials. Three distinct degradation stages are observed in the Si particles as shown in Figure 4.17 b,

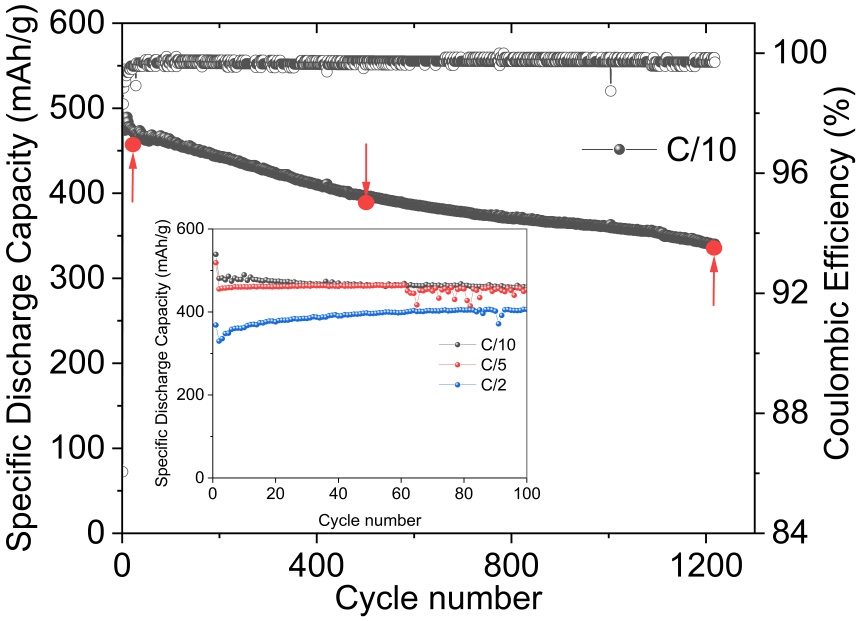

Figure 4.15: Electrochemical performance of the Si/Gr-20||Li cells cycles at C/10, C/5 and C/2. The red marks on the C/10 graph are at 20 cycles, 500 cycles, and 1200 cycles, where postmortem SEM/EDX analysis was performed on the Si/Gr anode.

marked with green, orange, and red circles and named stage 1, stage 2, and stage 3, respectively. Upon electrochemical cycling, the large volume changes of Si particles result in particle pulverization and degradation, leading to morphology changes of Si particles and their surrounding. Figure 4.17c provides a higher magnification of the green and orange areas marked on Figure 4.17b, showing stages 1 and 2 of Si-degradation. Figure 4.17d focuses on the red area marked on Figure 4.17a, representing stage 3 of Si degradation, where the Si particles are pulverized and distributed. Depending on the size of the Si particles, the cycle number, and lithiation state, the particles may undergo one of the three degradation stages mentioned above. The repeated stress and volume changes of Si particles during lithiation and delithiation result in the formation of cracks and pores in the vicinity of Si particles. These defects may lead to the redistribution of Si particles and modification of the structure and morphology of the electrode. A comparison of Figure 4.17 and Figure 4.12, shows less porosity in the anode after electrochemical cycling and more closely packed particles, which may be due to changes in structure and redistribution of Si particles. Figure 4.17e shows the cross-section SEM and EDX (results depicted in Figure A.4 in the Appendix section) of Si/Gr anode after ∼1200 cycles. Regions 1, 2, and 3 exhibit a high Si signal, which shows the presence of Si particles in these areas. Region 4 shows a strong C signal, indicating the Gr particles. Region 5, with a similar structure to Figure 4.17d, shows a high level of O, followed by Si and C, illustrating stage 3 in Si particle degradation. Figure 4.17f shows a cross-section of the pristine anode, where the

Si particles are intact.

To investigate the effect of C-rate on the morphology changes and degradation of Si/Gr electrodes, further SEM/EDX investigation was performed on Si/Gr electrodes after lithiation/delithiation in Si/Gr-20‖Li configuration at C/5 and C/2 for 100 cycles. The cross-sectional SEM images were studied as shown in Figure 4.18. The morphological changes of Si particles are consistent with those observed in Figure 4.17. In Figure 4.18 a1-a3, the Si/Gr anode was lithiated/delithiated at C/5 for 100 cycles. The intact Si particles and particles at the initial degradation stage (stage 1, marked in green) are observed along with the particles at the higher stages of degradation (stage 2, marked in orange). The Si-core is visible, indicating that the particles have not reached stage 3 degradation in these images. Figure 4.18b1-b3 shows the Si/Gr anode lithiated/delithiated at C/2 for 100 cycles, indicating a severe degradation of Si particles (stage 3, marked in red). However, the extent of degradation, shrinking of Si core, and pulverization of Si particles in Figure 4.18 b1-b3 is less severe than after 1200 cycles, Figure 4.17. Figure 4.18 b1-b3 may capture the onset of morphological changes and redistribution of Si particles, which leads to the final degradation morphology observed in Figure 4.17. The observed Si redistribution may affect long-term capacity retention, as shown in Figure 4.15. As observed in Figure 4.17 and 4.18, not all Si particles undergo the same degree of stress and degradation. This variation suggests that some particles may not fully participate in the lithiation/delithiation process, which can explain the gap between the theoretical capacity and the practical capacity of the Si/Gr anodes.

Additional SEM/EDX analysis was performed on NMC622‖Si/Gr-20 full-cells after 100 cycles at C/2. Figure 4.19a shows the cross-section SEM/EDX analysis of the Si/Gr-20 anode, where the redistribution and degradation of Si particles exhibit a pattern similar to that observed in the half-cell configuration. Figure 4.19b shows the EDX mapping (of the highlighted region in Figure 4.19a), and Figure 4.19c shows the individual EDX elemental mapping. The presence of oxygen at the border of Si particles indicates ongoing chemical reactions between the electrolyte and Si particles. These reactions might be related to the reformation and growth of the SEI and degradation layer due to the breakdown and redistribution of Si particles upon electrochemical cycling. The inhomogeneous stress distribution due to these chemical reactions can enhance the formation of cracks and pores and accelerate the degradation of Si particles [181].

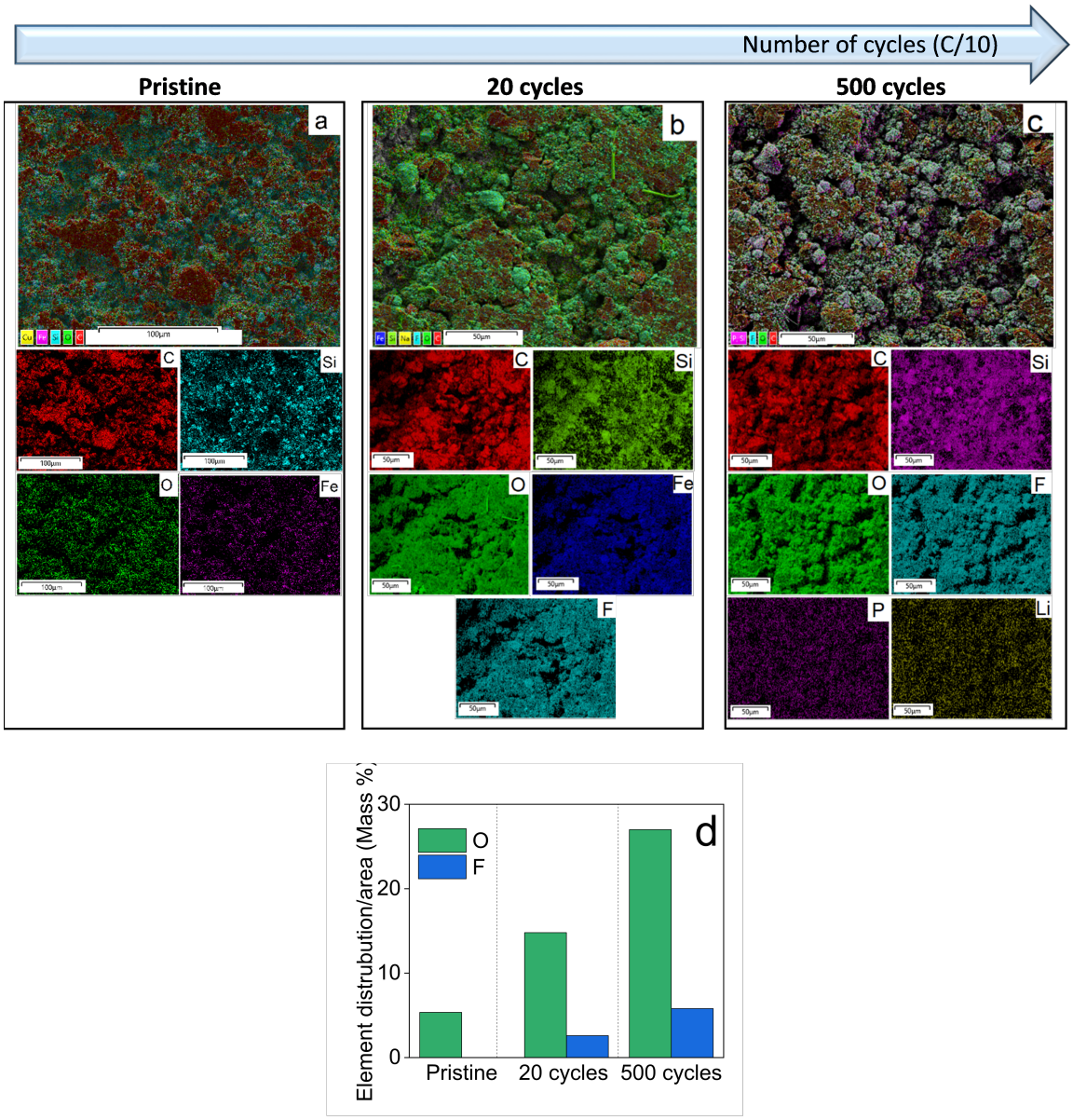

Figure 4.16: EDX mapping of a) Pristine Si/Gr-20 electrode, and Si/Gr electrodes after lithiation/delithiation in Si/Gr‖Li cell configuration at C/10 after b) 20 cycles and c) 500 cycles, d)Element distribution of O and F in the whole EDX spectrum (mass%) for pristine, 20 cycles and 500 cycles

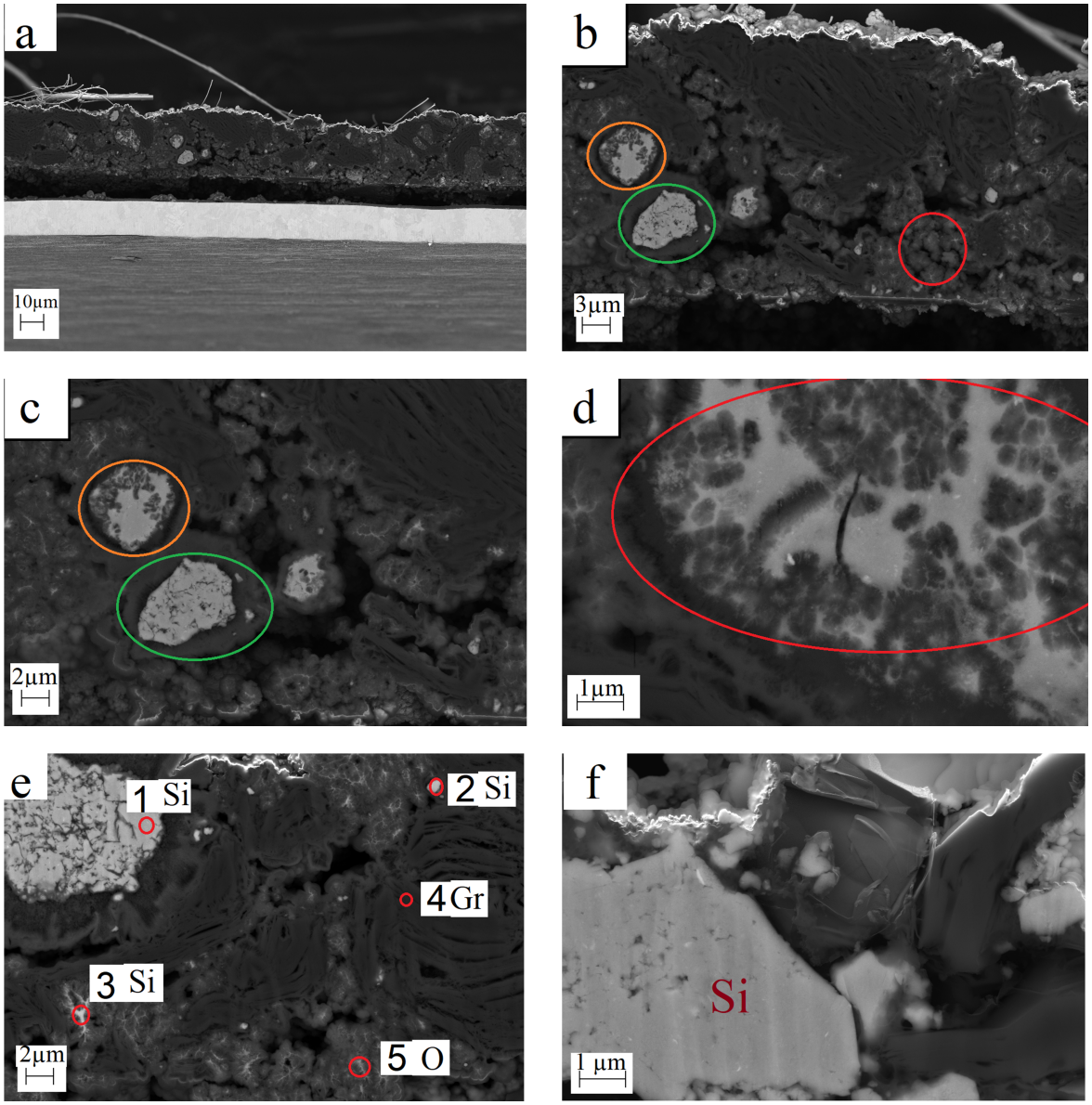

Figure 4.17: Cross-section SEM analysis of Si/Gr-20 electrodes after ∼ 1200 cycles in a Si/Gr||Li cell configuration at C/10 a) Si/Gr anode after cycling, b) Three different stages of Si degradation is marked on the image, c, d, e) Higher magnification of Si particles degradation, and f) Pristine Si/Gr anode. EDX analysis is depicted in the Appendix (Figure A.4)

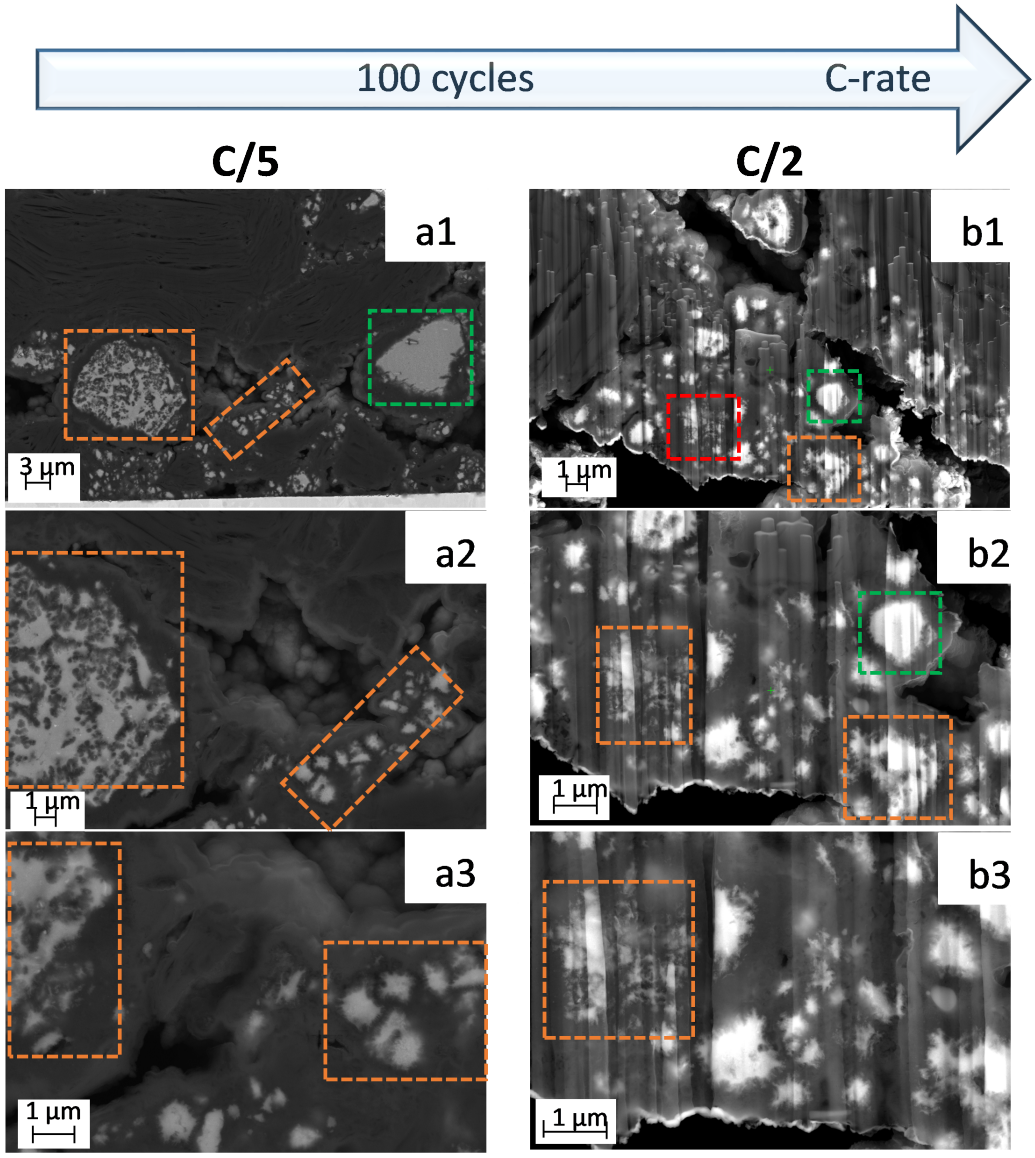

Figure 4.18: Cross-section SEM images of Si/Gr anodes after lithiation/delithiation in Si/Gr||Li after 100 cycles at a1-a3) C/5 and b1-b3) C/2

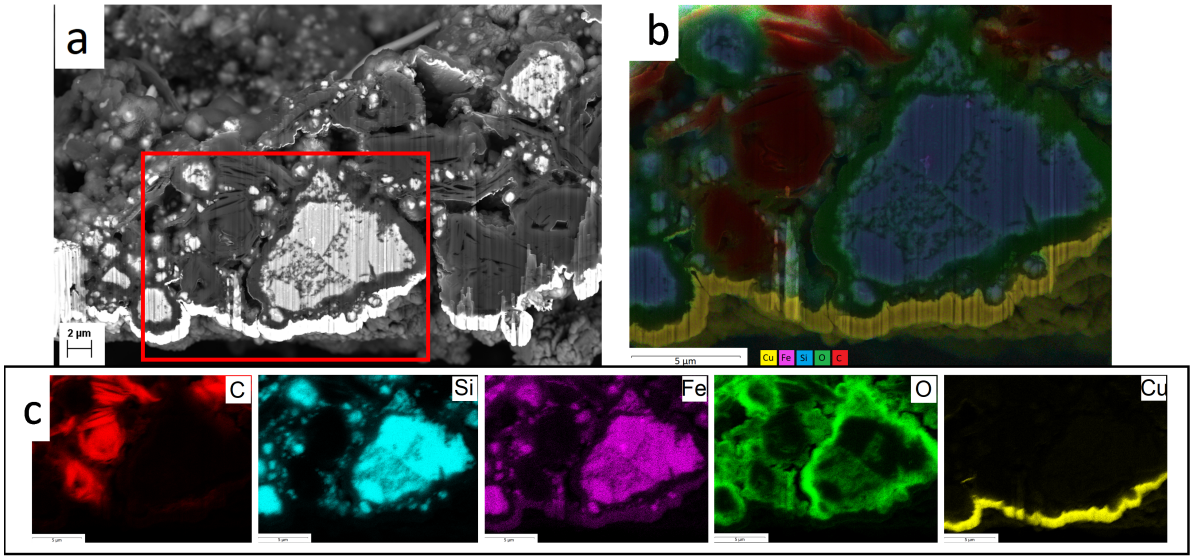

Figure 4.19: Cross-section a) SEM image, b) Layered EDX mapping, and c) Elemental EDX mapping of Si/Gr anodes after 100 cycles at C/2 in NMC622‖Si/Gr full-cell

4.3 Integration of the optimized silicon/graphite anode-based lithium-ion battery in a photovoltaic charging battery system

This chapter is based on the results from the publication entitled *"Toward the Integration of a Silicon/Graphite Anode-Based Lithium-Ion Battery in Photovoltaic Charging Battery Systems"*, which was published during this thesis by Hamzelui et al. [183]. The content and figures of this chapter are reproduced and modified from Ref. [183] with permission from American Chemical Society, Copyright 2022. This work was in collaboration with IEK-5, Forschungszentrum Jülich. The battery development was performed at ISEA, and the PV-Battery integrated system design and solar charging experiments were performed by IEK-5. Detailed information on the perovskite solar cell and solar charging set-up is fully discussed in Ref [183].

Solar photovoltaic (PV) energy generation depends on the weather conditions during daylight hours, resulting in a mismatch between supply and demand [184]. Combining or integrating PV with batteries is an environmentally friendly solution to overcome the intermittency of solar generation and to produce and store sustainable energy. The integration of PVs and batteries not only stabilizes the output but also minimizes wiring and power management. PV-Battery integration can be implemented in various configurations and scales, depending on the application. In directly coupled PV-Battery system, a proper voltage matching of the PV and battery is critical, which can provide the opportunity to eliminate the need for maximum power point tracking (MPPT) [185], [186]. The batteries used in a PV-Battery system must be cost-effective and operate under elevated temperatures [187]. Typically, the module temperature is in the range of 30–60 °C (reaching a maximum of 70 °C) depending on the climate zone.

As discussed theoretically in Chapter 2.4 and experimentally in Chapter 4.1, the co-utilization of Si and Gr, combined with an optimized polymeric binder system, can overcome the limitations of each active material, by leveraging their synergistic properties. In this chapter, the NMC622‖Si/Gr cell developed in Chapter 4.1.3 is further optimized for high-temperature operation and integration into PV-battery system. This optimization includes the use of additives, such as fluoroethylene carbonate (FEC), vinylene carbonate (VC), and (2-cyanoethyl)triethoxysilane (TEOSCN) additives [46], [174]. Using suitable electrolyte additive improves the electrochemical performance and stability of the cell at elevated temperatures [46], making the batteries more suitable for PV integration.

A perovskite solar cell (PSC) has been used in this work, due to its high efficiency and suitability for small-scale applications and coupling with coin-cell scale batteries, which is challenging to achieve with wafer-based Si PV devices. No specific voltage matching development was performed for direct matching of the PSC and battery. Therefore, a direct-current—direct-current (DC-DC) boost converter with MPPT has been used for effective coupling between the battery and the PSC [188].

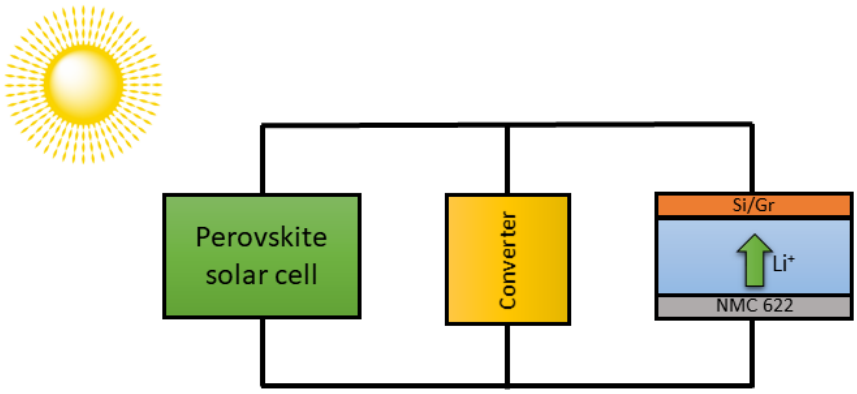

Figure 4.20: Schematic illustration of PV-Battery setup, using a perovskite solar cell, DC-DC converter, and LIB

4.3.1 Battery development

To optimize a full-cell for integration into the PV-battery system, electrolyte, anode, and cathode optimization is necessary. In this work, the electrolyte system consists of 1 M $LiPF_6$ in EC:DEC (1:1), with 5 wt% FEC, 2 wt% VC, and 1 wt% TEOSCN[174]. The FEC additive significantly influences the electrolyte degradation and SEI formation process. VC improves the cycle life, thermal stability, and SEI layer formation of the Si-based anodes. However, despite all the advantages of FEC and VC, there are some critical disadvantages. For example, VC forms a thicker SEI layer on Si-based anodes and increases the impedance of the cell. FEC increases the gassing at elevated temperatures, which results in the consumption of the FEC additive, therefore, reducing the performance of the cell. TEOSCN has been reported to improve the electrochemical performance of the cell under high temperatures [46], [174]. Therefore, the combination of FEC, VC, and TEOSCN electrolyte additives results in synergistic effects that improve the overall cell performance.

The optimized Si/Gr anode developed in Chapter 4 paired with an NMC622 cathode with a loading of 6.4 mg/cm^2 was investigated for application in the PV-battery system. NMC622 cathode was chosen over alternatives such as lithium cobalt oxide (LCO) and lithium iron phosphate (LFP) due to its balanced trade-off between safety and performance. Although LFP offers high safety, long cycle life, and stable chemical structure, it has a lower energy density than NMC622. LCO has a less stable structure and is subjected to structural changes, oxygen release, and electrolyte decomposition.

To design and optimize a full-cell, the ratio of the capacity of the negative to the positive electrode (N/P ratio) needs to be balanced. In this work, the thickness of the Si/Gr anodes was adjusted (active mass balance) using 125, 250, 300, and 350 μm draw-bar

gaps (wet-thickness) to optimize the N/P ratio of the full-cell. NMC622 cathode with an areal capacity of 1.15 mAh cm^{-2} was used. The N/P ratio is a critical parameter and has an impact on the cycle life, energy density, safety, and cost of the LIB. An unbalanced N/P ratio can lead to severe performance issues of the LIB. For example, if the N/P ratio is less than 1, there will not be enough sites on the anode to accommodate all the Li ions coming from the cathode, which can lead to lithium plating, irreversible capacity loss, and internal short-circuit upon long-term cycling [19], [20]. Therefore, to enhance the cycle life and safety of the battery, a slightly higher areal capacity of the anode is used in industrial applications. However, if the anode is oversized, the inactive mass (unused mass and volume) increases and energy density decreases. An optimization of the N/P ratio is necessary for balancing between safety ($\frac{Q_{\text{Anode}}}{Q_{\text{Cathode}}} > 1$) and specific capacity ($\frac{Q_{\text{Anode}}}{Q_{\text{Cathode}}} = 1$), which is found to be between 1.1 and 1.2 [18].

Figure 4.21a shows the charge-discharge curve of NMC622||Li and Si/Gr||Li with different thicknesses cycled at 0.05C. The corresponding N/P ratios are listed in Table 4.2. Full-cells using Si/Gr-250 have an N/P ratio of 1.18, which is in the optimized range reported in the literature [18]. Figure 4.21b shows the rate capability measurements of Si/Gr||Li cells with different thicknesses at C-rates ranging from 0.05C to 3C. It can be observed that Si/Gr-250 has stable electrochemical performance at different C-rates and a capacity recovery of 98.36% after deep charge/discharge at 3C. The capacity recovery for the other thicknesses of Si/Gr can be seen in Table 4.2. Based on these results, Si/Gr-250 anode with an areal capacity of 1.37 mAh cm^{-2} and an active mass loading of 2.6 mg cm^{-2} was selected for further full-cell experiments.

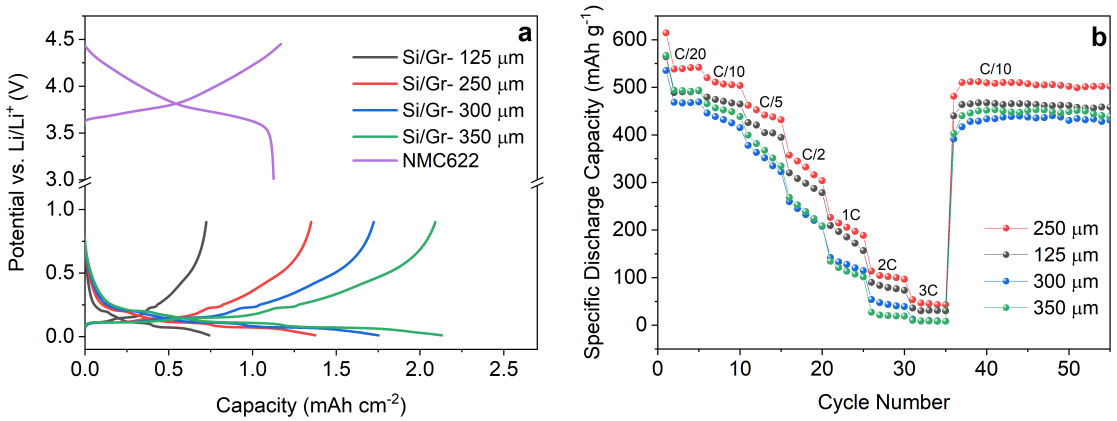

Figure 4.21: a) Charge-discharge profile at the second cycle at 0.05C for the NMC622||Li and Si/Gr||Li (with different thicknesses) cells, b) Rate capability measurements at different C-rates (0.05C to 3C) for Si/Gr anode half-cells with different thicknesses.

Since the solar cells operate at elevated temperatures, the electrochemical performance of NMC622||Si/Gr, Si/Gr||Li, and NMC622||Li cells was investigated at RT, 45, and 60 °C. Figure 4.22a shows the electrochemical performance of Si/Gr||Li cells at 0.2C at the three different temperatures. At elevated temperatures (45 and 60°C) the cells show higher

Table 4.2: N/P ratio of NMC622‖Si/Gr cells and capacity recovery of Si/Gr‖Li cells.

Anode	N/P ratio	Half-cell capacity recovery after (dis)charge at 3C (%)
Si/Gr-125	0.63	97.47
Si/Gr-250	1.18	98.36
Si/Gr-300	1.36	97.31
Si/Gr-350	1.81	97.25

initial capacities (454.05, 544.04, and 582.31 mAh g^{-1} at RT, 45, and 60°C, respectively). However, the rate of capacity loss is significantly higher at elevated temperatures and the capacity retention is 92.41, 79.24, and 62.46% at RT, 45, and 60°C, respectively. In the initial cycles, lithiation/delithiation is controlled by diffusion, and due to the high mobility of Li ions at higher temperatures, the initial capacities are higher at elevated temperatures [189]. Nevertheless, after prolonged exposure to high temperatures, parasitic reactions such as electrolyte decomposition and oxygen evolution from the NMC cathode are increased, leading to a faster rate of capacity loss compared to RT [189]. It has been reported that TEOSCN electrolyte additive has a more pronounced effect on the electrochemical performance of the cells at elevated temperatures compared to RT [46]. Additionally, the SEI layer can break down at elevated temperatures (∼57°C), resulting in a lower electrochemical performance of the cell [190]. $LiPF_6$ decomposes at high temperatures, leading to the formation of reactive species such as PF_5. In the presence of unavoidable traces of moisture in the cell, PF_5 reacts with water and forms HF and PO_3. PF_5 also reacts with EC and DEC solvents as depicted in Figure 4.23. These degradation pathways explain the initial high performance and rapid capacity loss of the cells cycled at 60°C.

Figure 4.22b shows the rate capability of Si/Gr‖Li cells at RT, 45, and 60 °C, with C-rate ranging from 0.05C to 3C. In the final step, the cells were cycled at 0.1C to measure the capacity recovery, which was 98.36, 95.74, and 88.65% at RT, 45, and 60 °C, respectively. Si/Gr‖Li cells cycled at higher temperatures show better performance and higher capacity at higher C-rates, which can be due to enhanced Li ion diffusion at elevated temperatures, although it comes at the expense of long-term cycling stability.

Figure 4.22c shows the long-term cycling performance of NMC622‖Li cells at 0.2C at three different temperatures. The NMC622‖Li cells show a similar trend to the Si/Gr‖Li cells (Figure 4.22a). However, at 60°C, faster capacity and CE loss is observed in the NMC622‖Li cells after ∼70 cycles (74.43% capacity retention), which is more rapid compared to Si/Gr‖Li cells. After 150 cycles, the NMC622‖Li cells at RT and 45°C show a capacity retention of 86.96 and 80.66%, respectively. Elevated temperatures reduce the

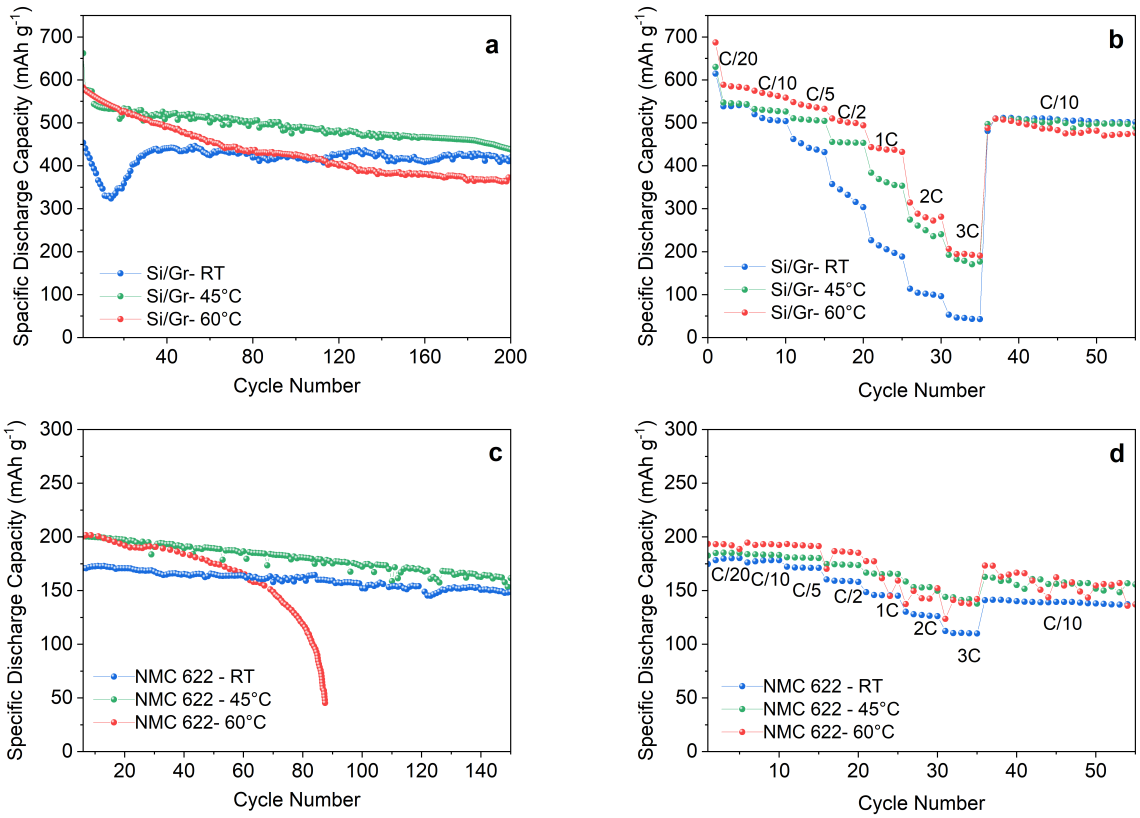

Figure 4.22: a) Long-term cycling performance at 0.2C and b) Rate-capability measurements (0.05C–3C) for Si/Gr||Li cells, c) Long-term cycling performance at 0.2C and b) Rate-capability measurements (0.05C–3C) for NMC622||Li cells at RT, 45, and 60 °C

cyclability of the NMC622 cathode due to accelerated metal dissolution, active oxygen evolution, reaction with electrolyte solvents, and cation mixing due to the similar radius of Li^+ and Ni^{2+} [191], [192]. At elevated temperatures, the $LiPF_6$ decomposition products (PF_5, HF, and POF_3) can catalyze the reactions on the cathode side and increase the battery's capacity loss. These acidic species can react directly with the NMC622 cathode, resulting in transition metal cation dissolution, oxygen evolution, electrolyte oxidation, and structural disorder. The TEOSCN electrolyte additive forms a robust cathode-electrolyte interphase and a physical barrier layer of –C≡N–TM complex (TM = transition metal), both of which mitigate the direct reaction between the cathode and acidic species derived from Li salt [46].

The rate capability measurements of the NMC622||Li cells is presented in Figure 4.22d. Higher capacities are observed for the NMC622||Li cells at elevated temperatures, especially at higher C-rates. However, the differences in capacities at elevated and room temperature are less pronounced that those observed in Si/Gr||Li cells. The capacity recovery of the NMC622||Li cells at 0.1C, after deep lithiation/delithiation at 3C, is 80.24, 88.17, and 88.92% at RT, 45, and 60 °C, respectively.

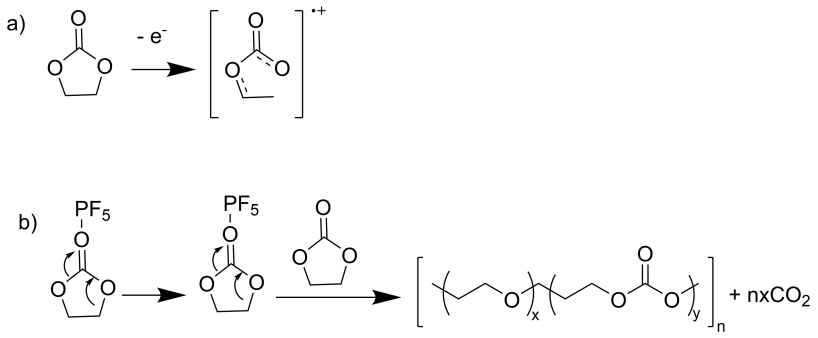

Figure 4.23: Possible mechanism of EC decomposition via a strong Lewis acid, PF_5

Figure 4.24a shows the differential capacity (dQ/dV) vs. voltage (V) for NMC622‖Si/Gr cells at RT, 45, and 60 °C. The dQ/dV measurements were performed at a low C-rate of 0.05C to better investigate the electrochemical and degradation phenomena. It is observed that increasing the temperature leads to reduced peak intensities, narrower peaks, and shifts the peaks to higher voltages.

Figure 4.24b shows the charge/discharge profile of the NMC622‖Si/Gr cells, indicating lower capacities and capacity retentions at elevated temperatures. Figure 4.24c shows the specific capacity and CE of NMC622‖Si/Gr cells at 0.2C and at different temperatures. Capacity retention values after the second cycle were 98.78%, 98.71%, and 97.23% at RT, 45, and 60 °C, respectively, and decrease to 74.23%, 69.25%, and 50.31% at the 50^{th} cycle. The CEs at the second cycle at RT, 45, and 60 °C are 97.99%, 96.76%, and 93.22%, respectively, and increasing to 99.11%, 97.85%, and 96.85%, by the 50^{th} cycle. The CEs can be further optimized by improving the electrolyte formulation and the electrode-electrolyte interphases.

The rate capability measurements of the NMC622‖Si/Gr cells at different temperatures are depicted in Figure 4.24d, which aligns with the results presented in Figure 4.24c, where the highest capacities are observed for the cells cycled at RT. The capacity recovery values at 0.1C, after deep charge/discharge at 3C, are 81.43%, 69.44%, and 67.55% at RT, 45, and 60 °C, respectively. In NMC622‖Si/Gr cells, the electrochemical performance is limited by the kinetics of Li ion insertion and extraction, as well as diffusion through the SEI and cathode electrolyte interphase (CEI) layer. Hence, regardless of the high initial capacity in Si/Gr‖Li and NMC622‖Li cells at elevated temperatures, NMC622‖Si/Gr cells show a higher initial capacity and a lower rate of capacity loss at RT.

4.3.2 PV-Battery integrated system

After the characterization of the battery (as described in Chapter 4.3.1) and the solar cell [183], tests were carried out on the coupled device. The batteries were connected to the solar cells via a DC-DC booster converter and then charged by the solar cells, which

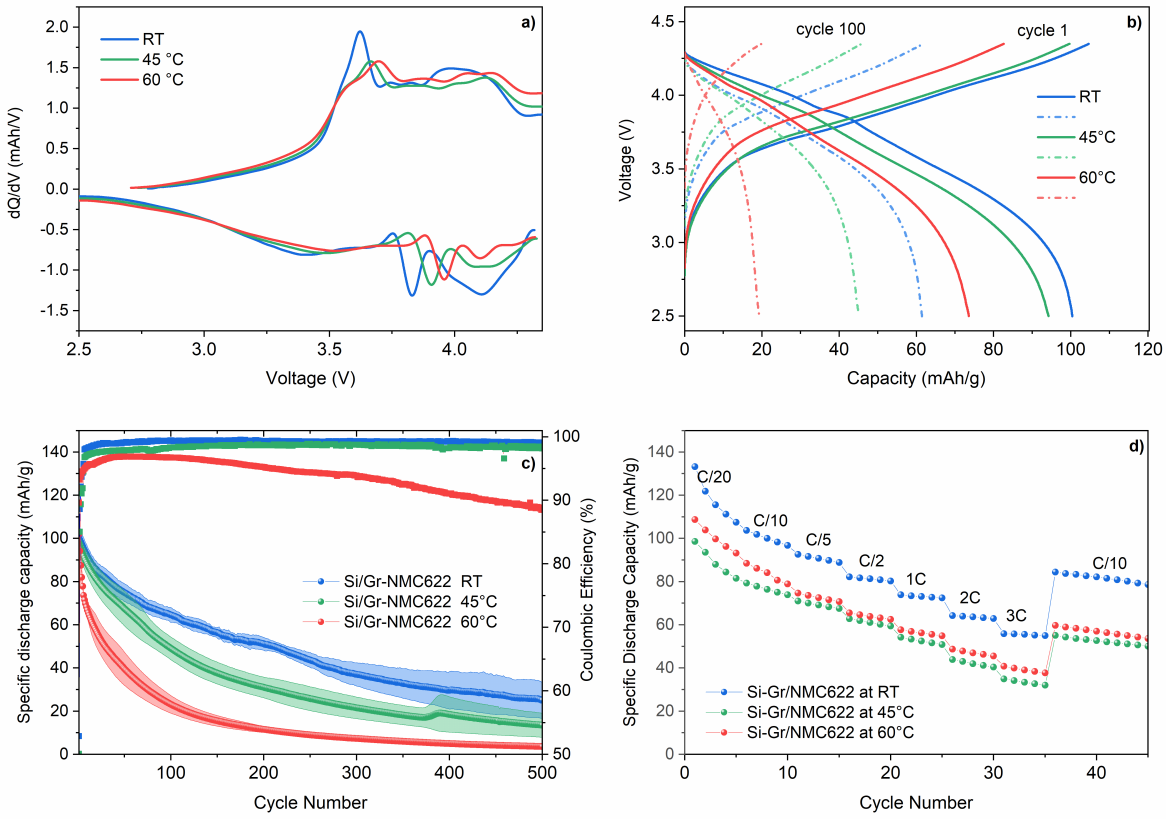

Figure 4.24: a) Differential capacity (dQ/dV) vs. voltage at the second cycle at 0.05C, b) Charge-discharge profile at 0.2C, c) Specific capacity and coulombic efficiency at 0.2C, and d) Rate capability at0.05C to 3C for NMC622||Si/Gr cells at RT, 45, and 60 °C

were illuminated using a solar simulator. Prior to the measurement, the batteries were discharged to 2.5 V to ensure an equal state of charge. The battery charging time (t_c) was set to 700 s, and the discharge time (t_d) is the time that the battery starts to discharge until it reaches 2.5 V, which is the initial charge voltage. Tests were conducted under an illumination intensity of 100 mW cm^{-2} with an AM1.5G spectrum at a temperature of 25 °C.

Figure 4.25 illustrates the charge-discharge cycle of a solar-charged battery, with black lines representing the voltage and red lines showing the current. The solar cell supplies an incoming voltage of almost 1 V (V_{inConv}, shown as negative for plot clarity), which is boosted by the converter to ∼4 V within the battery voltage range. As the battery charges, the voltage changes from 3.5 V to 4.24 V over a period of 700 s. During this process, the current delivered from the solar cell to the converter (I_{inConv}) decreases proportionally to the voltage boost. Upon completing the charging step, the battery's open circuit voltage (V_{OCV}) stabilizes at 4.09 V. At the start of the discharge phase, the voltage drops to 3.93 V and gradually reduces to 2.5 V after 1200 s of discharge. The I_{inConv} curve exhibits

two different slopes, initially showing a very steep decline that later stabilizes. The rapid initial loss in current is attributed to the quick increase in output voltage (V_{OConv}) during the battery's charging phase. Subsequently, as the battery charges, the voltage follows a semi-linear pattern and the converter input current stabilizes accordingly.

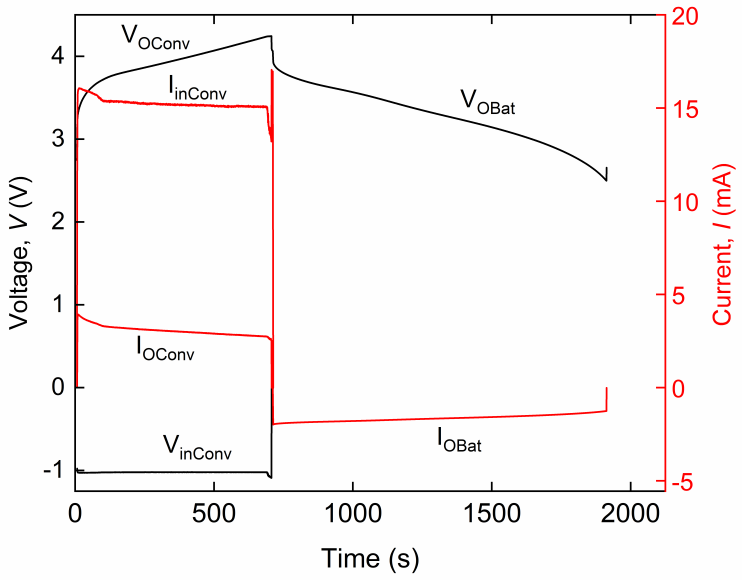

Figure 4.25: Charge and discharge voltages (black) and currents (red) of the solar-charged battery. Charge and discharge time are 700 s and 1200 s, respectively.

The energy-loss analysis of the solar-charged battery was conducted to gain insights into the source of losses. In Figure 4.26, the right bar chart shows the average efficiencies and losses, while the left side presents the overall solar cell efficiency and solar-to-battery efficiency. Based on the I-V curve (Figure A.5), the solar cell efficiency is calculated to be 15.31%. The performance of a PV-battery integrated system is defined by solar charging efficiency ($\eta_{\mathrm{solar-to-batt}}$):

$$\eta_{\mathrm{solar-to-batt}} = \frac{V_{\mathrm{c}} \cdot I_{\mathrm{c}}}{A \cdot P_{\mathrm{AM1.5}}} \times 100\% \tag{4.8}$$

where V_{c} and I_{c} are the charging voltage and current of the battery, respectively. The $P_{\mathrm{AM1.5}}$ is the incident light power density under AM1.5 conditions (100 mW cm^{-2}) and A is the effective area of PSC.

The battery round-trip efficiency ($\eta_{\mathrm{round-trip}}$) is the fraction of energy put into the battery that can be retrieved from the immediately preceding charge cycle:

$$\eta_{\mathrm{round-trip}} = \frac{\int_0^{t_\mathrm{d}} P_\mathrm{d} dt}{\int_0^{t_\mathrm{c}} P_\mathrm{out} dt} \times 100\% \tag{4.9}$$

where P_{out} and P_d are the charge and discharging power of the battery, respectively. t_d and t_c are the discharging and charging time, respectively. Solar charging efficiency indicates how efficiently the input power of light is delivered to the battery, which includes the voltage setup losses and power overheads from the converter. The overall efficiency (η_{overall}) is calculated as:

$$\eta_{\mathrm{overall}} = \eta_{\mathrm{solar-to-battery}} \times \eta_{\mathrm{round-trip}} \tag{4.10}$$

The coupling losses are initially low but increase as the battery charges. The primary contributors to these losses are the converter, followed by the battery. Notably, the battery loss in this study is 2.47%, which is lower compared to the previously reported values [188]. These findings indicate an improved battery performance within this work. The overall efficiency is 8.74% under a 2C charging rate at RT, considering the initial PSC efficiency (15.31%). Given the relatively high C-rate, the achieved efficiency is notable and confirms the success of the developed battery. These results demonstrate promising advancements in PV-battery technology, leading toward a more efficient integration of solar energy conversion and energy storage systems.

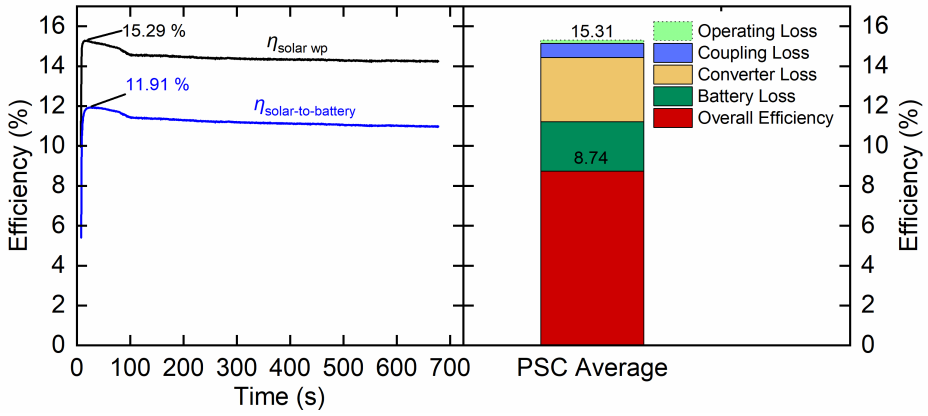

Figure 4.26: Energy loss analysis of the solar charging process

4.3.3 Summary

In summary, NMC622||Si/Gr cells were successfully paired with a perovskite solar cell, with an efficiency of 15.31%, using a DC-DC booster converter. To address the challenges of elevated temperatures during solar-charging, the NMC622||Si/Gr cells were further developed using TEOSCN electrolyte additive.

The electrochemical performance of NMC622‖Li and Si/Gr‖Li was systematically evaluated at different temperatures (RT, 45, and 60 °C). Both cell types exhibited high initial capacities, followed by a rapid capacity loss at elevated temperatures. Notably, the NMC622‖Li cells demonstrated more severe capacity and CE losses compared to Si/Gr‖Li cells. The NMC622‖Si/Gr cells show comparable initial capacities at RT and elevated temperature. However, the capacity loss upon long-term cycling is more pronounced at 60 °C (similar trend to NMC622‖Li). These results suggest that further development on the cathode side is required to achieve a stable performance at elevated temperatures and reduce the cathode-driven degradation.

The PV-battery system showed an overall efficiency of 8.74%, a notably high value under a 2C charging rate at RT. This confirms the effectiveness of the developed Si-based battery. These results demonstrate the promising potential of combining a Si/Gr anode with high-temperature stable electrolyte additives in developing a compact integrated PV-battery system. For further advancements, additional cathode developments and suitable electrolyte formulations are crucial to ensure the safety and environmental stability of the PV-battery system.

Overall, the findings presented in this work lay a strong foundation for future research on high-efficiency and eco-friendly PV-battery integrated systems, an essential step towards sustainable and clean energy solutions.

5 Polymeric binders for silicon-based negative electrodes in lithium-ion batteries

As discussed in Chapter 2.5, binders play a significant role in the electrode's mechanical stability and long-term electrochemical performance. In Chapter 4, the optimization of Si/Gr-based anode formulation was investigated using a dual binder system consisting of LiPAA and CMC. This chapter focuses on investigating and optimizing both bio-based and conventional polymeric binders in the previously optimized Si/Gr anode. Among the investigated binders, chitosan stands out as a bio-derived polymeric binder produced by partial deacetylation of chitin (depicted in Figure 2.14). Chitosan binder was investigated and optimized in Si/Gr anodes. The detailed results of this research are fully explained in Chapter 5.1.

5.1 Bio-derived chitosan polymeric binder

This chapter is based on the results of the publication entitled *"Chitosan as Enabling Polymeric Binder Material for Silicon-Graphite-Based Anodes in Lithium-Ion Batteries"*, which was published during this thesis by Hamzelui et al. [50]. This work was in collaboration with the Institute for Biology and Biotechnology of Plants (IBBP) and Münster Electrochemical Energy Technology (MEET), at the University of Münster. Chitosan samples were provided and characterized at IBBP, using ^{1}H NMR spectroscopy and size exclusion chromatography coupled with refractive index and multiple angle laser light scattering detection (SEC-MALLS-RI). XPS measurements presented in this chapter were conducted at MEET. The contents and figures of this chapter are reproduced and modified from Ref. [50] with permission from Wiley Online Library. Copyright 2023.

In this work, chitosan binders with different degrees of acetylation (DAs) and degrees of polymerization (DPs) were characterized and systematically investigated in Si/Gr composite anodes. The theoretical remarks on the chitosan biopolymer and its functional groups are explained in Chapter 2.5.2. Based on the chemical structure of chitin and chitosan, in Figure 2.14, chitosan consists of acetylated and deacetylated units, therefore, the DA plays a crucial role in the chemical and physical properties of chitosan. Meanwhile, DP holds a significant influence over the mechanical properties of the binder.

The chitosan binder was prepared at IBBP as described in Chapter 3.1.1, and its DA

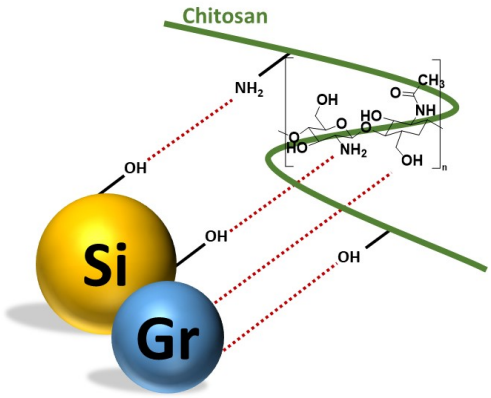

Figure 5.1: Schematic illustration of chitosan binder used in Si/Gr anode and its interactions with the surface of active materials

values were determined by ^{1}H NMR spectroscopy. Additionally, the chitosan samples were analyzed by size exclusion chromatography coupled with refractive index and multiple angle laser light scattering detection (SEC-MALLS-RI) (Figure A.6) at IBBP and FTIR at ISEA. To adapt the novel chitosan binder, the Si/Gr electrode formulation was further fine-tuned, as depicted in Figure 3.4. The optimized anodes were investigated in Si/Gr‖Li and NMC622‖Si/Gr cells. Moreover, the binders were cross-linked, and the films were subsequently coated on a glass microfiber separator to exclude the use of the Cu current collector, which is beneficial to increase the flexibility of the electrode and reduce the weight of the anode and the battery cell. To get a deeper insight into the effects and operational mechanism of the chitosan binder, post-mortem analysis was performed using XPS on the samples derived from Si/Gr‖Li cells utilizing both chitosan and LiPAA/CMC binders.

5.1.1 Optimization of degrees of acetylation and polymerization of chitosan

Five chitosan samples, each possessing different DAs and DPs were investigated within this work (Table 3.1). Figure 5.2 displays the FTIR spectra of chitosan samples, including DA50, DA30, and three samples with DA0 (DA0-1, DA0-2, DA0-3), along with variations in DP. In Figure 5.2a, a broad peak is observed at ∼3400 cm^{-1} in all samples, attributed to O–H stretching and N–H extension vibration, with the C–H stretching observed at ∼2874 cm^{-1} [94], [193]–[196].

Figure 5.2b shows the spectra in the range of 1500–1800 cm^{-1}, which contains critical information regarding the DA of the chitosan. Characteristic bands of amide I and amide II are situated at 1630–1660 cm^{-1} and 1560 cm^{-1}, respectively. These amide and amine bands are useful for determining the DA of chitosan samples. Primary amines and OH

groups are located at 1597 and 1640 cm^{-1}, respectively [194], [197]. Chitosan samples with DA30 and DA50 exhibit peaks at ∼1650 (amide I) and ∼1555 cm^{-1} (amide II). Conversely, in all DA0 samples, no visible amide bands are observed; however, these samples show a characteristic peak at ∼1600 cm^{-1}. This peak corresponds to the primary amines ($–NH_2$) and a nearly zero DA. Notably, Figure 5.2c shows a peak at 1374 cm^{-1} attributed to CH bending and symmetric CH_3 deformation, which is only present in DA50 and DA30 samples [194].

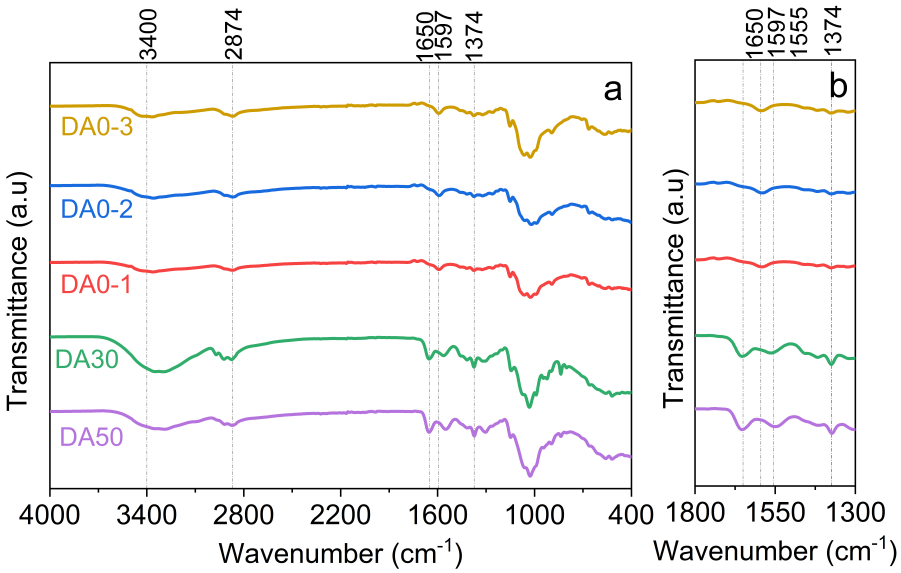

Figure 5.2: Fourier transform infrared spectroscopy (FTIR) characterization of chitosan samples with different degrees of acetylation (DA) over the a) Full measurement spectrum, and b,c) Selected wavenumbers

As mentioned in the experimental section (Chapter 3.1.4), the electrode formulation and binder content were optimized based on the homogeneity and adhesion of the film to the Cu current collector, and 4 wt% chitosan binder was the optimum binder content in these electrodes. Figure 5.3a shows the specific capacity vs. cycle number for Si/Gr‖Li cells with different chitosan binders and the reference LiPAA/CMC binder, all cycled at 0.2C. Half-cells utilizing DA0-1, DA0-2, and DA50 have a similar initial capacity as the reference cell (with LiPAA/CMC). Si/Gr‖Li cells employing DA50 and DA0-1 have a stable electrochemical performance and maintain capacity retention higher than 80% up to ∼300 cycles. Half-cells with the DA0-2 binder show a capacity retention of ∼74.0% at the 300th cycle. In contrast, cells with DA30 and DA0-3 binders exhibit lower capacities, with capacity retentions of approximately ∼70.6%, and ∼64.4%, respectively. The reference half-cells with LiPAA/CMC binder show the highest capacity retention of 93.5% after 300 cycles. Figure 5.3b demonstrates the rate capability of the Si/Gr anodes at different C-rates ranging from 0.1C to 5C. While all cells show stable electrochemical performance at different C-rates, cells with DA30 display lower capacities, initial Coulombic efficiency, and capacity recovery. All these values are summarized in Table 5.1. After deep lithiation/delithiation at 5C, the capacity recovery test at 0.1C shows that, except DA0-3, all other cells have a capacity recovery within the range of 96.1–97.2%.

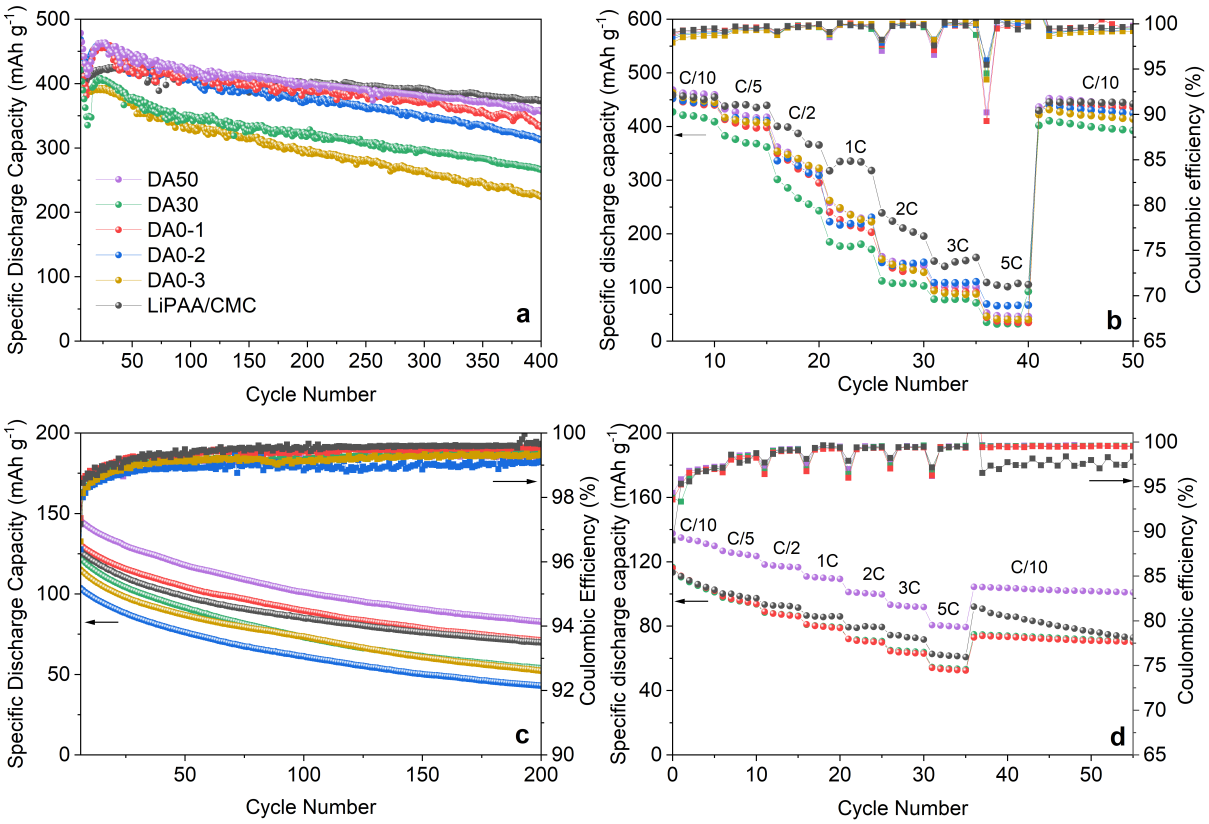

Figure 5.3: Capacity vs. cycle number and rate capability measurements for Si/Gr anodes with chitosan binders with different DAs and DPs (DA50, DA30, DA0-1, DA0-2, DA0-3) and LiPAA/CMC binder system as reference binder in a,b) Si/Gr||Li metal and c,d) NMC622||Si/Gr cells

Figure 5.3c shows the long-term capacity and Coulombic efficiency measurements for NMC622||Si/Gr utilizing different binder systems. The cells with DA50 binder show the highest initial capacity of 145.7 mAh g^{-1} at 0.2C compared to other chitosan binders with different DAs and DPs, as well as LiPAA/CMC binders (125.6 mAh g^{-1}). Table 5.2 presents the Coulombic efficiencies of the NMC622||Si/Gr with different binder systems at the 2nd and 200th cycles. Among the NMC622||Si/Gr cells with DA0 binders, DA0-1 has the highest initial capacity (130.3 mAh g^{-1}), low rate of capacity loss, and higher Coulombic efficiency. This trend might be attributed to the difference in DP within these binders. As a result, the chitosan DA0 binder, with the highest DP of 1154, exhibits superior performance compared to the lower DPs. Both DA30 and DA50 samples have a high DP of 1618 (as detailed in Table 3.1). To comprehensively investigate the impact of chitosan DA on electrochemical performance, rate capability tests were conducted on NMC622||Si/Gr cells with different DAs and higher DPs, i.e., DA50, DA30, and DA0-1.

Figure 5.3d illustrates the capacity and Coulombic efficiency of rate capability measurements conducted on NMC622||Si/Gr cells containing DA50, DA30, DA0, and LiPAA/CMC binders within a C-rate range of 0.1C to 5C. Cells containing DA30, DA0-1,

Table 5.1: Initial Coulombic efficiencies and capacity recoveries at C/10 after imposed to high-rate measurements of Si/Gr half-cells with different chitosans and LiPAA/CMC binders.

	Si/Gr half-cells with different binders					
	DA50	DA30	DA0-1	DA0-2	DA0-3	LiPAA/CMC
Capacity recovery at 0.1C [%]	96.5	96.1	97.9	97.2	93.2	97.2
Initial Coulombic efficiency at 0.1C [%]	98.7	98.6	98.9	98.3	97.9	99.1

and LiPAA/CMC show similar capacities at lower C-rates, which is in agreement with the long-term cycling results at 0.2C depicted in Figure 5.3c. However, by increasing the C-rate, the LiPAA/CMC reference cell shows higher capacities compared to DA30 and DA0-1. In contrast, the cells using DA50 binder exhibit the highest capacity across all C-rates, with an approximately 27% increase compared to the LiPAA/CMC reference cells. Notably, cells using DA50 binder also show a stable performance after deep lithiation/delithiation at 5C. Conversely, the reference LiPAA/CMC cells exhibit rapid capacity loss at 0.1C after deep cycling at 5C.

Table 5.2: Coulombic efficiencies of NMC622‖Si/Gr cells with different binder systems cycled at 0.2C

	Coulombic efficiency [%]					
	DA50	DA30	DA0-1	DA0-2	DA0-3	LiPAA/CMC
2^{nd} cycle	98.2	98.1	98.5	98.0	98.1	98.4
200^{th} cycle	99.2	99.4	99.5	99.0	99.3	99.6

Based on the electrochemical performance of Si/Gr‖Li and NMC622‖Si/Gr cells (Figure 5.3), the cells with DA50 binder demonstrated higher capacities and maintained stable performance throughout long-term and rate capability measurements. Based on the FTIR results in Figure 5.2, chitosan with DA50 exhibits a higher number of N-acetyl functional groups. The acetyl groups within the chitosan structure can contribute to hydrogen bond formation and improve the mechanical properties of the biopolymer, such as stress-strain behavior and fracture energy [110]. The acetyl functional groups appear to interact with the surface of Si particles and better accommodate Si volume change. Therefore, it is evidenced that the DA of chitosan binder plays an important role in the mechanical and subsequently electrochemical performance of the cell. Cui et al. [110] investigated the mechanical properties of chitin and chitosan, demonstrating that acetyl groups show strong hydrogen bonding, increase stiffness, reduce ductility, and therefore, enhance the fracture energy. Based on the electrochemical measurements in Figure 5.3 and considering the electrochemical performance of chitosan binders with different DAs and DPs, DA50 was selected as the optimized binder for Si/Gr anodes investigated in this study.

5.1.2 Cross-linking of chitosan binder

Chitosan has a linear structure, in which repeating units are connected in a single flexible chain, which can facilitates deformation [198]. To reduce this tendency and improve the durability during lithiation/delithiation, cross-linking has been employed to form a 3D and robust binder network. Glutaraldehyde [94] and citric acid [199], [200] have been commonly reported as effective cross-linkers for chitosan biopolymer. In consideration of safety concerns associated with glutaraldehyde, this work opted for citric acid monohydrate (CA) as a cross-linker. The cross-linking process involves thermal interaction between the free amino functional groups (–NH_2) of chitosan and the carboxylic acid groups (–COOH) of citric acid (Figure 5.4a) due to amino condensation. Concurrently, unreacted acetic acid undergoes evaporation during the electrode drying process at elevated temperatures [199]–[201].

Figure 5.4b shows the ATR-FTIR spectra of CA powder, chitosan DA50, and cross-linked chitosan samples with DA50:CA ratio of 9:1, 8:2, 7:3, and 6:4. The spectra of DA50 have been previously discussed in Figure 5.2. The CA powder spectrum shows a characteristic peak at 1721 cm^{-1}, attributed to its –COOH functional groups. The cross-linking process induces shifts, weakening, or concealing of the characteristic absorption bands of chitosan, which are indicators of functional group interactions. All cross-linked DA50/CA samples exhibit a peak at 1710 cm^{-1}, which is due to the secondary amide groups and becomes sharper by reducing the DA50 to CA ratio. The peak at ∼1550 cm^{-1} corresponds to amide bond formation (–N–C=O) [201]. Consequently, the characteristic peak of DA50 at 1650 cm^{-1} widens and shifts to lower wave numbers (1638–1619 cm^{-1}) due to the formation of amide bonds. A decrease in the DA50 to CA ratio reduces the intensity and sharpness of this peak and intensifies the peak shift, which indicates the cross-linking of the binder.

Figure 5.4c shows the N 1s spectra of the XPS measurements performed on DA50 and cross-linked DA50/CA (8:2) polymers. A peak is observed at 399.95 eV in both samples, attributed to –NH_2 functional groups. An additional peak at 401.85 eV, is significantly more pronounced in the cross-linked sample, due to the –NHR bonds and confirming the cross-linking of the DA50/CA sample. The thermal performance of the DA50 and DA50/CA binders was investigated using DSC measurements as depicted in Figure 5.4d. An endothermic peak at ∼128 °C is related to the evaporation of the residual water. In the DA50 sample the peak at ∼290 °C is related to the degradation of chitosan, which happens as a result of saccharide ring dehydration, depolymerization, and decomposition of acetylated and deacetylated units of chitosan [202]. In the DA50/CA sample, the degradation peak is shifted to ∼345 °C, indicating enhancement of the degradation temperature of chitosan attributed to cross-linking.

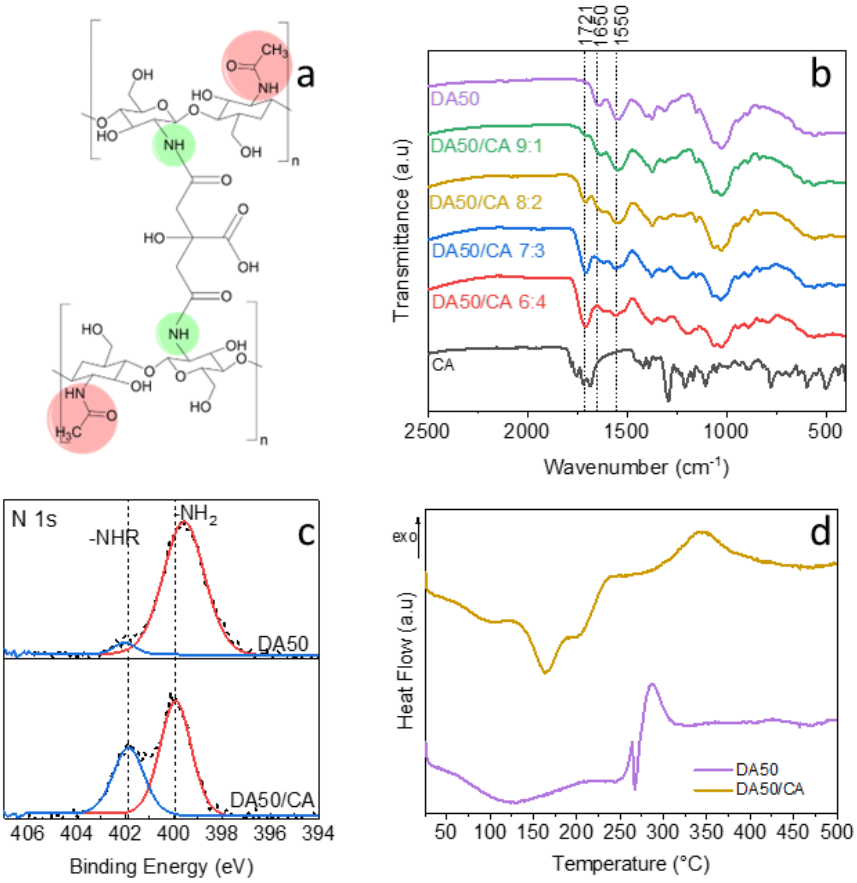

Figure 5.4: a) Chemical structure cross-linking of chitosan binder with citric acid monohydrate (CA), b) FTIR spectra, c) XPS spectra, and d) DSC curves for chitosan DA50 and cross-linked chitosan DA50/CA samples.

5.1.3 Towards developing a free-standing Si-based anode

It was previously reported that the Si/Gr anodes with 10 wt% chitosan binder exhibited poor adhesion to the Cu foil. Therefore, in order to eliminate the need for Cu current collector, the slurry was coated on the separator to create a free-standing electrode. This modification not only reduces the weight of the electrode but also increases its flexibility. In this study, a fiberglass separator (Whatman GF/C) was employed, which has ∼45% less areal density compared to Cu current collector used in this work. Figure 5.5 shows the SEM images of the surface and cross-section of Si/Gr coated on Cu and fiberglass separator. The surface morphology of the films in Figures 5.5a and 5.5c exhibits a more compact structure of active particles in anodes with Cu current collector (Figure 5.5a) compared to the free-standing electrodes (Figures 5.5c and 5.5d). This might be due to the structure of glass fiber and the calendering process, which was not possible to be done on the free-standing electrodes and was only applied to the electrodes with Cu current collector, leading to more dense coatings. Figures 5.5 b and 5.5d show the SEM

cross-section images of coatings on Cu and on the separator, respectively. Base on the observations, the fiber network of the separator enhances the adhesion of the coating to the substrate, which may improve the electrochemical properties of the electrodes.

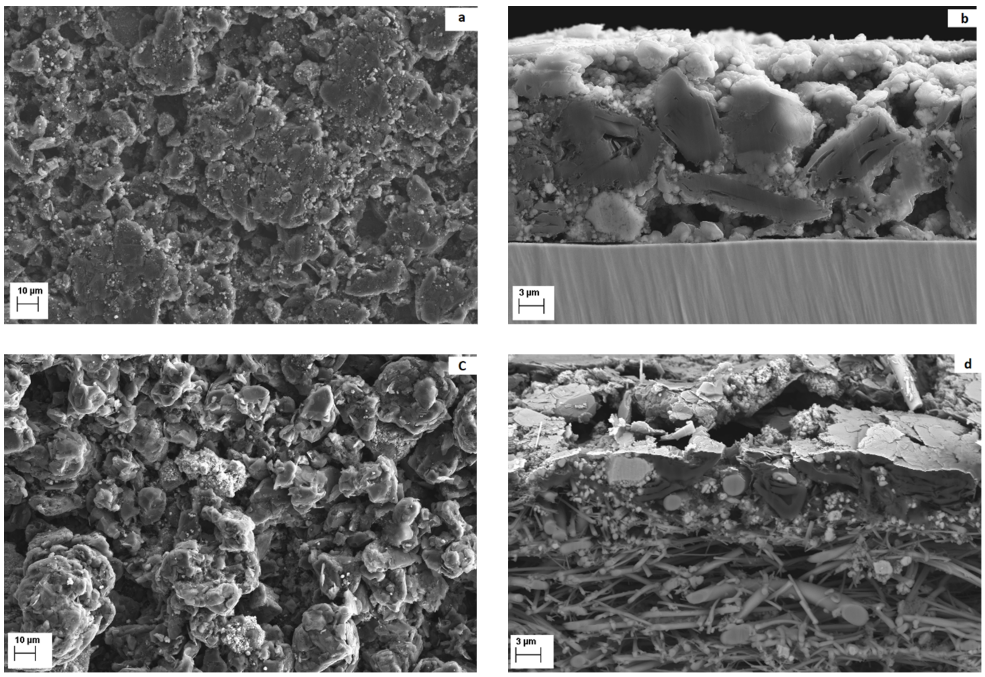

Figure 5.5: Scanning electron microscopy (SEM) images of Si/Gr anodes with DA50 binder. a) Surface morphology of the film coated on Cu current collector, b) Cross-section of the film coated on Cu current collector, c) Surface morphology of the film coated on separator, and d) Cross-section of the film coated on separator

The electrochemical performance of the free-standing electrodes was studied in Si/Gr‖Li and NMC622‖Si/Gr cells as depicted in Figures 5.6a and 5.6b, respectively. It is observed in Figure 5.6a that Si/Gr‖Li cells with anodes coated on Cu foil displayed higher capacity compared to the free-standing electrodes. Si/Gr‖Li cells, with and without CA cross-linker, exhibited similar electrochemical behavior up to 400 cycles. However, by the 500^{th} cycle, half-cells with and without cross-linker demonstrated capacity retention of 74.2% and 57.2%, respectively. The benefit of cross-linking is more noticeable in the free-standing electrodes. Si/Gr‖Li cells with free-standing anodes and CA cross-linker show higher capacity, enhanced electrochemical stability, and less capacity loss after 500 cycles compared to the same cells without the cross-linker. The free-standing anodes, with and without CA cross-linker, show capacity retention of 82.7% and 76.6% after 200 cycles, respectively. These values decrease to 55.5% and 43.1% after 500 cycles. The effect of cross-linking was investigated in NMC622‖Si/Gr cells with free-standing anodes as depicted in Figure 5.6b. Since DA50 and DA50.CA containing anodes coated on Cu foil showed similar electrochemical performance in Si/Gr‖Li cells, full-cell investigations were conducted and compared for free-standing anodes with and without cross-linker.

The NMC622||Si/Gr cells with free-standing anode show higher capacity compared to the full-cells utilizing Cu current collector. However, the free-standing NMC622||Si/Gr cell with DA50 binder shows rapid capacity loss after ∼90 cycles. On the other hand, the free-standing NMC622||Si/Gr cell with the cross-linked DA50/CA binder shows a more stable cycle life. The free-standing NMC622||Si/Gr cell has a ∼10% higher initial capacity compared to the same cells with Cu current collector, this value increases to ∼20% by the 100^{th} cycle. The error bars in Figure 5.6b show the standard deviation of the discharge capacity. NMC622||Si/Gr cells with free-standing anodes and DA50/CA binder exhibited the lowest standard deviation of 2.6 mAh g^{-1}. This value increases to 17.23 mAh g^{-1} and 12.24 mAh g^{-1} in full-cells with DA50 containing anodes coated on the separator and Cu foil, respectively. Utilizing free-standing anodes in full-cells increases the coulombic efficiency from 98.45% to 98.94% at the second cycle in DA50 containing anodes. The addition of a cross-linker increases this value to 99.32%. After 200 cycles, free-standing anodes containing DA50 and DA50/CA displayed coulombic efficiencies of 99.5% and 99.7% respectively. This value is 99.3% for the DA50 containing anodes coated on Cu foil.

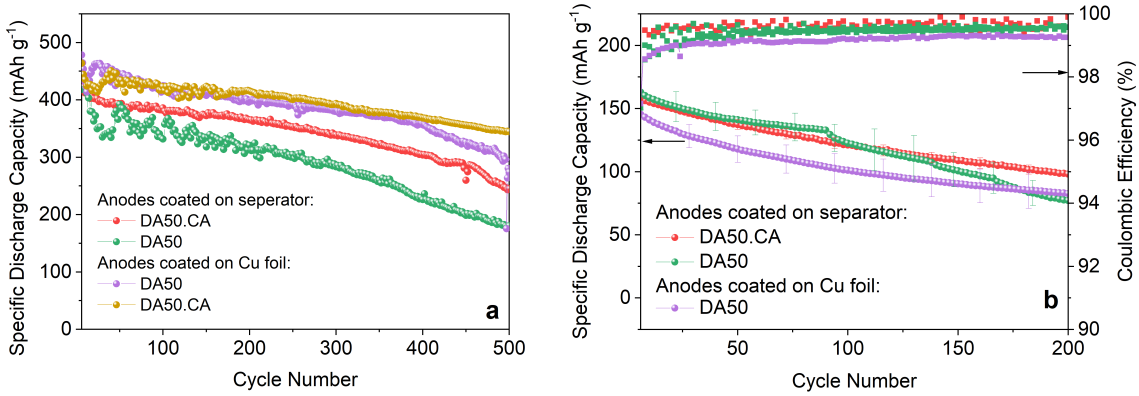

Figure 5.6: Electrochemical performance of Si/Gr anodes containing DA50 and DA50.CA binders coated on separator (free-standing) and on Cu current collector in a) Si/Gr||Li cell and b) NMC622||Si/Gr cells.

Corrosion of the metallic current collectors (Cu and Al) may occur in contact with the electrolyte during the lithiation/delithation process, resulting in diminished adhesion between the electrode film and current collector, loss of electrical contact, and limiting the battery power. Corrosion products may hinder the mobility of Li ions and electronic conductivity, leading to capacity loss in the battery. This effect is more noticeable in full-cells, as it can be observed in Figure 5.6 because of the limitation in the Li ion source [203]. Electrical contact resistance occurs at the interface between the electrode and current collector, which is a result of surface imperfections (such as roughness and out-of-flatness) and the accumulated corrosion products at the contact surface. Remarkably, the energy loss attributed to electrical contact resistance can reach as high as 20% of the total energy flowing in and out of the battery [204]. Hence, the exclusion of the Cu current collector can reduce the energy losses within the battery system.

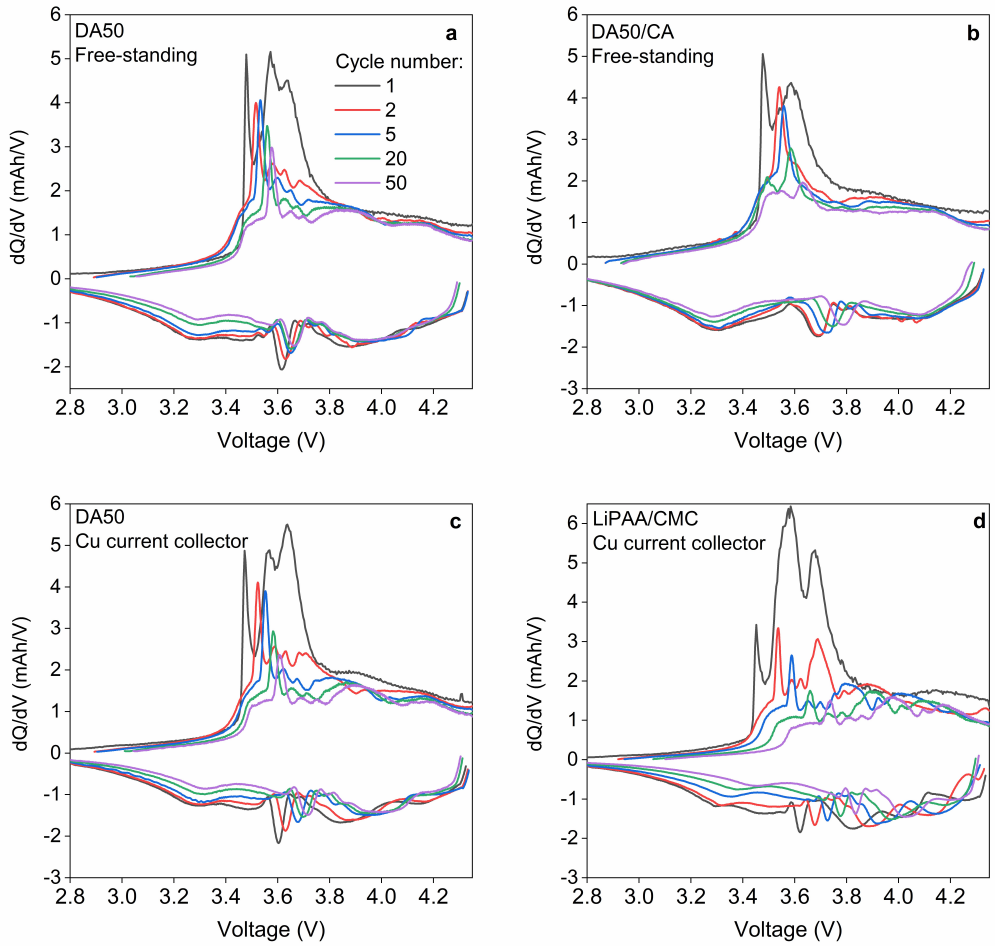

Figure 5.7: The dQ/dV versus voltage plots for NMC622||Si/Gr cells with freestanding anodes with a) DA50 binder, b) DA50.CA binder, and anodes coated on Cu current collector with c) DA50 binder, and d) LiPAA/CMC binder system. The first five cycles are performed at 0.05C ,and afterward, cells were cycled at 0.2C.

Figure 5.7 illustrates the dQ/dV vs. V plot at different cycle numbers for NMC622||Si/Gr full-cells using free-standing anodes and anodes coated on Cu foil. The intensity, position, and shape of the dQ/dV curves provide information on electrochemical activity and accompanying parasitic reactions. The shift of the peak to higher potentials increases the internal resistance (based on Ohm's law), and the expansion of the peaks relates to chemical changes within the cell. Changes in peak intensity is related to electrochemical changes within the cell. Figure 5.7a and b show the dQ/dV of NMC622||Si/Gr without and with the addition of CA cross-linker, respectively. It is observed that utilizing a free-standing system with cross-linked binder leads to the broadening of the peaks and a decrease in peak intensity at higher cycle numbers. This phenomenon can be attributed to the chemical changes and transformations due to the addition of the cross-linker. Figure 5.7a and c show the dQ/dV plot of full-cells containing DA50 coated on the separator

and Cu foil, respectively. By increasing the cycle number, the observed peak shifts are less pronounced in the free-standing electrode (Figure 5.7a) due to the lower internal resistance resulting from eliminating the Cu foil. For the anodes with the LiPAA/CMC binder system and using a Cu current collector (Figure 5.7d), a pronounced decrease in the peaks' intensity and a significant shift of the peaks is observed. The dQ/dV results also confirm the long-term performance trends of the full-cells, as depicted in Figure 5.6. This indicates the enhancements in electrochemical performance of the NMC622‖Si/Gr full-cells due to eliminating the Cu foil and the addition of the CA cross-linker.

5.1.4 Surface chemistry of Si-based anodes after electrochemical cycling

The impact of binders on the surface chemistry of lithiated Si/Gr anodes was investigated using XPS. This analysis was conducted on the anodes employing DA50 and LiPAA/CMC binder systems after the initial three cycles at 0.05C in Si/Gr‖Li configuration, after the SEI formation during the initial cycles. The electrochemical data of the first three cycles are summarized in Table 5.3.

Table 5.3: Electrochemical parameters of the Si/Gr‖Li cells with DA50 and LiPAA/CMC binder system after three cycles at 0.05C

	LiPAA/CMC			DA50		
Cycle number	1	2	3	1	2	3
Initial discharge capacity (mAh g^{-1})	525.19	458.67	459.53	625.76	533.97	529.54
Irreversible capacity (mAh)	0.2028	0.0279	0.0233	0.3803	0.0491	0.0387
Coulombic efficiency (%)	85.0	97.6	98.0	82.72	97.4	97.9

The atomic fractions of elements and components within the surface layer of the lithiated Si/Gr anode (SEI layer) with DA50 and LiPAA/CMC binder systems are presented in Figure 5.8. For a better understanding, the XPS results will be explained in two different sections: the organic and inorganic SEI composition.

Organic SEI Composition

The organic part of the SEI layer, such as lithium alkyl carbonates ($ROCO_3Li$), lithium alkoxides (ROLi), ethylene oxide oligomers (polyethylene oxide, PEO, $(CH_2\text{-}CH_2\text{-}O)_n$), semi-carbonates, and dilithium ethylene dicarbonate (LiEDC), is usually formed due to organic electrolyte solvents degradation (EC and EMC in this study). Lithium carbonate

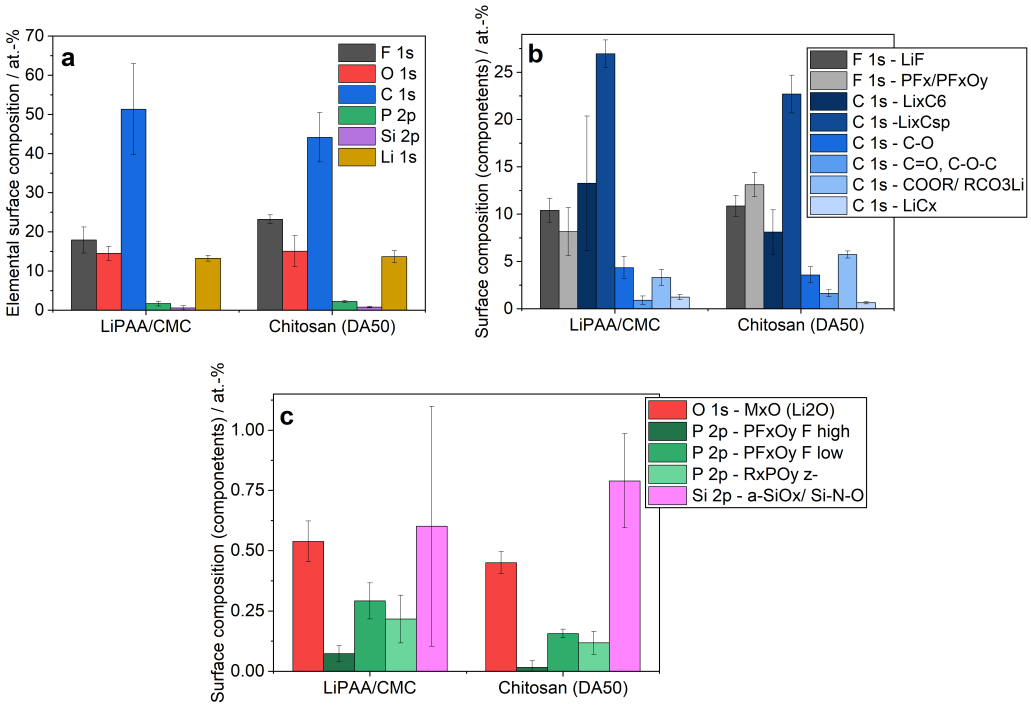

Figure 5.8: Atomic fraction of a) Elemental surface layer composition, and b,c) Components of the surface layer (SEI) of cycled Si/Gr||Li cells with LiPAA/CMC and DA50 binder systems after 3 cycles at 0.05C.

(Li_2CO_3) and lithium ethylene dicarbonate ($(CH_2OCO_2Li)_2$) are formed as a result of electrochemical reduction of EC and depend on the EC concentration (Equations 5.1 and 5.2) [205]:

$$2(CH_2)_2CO + 2Li^+ + 2e^- \rightarrow (CH_2OCO_2Li)_2 + C_2H_4 \text{ (High EC concentration)} \quad (5.1)$$

$$(CH_2)_2CO + 2Li^+ + 2e^- \rightarrow Li_2CO_3 + C_2H_4 \text{ (Low EC concentration)} \quad (5.2)$$

It is reported that $(CH_2OCO_2Li)_2$ is among the SEI components that is very soluble in organic solvents [206]. Inorganic products can hardly dissolve, however, if they are surrounded by organic species, they can diffuse into the electrolyte. The mechanical stability of the SEI layer is an important factor in accommodating the Si particle volume changes [207]. Organic and inorganic layers of the SEI are schematically depicted in Figure 2.9. The layer close to the electrolyte interface contains mostly organic species, and the layer close to the Si surface is mainly composed of inorganic species. Organic materials are known to have lower elastic modulus (more brittle), and higher porosity compared to inorganic materials [208].

Table 5.4: The atomic fraction of the C 1s peaks with XPS measurements on Si/Gr‖Li cells with DA50 and LiPAA/CMC binder systems after 3 cycles at 0.05C

		LiPAA/CMC	DA50
Components	Position	Atomic fraction (%)	
C–C, C sp2	284.35	13.26	8.11
C–C (carbon additive), C–H, C sp3	284.74	26.95	22.69
Li_xC_y	282.34	1.23	0.63
C-O	286.63	4.35	3.58

The C 1s and O 1s XPS core spectra of cycled Si/Gr‖Li cells are displayed in Figure 5.9 for anodes with DA50 and LiPAA/CMC binder systems. The C 1s spectra can be due to carbon-based SEI species, as well as conductive additives (carbon black), polymeric binders, and electrolyte solvents. Figure 5.8a indicates a lower amount of atomic fraction of elemental carbon (C 1s) in DA50 containing anodes (44%) compared to LiPAA/CMC containing anodes (51%). The peaks at ∼284.4 eV (C–C, sp2), 284.7 eV (conductive additive/C_{sp}, C–H, sp3 carbons), and 282.3 eV (Li_xC_y) are an indication of the SEI layer thickness. The atomic fractions of these peaks are provided in Table 5.4, suggesting a thicker SEI layer on the anodes with DA50 binder compared to the LiPAA/CMC binder. A thicker SEI layer can better accommodate the volume change of Si-based anodes during lithiation/delithiation. However, this may also lead to higher Li consumption and greater irreversible capacity, as shown in Table 5.3. On the other hand, DA50 containing electrodes have a lower amount of organic species, which can result in more mechanical stability of the SEI layer compared to LiPAA/CMC containing electrodes. The peak at 286.6 eV (C–O) and the peak at 288–290 eV (CO_2/CO_3) might indicate the presence of thium alkoxides, lithium alkyl carbonates,and/or semicarbonates, and/or ethylene oxide oligomers, which have nearly the same amount for anodes with both types of binders. The peak at 533.98 eV in O 1s spectra (Figure 5.8 c, d) further confirms the presence of C–O polymeric species.

Inorganic SEI Composition

The inorganic components within the SEI layer primarily result from the decomposition reactions of the electrolyte salt anions (PF_6^-). The inorganic part of the SEI layer exhibits limited solubility in organic electrolyte solvents. Consequently, the inorganic species within the SEI layer demonstrate enhanced chemical and mechanical stability, including a high shear modulus, thus better accommodating the Si volume change compared to the organic species. The P 2p and F 1s XPS spectra of the Si/Gr anodes with DA50 and

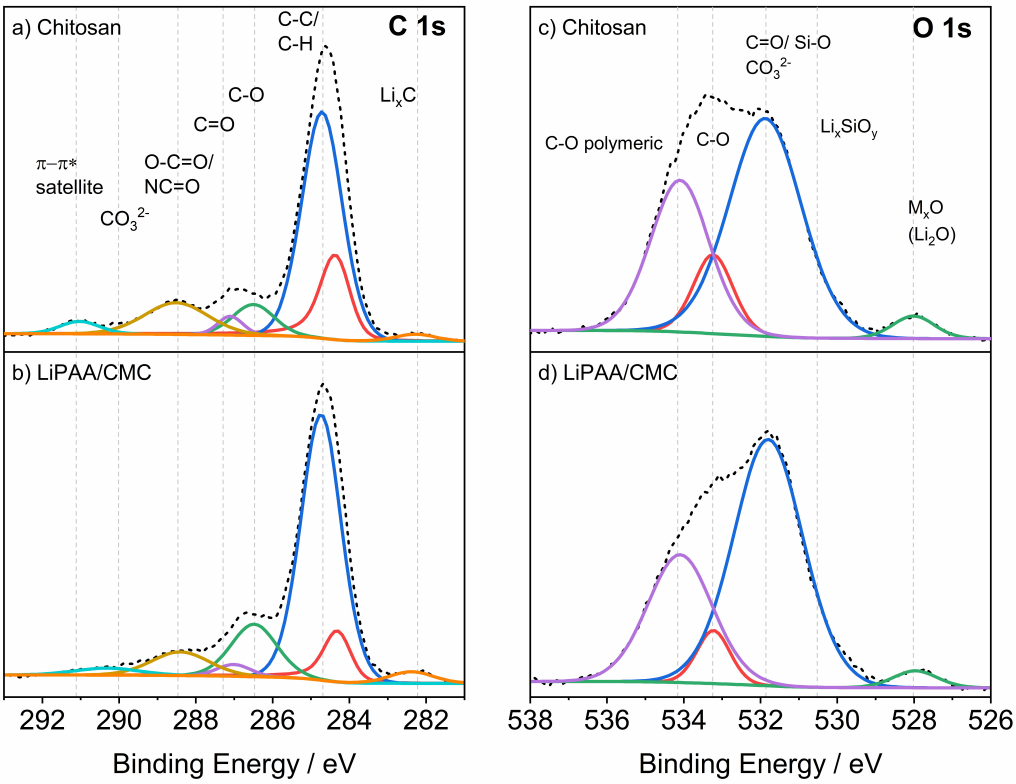

Figure 5.9: a,b) C 1s and c,d) O 1s XPS core spectra of cycled (after 3 cycles at 0.05C) Si/Gr||Li cells with DA50 and LiPAA/CMC binder systems

LiPAA/CMC binder systems are presented in Figure 5.10. The P 2p peaks are located at 135.23, 134.05, and 132.79 eV, indicating the atomic fraction of decomposition species of the electrolyte salt (PF_xO_y). These values are higher by 77.27, 46.28, and 45.38% in LiPAA/CMC-containing electrodes, indicating fewer $LiPF_6$ decomposition products in the DA50-containing electrodes. Young et al. [170] suggested that high amounts of carboxylic and hydroxyl groups in LiPAA and CMC enhance the $LiPF_6$ decomposition. $LiPF_6$ decomposition and formation of PF_5 may initiate the transesterification of EMC to DEC and DMC, which results in more electrolyte degradation and poor electrochemical performance [209]. The decomposition of $LiPF_6$ leads to the formation of PF_5, POF_3, and HF as depicted in Equations 5.3–5.5.

$$LiPF_6 \leftrightarrow LiF + PF_5 \tag{5.3}$$

$$PF_5 + H_2O \rightarrow POF_3 + 2HF \tag{5.4}$$

$$PF_5 + ROH \rightarrow POF_3 + HF + RF \tag{5.5}$$

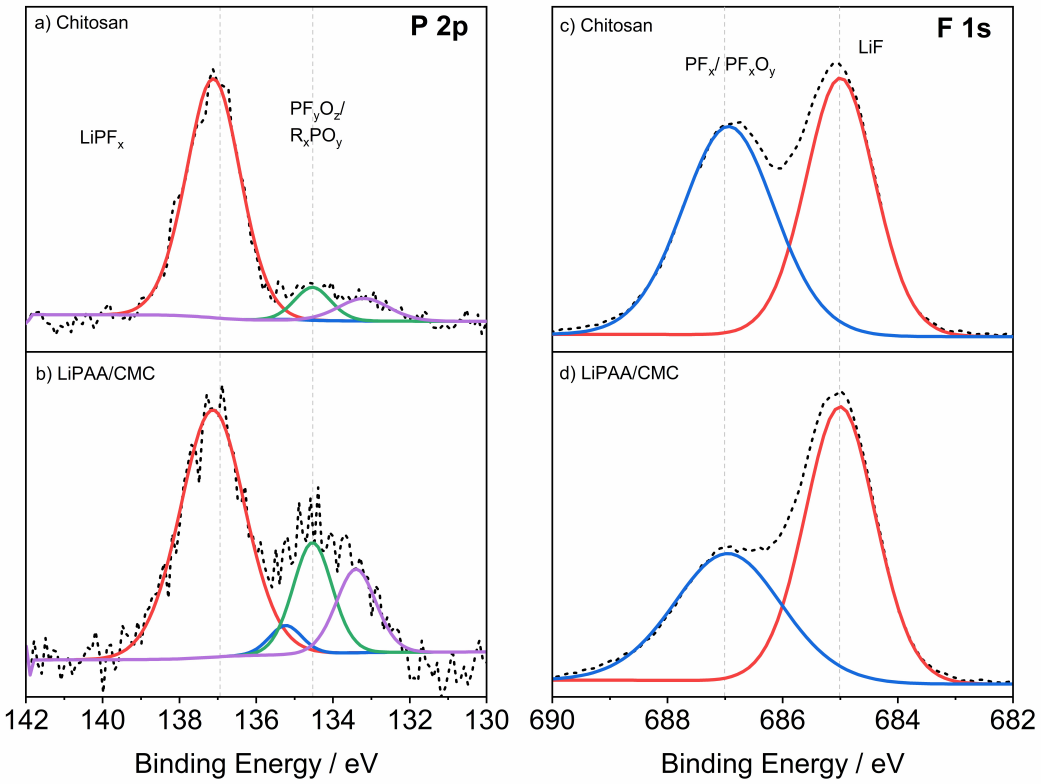

Figure 5.10: a,b) P 2p and c,d) F 1s XPS core spectra of cycled (after 3 cycles at 0.05C) Si/Gr‖Li cells with DA50 and LiPAA/CMC binder systems

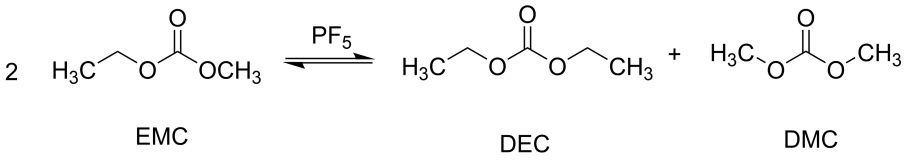

Figure 5.11: Transesterification of EMC to DEC and DMC

Due to the different basicity of the main SEI components (Li_2O > LiOR > Li_2CO_3 > RCO_2Li ≈ $ROCO_2Li$ > $Li_2C_2O_4$) [210], acid-base reactions (Equations 5.6–5.10) might occur between the SEI components and the degradation byproducts of Li salt ($LiPF_6$). This leads to the formation of insoluble, partially soluble, or gaseous compounds within the electrolyte. Chitosan reduces the decomposition of $LiPF_6$ and therefore, fewer reactions occur within the SEI or CEI layers, presumably resulting in improved mechanical and electrochemical performance upon lithiation/delithiation. The decomposition products of $LiPF_6$, such as HF, significantly influence the CEI layer and can trigger metal dissolution. The reduction of $LiPF_6$ degradation due to the presence of DA50 binder improves the mechanical and electrochemical performance of the full-cells (Figures 5.3 c, d).

$$LiPF_6 + Li_2CO_3 \rightarrow 3LiF + POF_3 + CO_2 \tag{5.6}$$

$$Li_2CO_3 + PF_5 \rightarrow POF_3 + LiF + CO_2 \tag{5.7}$$

$$Li_2CO_3 + 2HF \rightarrow 2LiF + CO_2 + H_2O \tag{5.8}$$

$$ROCO_2Li + 2HF \rightarrow LiF + CO_2 + H_2O + CH_3F \tag{5.9}$$

$$CH_3OCO_2Li + PF_5 \rightarrow POF_3 + LiF + CH_3F + CO_2 \tag{5.10}$$

The Si 2p peak at 106.13 eV corresponds to the presence of amorphous Si oxide and/or Si–N–O-based oxynitride phase [211], [212]. The Si-oxide on the surface of Si-particles can react with electrolyte decomposition products (such as PF_5 or HF) to form products such as SiO_yF_z [171].

In summary, the XPS findings indicate that the binder's influence extends to the chemistry of SEI layer. Anodes with DA50 binder display a thicker SEI layer containing less $LiPF_6$ degradation products. The improved electrochemical results of the full-cells with DA50 binder align with the XPS data.

5.1.5 Summary

This study investigated the highly promising potential of chitosan as a biopolymeric binder material for Si/Gr-based anodes. Five different chitosan biopolymers with different degrees of acetylation (DA) and degrees of polymerization (DP) were systematically characterized and investigated in Si/Gr anodes. The electrochemical performance of the anodes was investigated in Si/Gr‖Li and NMC622‖Si/Gr cells and evidenced a direct correlation between the properties of chitosan and the stability and cycle life of the cell. The findings indicate that chitosan DA50 (DA of 50% and DP of 1618) shows the optimum performance and was utilized for further investigations. NMC622‖Si/Gr cells with DA50 binder showed enhanced capacity at different C-rates and high capacity recovery after deep charge/discharge at 5C. The NMC622‖Si/Gr cells with DA50 show improved performance compared to the Si/Gr anodes with state-of-the-art LiPAA/CMC binder. Moreover, the introduction of citric acid (CA) as a cross-linker for DA50 binder (DA50/CA), further improved the performance of the Si/Gr anodes. Free-standing anodes were coated and

optimized by using both DA50 and DA50/CA binder systems. Free-standing anodes with DA50/CA binder exhibited longer cycle life and enhanced coulombic efficiency compared to free-standing anodes without cross-linker, as well as anodes with Cu current collector. It has to be noted that the electrochemical performance of Si/Gr‖Li and NMC622‖Si/Gr cells did not follow the same pattern, which emphasizes that Si/Gr‖Li cells measurements alone cannot predict the performance of the anodes in a full-cell. Therefore, to evaluate new electrode materials, both Si/Gr‖Li and NMC622‖Si/Gr cells measurements are necessary.

XPS analysis was used to further investigate the surface chemistry of electrochemically cycled Si/Gr anode using DA50 and LiPAA/CMC binder systems. The organic and inorganic SEI components showed different patterns due to the effect of different binders. Based on the atomic fraction of elemental surface composition in C 1s spectra, it can be suggested that a thicker SEI layer is formed for anodes with DA50 binder. Therefore, Si/Gr anodes with DA50 can better overcome the huge volume expansion of Si particles upon charge/discharge. Lower $LiPF_6$ decomposition is evidenced for anodes with DA50 based on the P 2p spectra, which might explain the better electrochemical performance of NMC622‖Si/Gr cells with DA50 compared to LiPAA/CMC. Fewer $LiPF_6$ decomposition products reduce the metal dissolution, oxygen evolution, and acidic species, and therefore, reduce the reactions on the cathode side.

Overall, this study shows that chitosan, with its unique properties and compatibility with cross-linking strategy, is a promising binder for enhancing the performance of Si/Gr anodes. The insight from this research can guide future efforts to further improve the stability, efficiency, and environmental friendliness of lithium-ion batteries.

5.2 Polymeric binders in Si-based anodes

5.2.1 Effect of the binder's pH on the Si-based anodes

Two extensively studied polymeric binders for Si-based anodes are CMC and PAA. However, PAA is the preferred choice in Si-containing electrodes due to its better electrochemical performance [86], [88]. Additionally, the neutralization degree (x in $PAAH_{1-x}Li_x$) can be adjusted, allowing the development of different formulations [86], [87]. The degree of neutralization influences the pH of the binder, which can directly impact the rheological properties of the slurry. The pH of the slurry can have an impact on the surface roughness and homogeneity of the electrode during the electrode manufacturing process [213]. Therefore, it is crucial to systematically investigate the effect of pH of the LiPAA binder in Si-containing electrodes. In this work, LiPAA with a pH ranging from 4 to 9 was prepared and characterized with ICP-OES, FTIR, and TGA. The binders were employed in Si/Gr anodes, with the formulation discussed in chapter 4.1, using only LiPAA as a binder. The mechanical (adhesion test) and electrochemical properties of the electrodes were investigated.

LiPAA binders with pH values of 4, 6, 7, 8, and 9 were prepared and coated on Cu foil, followed by drying at room temperature. Figure 5.12 depicts LiPAA films with different pH levels after overnight drying at room temperature. A blue-green color is observed for acidic pH (pH 4) and the film is very brittle and separates from the Cu foil upon drying. LiPAA with less acidic pH (pH 6) shows a brighter blue-green color, reduced brittleness compared to pH 4, and adheres to the Cu foil, although it can still be separated relatively easily. At neutral pH (pH 7), the film displays a transparent color when coated (a very light blue-green color observed upon separation) and robust adhesion to the Cu foil (difficult separation from Cu foil). LiPAA with pH 8 and 9 has a similar color to pH 7, when coated on Cu foil. However, they are significantly less brittle compared to films with acidic pH, and allows for easier separation from the Cu foil compared to pH 7. It was visibly observed that the viscosity of the binders varied at different pH levels. Acidic LiPAA with a lower pH exhibits low-viscosity and liquid-like behavior. However, as the pH increased, the binder demonstrated higher viscosity and a gel-like form. The neutralization of PAA and synthesis of LiPAA is shown in Equation 5.11:

$$-\mathrm{COOH} + \mathrm{Li^+} + \mathrm{OH^-} \rightarrow -\mathrm{COOLi} + \mathrm{H_2O} \tag{5.11}$$

It was assumed that the blue-green color of the binder resulted from the reaction of Cu with LiPAA and the corrosion of the Cu current collector. To investigate this, the binders were separated from the Cu foil, and the Cu content was analyzed using ICP-OES, as illustrated in Figure 5.13. It should be noted that the separation of the LiPAA binder with pH 7 from the Cu foil was considerably more challenging compared to the other

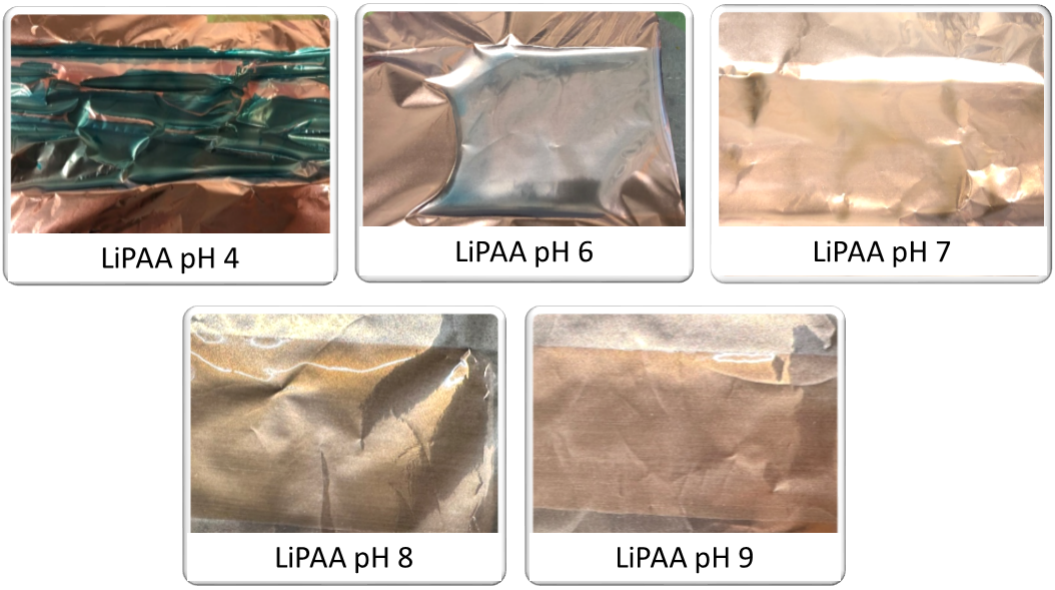

Figure 5.12: Images of LiPAA with pH 4, 6, 7, 8, and 9, coated on Cu foil and dried at room temperature.

binders. ICP-OES measurements revealed varying levels of Cu in the binders. The acidic binder with a pH of 4, displaying a dark blue-green color, contained the highest amount of Cu (3.88%). The less acidic LiPAA binder, with pH 6, exhibiting a light blue-green color, contained a much lower Cu content of 0.84%. The neutral LiPAA binder with pH 7, showing a lighter blue-green color, showed 1.20% Cu. The higher Cu content in the pH 7 sample compared to pH 6 may be attributed to the remarkable adhesion of LiPAA with pH 7 to the Cu foil, making the separation challenging and potentially leading to some Cu particles being attached to the binder. Both pH 6 and pH 7 exhibit lower Cu content compared to the acidic pH of 4. Basic LiPAA samples with pH 8 and 9 showed similar Cu contents of 0.35% and 0.22%, respectively, which are lower compared to the samples with lower pH values. Overall, the ICP-OES results suggest that LiPAA sample with the lowest pH levels (pH 4) contains a significantly higher amount of Cu compared to the other samples.

The presence of Cu in the binders is most likely attributed to atmospheric corrosion caused by the organic acids (–COOH groups) in the binders. Atmospheric corrosion refers to the corrosion caused by the atmospheric environment, to which the metal or alloy is exposed [214]. Gil et al. [215] investigated the initial atmospheric corrosion of Cu induced by carboxylic acids and found that the corrosion products primarily consist of cuprous oxide (copper(I)oxide, Cu_2O) and copper carboxylate. The existence of a water layer or moisture facilitates the electrochemical reactions and deposition of organic acid. The primary reactions involve copper oxidation and oxygen reduction. Subsequently, Cu ions react with the hydroxyl ions and form Cu_2O. This process is initially rapid and stabilizes over time. Another pathway involves carboxylate-induced dissolution of

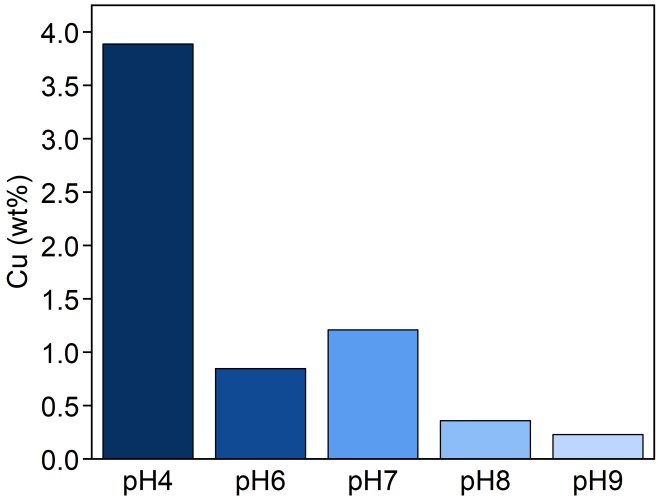

Figure 5.13: Cu content in LiPAA binders with pH 4, 6, 7, 8, and 9 coated on Cu foil after drying at room temperature. The values are measured by ICP-OES analysis and the samples were separated from the Cu foil prior to the measurement.

Cu^{+}, leading to the formation of dissolved Cu^{2+} carboxylate species that can precipitate as copper(II)carboxylate, exhibiting linear growth [215], [216]. Based on the Pourbaix diagram of copper, the corrosion of copper current collector and release of Cu^{2+} species are more favorable at pH $\leq$7 at 25°C [217]. In this work, the exposure of the coated LiPAA binder solution on Cu and its contact with atmospheric humidity and water in the slurry results in the corrosion of the Cu current collector, and the formation of Cu_2O. The carboxyl groups of LiPAA react with Cu, forming $–COO^{-}–Cu^{2+}$ complex, which is the reason for the blue-green color of the film [218]. Since there are more unsubstituted –COOH groups available in LiPAA with lower pH, these films exhibit a more pronounced blue-green color. The wet LiPAA film can enhance the diffusion of copper carboxylates and complexes formed between Cu^{2+} and LiPAA.

The LiPAA films were analyzed with ATR-FTIR, as depicted in Figure 5.14. The peak at 1700 cm^{-1} corresponds to the carboxylic acid stretch of PAA [87], exhibiting a significantly higher intensity for LiPAA with pH 4. The intensity decreases as the pH values increase. This observation indicates that more PAA converts to LiPAA with the increase in the pH values and the degree of neutralization, as expected. The lower intensity of the peak at 1700 cm^{-1} in LiPAA samples with higher pH values is attributed to the reduced amount of residual carboxylic acid groups.

The $–COO^{-}Li^{+}$ bands, include symmetric ($COO^{-}s$) and asymmetric ($COO^{-}as$) stretching of carboxylate groups at 1406 and 1550 cm^{-1}, respectively, exhibit a higher intensity at elevated pH levels due to the presence of $–COOH^{-}Li^{+}$. The broad band at 3400 cm^{-1} is attributed to the stretching vibration of the –OH groups, displaying a higher intensity in samples with higher pH. This higher intensity suggests the presence of a greater

number of hydroxyl groups in these samples. The peak at 2940 cm^{-1} corresponds to the C–H stretching. Within the electrochemical cell, the reduction of carboxylic acid functional groups of PAA and formation of LiPAA were investigated by Nguyen et al. [171] as described in Equation 5.12:

$$-COOH + Li^+ + e^- \rightarrow -COOLi + 1/2H_2 \tag{5.12}$$

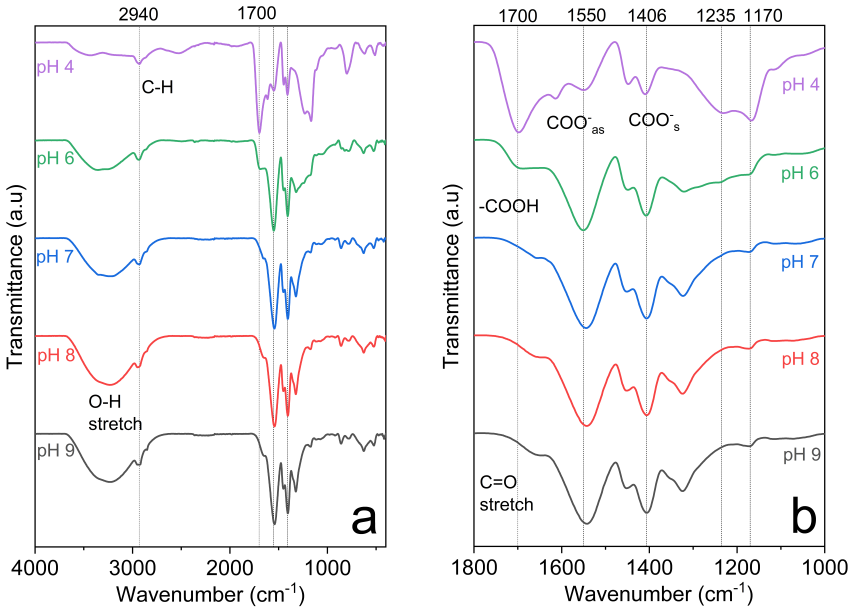

Figure 5.14: FTIR characterization of LiPAA binder with pH 4, 6, 7, 8, and 9 after coating on Cu foil and drying at room temperature (The binders were separated from the Cu foil prior to the FTIR measurements), at a) Full measurement spectrum and b) Selected wavenumber range

TGA measurements were conducted on LiPAA binders with different pH values and PAA powder to investigate the thermal properties of the binders and identify the optimal temperature for water removal. Figure 5.15a and b illustrate the TGA and first derivative of TGA (DTG) plots, respectively. DTG peaks help to identify the weight loss regions. The peak at ∼40 °C is attributed to free water and the peak for adsorbed water is observed at ∼80 °C for PAA powder. This peak increases to ∼100 °C and ∼115 °C for pH7 and pH9, respectively. Dehydration of carboxylic acid groups starts at ∼150 °C, between the neighboring COOH groups, leading to the anhydride formation and water byproduct, as depicted in Figure 5.16 [87], [219]. The dehydration of carboxylic acid groups and anhydride formation is less pronounced for LiPAA with higher pH, since samples with higher pH predominantly contain carboxylate groups with Li^+ counter ions. Decomposition continues above 250 °C for PAA and LiPAA pH 4, resulting in the breakdown of anhydrides and release of CO_2. Main chain and side group breaking occur at temperatures above 400 °C, indicating the stability of LiPAA during the electrode drying conditions [220].

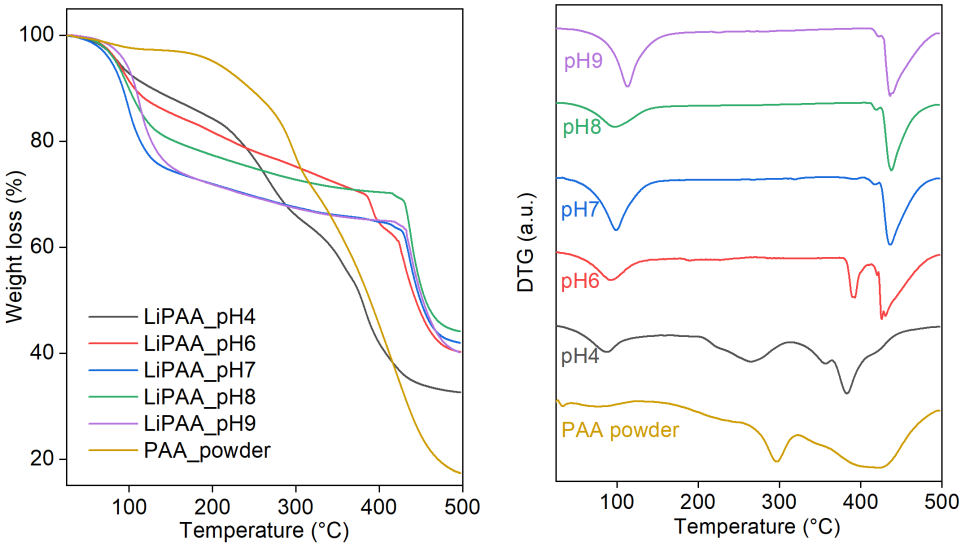

Figure 5.15: a) TGA curve and b) DTG curve of LiPAA with pH 4, 6, 7, 8, 9 and PAA powder from 25–500 °C under nitrogen atmosphere.

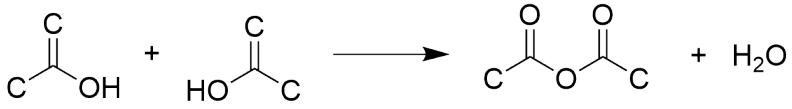

Figure 5.16: Dehydration of carboxylic acid groups

The optimized Si:Gr ratio was used in the slurry and LiPAA with various pH values was used as binder (20 wt% Si, 68 wt% Gr 10 wt% LiPAA, and 2 wt% SuperP). A 90-degree peel adhesion test was conducted on Si/Gr anodes containing LiPAA binders with different pH values to investigate the relationship between adhesion/cohesion strength of the Si/Gr electrodes and the pH of the LiPAA binder. The peel strength of the Si/Gr anodes is depicted in Figure 5.17a, and the average peel strength of the electrodes is shown in 5.17b. It should be noted that the electrodes were not calendered before the measurement, due to the high adhesion of the electrodes with pH 8 and 9 to the calender rolls. The Si/Gr anode with pH 4 shows very poor adhesion to the Cu current collector and was disconnected from the Cu foil after drying overnight at room temperature (Figure A.7). The anode with LiPAA binder at pH 6 shows significantly lower peel strength compared to the anodes with neutral and basic pH. Increasing the pH of the binder to 9 leads to a reduction in the average peel strength. In acidic pH, the electrode failure during the adhesion test occurred at the film/current collector interface, and at basic pH the failure happened within the bulk of the electrode, as it is depicted in Figure 5.18. The electrode with LiPAA-pH6 binder is completely removed from the Cu current collector, which shows better cohesion of the film and a lack of adhesion to the current collector. In contrast, in the other samples, after the adhesion test, a layer of the electrode is removed with the tap,e and the rest of the electrode adheres to the current collector, which shows lower cohesion in the film and higher adhesion to the Cu foil compared to the sample

with acidic binder. Based on the results of this work, a neutral pH, between 7 and 8, is considered optimal for LiPAA binder to achieve the highest adhesion properties in Si/Gr anodes.

In some studies [221], [222] it was reported that Si-nanoparticles/Gr electrodes with acidic LiPAA binder have the highest mechanical strength due to the formation of strong covalent bonds with the Cu current collector. It was suggested that the atmospheric-induced copper corrosion and the formation of Cu^{2+} and copper carboxylates physically cross-link the binder, increasing the adhesion of the electrode. However, strong crack formation was reported by Xiong et al. [221] during the first electrochemical cycle, due to the irreversible covalent bonds and the rigidity of the binder (as depicted in Figure 2.15). It was also reported that the acidic LiPAA binders form a non-uniform layer on the surface of active materials, leading to electrolyte degradation. However, the less acidic LiPAA binder forms a uniform layer on the surface of active materials, which was referred to as an artificial SEI layer [86], that reduces the electrolyte degradation and maximizes the initial Coulombic efficiency.

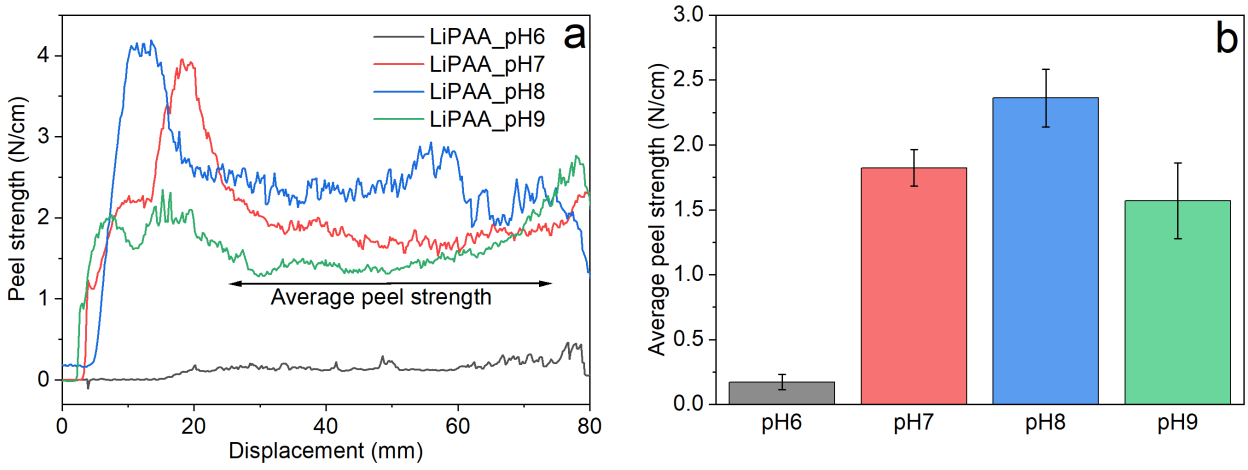

Figure 5.17: Adhesion test measurements for the Si/Gr anodes with LiPAA binder with different pH, a) Peel strength vs. displacement and b) Average peel strength.

A schematic illustration of different types of bonds between LiPAA binders as well as LiPAA binders and Si particles is depicted in Figure 5.19. Under acidic conditions, the esterification of carboxylic groups may occur, and electrostatic interactions can form due to the presence of Cu^{2+} species, originating from Cu foil corrosion. Strong covalent bonds may form between the functional groups of the binder and the surface of Si particles. At a neutral pH, more supramolecular bonds, such as hydrogen and ionic bonds, will form, which increase the flexibility of the binder network and can better accommodate the volume change of Si particles upon lithiation/delithiation. The type of bonding and interactions within the binder network, as well as between the binder and Si particles, is directly influenced by the pH value and directly affects the cohesion of the electrode and its adhesion to the current collector[221].

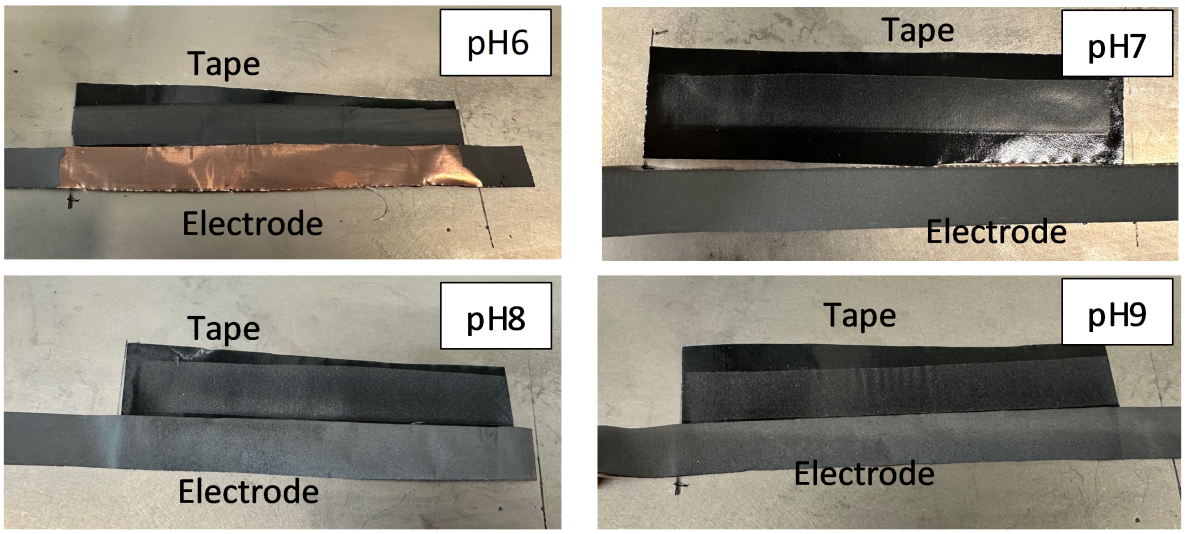

Figure 5.18: Si/Gr anodes with LiPAA binder with different pH after 90-degree peel adhesion test

The rate capability measurements were performed on Si/Gr‖Li half-cells at C-rates ranging from 0.05C to 2C to investigate the electrochemical performance and mechanical robustness of the electrodes, as depicted in Figure 5.20. All Si/Gr‖Li cells show stable electrochemical performance at 0.05C and 0.1C. It should be noted that the electrodes were not calendered, which can lead to capacity loss and low specific capacities at higher C-rates (0.5C to 2C). However, after deep lithiation/delithiation at 2C, the recovery test at 0.1C (Table 5.5) shows values higher than 99% capacity recovery. Si/Gr anodes with LiPAA pH 7 show even higher capacities at 0.1C after deep lithiation/delithiation at 2C. The initial coulombic efficiencies at 0.05C and 0.1C are shown in Table 5.5. In both C-rates, acidic pH 6 shows the lowest Coulombic efficiency, and neutral pH 7 and 8 show similar values, with pH 8 having slightly higher values. The initial specific capacity of Si/Gr‖Li cells with LiPAA-pH8 is higher compared to the other samples. Also, as it can be observed in Figure 5.20, LiPAA-pH8 shows slightly higher capacities at 0.05C to 0.5C. These results are in line with the results obtained from the adhesion test in Figure 5.17.

In Si/Gr anodes with higher Gr content, it is mostly reported that better electrochemical performance is achieved using LiPAA or NaPAA with neutral pH compared to the PAA binder. A more homogeneous distribution of active materials in the slurry and a more uniform coating were observed using LiPAA or NaPAA [87], [223]. It was reported by Yabuuchi et al.[223] and Porcher et al. [86] that a thin layer of NaPAA and LiPAA binder, respectively, covers the surface of Si and Gr particles. This layer acts as an artificial SEI, minimizing the direct contact with the electrolyte and reducing the capacity loss in the first cycle. In acidic LiPAA binders, the carboxylic acid groups can be reduced electrochemically and converted to lithium carboxylate. The protons that are released are more likely to accelerate the $LiPF_6$ decomposition rate compared to binders with neutral pH [86], [171], [221].

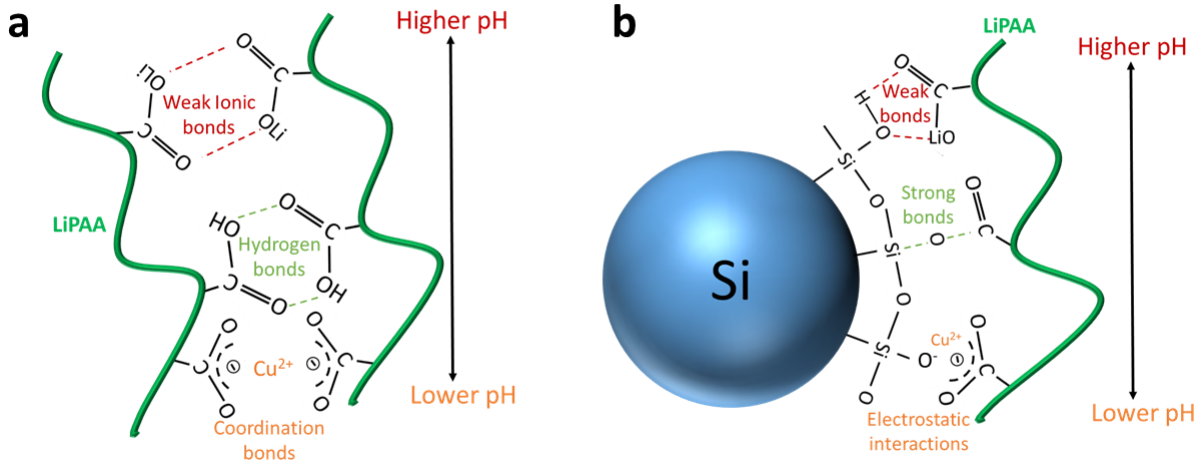

Figure 5.19: Schematic representation of pH-dependent interactions in LiPAA-based Si/Gr anodes. a) Intermolecular interactions within the LiPAA binder network under varying pH conditions, and b) Schematic of interfacial interactions between LiPAA and Si particle surfaces, demonstrating how pH influences the dominant bonding mechanisms. Inspired and redrawn from Ref [221], with permission from ACS publications. Copyright 2021.

5.2.2 Cross-linking of polymeric binders

The condensation reaction between carboxyl (–COOH) and hydroxyl (–OH) groups of binders can form a covalently cross-linked binder network. Many of the binders used for Si-based anodes, such as LiPAA, CMC, alginate, etc., contain these functional groups. The strong covalent cross-linking forms a 3D binder network and better accommodates the volume change of Si particles. However, strong covalent bonds are irreversible and can lead to gradual plastic damage during lithiation/delithiation. Strong supramolecular interactions, such as ion-dipole interactions, have a self-healing and reversible nature, which can accommodate the volume change of Si. However, the bond strength is weaker compared to covalently cross-linked. Therefore, a balance between bond strength and reversibility (self-healing) is necessary for optimal electrochemical performance of Si-based anodes [69], [126].

As reported in Chapter 4.6, a dual binder system of LiPAA and CMC was used in Si-based anodes. In this chapter, LiPAA and CMC are thermally cross-linked at 150°C. In addition to the LiPAA/CMC binder system, LiPAA/sodium alginate (SA) and LiPAA/tragacanth gum (TG) cross-linked systems were also investigated. The chemical structures of LiPAA, CMC, SA, and TG are shown in Figure 2.13.

The thermal properties of CMC, SA, and TG polymers were evaluated by the TGA

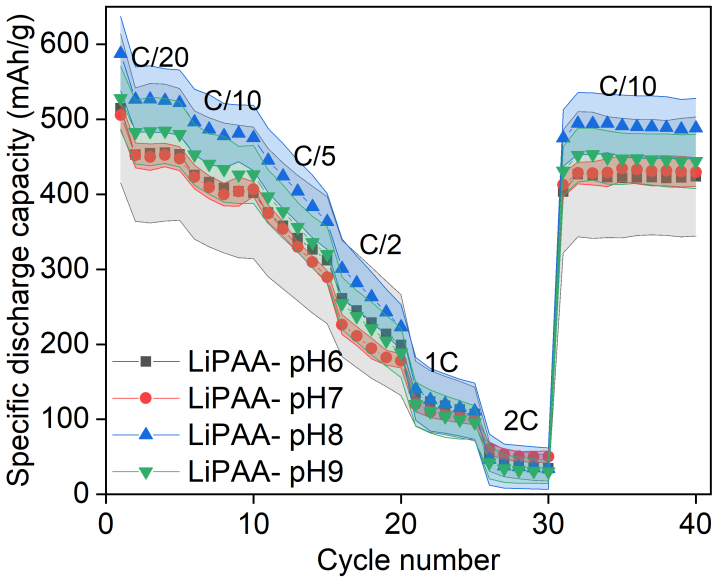

Figure 5.20: Rate capability measurements of Si/Gr||Li cells containing LiPAA binder with pH6, 7, 8, and 9 performed at C/20, C/10, C/5, C/2, 1C, and 2C

method. Figure 5.21a and b show the TGA and DTG analysis of CMC, SA, and TG polymers from 25 to 500 °C at a rate of 5 °C/min under a nitrogen atmosphere. For the TG sample, the first weight loss of 10 wt% is observed at ∼100 °C, which is due to the adsorbed water evaporation. The corresponding peak can be observed in the DTG curve at ∼100 °C. The next weight loss region is from 230 to 270 °C, followed by another weight loss region from 270 to 350 °C with 30 wt% and 20 wt% weight loss due to the initial decomposition of hydroxylated polysaccharide in the polymer's side group and backbone[108], [109], [224]. The total mass loss at 500 °C was 70 wt% of the initial TG sample mass. For the SA sample, the DTG peak at 120 °C is due to moisture evaporation, leading to ∼15 wt% mass loss. The next weight loss region is from 200 to 250 °C, with 34 wt% weight loss, due to the degradation of the sample [225]. The total mass loss at 500°C was 63 wt% of the initial SA sample mass. The TGA and DTG curves of CMC show a weight loss of ∼12 wt% at 109°C due to adsorbed water evaporation. The DTG peaks at 280 and 303 °C indicate the dehydration and initial decomposition of saccharide rings with a total of 36 wt% weight loss [226]. The total mass loss at 500°C was 62 wt% of the initial CMC sample mass. In all cases, the polymers are thermally stable during the electrode drying process.

FTIR spectra of CMC, SA, and TG are presented in Figure 5.22. TG was reported to provide strong adhesion between active material particles and the current collector, and to improve the elasticity of the electrode due to the presence of hydroxyl and carboxyl groups [109]. In all samples, the broad band observed at 3230–3325 cm^{-1} represents the –OH groups stretching vibrations related to hydroxyl groups and adsorbed water,

Table 5.5: The areal capacity, initial specific capacity, initial Coulombic efficiency, and capacity recovery at 0.1C, after high-rate measurements for Si/Gr‖Li cells with LiPAA binder at different pH values

pH	Areal capacity [mAh cm^{-2}]	Initial specific capacity [mAh g^{-1}]	Initial Coulombic efficiency [%]		Capacity recovery [%]
	2^{nd} cycle at 0.05C		at 0.05C	at 0.1C	at 0.1C
6	3.48	452.91	84.19	99.12	99.33
7	3.58	451.86	87.14	99.32	101.29
8	3.35	526.66	87.92	99.36	99.63
9	3.47	482.85	86.77	99.31	99.89

and its intensity decreases, and a peak shift is observed upon cross-linking the binders with LiPAA and the condensation reaction between the COOH groups of LiPAA and OH groups of CMC, SA, and TG [157]. The band at 2908–2931 cm^{-1} corresponds to C-H stretching. The peak observed at 2355 cm^{-1} is due to O–H bending and C–O stretching vibrations [227], which has a higher intensity in the cross-linked samples. The peaks between 1000–1200 cm^{-1} are due to carbohydrate fingerprint in polysaccharide chemical structure, representing the C–O and C–O–C stretching vibrations [109], [228]–[230]. The region between 750–950 cm^{-1} can be assigned to the vibrations of the uronic acid residues [231]. In the TG sample, the peak at 1742 cm^{-1} is attributed to C=O stretching in carboxyl groups, and the peak at 1606 cm^{-1} is assigned to asymmetric -COO^- stretching. In the CMC sample, the peak at 1588 cm^{-1} is due to the –COO^- stretching of carboxyl groups. The peaks at around 1407 and 1320 cm^{-1} are assigned to O–H and C-H stretching, respectively. In the SA sample, the characteristic peaks at 1597 and 1407 cm^{-1} are assigned to asymmetric and symmetric stretching vibrations of -COO^- and free carboxyl groups (–COONa), respectively [230], [232]. The peak at 950 cm^{-1} can be assigned to C–O stretching of uronic acid residues [233]. The shift in COO^- bands is important to determine the complex formation between polymers, which is an indication of cross-linking of LiPAA/CMC, LiPAA/SA, and LiPAA/TG samples. A small peak is observed for the cross-linked samples at $\sim$ 1700–1720 cm^{-1}, which can be related to the cross-linking due to esterification by anhydride formation. However, since the intensity of this peak is rather small for LiPAA/CMC and LiPAA/SA samples, it suggests that the crosslinking occurs mainly due to ion–dipole interactions between the functional groups of the two binders [234].

The Si/Gr-20 and Si/Gr-60 anode films were prepared according to the slurry formulations in Table 5.6.

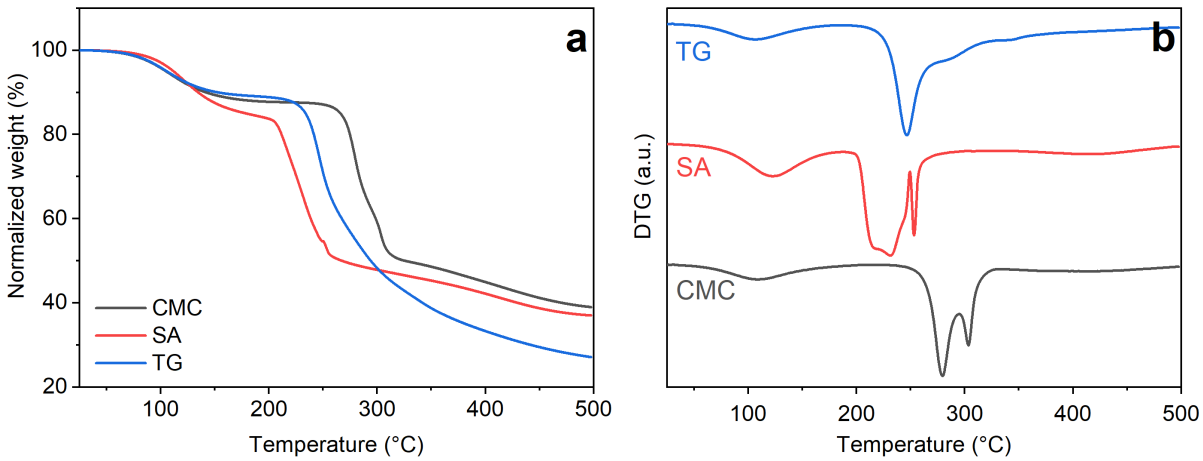

Figure 5.21: a) TGA and b) DTG analysis of CMC, SA, and TG polymers, at a temperature range of 25 to 500°C at a rate of 5 K/min under nitrogen atmosphere

Table 5.6: Different Si/Gr anode formulations used in this chapter. Binder 1 is LiPAA, and Binder 2 is CMC, SA, or TG, which were crosslinked with LiPAA. LiPAA binders with two different pH values of 7.5 and 4 were used.

Anode	Si-alloy (wt%)	Graphite (wt%)	Binder 1 (wt%)	Binder 2 (wt%)	SuperP (wt%)
Si/Gr-20	20	68	7.73	2.27	2
	20	68	10	0	2
Si/Gr-60	60	28	3.18	6.82	2
	60	28	10	0	2

A 90-degree peel test was performed on the Si/Gr-20 and Si/Gr-60 electrodes after drying. It was observed that using LiPAA with pH 4 resulted in a very low peel strength value of 0.25–0.43 N/cm in both 20 and 60 wt% Si electrodes. Cross-linking the binder increased the peel strength (Figure A.8, Appendix), and in most of the electrodes, this value was higher than the limit of the device (10 N), therefore, the exact value could not be reported. However, this is a good indication that cross-linking enhances the adhesion properties of the electrodes. The adhesion test results of electrodes within the measuring range of the device are shown in Figure A.8a. The current collector with LiPAA pH 4 binder undergoes severe corrosion, as visibly observed in Figure A.8b.

Figure 5.23a and b show the rate capability of Si/Gr-20 and Si/Gr-60 electrodes in Si/Gr||Li cells, respectively. In both types of electrodes, LiPAA binder with neutral pH, as well as cross-linked LiPAA binder (neutral and acidic pH) with CMC, SA, and TG was used. As reported in Chapter 5.2.1, electrodes with only LiPAA pH 4 did not adhere to the Cu current collector; therefore, the electrochemical performance could not be measured. Electrodes with cross-linked binders containing LiPAA pH 7.5 and pH 4 are depicted with different shades of blue and red colors, respectively. As it is observed in Figure 5.23a,

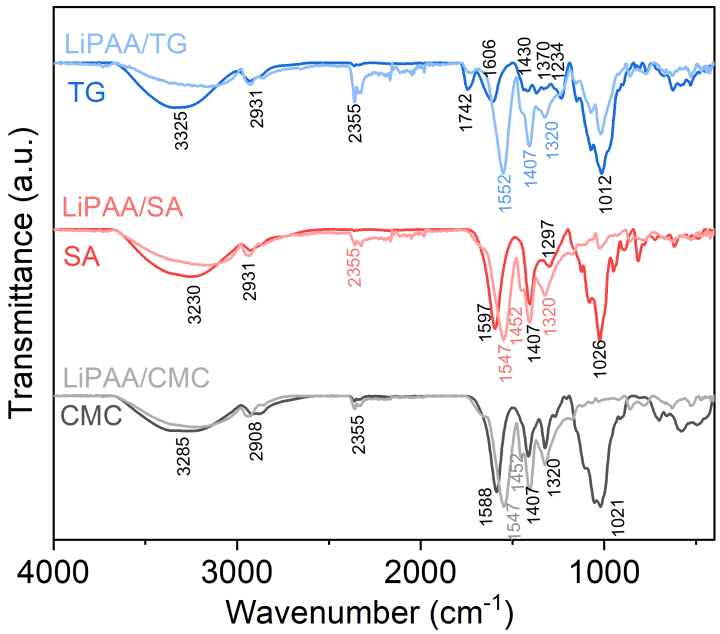

Figure 5.22: FTIR spectra of CMC, SA, and TG and the cross-linked LiPAA/CMC, LiPAA/SA, and LiPAA/TG

in Si/Gr-20 electrodes, the cross-linked electrodes are showing better (LiPAA/SA and LiPAA/CMC systems) or similar (LiPAA/TG system) performance compared to only LiPAA binder. In the cross-linked binder systems, the electrodes with neutral pH binders show better performance compared to the acidic binders. The best performance was observed in electrodes with LiPAA/CMC binder at neutral pH, with a capacity recovery of 98.11%. The capacity recovery of all the cells is shown in Table 5.7.

For the Si/Gr-60 anodes, Figure 5.23b shows that the cross-linked electrodes with pH 7.5 binder has a better electrochemical performance, especially at higher C-rates, compared to the acidic pH. The reason for that could be the difference in LiPAA to CMC ratio as well as the different Si content in Si/Gr-20 and Si/Gr-60 electrodes, as reported in Chapter 3.1.3. Since more LiPAA is used in Si/Gr-60 electrode, in the case of acidic pH, higher mechanical instability and separation of the electrode from the Cu current collector can happen, especially at higher C-rates, which can reduce the electrochemical performance of the cells. However, after deep charge/discharge at 3C, a capacity recovery of $\geq$ 92% was observed in almost all the cells.

Overall, it is observed that cross-linked binders with a neutral pH show better electrochemical performance compared to those with acidic pH, especially at electrodes with higher Si content and higher C-rates. Cross-linking LiPAA (pH 7.5) with CMC and SA enhances the electrochemical performance of the Si/Gr||Li cells. Si/Gr||Li cells with cross-

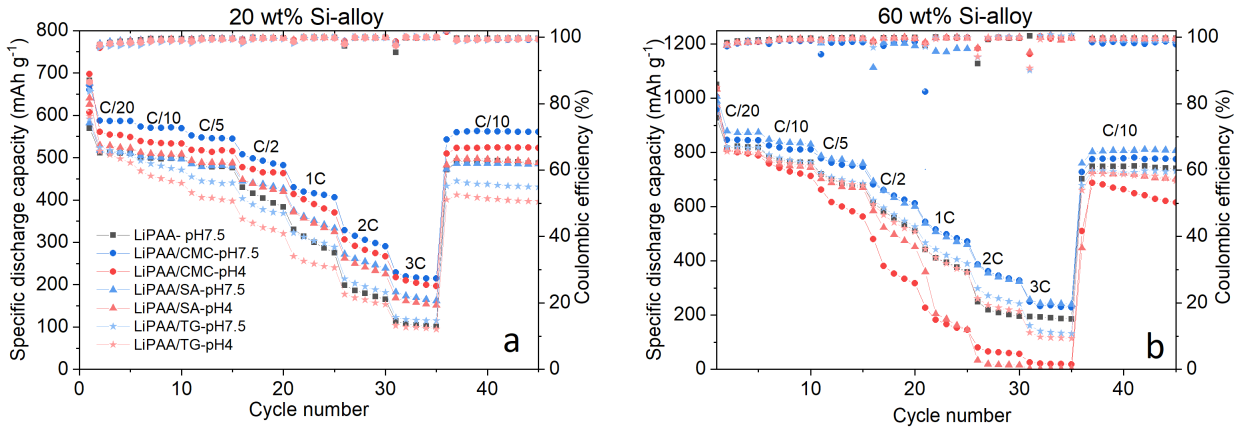

Figure 5.23: Rate capability measurements of Si/Gr||Li cells containing LiPAA binder with neutral (pH 7.5) and acidic (pH 4) cross-linked with CMC, SA, and TG using Si/Gr anodes: a) Si/Gr-20, and b) Si/Gr-60

Table 5.7: Capacity recovery of anodes with 20 and 60 wt% Si and cross-linked LiPAA/CMC, LiPAA/SA, and LiPAA/TG binders at C/10, after deep lithiation/delithiation at 3C.

	Capacity recovery (%)	
Sample	Si/Gr-20	Si/Gr-60
LiPAA(pH7.5)	98.08	95.24
LiPAA(pH7.5)/CMC	98.11	94.09
LiPAA(pH4)/CMC	96.92	89.67
LiPAA(pH7.5)/SA	96.53	94.68
LiPAA(pH4)/SA	97.02	93.55
LiPAA(pH7.5)/TG	90.19	92.48
LiPAA(pH4)/TG	87.92	92.51

linked LiPAA/TG binder show similar performance to Si/Gr||Li cells with pure LiPAA binder.

5.2.3 Summary

This study investigated the properties of the Si/Gr-based anodes with respect to the pH of the binder. LiPAA binders with different pH values ranging from 4 to 9 were prepared and coated on the Cu current collector. The binder films were then systematically investigated using ICP-OES, FTIR, and TGA. Based on the observed blue-green color of the binders after coating on Cu foil and the ICP-OES results, the acidic binders contained higher amounts of Cu. The Cu in the binders can be attributed to the atmospheric corrosion of current collector due to the presence of organic acids. The higher number of unsubstituted –COOH groups in LiPAA with acidic pH, results in the presence of higher amounts of Cu and a more pronounced blue-green color. It was observed that the binder with the highest acidity does not adhere to the Cu foil and separates upon drying. The Si/Gr anodes containing LiPAA binders with different pH values between 6 to 9 were coated on Cu current collector, and the adhesion properties were tested using a 90-degree peel test. The adhesion test indicates that the cohesion of the electrode and its adhesion to the Cu current collector are directly related to the pH of the binder, affecting the mechanical and electrochemical properties of the electrodes. A neutral pH, between 7 and 8, shows the optimum adhesion and enhanced mechanical properties in Si/Gr anodes. At neutral pH, more supramolecular bonds, hydrogen and ionic bonds, can form between the binder and Si particles, resulting in better accommodation to Si volume change during electrochemical cycling of the cells. The rate capability of the Si/Gr‖Li cells with LiPAA binders with different pH values shows better electrochemical performance for electrodes with a neutral pH binder. These results are in line with the adhesion test results.

In the second part of this section, the neutral (pH 7.5) and acidic (pH 4) LiPAA binders were cross-linked with CMC, SA, and TG polymeric binders to form a 3D binder network, which can help to reduce the effect of Si volume expansion. The binders were characterized with TGA and FTIR, and the rate capability of the Si/Gr‖Li cells was investigated using cross-linked and non-cross-linked LiPAA binder within the Si/Gr-20 and Si/Gr-60 electrodes. It was observed that cross-linked binders with neutral pH show better electrochemical performance compared to acidic pH, especially in electrodes with higher Si content and higher C-rates. Cross-linking LiPAA-pH 7.5 with CMC and SA enhanced the electrochemical performance of the Si/Gr‖Li cells. Si/Gr‖Li cells with cross-linked LiPAA/TG binder showed similar performance to Si/Gr‖Li cells with pure LiPAA binder. This study indicates that LiPAA with neutral pH provides better mechanical and electrochemical properties, as well as cross-linking ability, in Si/Gr-based anodes.

6 Conclusions and outlook

This thesis focused on optimizing and developing Si-based anodes and suitable natural biopolymeric binders to achieve a sustainable negative electrode that can increase the energy density of LIBs compared to the state-of-the-art Gr electrode. The formulation of Si/Gr anodes was optimized, and the electrochemical performance of Si/Gr‖Li and NMC622‖Si/Gr cells was systematically investigated for different active materials and binder ratios. The evaluation of Si/Gr‖Li indicated that 20 wt% Si and a LiPAA to CMC ratio equal to the Si to Gr ratio (2.27:7.73) is the optimal formulation. The optimized Si/Gr‖Li cells showed more than 80% capacity recovery after over 900 cycles. The rate capability of NMC622‖Si/Gr cells indicated an 81.93% capacity recovery after deep lithiation/delithiation at 5C. Postmortem SEM/EDX analysis of the Si/Gr electrodes was conducted after 1200 cycles in Si/Gr‖Li cell, in which the redistribution and morphological changes of Si particles after long-term lithiation/delithiation were observed. The NMC622‖Si/Gr cell was further optimized with an electrolyte containing a high-temperature enabling additive system to withstand high temperature and C-rates for integration in a PV-battery system. The developed LIB was paired with a PSC, using a DC-DC boost converter, resulting in an 8.74% overall efficiency under 2C charge rates at room temperature.

Chitosan biopolymer with different degrees of acetylation (DA) and polymerization (DP) was investigated as a binder in Si/Gr anode. Adjustments in the slurry composition of the optimized Si/Gr electrode were performed to adapt the use of chitosan binder. According to the electrochemical measurement results of the Si/Gr‖Li and NMC622‖Si/Gr cells, chitosan binder with the highest DP of 1618 and DA of 50% (DA50) was considered as the optimized binder for Si/Gr anodes. The NMC622‖Si/Gr cells with DA50 chitosan binder showed improved capacity and high capacity recovery after deep lithiation/delithiation at 5C, demonstrating enhanced performance compared to the state-of-the-art LiPAA/CMC containing anode. Cross-linked chitosan binder with citric acid (DA50/CA) further improved the performance of the Si/Gr anode. Free-standing Si/Gr electrodes were developed using DA50 and DA50/CA binder systems. It was observed that free-standing anodes with the cross-linked chitosan binder had longer cycle life and improved Coulombic efficiency. Post-mortem XPS analysis was performed on the electrochemically cycled Si/Gr anodes to study the surface chemistry of the electrodes with DA50 and LiPAA/CMC binders. Based on the XPS data, it is suggested that Si/Gr anodes with DA50 binder form less $LiPF_6$ decomposition products compared to LiPAA/CMC binder system. A lower amount of organic species can result in better mechanical stability of the SEI layer, which is in agreement with the better electrochemical performance of these

DA50 containing cells.

The LiPAA binder, which is a superior binder for Si-based anodes, has been systematically investigated by adjusting its neutralization degree, which directly influences the binder's pH. LiPAA binders with pH values ranging from 4 to 9 were characterized with FTIR and TGA and utilized in Si/Gr anodes. It was observed that LiPAA binders with an acidic pH, due to a higher number of unsubstituted –COOH groups, react with the Cu foil, as observed by the change in the binder's color from transparent to blue-green and confirmed by the ICP-OES results. The cohesion of the electrode film and its adhesion to the Cu current collector are related to the pH of the binder, as it is investigated by the 90-degree peel angle test. A neutral pH (between 7 and 8) shows the optimum adhesion and cohesion properties. The mechanical properties of the electrode directly impact its electrochemical performance. The electrochemical performance of the Si/Gr‖Li cells confirms this, showing better electrochemical performance for anodes containing a LiPAA binder with a neutral pH. The LiPAA binder was then cross-linked with CMC, SA, and TG in Si/Gr anodes. The electrochemical performance was investigated in Si/Gr‖Li cells using 20 wt% and 60 wt% Si content. It was observed that cross-linked LiPAA with neutral pH showed improved electrochemical performance, especially at higher C-rates. Si/Gr‖Li cells using LiPAA with acidic pH showed lower electrochemical performance, especially in electrodes with higher Si content (60 wt% Si) and at higher C-rates.

The importance of binder chemistry and content in Si/Gr anodes suggests that binders can affect the electrochemical properties of the electrodes for several possible reasons. The interaction of binders with active materials is of high importance and directly impacts the dispersion of active materials, contact between the particles, and the electrode's porosity. Binders with suitable functional groups that interact with the surface of active materials can result in a homogeneous and stable electrode coating. Binders impact the adhesion strength of the electrodes, which is the attachment of the active materials to the conductive additive and the adhesion of the coating to the Cu current collector. The balance between the cohesion of the electrode film and the adhesion of the film to the current collector can improve the adhesion strength of electrode films. The electrodes need to be mechanically stable upon lithiation/delithiation, especially in high-capacity Si-based anodes. Therefore, the elasticity of the binders can help to better accommodate the volume change of Si particles, reducing the risk of electrode cracking, particle detachment, and pulverization during battery operation. The chemical and electrochemical stability of the binder affects the SEI formation and battery life. Binder decomposition or reaction with the electrolyte upon lithiation/delithiation can negatively impact the electrochemical performance of the battery. The ionic conductivity of the binders is also another factor that can influence the transport of Li ions and improve the electrochemical performance. Therefore, as observed in this work and due to all the mentioned reasons, electrodes with the same active materials but different binders can have different electrochemical properties.

The focus of this work was to develop and optimize the Si/Gr anode using environmentally friendly biopolymeric binders. It should be noted that electrode manufacturing is a

very complex process and many factors can affect the electrode properties. In the slurry production step, small changes in the slurry chemistry, formulation, mixing process, and atmospheric conditions (such as temperature, humidity, etc.) can affect the viscosity of the slurry and subsequently the coating properties. In the coating process, parameters such as coating speed, coating temperature, Cu current collector, draw-bar thickness, etc., can result in different coating properties. In the calendering step, the calendering pressure can directly affect the porosity and thickness of the electrodes. Finally, in the drying step, the drying temperature, time, and atmospheric conditions can directly impact the quality of the electrode film. Also, it should be taken into account that for each electrode chemistry and formulation, all the parameters need to be optimized. Therefore, introducing a new binder or active material requires optimization of the slurry preparation, coating process, calendering, and drying. In this work, different chemistries and formulations have been investigated and optimized. The other parameters were kept constant for all coating procedures to ensure comparable and reproducible results. Therefore, the following suggestions can be taken into account for the future work:

- This work focused on a specific type of Si-alloy material (3M) and graphite (MagE3) and the obtained results are valid for these types of materials and formulation. Using pure Si material in the optimized Si/Gr electrode and its combination with the natural biopolymeric binders investigated in this work can be the next step for future investigations.

- Investigation and optimization of coating parameters such as slurry viscosity, mixing, and drying process can help to improve the coating quality for future Si/Gr anodes.

- To improve the overall performance of the full-cells, further optimization of the electrolyte and electrolyte additives is suggested, especially for high-temperature applications, such as PV-battery systems.

- Development and optimization of suitable and sustainable cathode materials, to be used with the optimized Si/Gr anode, is also of high interest, which can result in the development of sustainable LIBs with improved electrochemical performance.

- Further investigation and optimization of free-standing anodes and cathodes, as well as cross-linked biopolymeric binders is suggested to be investigated in future works to further enhance the mechanical and electrochemical performance of free-standing electrodes.

The mentioned steps can result in high-performance LIBs in the future, with sustainable and green chemistries, cell design, manufacturing, and recycling processes.

A Appendix

A.1 Chemicals and Materials

Table A.1: List of chemicals and materials used in this thesis.

Substance	Supplier	Purity
Si-alloy	3M	battery grade
MagE3	Hitachi	battery grade
SuperP	Imerys Graphite & Carbon	battery grade
Copper foil	Schlenk	battery grade
Polyacrylic acid	Acros Organics	25 wt% solution in water
Carboxymethyl cellulose	MTI Corporation	$\geq$ 99.5%
Li chips	LTS Research Laboratories, Inc.	battery grade
Whatman GF/C	Sigma-Aldrich	-
Lithium hydroxide monohydrate	Alfa Aesar	battery grade
Sodium alginate	Sigma-Aldrich	
Tragacanth gum	Sigma-Aldrich	
Acetic acid	Carl Roth	ROTIPURAN® 100 %
Citric acid	Sigma-Aldrich	$\geq$ 99.5%
1.2 M $LiPF_6$, EC:EMC (3:7) + 10 wt% FEC	E-Lyte Innovations	battery grade
1M $LiPF_6$, EC:DEC (1:1)	Sigma-Aldrich	battery grade
1M $LiPF_6$	Sigma-Aldrich	$\geq$ 99.99%
FEC	Solvionic	99.9%
VC	Sigma-Aldrich	99.999%
TEOSCN	Sigma-Aldrich	99.999%
NMC622	Custom Cells	-
NMC622	MEET	-

A.2 Active materials optimization

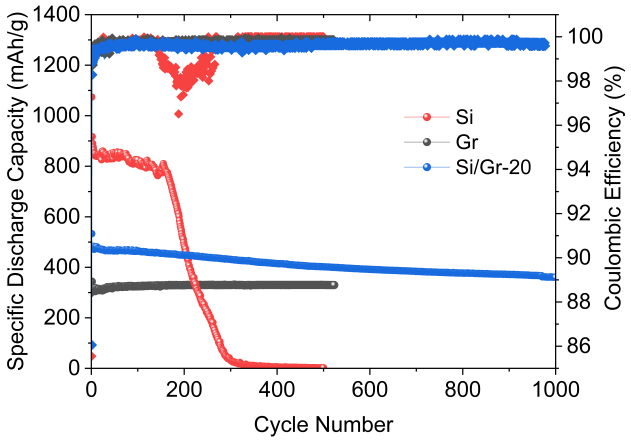

Figure A.1: Discharge capacity and Coulombic efficiency vs. cycle number for Si/Gr, pure Si, and pure Gr anode half cells.

A.3 SEM/EDX analysis

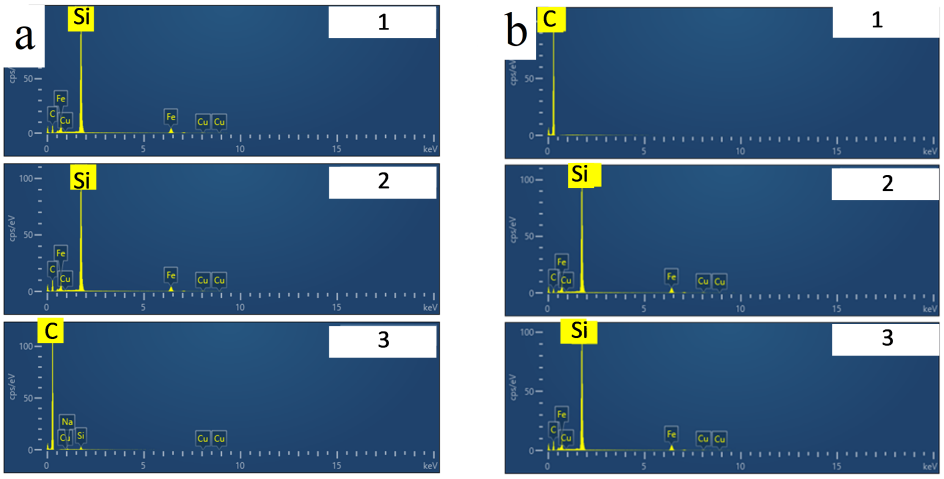

Figure A.2: EDX analysis of Si/Gr-20 samples a) before and b) after calender. These results are linked to the SEM images in Figure 4.14

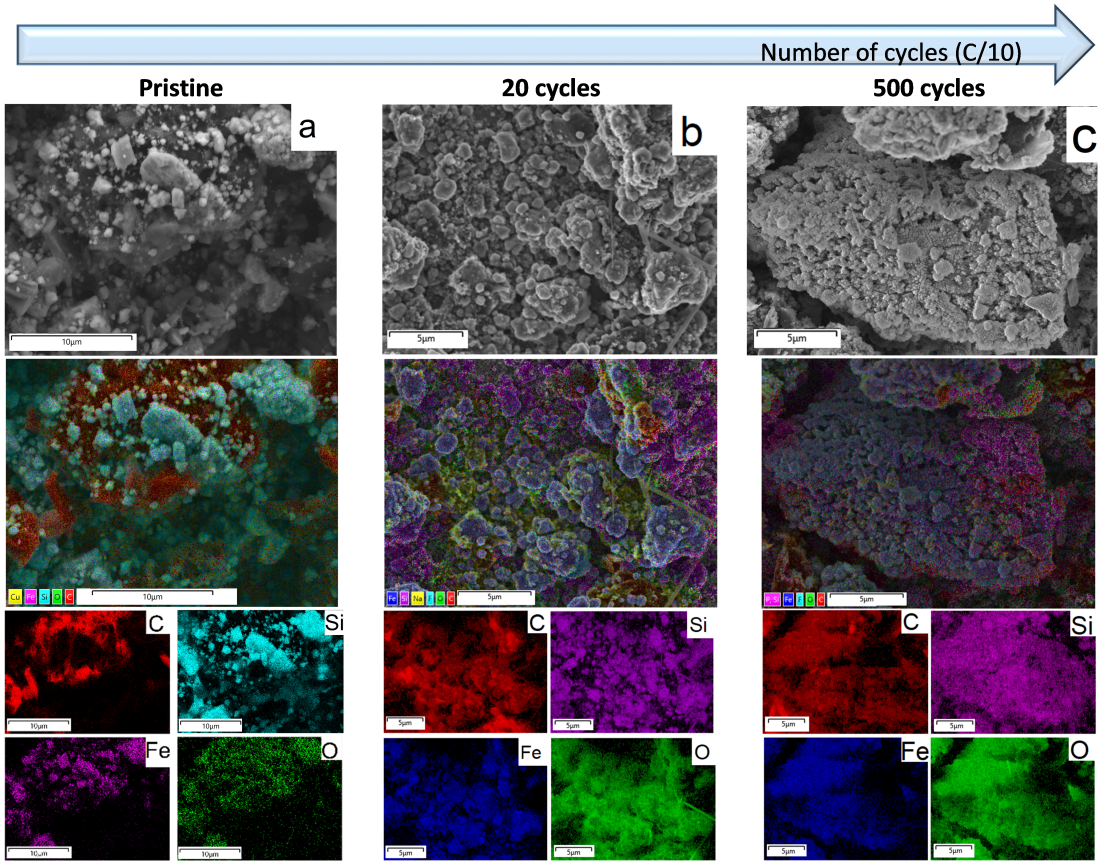

Figure A.3: EDX mapping of a) pristine Si/Gr electrode and Si/Gr electrodes after lithiation/delithiation in Si/Gr||Li cell configuration at C/10 after b) 20 cycles and c) 500 cycles

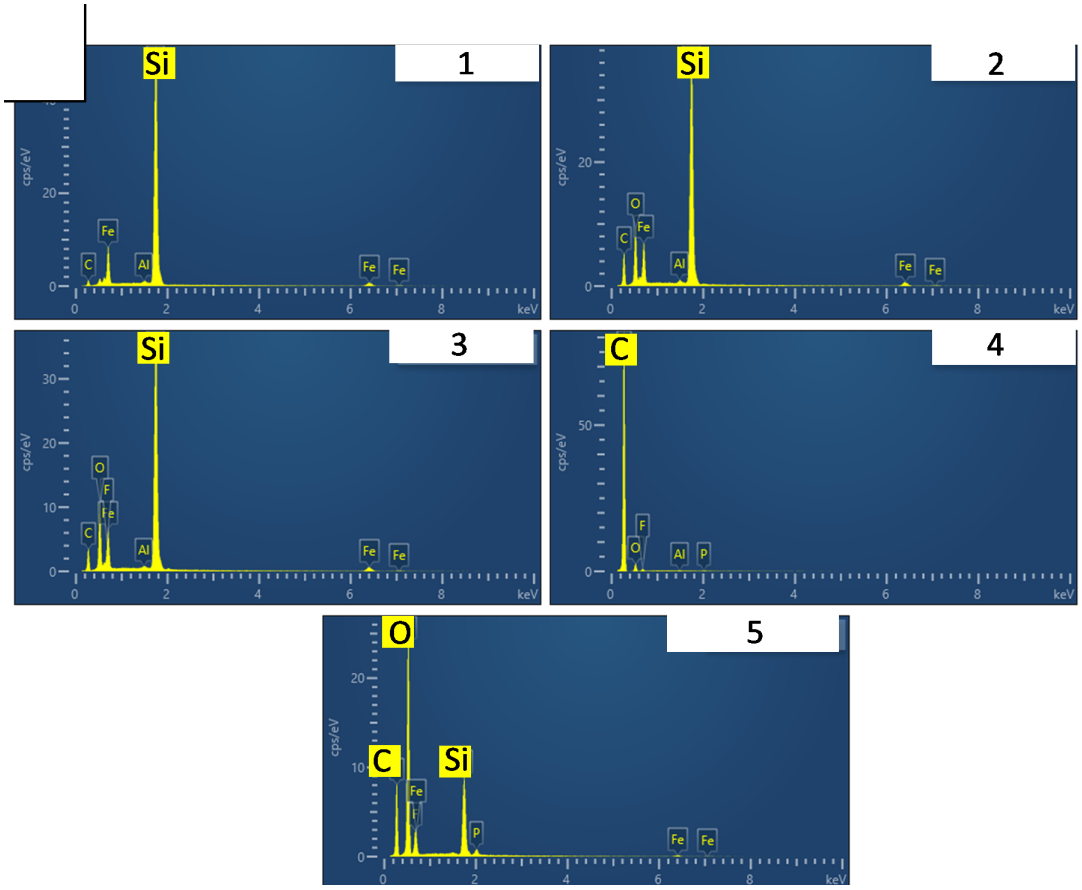

Figure A.4: EDX mapping of a) pristine Si/Gr electrode and Si/Gr electrodes after lithiation/delithiation in Si/Gr||Li cell configuration at C/10 after b) 20 cycles and c) 500 cycles

A.4 Perovskite solar cell

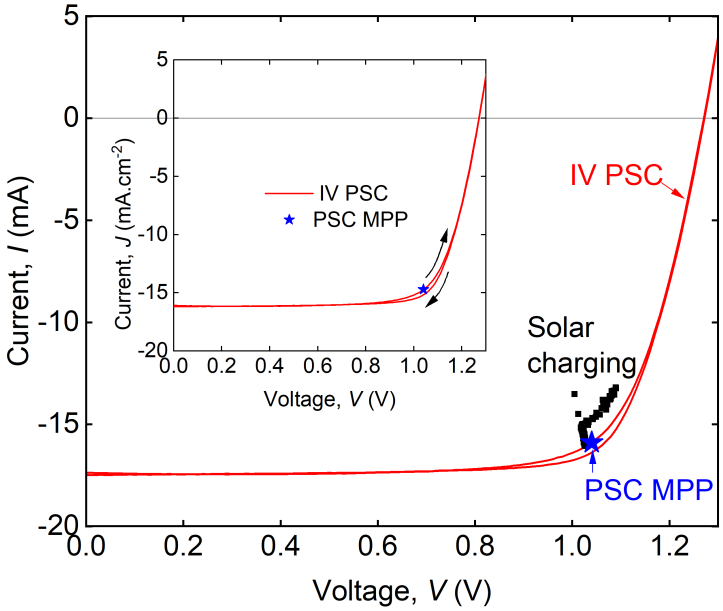

Figure A.5: Current-voltage (I-V) curve of the PSC with the MPP (blue) and solar charging working points (black). The inset shows the IV characteristic of the PSC with indicated short-current density J_{sc} values

A.5 Polymeric binders

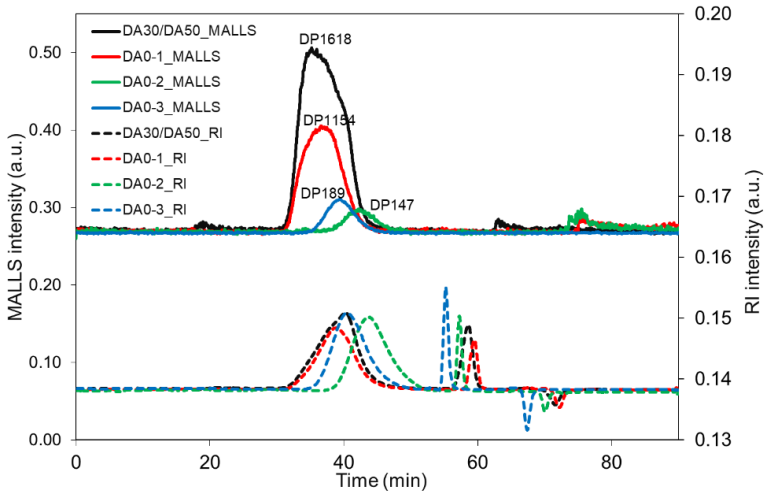

Figure A.6: Size exclusion chromatograph (SEC) chromatograms of chitosan, DA50, DA30, DA0-1, DA0-2, and DA0-3 samples

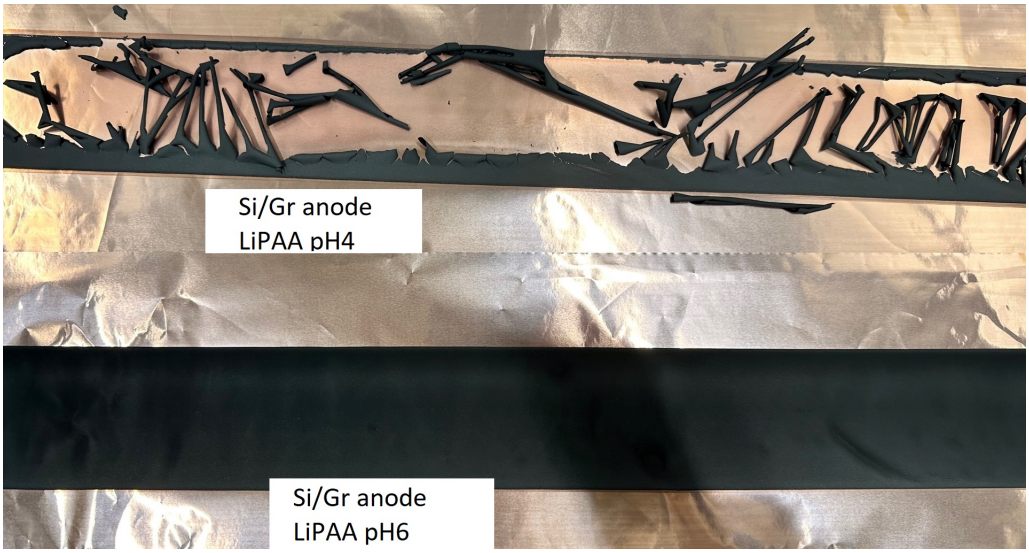

Figure A.7: Si/Gr anodes with LiPAA binders pH4 and pH6 after drying at room temperature over night

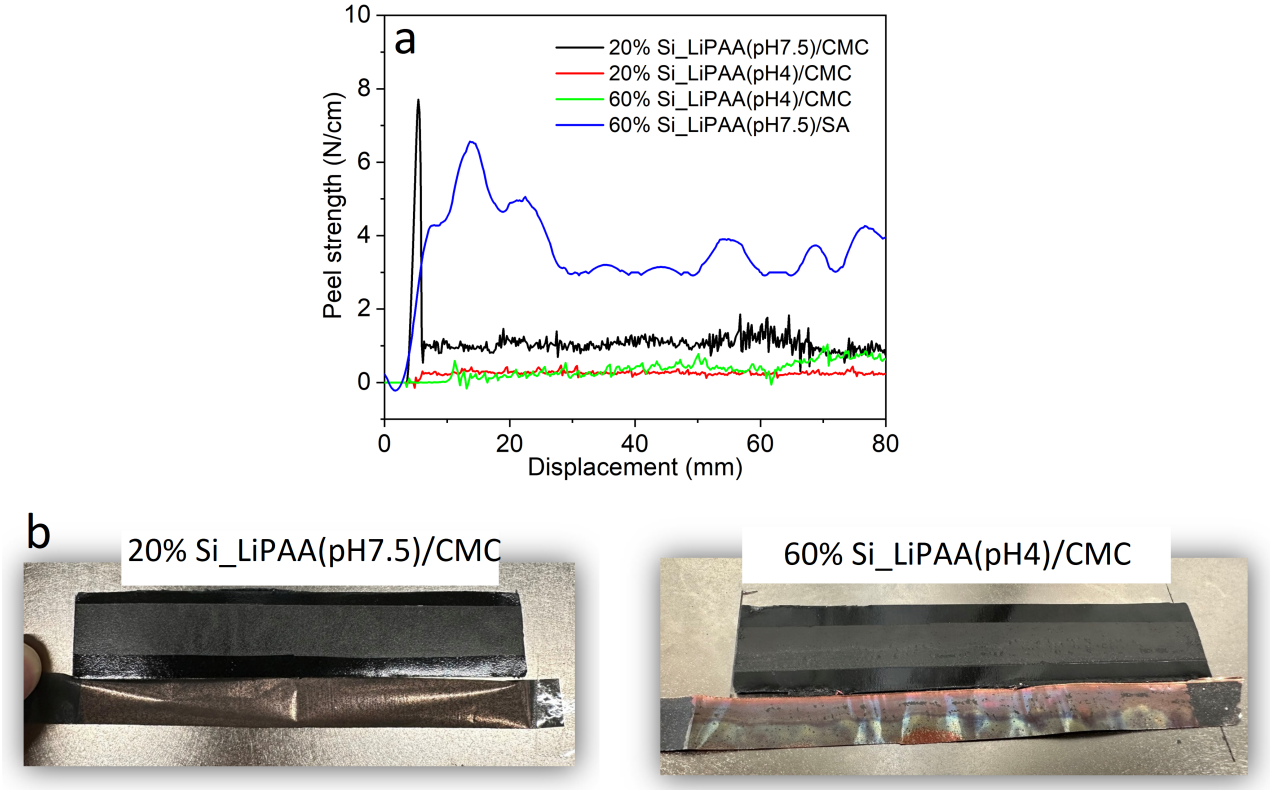

Figure A.8: a)Adhesion test of Si/Gr anodes with cross-linked binders, b) Cu foil and tape after the adhesion test with binders with acidic and neutral pH

A.6 List of Acronyms

AIC	Accumulated irreversible capacity
ATR	Attenuated total reflectance
BSE	Backscattered electron
CA	Citric acid
CE	Coulombic efficiency
CMC	Carboxymethyl cellulose
Cu	Copper
DA	Degree of acetylation
DA50	Degree of acetylation 50%
DEC	Diethyl carbonate
DMC	Dimethyl carbonate
DP	Degree of polymerization
DS	Degree of substitution
DSC	Differential scanning calorimetry
DTG	Derivative thermogravimetr
EC	Ethylene carbonate
EDX	Energy dispersive X-Ray analysis
EE	Energy efficiency
EMC	Ethyl methyl carbonate
FEC	Fluoroethylene carbonate
FTIR	Fourier-transform infrared spectroscopy
Gr	Graphite
LCO	Lithium cobalt oxide
LFP	Lithium iron phosphate
Li	Lithium
LIB	Lithium ion battery
LMO	Lithium manganese oxide
LiPAA	Lithium polyacrylic acid
$LiPF_6$	Lithium hexafluorophosphate
NMC	Lithium nickel manganese cobalt oxide
NMP	N-Methyl-2-pyrrolidone
OCV	Open circuit voltage
PSC	Perovskite solar cell

PV	Photovoltaic
PVDF	Polyvinylidene fluoride
RT	Room temperature
SA	Sodium alginate
SE	Secondary electron
SEI	Solid electrolyte interphase
SEM	Scanning electron microscopy
Si	Silicon
Si/Gr-x	Silicon/Graphite anode with x% Si-alloy (x = 10-70)
TEOSCN	(2-cyanoethyl) triethoxysilane
TG	Tragacanth gum
TGA	Thermogravimetric analysis
VE	Voltage efficiency
VC	Vinylene carbonate
XPS	X-ray photoelectron spectroscopy

List of Figures

List of Tables

Bibliography

[1] V. Etacheri, R. Marom, R. Elazari, G. Salitra, and D. Aurbach, "Challenges in the development of advanced li-ion batteries: A review," *Energy & Environmental Science*, vol. 4, no. 9, pp. 3243–3262, 2011.

[2] M. Winter, B. Barnett, and K. Xu, "Before li ion batteries," *Chemical reviews*, vol. 118, no. 23, pp. 11 433–11 456, 2018.

[3] G. G. Eshetu and E. Figgemeier, "Confronting the challenges of next-generation silicon anode-based lithium-ion batteries: Role of designer electrolyte additives and polymeric binders," *ChemSusChem*, vol. 12, no. 12, pp. 2515–2539, 2019.

[4] S. Duehnen, J. Betz, M. Kolek, R. Schmuch, M. Winter, and T. Placke, "Toward green battery cells: Perspective on materials and technologies," *Small Methods*, vol. 4, no. 7, p. 2 000 039, 2020.

[5] J. Mitali, S. Dhinakaran, and A. Mohamad, "Energy storage systems: A review," *Energy Storage and Saving*, 2022.

[6] K. Feng, M. Li, W. Liu, *et al.*, "Silicon-based anodes for lithium-ion batteries: From fundamentals to practical applications," *Small*, vol. 14, no. 8, p. 1 702 737, 2018.

[7] S. Chae, S.-H. Choi, N. Kim, J. Sung, and J. Cho, "Integration of graphite and silicon anodes for the commercialization of high-energy lithium-ion batteries," *Angewandte Chemie International Edition*, vol. 59, no. 1, pp. 110–135, 2020.

[8] D. Bresser, D. Buchholz, A. Moretti, A. Varzi, and S. Passerini, "Alternative binders for sustainable electrochemical energy storage–the transition to aqueous electrode processing and bio-derived polymers," *Energy & Environmental Science*, vol. 11, no. 11, pp. 3096–3127, 2018.

[9] N. Lingappan, L. Kong, and M. Pecht, "The significance of aqueous binders in lithium-ion batteries," *Renewable and Sustainable Energy Reviews*, vol. 147, p. 111 227, 2021.

[10] M. Winter and R. J. Brodd, "What are batteries, fuel cells, and supercapacitors?" *Chemical reviews*, vol. 104, no. 10, pp. 4245–4270, 2004.

[11] N. Kanani, *The Parthian Battery*. Bad Saulgau : Leuze, 2004.

[12] J. Li and J. Dahn, "An in situ x-ray diffraction study of the reaction of li with crystalline si," *Journal of The Electrochemical Society*, vol. 154, no. 3, A156, 2007.

[13] M. V. Reddy, A. Mauger, C. M. Julien, A. Paolella, and K. Zaghib, "Brief history of early lithium-battery development," *Materials*, vol. 13, no. 8, p. 1884, 2020.

[14] M. Armand, P. Axmann, D. Bresser, *et al.*, "Lithium-ion batteries–current state of the art and anticipated developments," *Journal of Power Sources*, vol. 479, p. 228 708, 2020.

[15] J. B. Goodenough and K.-S. Park, "The li-ion rechargeable battery: A perspective," *Journal of the American Chemical Society*, vol. 135, no. 4, pp. 1167–1176, 2013.

[16] M. Winter, J. O. Besenhard, M. E. Spahr, and P. Novak, "Insertion electrode materials for rechargeable lithium batteries," *Advanced materials*, vol. 10, no. 10, pp. 725–763, 1998.

[17] F. Holtstiege, A. Wilken, M. Winter, and T. Placke, "Running out of lithium? a route to differentiate between capacity losses and active lithium losses in lithium-ion batteries," *Physical Chemistry Chemical Physics*, vol. 19, no. 38, pp. 25 905–25 918, 2017.

[18] J. Kasnatscheew, T. Placke, B. Streipert, *et al.*, "A tutorial into practical capacity and mass balancing of lithium ion batteries," *Journal of the electrochemical society*, vol. 164, no. 12, A2479, 2017.

[19] Z. Chen, L. Zhang, X. Wu, *et al.*, "Effect of n/p ratios on the performance of lini0. 8co0. 15al0. 05o2—— siox/graphite lithium-ion batteries," *Journal of Power Sources*, vol. 439, p. 227 056, 2019.

[20] C.-S. Kim, K. M. Jeong, K. Kim, and C.-W. Yi, "Effects of capacity ratios between anode and cathode on electrochemical properties for lithium polymer batteries," *Electrochimica Acta*, vol. 155, pp. 431–436, 2015.

[21] Y. Pan, S. Gao, F. Sun, H. Yang, and P.-F. Cao, "Polymer binders constructed through dynamic noncovalent bonds for high-capacity silicon-based anodes," *Chemistry–A European Journal*, vol. 25, no. 47, pp. 10 976–10 994, 2019.

[22] R. Yazami and P. Touzain, "A reversible graphite-lithium negative electrode for electrochemical generators," *Journal of Power Sources*, vol. 9, no. 3, pp. 365–371, 1983.

[23] R. Fong, U. Von Sacken, and J. R. Dahn, "Studies of lithium intercalation into carbons using nonaqueous electrochemical cells," *Journal of The Electrochemical Society*, vol. 137, no. 7, p. 2009, 1990.

[24] H. L. Andersen, L. Djuandhi, U. Mittal, and N. Sharma, "Strategies for the analysis of graphite electrode function," *Advanced Energy Materials*, vol. 11, no. 48, p. 2 102 693, 2021.

[25] H. Badenhorst, "Microstructure of natural graphite flakes revealed by oxidation: Limitations of xrd and raman techniques for crystallinity estimates," *Carbon*, vol. 66, pp. 674–690, 2014.

[26] J. Asenbauer, T. Eisenmann, M. Kuenzel, A. Kazzazi, Z. Chen, and D. Bresser, "The success story of graphite as a lithium-ion anode material–fundamentals, remaining challenges, and recent developments including silicon (oxide) composites," *Sustainable Energy & Fuels*, vol. 4, no. 11, pp. 5387–5416, 2020.

[27] U. Hofmann and W. Rüdorff, "The formation of salts from graphite by strong acids," *Transactions of the Faraday Society*, vol. 34, pp. 1017–1021, 1938.

[28] N. Daumas and A. Herold, "Relations between phase concept and reaction mechanics in graphite insertion compounds," *Comptes Rendus Hebdomadaires Des Seances De L Academie Des Sciences Serie C*, vol. 268, no. 5, p. 373, 1969.

[29] J. Dahn, "Phase diagram of li x c 6," *Physical Review B*, vol. 44, no. 17, p. 9170, 1991.

[30] E. Peled, "The electrochemical behavior of alkali and alkaline earth metals in nonaqueous battery systems—the solid electrolyte interphase model," *Journal of The Electrochemical Society*, vol. 126, no. 12, p. 2047, 1979.

[31] K. Xu, "Electrolytes and interphases in li-ion batteries and beyond," *Chemical reviews*, vol. 114, no. 23, pp. 11 503–11 618, 2014.

[32] E. Peled and S. Menkin, "Sei: Past, present and future," *Journal of The Electrochemical Society*, vol. 164, no. 7, A1703, 2017.

[33] E. Peled, D. Golodnitsky, and G. Ardel, "Advanced model for solid electrolyte interphase electrodes in liquid and polymer electrolytes," *Journal of the Electrochemical Society*, vol. 144, no. 8, p. L208, 1997.

[34] S. Shi, P. Lu, Z. Liu, *et al.*, "Direct calculation of li-ion transport in the solid electrolyte interphase," *Journal of the American Chemical Society*, vol. 134, no. 37, pp. 15 476–15 487, 2012.

[35] X. Yu and A. Manthiram, "Electrode–electrolyte interfaces in lithium-based batteries," *Energy & environmental science*, vol. 11, no. 3, pp. 527–543, 2018.

[36] S. K. Heiskanen, J. Kim, and B. L. Lucht, "Generation and evolution of the solid electrolyte interphase of lithium-ion batteries," *Joule*, vol. 3, no. 10, pp. 2322–2333, 2019.

[37] B. Boukamp, G. Lesh, and R. Huggins, "All-solid lithium electrodes with mixed-conductor matrix," *Journal of the Electrochemical Society*, vol. 128, no. 4, p. 725, 1981.

[38] C. J. Wen and R. A. Huggins, "Chemical diffusion in intermediate phases in the lithium-silicon system," *Journal of solid state chemistry*, vol. 37, no. 3, pp. 271–278, 1981.

[39] H. Kim, M. Seo, M.-H. Park, and J. Cho, "A critical size of silicon nano-anodes for lithium rechargeable batteries," *Angewandte Chemie International Edition*, vol. 49, no. 12, pp. 2146–2149, 2010.

[40] N. Liu, H. Wu, M. T. McDowell, Y. Yao, C. Wang, and Y. Cui, "A yolk-shell design for stabilized and scalable li-ion battery alloy anodes," *Nano letters*, vol. 12, no. 6, pp. 3315–3321, 2012.

[41] M. A. Rahman, G. Song, A. I. Bhatt, Y. C. Wong, and C. Wen, "Nanostructured silicon anodes for high-performance lithium-ion batteries," *Advanced Functional Materials*, vol. 26, no. 5, pp. 647–678, 2016.

[42] N. Liu, L. Hu, M. T. McDowell, A. Jackson, and Y. Cui, "Prelithiated silicon nanowires as an anode for lithium ion batteries," *ACS nano*, vol. 5, no. 8, pp. 6487–6493, 2011.

[43] S. Poetke, F. Hippauf, A. Baasner, S. Dörfler, H. Althues, and S. Kaskel, "Nanostructured si- c composites as high-capacity anode material for all-solid-state lithium-ion batteries," *Batteries & Supercaps*, vol. 4, no. 8, pp. 1323–1334, 2021.

[44] N. Hamzelui, G. G. Eshetu, and E. Figgemeier, "Customizing active materials and polymeric binders: Stern requirements to realize silicon-graphite anode based lithium-ion batteries.," *Journal of Energy Storage*, vol. 35, p. 102 098, 2021.

[45] Z. Xu, J. Yang, H. Li, Y. Nuli, and J. Wang, "Electrolytes for advanced lithium ion batteries using silicon-based anodes," *Journal of Materials Chemistry A*, vol. 7, no. 16, pp. 9432–9446, 2019.

[46] F. Aupperle, N. von Aspern, D. Berghus, *et al.*, "The role of electrolyte additives on the interfacial chemistry and thermal reactivity of si-anode-based li-ion battery," *ACS applied energy materials*, vol. 2, no. 9, pp. 6513–6527, 2019.

[47] N. P. Wagner, A. Tron, J. R. Tolchard, G. Noia, and M. P. Bellmann, "Silicon anodes for lithium-ion batteries produced from recovered kerf powders," *Journal of Power Sources*, vol. 414, pp. 486–494, 2019.

[48] Y. Lai, H. Li, Q. Yang, *et al.*, "Revisit the progress of binders for a silicon-based anode from the perspective of designed binder structure and special sized silicon nanoparticles," *Industrial & Engineering Chemistry Research*, vol. 61, no. 19, pp. 6246–6268, 2022.

[49] Y.-M. Zhao, F.-S. Yue, S.-C. Li, *et al.*, "Advances of polymer binders for silicon-based anodes in high energy density lithium-ion batteries," *InfoMat*, vol. 3, no. 5, pp. 460–501, 2021.

[50] N. Hamzelui, M. Linhorst, G. Martin Nyenhuis, *et al.*, "Chitosan as enabling polymeric binder material for silicon-graphite-based anodes in lithium-ion batteries," *Energy Technology*, vol. 11, p. 2 201 239, 2023.

[51] M. Ashuri, Q. He, and L. L. Shaw, "Silicon as a potential anode material for li-ion batteries: Where size, geometry and structure matter," *Nanoscale*, vol. 8, no. 1, pp. 74–103, 2016.

[52] K. A. Hays, B. Key, J. Li, D. L. Wood III, and G. M. Veith, "Si oxidation and h2 gassing during aqueous slurry preparation for li-ion battery anodes," *The Journal of Physical Chemistry C*, vol. 122, no. 18, pp. 9746–9754, 2018.

[53] M. Morita, T. Ohmi, E. Hasegawa, M. Kawakami, and M. Ohwada, "Growth of native oxide on a silicon surface," *Journal of Applied Physics*, vol. 68, no. 3, pp. 1272–1281, 1990.

[54] J. Shin, T.-H. Kim, Y. Lee, and E. Cho, "Key functional groups defining the formation of si anode solid-electrolyte interphase towards high energy density li-ion batteries," *Energy Storage Materials*, vol. 25, pp. 764–781, 2020.

[55] T. M. Fears, R. L. Sacci, J. G. Winiarz, H. Kaiser, H. Taub, and G. M. Veith, "A study of perfluorocarboxylate ester solvents for lithium ion battery electrolytes," *Journal of Power Sources*, vol. 299, pp. 434–442, 2015.

[56] C. Cao, I. I. Abate, E. Sivonxay, *et al.*, "Solid electrolyte interphase on native oxide-terminated silicon anodes for li-ion batteries," *Joule*, vol. 3, no. 3, pp. 762–781, 2019.

[57] T. Fears, M. Doucet, J. Browning, *et al.*, "Evaluating the solid electrolyte interphase formed on silicon electrodes: A comparison of ex situ x-ray photoelectron spectroscopy and in situ neutron reflectometry," *Physical Chemistry Chemical Physics*, vol. 18, no. 20, pp. 13 927–13 940, 2016.

[58] Y. Deng, C. Eames, J.-N. Chotard, *et al.*, "Structural and mechanistic insights into fast lithium-ion conduction in li4sio4–li3po4 solid electrolytes," *Journal of the American Chemical Society*, vol. 137, no. 28, pp. 9136–9145, 2015.

[59] E. Radvanyi, E. De Vito, W. Porcher, and S. J. S. Larbi, "An xps/aes comparative study of the surface behaviour of nano-silicon anodes for li-ion batteries," *Journal of Analytical Atomic Spectrometry*, vol. 29, no. 6, pp. 1120–1131, 2014.

[60] K. Tasaki, A. Goldberg, J.-J. Lian, M. Walker, A. Timmons, and S. J. Harris, "Solubility of lithium salts formed on the lithium-ion battery negative electrode surface in organic solvents," *Journal of The Electrochemical Society*, vol. 156, no. 12, A1019, 2009.

[61] P. Lu, C. Li, E. W. Schneider, and S. J. Harris, "Chemistry, impedance, and morphology evolution in solid electrolyte interphase films during formation in lithium ion batteries," *The Journal of Physical Chemistry C*, vol. 118, no. 2, pp. 896–903, 2014.

[62] B. T. Young, D. R. Heskett, C. C. Nguyen, M. Nie, J. C. Woicik, and B. L. Lucht, "Hard x-ray photoelectron spectroscopy (haxpes) investigation of the silicon solid electrolyte interphase (sei) in lithium-ion batteries," *ACS applied materials & interfaces*, vol. 7, no. 36, pp. 20 004–20 011, 2015.

[63] W.-J. Zhang, "Lithium insertion/extraction mechanism in alloy anodes for lithium-ion batteries," *Journal of Power Sources*, vol. 196, no. 3, pp. 877–885, 2011.

[64] A. Anani and R. Huggins, "Multinary alloy electrodes for solid state batteries i. a phase diagram approach for the selection and storage properties determination of candidate electrode materials," *Journal of power sources*, vol. 38, no. 3, pp. 351–362, 1992.

[65] H. Okamoto, "Li-si (lithium-silicon)," *Journal of Phase Equilibria and Diffusion*, vol. 30, pp. 118–119, 2009.

[66] M. T. McDowell, S. W. Lee, W. D. Nix, and Y. Cui, "25th anniversary article: Understanding the lithiation of silicon and other alloying anodes for lithium-ion batteries," *Advanced Materials*, vol. 25, no. 36, pp. 4966–4985, 2013.

[67] P. Limthongkul, Y.-I. Jang, N. J. Dudney, and Y.-M. Chiang, "Electrochemically-driven solid-state amorphization in lithium-silicon alloys and implications for lithium storage," *Acta Materialia*, vol. 51, no. 4, pp. 1103–1113, 2003.

[68] H. Kim, C.-Y. Chou, J. G. Ekerdt, and G. S. Hwang, "Structure and properties of li- si alloys: A first-principles study," *The Journal of Physical Chemistry C*, vol. 115, no. 5, pp. 2514–2521, 2011.

[69] T.-w. Kwon, J. W. Choi, and A. Coskun, "The emerging era of supramolecular polymeric binders in silicon anodes," *Chemical Society Reviews*, vol. 47, no. 6, pp. 2145–2164, 2018.

[70] C.-H. Yim, F. M. Courtel, and Y. Abu-Lebdeh, "A high capacity silicon–graphite composite as anode for lithium-ion batteries using low content amorphous silicon and compatible binders," *Journal of Materials Chemistry A*, vol. 1, no. 28, pp. 8234–8243, 2013.

[71] Z. Liu, C. Fang, X. He, *et al.*, "In situ-formed novel elastic network binder for a silicon anode in lithium-ion batteries," *Acs Applied Materials & Interfaces*, vol. 13, no. 39, pp. 46 518–46 525, 2021.

[72] S. Guo, H. Li, Y. Li, *et al.*, "Sio2-enhanced structural stability and strong adhesion with a new binder of konjac glucomannan enables stable cycling of silicon anodes for lithium-ion batteries," *Advanced Energy Materials*, vol. 8, no. 24, p. 1 800 434, 2018.

[73] D. Choi and K. L. Choy, "Spider silk binder for si-based anode in lithium-ion batteries," *Materials & Design*, vol. 191, p. 108 669, 2020.

[74] T. Kang, J. Chen, Y. Cui, *et al.*, "Three-dimensional rigidity-reinforced sio x anodes with stabilized performance using an aqueous multicomponent binder technology," *ACS applied materials & interfaces*, vol. 11, no. 29, pp. 26 038–26 046, 2019.

[75] Z. Chen, L. Christensen, and J. Dahn, "Large-volume-change electrodes for li-ion batteries of amorphous alloy particles held by elastomeric tethers," *Electrochemistry communications*, vol. 5, no. 11, pp. 919–923, 2003.

[76] ——, "Comparison of pvdf and pvdf-tfe-p as binders for electrode materials showing large volume changes in lithium-ion batteries," *Journal of The Electrochemical Society*, vol. 150, no. 8, A1073, 2003.

[77] Y. Cai, C. Liu, Z. Yu, *et al.*, "Slidable and highly ionic conductive polymer binder for high-performance si anodes in lithium-ion batteries," *Advanced Science*, vol. 10, no. 6, p. 2 205 590, 2023.

[78] V. A. Nguyen and C. Kuss, "Conducting polymer-based binders for lithium-ion batteries and beyond," *Journal of the Electrochemical Society*, vol. 167, no. 6, p. 065 501, 2020.

[79] Z. Hu, R. Zhao, J. Yang, C. Wu, and Y. Bai, "Binders for si based electrodes: Current status, modification strategies and perspective," *Energy Storage Materials*, p. 102 776, 2023.

[80] J. Li, R. Lewis, and J. Dahn, "Sodium carboxymethyl cellulose: A potential binder for si negative electrodes for li-ion batteries," *Electrochemical and Solid-State Letters*, vol. 10, no. 2, A17, 2006.

[81] B. Lestriez, S. Bahri, I. Sandu, L. Roué, and D. Guyomard, "On the binding mechanism of cmc in si negative electrodes for li-ion batteries," *Electrochemistry Communications*, vol. 9, no. 12, pp. 2801–2806, 2007.

[82] H. Buqa, M. Holzapfel, F. Krumeich, C. Veit, and P. Novák, "Study of styrene butadiene rubber and sodium methyl cellulose as binder for negative electrodes in lithium-ion batteries," *Journal of Power Sources*, vol. 161, no. 1, pp. 617–622, 2006.

[83] J. Liu, Q. Zhang, Z.-Y. Wu, *et al.*, "A high-performance alginate hydrogel binder for the si/c anode of a li-ion battery," *Chemical communications*, vol. 50, no. 48, pp. 6386–6389, 2014.

[84] R. Guo, S. Zhang, H. Ying, W. Yang, J. Wang, and W. Han, "Preparation of an amorphous cross-linked binder for silicon anodes," *ChemSusChem*, vol. 12, no. 21, pp. 4838–4845, 2019.

[85] A. Magasinski, B. Zdyrko, I. Kovalenko, *et al.*, "Toward efficient binders for li-ion battery si-based anodes: Polyacrylic acid," *ACS applied materials & interfaces*, vol. 2, no. 11, pp. 3004–3010, 2010.

[86] W. Porcher, S. Chazelle, A. Boulineau, *et al.*, "Understanding polyacrylic acid and lithium polyacrylate binder behavior in silicon based electrodes for li-ion batteries," *Journal of The Electrochemical Society*, vol. 164, no. 14, A3633, 2017.

[87] K. A. Hays, R. E. Ruther, A. J. Kukay, *et al.*, "What makes lithium substituted polyacrylic acid a better binder than polyacrylic acid for silicon-graphite composite anodes?" *Journal of Power Sources*, vol. 384, pp. 136–144, 2018.

[88] Z. Karkar, D. Guyomard, L. Roué, and B. Lestriez, "A comparative study of polyacrylic acid (paa) and carboxymethyl cellulose (cmc) binders for si-based electrodes," *Electrochimica Acta*, vol. 258, pp. 453–466, 2017.

[89] H. Cho, K. Kim, C.-M. Park, and G. Jeong, "Partially carbonized poly (acrylic acid) grafted to carboxymethyl cellulose as an advanced binder for si anode in li-ion batteries," *Journal of Electrochemical Science and Technology*, vol. 10, no. 2, pp. 131–138, 2019.

[90] P. Parikh, M. Sina, A. Banerjee, *et al.*, "Role of polyacrylic acid (paa) binder on the solid electrolyte interphase in silicon anodes," *Chemistry of Materials*, vol. 31, no. 7, pp. 2535–2544, 2019.

[91] D. Liu, Y. Zhao, R. Tan, *et al.*, "Novel conductive binder for high-performance silicon anodes in lithium ion batteries," *Nano Energy*, vol. 36, pp. 206–212, 2017.

[92] H. Shen, Q. Wang, Z. Chen, C. Rong, and D. Chao, "Application and development of silicon anode binders for lithium-ion batteries," *Materials*, vol. 16, no. 12, p. 4266, 2023.

[93] L. Yue, L. Zhang, and H. Zhong, "Carboxymethyl chitosan: A new water soluble binder for si anode of li-ion batteries," *Journal of power sources*, vol. 247, pp. 327–331, 2014.

[94] C. Chen, S. H. Lee, M. Cho, J. Kim, and Y. Lee, "Cross-linked chitosan as an efficient binder for si anode of li-ion batteries," *ACS Applied Materials & Interfaces*, vol. 8, no. 4, pp. 2658–2665, 2016.

[95] Z. Xu, J. Yang, T. Zhang, Y. Nuli, J. Wang, and S.-i. Hirano, "Silicon microparticle anodes with self-healing multiple network binder," *Joule*, vol. 2, no. 5, pp. 950–961, 2018.

[96] M.-H. Ryou, J. Kim, I. Lee, *et al.*, "Mussel-inspired adhesive binders for high-performance silicon nanoparticle anodes in lithium-ion batteries," *Advanced materials*, vol. 25, no. 11, pp. 1571–1576, 2013.

[97] W. Li, S. Huang, D. Xu, Y. Zhao, Y. Zhang, and L. Zhang, "Molecular dynamics simulations of the characteristics of sodium carboxymethyl cellulose with different degrees of substitution in a salt solution," *Cellulose*, vol. 24, no. 9, pp. 3619–3633, 2017.

[98] J. S. Behra, J. Mattsson, O. J. Cayre, E. S. Robles, H. Tang, and T. N. Hunter, "Characterization of sodium carboxymethyl cellulose aqueous solutions to support complex product formulation: A rheology and light scattering study," *ACS Applied Polymer Materials*, vol. 1, no. 3, pp. 344–358, 2019.

[99] X. Wang, J. Liu, Z. Gong, *et al.*, "Influence of degree of substitution of carboxymethyl cellulose on high performance silicon anode in lithium-ion batteries," *Electrochemistry*, vol. 87, no. 1, pp. 94–99, 2019.

[100] Z.-J. Han, K. Yamagiwa, N. Yabuuchi, *et al.*, "Electrochemical lithiation performance and characterization of silicon–graphite composites with lithium, sodium, potassium, and ammonium polyacrylate binders," *Physical Chemistry Chemical Physics*, vol. 17, no. 5, pp. 3783–3795, 2015.

[101] I. Kovalenko, B. Zdyrko, A. Magasinski, *et al.*, "A major constituent of brown algae for use in high-capacity li-ion batteries," *Science*, vol. 334, no. 6052, pp. 75–79, 2011.

[102] A. Garcıa, M. Culebras, M. N. Collins, and J. J. Leahy, "Stability and rheological study of sodium carboxymethyl cellulose and alginate suspensions as binders for lithium ion batteries," *Journal of Applied Polymer Science*, vol. 135, no. 17, p. 46 217, 2018.

[103] M. Nejatian, S. Abbasi, and F. Azarikia, "Gum tragacanth: Structure, characteristics and applications in foods," *International Journal of Biological Macromolecules*, vol. 160, pp. 846–860, 2020.

[104] M. E. Taghavizadeh Yazdi, S. Nazarnezhad, S. H. Mousavi, *et al.*, "Gum tragacanth (gt): A versatile biocompatible material beyond borders," *Molecules*, vol. 26, no. 6, p. 1510, 2021.

[105] C. Verma, D. Pathania, S. Anjum, and B. Gupta, "Smart designing of tragacanth gum by graft functionalization for advanced materials," *Macromolecular Materials and Engineering*, vol. 305, no. 4, p. 1 900 762, 2020.

[106] R. Mohan, S. Singh, G. Kumar, and M. Srivastava, "Evaluation of gelling behavior of natural gums and their formulation prospects," *Indian J. Pharm. Educ. Res*, vol. 54, pp. 1016–1023, 2020.

[107] D. Versaci, R. Nasi, U. Zubair, *et al.*, "New eco-friendly low-cost binders for li-ion anodes," *Journal of Solid State Electrochemistry*, vol. 21, pp. 3429–3435, 2017.

[108] A. Scalia, P. Zaccagnini, M. Armandi, *et al.*, "Tragacanth gum as green binder for sustainable water-processable electrochemical capacitor," *ChemSusChem*, vol. 14, no. 1, pp. 356–362, 2021.

[109] D. Versaci, O. D. Apostu, D. Dessantis, *et al.*, "Tragacanth, an exudate gum as suitable aqueous binder for high voltage cathode material," *Batteries*, vol. 9, no. 4, p. 199, 2023.

[110] J. Cui, Z. Yu, and D. Lau, "Effect of acetyl group on mechanical properties of chitin/chitosan nanocrystal: A molecular dynamics study," *International journal of molecular sciences*, vol. 17, no. 1, p. 61, 2016.

[111] M. Rinaudo, "Chitin and chitosan: Properties and applications," *Progress in polymer science*, vol. 31, no. 7, pp. 603–632, 2006.

[112] D. A. Gopakumar, A. R. Pai, D. Pasquini, L. S.-Y. Ben, A. K. HPS, and S. Thomas, "Nanomaterials—state of art, new challenges, and opportunities," *Nanoscale Materials in Water Purification*, pp. 1–24, 2019.

[113] H. Honarkar and M. Barikani, "Applications of biopolymers i: Chitosan," *Monatshefte für Chemie-Chemical Monthly*, vol. 140, no. 12, pp. 1403–1420, 2009.

[114] J. Wattjes, S. Sreekumar, C. Richter, *et al.*, "Patterns matter part 1: Chitosan polymers with non-random patterns of acetylation," *Reactive and Functional Polymers*, vol. 151, p. 104 583, 2020.

[115] S. Künne, F. Püttmann, M. Linhorst, *et al.*, "Comparative study on chitosans as green binder materials for limn2o4 positive electrodes in lithium ion batteries," *ChemElectroChem*, vol. 9, no. 17, e202200600, 2022.

[116] K. Rajeev, E. Kim, J. Nam, S. Lee, J. Mun, and T.-H. Kim, "Chitosan-grafted-polyaniline copolymer as an electrically conductive and mechanically stable binder for high-performance si anodes in li-ion batteries," *Electrochimica Acta*, vol. 333, p. 135 532, 2020.

[117] S. Hu, Z. Cai, T. Huang, H. Zhang, and A. Yu, "A modified natural polysaccharide as a high-performance binder for silicon anodes in lithium-ion batteries," *ACS applied materials & interfaces*, vol. 11, no. 4, pp. 4311–4317, 2019.

[118] N. S. Hochgatterer, M. R. Schweiger, S. Koller, *et al.*, "Silicon/graphite composite electrodes for high-capacity anodes: Influence of binder chemistry on cycling stability," *Electrochemical and solid-state letters*, vol. 11, no. 5, A76, 2008.

[119] D. Mazouzi, B. Lestriez, L. Roué, and D. Guyomard, "Silicon composite electrode with high capacity and long cycle life," *Electrochemical and Solid-State Letters*, vol. 12, no. 11, A215, 2009.

[120] C.-H. Jung, K.-H. Kim, and S.-H. Hong, "Stable silicon anode for lithium-ion batteries through covalent bond formation with a binder via esterification," *ACS applied materials & interfaces*, vol. 11, no. 30, pp. 26 753–26 763, 2019.

[121] J.-K. Yoo, J. Jeon, K. Kang, and Y. S. Jung, "Glyoxalated polyacrylamide as a covalently attachable and rapidly cross-linkable binder for si electrode in lithium ion batteries," *Electronic Materials Letters*, vol. 13, no. 2, pp. 136–141, 2017.

[122] D.-E. Yoon, C. Hwang, N.-R. Kang, *et al.*, "Dependency of electrochemical performances of silicon lithium-ion batteries on glycosidic linkages of polysaccharide binders," *ACS applied materials & interfaces*, vol. 8, no. 6, pp. 4042–4047, 2016.

[123] H. Chen, M. Ling, L. Hencz, *et al.*, "Exploring chemical, mechanical, and electrical functionalities of binders for advanced energy-storage devices," *Chemical reviews*, vol. 118, no. 18, pp. 8936–8982, 2018.

[124] X. Fu and W.-H. Zhong, "Biomaterials for high-energy lithium-based batteries: Strategies, challenges, and perspectives," *Advanced energy materials*, vol. 9, no. 40, p. 1 901 774, 2019.

[125] L. Qiu, Y. Shen, H. Fan, X. Yang, and C. Wang, "Carboxymethyl fenugreek gum: Rheological characterization and as a novel binder for silicon anode of lithium-ion batteries," *International journal of biological macromolecules*, vol. 115, pp. 672–679, 2018.

[126] T.-w. Kwon, Y. K. Jeong, I. Lee, T.-S. Kim, J. W. Choi, and A. Coskun, "Systematic molecular-level design of binders incorporating meldrum's acid for silicon anodes in lithium rechargeable batteries," *Advanced materials*, vol. 26, no. 47, pp. 7979–7985, 2014.

[127] M. S. Islam and C. A. Fisher, "Lithium and sodium battery cathode materials: Computational insights into voltage, diffusion and nanostructural properties," *Chemical Society Reviews*, vol. 43, no. 1, pp. 185–204, 2014.

[128] H.-J. Noh, S. Youn, C. S. Yoon, and Y.-K. Sun, "Comparison of the structural and electrochemical properties of layered li [nixcoymnz] o2 (x= 1/3, 0.5, 0.6, 0.7, 0.8 and 0.85) cathode material for lithium-ion batteries," *Journal of power sources*, vol. 233, pp. 121–130, 2013.

[129] A. Manthiram, "A reflection on lithium-ion battery cathode chemistry," *Nature communications*, vol. 11, no. 1, p. 1550, 2020.

[130] C. Zhan, J. Lu, A. Jeremy Kropf, *et al.*, "Mn (ii) deposition on anodes and its effects on capacity fade in spinel lithium manganate–carbon systems," *Nature communications*, vol. 4, no. 1, p. 2437, 2013.

[131] J. Ling, C. Karuppiah, S. G. Krishnan, *et al.*, "Phosphate polyanion materials as high-voltage lithium-ion battery cathode: A review," *Energy & Fuels*, vol. 35, no. 13, pp. 10 428–10 450, 2021.

[132] A. K. Padhi, K. S. Nanjundaswamy, and J. B. Goodenough, "Phospho-olivines as positive-electrode materials for rechargeable lithium batteries," *Journal of the electrochemical society*, vol. 144, no. 4, p. 1188, 1997.

[133] Y. Wang, P. He, and H. Zhou, "Olivine lifepo 4: Development and future," *Energy & Environmental Science*, vol. 4, no. 3, pp. 805–817, 2011.

[134] L.-X. Yuan, Z.-H. Wang, W.-X. Zhang, *et al.*, "Development and challenges of lifepo 4 cathode material for lithium-ion batteries," *Energy & Environmental Science*, vol. 4, no. 2, pp. 269–284, 2011.

[135] H. Zhang, L. Qiao, H. Kühnle, E. Figgemeier, M. Armand, and G. G. Eshetu, "From lithium to emerging mono-and multivalent-cation-based rechargeable batteries: Non-aqueous organic electrolyte and interphase perspectives," *Energy & Environmental Science*, 2023.

[136] J. B. Goodenough and Y. Kim, "Challenges for rechargeable li batteries," *Chemistry of materials*, vol. 22, no. 3, pp. 587–603, 2010.

[137] T. Zhang, M. Hong, J. Yang, *et al.*, "A high performance lithium-ion–sulfur battery with a free-standing carbon matrix supported li-rich alloy anode," *Chemical Science*, vol. 9, no. 47, pp. 8829–8835, 2018.

[138] A. Rezqita, M. Sauer, A. Foelske, H. Kronberger, and A. Trifonova, "The effect of electrolyte additives on electrochemical performance of silicon/mesoporous carbon (si/mc) for anode materials for lithium-ion batteries," *Electrochimica Acta*, vol. 247, pp. 600–609, 2017.

[139] L. Martin, H. Martinez, M. Ulldemolins, B. Pecquenard, and F. Le Cras, "Evolution of the si electrode/electrolyte interface in lithium batteries characterized by xps and afm techniques: The influence of vinylene carbonate additive," *Solid State Ionics*, vol. 215, pp. 36–44, 2012.

[140] L. El Ouatani, R. Dedryvère, C. Siret, *et al.*, "The effect of vinylene carbonate additive on surface film formation on both electrodes in li-ion batteries," *Journal of the Electrochemical Society*, vol. 156, no. 2, A103, 2008.

[141] Y. S. Choudhary, L. Jothi, and G. Nageswaran, "Electrochemical characterization," in *Spectroscopic Methods for Nanomaterials Characterization*, Elsevier, 2017, pp. 19–54.

[142] A. Smith, J. Burns, and J. Dahn, "High-precision differential capacity analysis of limn2o4/graphite cells," *Electrochemical and solid-state letters*, vol. 14, no. 4, A39, 2011.

[143] I. Bloom, A. N. Jansen, D. P. Abraham, *et al.*, "Differential voltage analyses of high-power, lithium-ion cells: 1. technique and application," *Journal of Power Sources*, vol. 139, no. 1-2, pp. 295–303, 2005.

[144] M. Loveridge, M. Lain, I. Johnson, *et al.*, "Towards high capacity li-ion batteries based on silicon-graphene composite anodes and sub-micron v-doped lifepo4 cathodes," *Scientific reports*, vol. 6, no. 1, p. 37 787, 2016.

[145] M. Obrovac and L. Christensen, "Structural changes in silicon anodes during lithium insertion/extraction," *Electrochemical and solid-state letters*, vol. 7, no. 5, A93, 2004.

[146] A. Hassid, M. Klinger, S. Krzack, and H. Cohen, "Tga–dsc combined coal analysis as a tool for qc (quality control) and reactivity patterns of coals," *Acs Omega*, vol. 7, no. 2, pp. 1893–1907, 2022.

[147] Shehala, K. Baranwal, M. Prabha, T. Malviya, A. Gaurav, and V. Singh, "Carboxymethyl cellulose-nio nanoparticles as peroxidase mimic for sensitive colorimetric detection of hydrogen peroxide," *Chemical Papers*, vol. 77, no. 3, pp. 1299–1316, 2023.

[148] N. S. Capanema, A. A. Mansur, A. C. de Jesus, S. M. Carvalho, L. C. de Oliveira, and H. S. Mansur, "Superabsorbent crosslinked carboxymethyl cellulose-peg hydrogels for potential wound dressing applications," *International journal of biological macromolecules*, vol. 106, pp. 1218–1234, 2018.

[149] M. A. Mohamed, J. Jaafar, A. Ismail, M. Othman, and M. Rahman, "Fourier transform infrared (ftir) spectroscopy," in *Membrane characterization*, Elsevier, 2017, pp. 3–29.

[150] J. Anderson and G. Voskerician, "The challenge of biocompatibility evaluation of biocomposites," in *Biomedical Composites*, Elsevier, 2010, pp. 325–353.

[151] J. C. Spence and W. Hawkes Peter, *Springer handbook of microscopy*. Springer, 2019.

[152] D. C. Joy, "Scanning electron microscopy: Theory, history and development of the field emission scanning electron microscope," *Biological Field Emission Scanning Electron Microscopy*, vol. 1, pp. 1–6, 2019.

[153] L. Krause, T. Brandt, V. Chevrier, and L. Jensen, "Surface area increase of silicon alloys in li-ion full cells measured by isothermal heat flow calorimetry," *Journal of The Electrochemical Society*, vol. 164, no. 9, A2277, 2017.

[154] D. N. G. Krishna and J. Philip, "Review on surface-characterization applications of x-ray photoelectron spectroscopy (xps): Recent developments and challenges," *Applied Surface Science Advances*, vol. 12, p. 100 332, 2022.

[155] S. Oswald, "X-ray photoelectron spectroscopy in analysis of surfaces," *Encyclopedia of Analytical Chemistry: Applications, Theory and Instrumentation*, 2006.

[156] M. Hekmatfar, A. Kazzazi, G. G. Eshetu, I. Hasa, and S. Passerini, "Understanding the electrode/electrolyte interface layer on the li-rich nickel manganese cobalt layered oxide cathode by xps," *ACS applied materials & interfaces*, vol. 11, no. 46, pp. 43 166–43 179, 2019.

[157] B. Koo, H. Kim, Y. Cho, K. T. Lee, N.-S. Choi, and J. Cho, "A highly cross-linked polymeric binder for high-performance silicon negative electrodes in lithium ion batteries," *Angewandte Chemie*, vol. 124, no. 35, pp. 8892–8897, 2012.

[158] W. Haselrieder, B. Westphal, H. Bockholt, A. Diener, S. Höft, and A. Kwade, "Measuring the coating adhesion strength of electrodes for lithium-ion batteries," *International Journal of Adhesion and Adhesives*, vol. 60, pp. 1–8, 2015.

[159] A. Kwade, W. Haselrieder, R. Leithoff, A. Modlinger, F. Dietrich, and K. Droeder, "Current status and challenges for automotive battery production technologies," *Nature Energy*, vol. 3, no. 4, pp. 290–300, 2018.

[160] Y. Liu, R. Zhang, J. Wang, and Y. Wang, "Current and future lithium-ion battery manufacturing," *IScience*, vol. 24, no. 4, 2021.

[161] G. Berckmans, M. Messagie, J. Smekens, N. Omar, L. Vanhaverbeke, and J. Van Mierlo, "Cost projection of state of the art lithium-ion batteries for electric vehicles up to 2030," *Energies*, vol. 10, no. 9, p. 1314, 2017.

[162] Z. Lin, T. Liu, X. Ai, and C. Liang, "Aligning academia and industry for unified battery performance metrics," *Nature communications*, vol. 9, no. 1, p. 5262, 2018.

[163] Y. Jin, B. Zhu, Z. Lu, N. Liu, and J. Zhu, "Challenges and recent progress in the development of si anodes for lithium-ion battery," *Advanced Energy Materials*, vol. 7, no. 23, p. 1 700 715, 2017.

[164] G. Zhu, Y. Wang, S. Yang, Q. Qu, and H. Zheng, "Correlation between the physical parameters and the electrochemical performance of a silicon anode in lithium-ion batteries," *Journal of Materiomics*, vol. 5, no. 2, pp. 164–175, 2019.

[165] G. Y. Gor, J. Cannarella, J. H. Prévost, and C. B. Arnold, "A model for the behavior of battery separators in compression at different strain/charge rates," *Journal of The Electrochemical Society*, vol. 161, no. 11, F3065, 2014.

[166] R. Jung, M. Metzger, D. Haering, *et al.*, "Consumption of fluoroethylene carbonate (fec) on si-c composite electrodes for li-ion batteries," *Journal of The Electrochemical Society*, vol. 163, no. 8, A1705, 2016.

[167] S.-B. Son, L. Cao, T. Yoon, *et al.*, "Interfacially induced cascading failure in graphite-silicon composite anodes," *Advanced Science*, vol. 6, no. 3, p. 1 801 007, 2019.

[168] Q. Huang, M. J. Loveridge, R. Genieser, M. J. Lain, and R. Bhagat, "Electrochemical evaluation and phase-related impedance studies on silicon–few layer graphene (flg) composite electrode systems," *Scientific Reports*, vol. 8, no. 1, p. 1386, 2018.

[169] R. W. Schmitz, P. Murmann, R. Schmitz, *et al.*, "Investigations on novel electrolytes, solvents and sei additives for use in lithium-ion batteries: Systematic electrochemical characterization and detailed analysis by spectroscopic methods," *Progress in Solid State Chemistry*, vol. 42, no. 4, pp. 65–84, 2014.

[170] B. T. Young, C. C. Nguyen, A. Lobach, D. R. Heskett, J. C. Woicik, and B. L. Lucht, "Role of binders in solid electrolyte interphase formation in lithium ion batteries studied with hard x-ray photoelectron spectroscopy," *Journal of Materials Research*, vol. 34, no. 1, pp. 97–106, 2019.

[171] C. C. Nguyen, T. Yoon, D. M. Seo, P. Guduru, and B. L. Lucht, "Systematic investigation of binders for silicon anodes: Interactions of binder with silicon particles and electrolytes and effects of binders on solid electrolyte interphase formation," *ACS applied materials & interfaces*, vol. 8, no. 19, pp. 12 211–12 220, 2016.

[172] F. Li, J. Xu, Z. Hou, M. Li, and R. Yang, "Silicon anodes for high-performance storage devices: Structural design, material compounding, advances in electrolytes and binders," *ChemNanoMat*, vol. 6, no. 5, pp. 720–738, 2020.

[173] C.-H. Yim, S. Niketic, N. Salem, O. Naboka, and Y. Abu-Lebdeh, "Towards improving the practical energy density of li-ion batteries: Optimization and evaluation of silicon: Graphite composites in full cells," *Journal of The Electrochemical Society*, vol. 164, no. 1, A6294, 2016.

[174] F. Aupperle, G. G. Eshetu, K. W. Eberman, A. Xioa, J.-S. Bridel, and E. Figgemeier, "Realizing a high-performance lini 0.6 mn 0.2 co 0.2 o 2/silicon–graphite full lithium ion battery cell via a designer electrolyte additive," *Journal of Materials Chemistry A*, vol. 8, no. 37, pp. 19 573–19 587, 2020.

[175] G. G. Eshetu, H. Zhang, X. Judez, *et al.*, "Production of high-energy li-ion batteries comprising silicon-containing anodes and insertion-type cathodes," *Nature communications*, vol. 12, no. 1, p. 5459, 2021.

[176] A. Rezqita, A.-R. Kathribail, J. Kahr, and M. Jahn, "Analysis of degradation of si/carbon—— lini0. 5mn0. 3co0. 2o2 full cells: Effect of prelithiation," *Journal of The Electrochemical Society*, vol. 166, no. 3, A5483, 2019.

[177] M. Klett, J. A. Gilbert, S. E. Trask, *et al.*, "Electrode behavior re-visited: Monitoring potential windows, capacity loss, and impedance changes in li1. 03 (ni0. 5co0. 2mn0. 3) 0.97 o2/silicon-graphite full cells," *Journal of The Electrochemical Society*, vol. 163, no. 6, A875, 2016.

[178] P. Meister, H. Jia, J. Li, R. Kloepsch, M. Winter, and T. Placke, "Best practice: Performance and cost evaluation of lithium ion battery active materials with special emphasis on energy efficiency," *Chemistry of Materials*, vol. 28, no. 20, pp. 7203–7217, 2016.

[179] A. Eftekhari, "Energy efficiency: A critically important but neglected factor in battery research," *Sustainable Energy & Fuels*, vol. 1, no. 10, pp. 2053–2060, 2017.

[180] A. Mayr, D. Schreiner, B. Stumper, and R. Daub, "In-line sensor-based process control of the calendering process for lithium-ion batteries," *Procedia CIRP*, vol. 107, pp. 295–301, 2022.

[181] T. Vorauer, J. Schöggl, S. Sanadhya, *et al.*, "Impact of solid-electrolyte interphase reformation on capacity loss in silicon-based lithium-ion batteries," *Communications Materials*, vol. 4, no. 1, p. 44, 2023.

[182] P. Kumar, C. L. Berhaut, D. Zapata Dominguez, *et al.*, "Nano-architectured composite anode enabling long-term cycling stability for high-capacity lithium-ion batteries," *Small*, vol. 16, no. 11, p. 1 906 812, 2020.

[183] N. Hamzelui, L.-C. Kin, J. Köhler, *et al.*, "Toward the integration of a silicon/graphite anode-based lithium-ion battery in photovoltaic charging battery systems," *ACS omega*, vol. 7, no. 31, pp. 27 532–27 541, 2022.

[184] V. Vega-Garita, L. Ramirez-Elizondo, N. Narayan, and P. Bauer, "Integrating a photovoltaic storage system in one device: A critical review," *Progress in Photovoltaics: research and applications*, vol. 27, no. 4, pp. 346–370, 2019.

[185] S. P. Ayeng'o, H. Axelsen, D. Haberschusz, and D. U. Sauer, "A model for direct-coupled pv systems with batteries depending on solar radiation, temperature and number of serial connected pv cells," *Solar Energy*, vol. 183, pp. 120–131, 2019.

[186] O. Astakhov, T. Merdzhanova, L.-C. Kin, and U. Rau, "From room to roof: How feasible is direct coupling of solar-battery power unit under variable irradiance?" *Solar Energy*, vol. 206, pp. 732–740, 2020.

[187] A. Gurung and Q. Qiao, "Solar charging batteries: Advances, challenges, and opportunities," *Joule*, vol. 2, no. 7, pp. 1217–1230, 2018.

[188] L.-c. Kin, Z. Liu, O. Astakhov, *et al.*, "Efficient area matched converter aided solar charging of lithium ion batteries using high voltage perovskite solar cells," *ACS Applied Energy Materials*, vol. 3, no. 1, pp. 431–439, 2019.

[189] M. J. Piernas-Munoz, S. E. Trask, A. R. Dunlop, E. Lee, and I. Bloom, "Effect of temperature on silicon-based anodes for lithium-ion batteries," *Journal of Power Sources*, vol. 441, p. 227 080, 2019.

[190] Q. Wang, J. Sun, X. Yao, and C. Chen, "Thermal stability of lipf6/ec+ dec electrolyte with charged electrodes for lithium ion batteries," *Thermochimica Acta*, vol. 437, no. 1-2, pp. 12–16, 2005.

[191] M.-T. F. Rodrigues, G. Babu, H. Gullapalli, *et al.*, "A materials perspective on li-ion batteries at extreme temperatures," *nature energy*, vol. 2, no. 8, pp. 1–14, 2017.

[192] R. Jung, P. Strobl, F. Maglia, C. Stinner, and H. A. Gasteiger, "Temperature dependence of oxygen release from lini0. 6mn0. 2co0. 2o2 (nmc622) cathode materials for li-ion batteries," *Journal of The Electrochemical Society*, vol. 165, no. 11, A2869, 2018.

[193] J.-W. Oh, S. C. Chun, and M. Chandrasekaran, "Preparation and in vitro characterization of chitosan nanoparticles and their broad-spectrum antifungal action compared to antibacterial activities against phytopathogens of tomato," *Agronomy*, vol. 9, no. 1, p. 21, 2019.

[194] I. K. D. Dimzon and T. P. Knepper, "Degree of deacetylation of chitosan by infrared spectroscopy and partial least squares," *International journal of biological macromolecules*, vol. 72, pp. 939–945, 2015.

[195] Y. Zheng, D. Huang, and A. Wang, "Chitosan-g-poly (acrylic acid) hydrogel with crosslinked polymeric networks for ni2+ recovery," *Analytica chimica acta*, vol. 687, no. 2, pp. 193–200, 2011.

[196] R. Ye, N. Hamzelui, M. Ihrig, M. Finsterbusch, and E. Figgemeier, "Water-based fabrication of a $Li|Li_7La_3Zr_2O_{12}|LiFePO_4$ solid-state battery toward green battery production," *ACS Sustainable Chemistry & Engineering*, vol. 10, no. 23, pp. 7613–7624, 2022.

[197] Y. Shigemasa, H. Matsuura, H. Sashiwa, and H. Saimoto, "Evaluation of different absorbance ratios from infrared spectroscopy for analyzing the degree of deacetylation in chitin," *International Journal of Biological Macromolecules*, vol. 18, no. 3, pp. 237–242, 1996.

[198] E. Huang, Y. Cao, X. Duan, Y. Yan, Z. Wang, and C. Jin, "Cross-linked chitosan as an eco-friendly binder for high-performance wood-based fiberboard," *International Journal of Polymer Science*, vol. 2021, pp. 1–7, 2021.

[199] M. Kuenzel, R. Porhiel, D. Bresser, *et al.*, "Deriving structure-performance relations of chemically modified chitosan binders for sustainable high-voltage lini0. 5mn1. 5o4 cathodes," *Batteries & Supercaps*, vol. 3, no. 2, pp. 155–164, 2020.

[200] H. Wu, Y. Lei, J. Lu, *et al.*, "Effect of citric acid induced crosslinking on the structure and properties of potato starch/chitosan composite films," *Food Hydrocolloids*, vol. 97, p. 105 208, 2019.

[201] X. Zhao, C.-H. Yim, N. Du, and Y. Abu-Lebdeh, "Crosslinked chitosan networks as binders for silicon/graphite composite electrodes in li-ion batteries," *Journal of The Electrochemical Society*, vol. 165, no. 5, A1110, 2018.

[202] S. Acosta-Ferreira, O. S. Castillo, J. T. Madera-Santana, *et al.*, "Production and physicochemical characterization of chitosan for the harvesting of wild microalgae consortia," *Biotechnology Reports*, vol. 28, e00554, 2020.

[203] L. Guo, D. B. Thornton, M. A. Koronfel, I. E. Stephens, and M. P. Ryan, "Degradation in lithium ion battery current collectors," *Journal of Physics: Energy*, vol. 3, no. 3, p. 032 015, 2021.

[204] P. Taheri, S. Hsieh, and M. Bahrami, "Investigating electrical contact resistance losses in lithium-ion battery assemblies for hybrid and electric vehicles," *Journal of Power Sources*, vol. 196, no. 15, pp. 6525–6533, 2011.

[205] D. Aurbach, M. Moshkovich, Y. Cohen, and A. Schechter, "The study of surface film formation on noble-metal electrodes in alkyl carbonates/li salt solutions, using simultaneous in situ afm, eqcm, ftir, and eis," *Langmuir*, vol. 15, no. 8, pp. 2947–2960, 1999.

[206] K. Tasaki and S. J. Harris, "Computational study on the solubility of lithium salts formed on lithium ion battery negative electrode in organic solvents," *The Journal of Physical Chemistry C*, vol. 114, no. 17, pp. 8076–8083, 2010.

[207] S. J. An, J. Li, C. Daniel, D. Mohanty, S. Nagpure, and D. L. Wood III, "The state of understanding of the lithium-ion-battery graphite solid electrolyte interphase (sei) and its relationship to formation cycling," *Carbon*, vol. 105, pp. 52–76, 2016.

[208] H. Shin, J. Park, S. Han, A. M. Sastry, and W. Lu, "Component-/structure-dependent elasticity of solid electrolyte interphase layer in li-ion batteries: Experimental and computational studies," *Journal of Power Sources*, vol. 277, pp. 169–179, 2015.

[209] Y. P. Stenzel, F. Horsthemke, M. Winter, and S. Nowak, "Chromatographic techniques in the research area of lithium ion batteries: Current state-of-the-art," *Separations*, vol. 6, no. 2, p. 26, 2019.

[210] G. G. Eshetu, S. Grugeon, G. Gachot, D. Mathiron, M. Armand, and S. Laruelle, "Lifsi vs. lipf6 electrolytes in contact with lithiated graphite: Comparing thermal stabilities and identification of specific sei-reinforcing additives," *Electrochimica Acta*, vol. 102, pp. 133–141, 2013.

[211] S. Yadav and S. Sahoo, "Interface study of thermally driven chemical kinetics involved in ti/si3n4 based metal-substrate assembly by x-ray photoelectron spectroscopy," *Applied Surface Science*, vol. 541, p. 148 465, 2021.

[212] A. Alam, M. Howlader, and M. Deen, "Oxygen plasma and humidity dependent surface analysis of silicon, silicon dioxide and glass for direct wafer bonding," *ECS Journal of Solid State Science and Technology*, vol. 2, no. 12, P515, 2013.

[213] S. H. Sung, D. H. Kim, S. Kim, M. H. Jeong, J. Nam, and K. H. Ahn, "Effect of neutralization of poly (acrylic acid) binder on the dispersion heterogeneity of li-ion battery electrodes," *Journal of Materials Science*, vol. 54, no. 20, pp. 13 208–13 220, 2019.

[214] C. Leygraf, T. E. Graedel, J. Tidblad, and I. O. Wallinder, *Atmospheric corrosion*. Wiley-interscience New York, 2000, vol. 40.

[215] H. Gil and C. Leygraf, "Initial atmospheric corrosion of copper induced by carboxylic acids: A comparative in situ study," *Journal of The Electrochemical Society*, vol. 154, no. 11, p. C611, 2007.

[216] D. Mazouzi, R. Grissa, M. Paris, *et al.*, "Cmc-citric acid cu (ii) cross-linked binder approach to improve the electrochemical performance of si-based electrodes," *Electrochimica Acta*, vol. 304, pp. 495–504, 2019.

[217] B. Beverskog and I. Puigdomenech, "Revised pourbaix diagrams for copper at 25 to 300 c," *Journal of The Electrochemical Society*, vol. 144, no. 10, p. 3476, 1997.

[218] Y. Gotoh, R. Igarashi, Y. Ohkoshi, M. Nagura, K. Akamatsu, and S. Deki, "Preparation and structure of copper nanoparticle/poly (acrylic acid) composite films," *Journal of Materials Chemistry*, vol. 10, no. 11, pp. 2548–2552, 2000.

[219] I. McNeill and S. Sadeghi, "Thermal stability and degradation mechanisms of poly (acrylic acid) and its salts: Part 1—poly (acrylic acid)," *Polymer degradation and stability*, vol. 29, no. 2, pp. 233–246, 1990.

[220] ——, "Thermal stability and degradation mechanisms of poly (acrylic acid) and its salts: Part 2—sodium and potassium salts," *Polymer degradation and stability*, vol. 30, no. 2, pp. 213–230, 1990.

[221] J. Xiong, N. Dupré, D. Mazouzi, D. Guyomard, L. Roué, and B. Lestriez, "Influence of the polyacrylic acid binder neutralization degree on the initial electrochemical behavior of a silicon/graphite electrode," *ACS Applied Materials & Interfaces*, vol. 13, no. 24, pp. 28 304–28 323, 2021.

[222] B. Hu, S. Jiang, I. A. Shkrob, *et al.*, "Understanding of pre-lithiation of poly (acrylic acid) binder: Striking the balances between the cycling performance and slurry stability for silicon-graphite composite electrodes in li-ion batteries," *Journal of Power Sources*, vol. 416, pp. 125–131, 2019.

[223] N. Yabuuchi, K. Shimomura, Y. Shimbe, *et al.*, "Graphite-silicon-polyacrylate negative electrodes in ionic liquid electrolyte for safer rechargeable li-ion batteries," *Advanced Energy Materials*, vol. 1, no. 5, pp. 759–765, 2011.

[224] D. Dollimore and R. Karimian, "The thermal decomposition of gum tragacanth in nitrogen," *Thermochimica Acta*, vol. 51, no. 2-3, pp. 353–361, 1981.

[225] A. Salisu, M. M. Sanagi, A. Abu Naim, K. J. Abd Karim, W. A. Wan Ibrahim, and U. Abdulganiyu, "Alginate graft polyacrylonitrile beads for the removal of lead from aqueous solutions," *Polymer Bulletin*, vol. 73, pp. 519–537, 2016.

[226] C. Zhang, X. Yang, Y. Li, *et al.*, "Multifunctional hybrid composite films based on biodegradable cellulose nanofibers, aloe juice, and carboxymethyl cellulose," *Cellulose*, vol. 28, pp. 4927–4941, 2021.

[227] V. K. Gupta, S. Sood, S. Agarwal, A. K. Saini, and D. Pathania, "Antioxidant activity and controlled drug delivery potential of tragacanth gum-cl-poly (lactic acid-co-itaconic acid) hydrogel," *International journal of biological macromolecules*, vol. 107, pp. 2534–2543, 2018.

[228] I. Nowrouzi, A. K. Manshad, and A. H. Mohammadi, "Effects of tragacanth gum as a natural polymeric surfactant and soluble ions on chemical smart water injection into oil reservoirs," *Journal of Molecular Structure*, vol. 1200, p. 127 078, 2020.

[229] M. Rozali, N. Ahmad, and M. Isa, "Effect of adipic acid composition on structural and conductivity solid biopolymer electrolytes based on carboxy methylcellulose studies," *American-Eurasian Journal of Sustainable Agriculture*, 2015.

[230] A. Rhimi, K. Zlaoui, K. Horchani-Naifer, and D. J. Ennigrou, "Characterization and extraction of sodium alginate from tunisian algae: Synthesizing a cross-linked ultrafiltration membrane," *Iranian Polymer Journal*, vol. 31, no. 3, pp. 367–382, 2022.

[231] H. H. Ammar, S. Lajili, N. Sakly, *et al.*, "Influence of the uronic acid composition on the gastroprotective activity of alginates from three different genus of tunisian brown algae," *Food chemistry*, vol. 239, pp. 165–171, 2018.

[232] H. Liu, B. Pan, Q. Wang, *et al.*, "Crucial roles of graphene oxide in preparing alginate/nanofibrillated cellulose double network composites hydrogels," *Chemosphere*, vol. 263, p. 128 240, 2021.

[233] D. Leal, B. Matsuhiro, M. Rossi, and F. Caruso, "Ft-ir spectra of alginic acid block fractions in three species of brown seaweeds," *Carbohydrate research*, vol. 343, no. 2, pp. 308–316, 2008.

[234] L. Rao, X. Jiao, C.-Y. Yu, *et al.*, "Multifunctional composite binder for thick high-voltage cathodes in lithium-ion batteries," *ACS Applied Materials & Interfaces*, vol. 14, no. 1, pp. 861–872, 2021.

Curriculum Vitae

Niloofar Hamzelui

Education

16.12.2024	**Doctoral Examination for Dr. rer. nat.** RWTH Aachen University, Germany
2018–2024	**ISEA, RWTH Aachen University, Germany** Research Assistant and Doctoral Candidate
2016–2017	**IEK-5, Forschungszentrum Jülich, Germany** Student Assistant
2014–2017	**RWTH Aachen University, Germany** Master of Science, Metallurgical Engineering
2010–2014	**Sharif University of Technology, Iran** Bachelor of Science, Materials Science and Engineering
2006–2010	**Manzoumeh Kherad Institute, Iran** High School and University Entrance Qualification
1992	**Born in Tehran, Iran**

List of Publications

Within the frame of this work, several publications have been prepared, which are listed below. Content from these publications is used for this thesis. This is in line with the rules for dissertation of the faculty for Electrical Engineering and Information Technology of the RWTH Aachen University and has been agreed with Prof. Egbert Figgemeier, the supervisor of this thesis. Text elements, graphs, pictures, or tables from these publications are not explicitly cited within the thesis, as far as they are mainly created by the author of this work. If such elements in the listed publications are mainly created by the co-authors, a direct link to the publication is given.

Journal Articles

1. N. Hamzelui, M. Linhorst, G. Martin Nyenhuis, L. Haneke, G. G. Eshetu, T. Placke, M. Winter, B. M. Moerschbacher, and E. Figgemeier, "Chitosan as enabling polymeric binder material for silicon-graphite-based anodes in lithium-ion batteries," *Energy Technology*, vol. 11, p. 2 201 239, 2023
2. N. Hamzelui, L.-C. Kin, J. Köhler, O. Astakhov, Z. Liu, T. Kirchartz, U. Rau, G. G. Eshetu, T. Merdzhanova, and E. Figgemeier, "Toward the integration of a silicon/graphite anode-based lithium-ion battery in photovoltaic charging battery systems," *ACS omega*, vol. 7, no. 31, pp. 27 532–27 541, 2022
3. N. Hamzelui, G. G. Eshetu, and E. Figgemeier, "Customizing active materials and polymeric binders: Stern requirements to realize silicon-graphite anode based lithium-ion batteries.," *Journal of Energy Storage*, vol. 35, p. 102 098, 2021
4. R. Ye, N. Hamzelui, M. Ihrig, M. Finsterbusch, and E. Figgemeier, "Water-based fabrication of a Li|$Li_7La_3Zr_2O_{12}$|$LiFePO_4$ solid-state battery toward green battery production," *ACS Sustainable Chemistry & Engineering*, vol. 10, no. 23, pp. 7613–7624, 2022

Conferences

1. N. Hamzelui, L. Kin, J. Köhler, O. Astakhov, Z. Liu, T. Kirchartz, U. Rau, G. G. Eshetu, T.Merdzhanova, E. Figgemeier, "Toward the Integration of a Silicon-Graphite

Anode-Based Lithium-ion Battery in Photovoltaic Charging Battery Systems", Advanced Battery Power Conference, Münster, Germany, 2022

2. N. Hamzelui, G. G. Eshetu, M. Linhorst, B. M. Moerschbacher, E. Figgemeier, "Optimization of Silicon-Graphite Anode and Chitosan Binder Material for Lithium-ion Batteries", Advanced Battery Power Conference, 2021, (Awarded poster prize)
3. N. Hamzelui, G. G. Eshetu, V. Adlfar, M. Hippler, E. Figgemeier, "Optimized Silicon- Graphite and Polymeric Binders for Silicon-Anode based Lithium ion Batteries", The Electrochemical Conference on Energy and the Environment: Bioelectrochemistry and Energy Storage (ECEE 2019), Glasgow, Scotland, 2019

ABISEA Band 1
Eßer, Albert
Berührungslose, kombinierte Energie- und Informationsübertragung für bewegliche Systeme
1. Aufl. 1992, 129 S.
ISBN 3-86073-046-0

ABISEA Band 2
Vogel, Ulrich
Entwurf und Beurteilung von Verfahren zur Hochausnutzung des Rad-Schiene-Kraftschlusses durch Triebfahrzeuge
1. Aufl. 1992, 131 S.
ISBN 3-86073-060-6

ABISEA Band 3
Reckhorn, Thomas
Stromeinprägendes Antriebssystem mit fremderregter Synchronmaschine
1. Aufl. 1992, 128 S.
ISBN 3-86073-061-4

ABISEA Band 4
Ackva, Ansgar
Spannungseinprägendes Antriebssystem mit Synchronmaschine und direkter Stromregelung
1. Aufl. 1992, 137 S.
ISBN 3-86073-062-2

ABISEA Band 5
Mertens, Axel
Analyse des Oberschwingungsverhaltens von taktsynchronen Delta - Modulationsverfahren zur Steuerung von Pulsstromrichtern bei hoher Taktzahl
1. Aufl. 1992, 178 S.
ISBN 3-86073-069-X

ABISEA Band 6
Geuer, Wolfgang
Untersuchungen über das Alterungsverhalten von Blei-Akkumulatoren
1. Aufl. 1993, 97 S.
ISBN 3-86073-097-5

ABISEA Band 7
Langheim, Jochen
Einzelradantrieb für Elektrostraßenfahrzeuge
1. Aufl. 1993, 213 S.
ISBN 3-86073-123-8
(vergriffen)

ABISEA Band 8
Fetz, Joachim
Fehlertolerante Regelung eines Asynchron-Doppelantriebes für ein Elektrospeicherfahrzeug
1. Aufl. 1993, 136 S.
ISBN 3-86073-124-6
(vergriffen)

ABISEA Band 9
Schülting, Ludger
Optimierte Auslegung induktiver Bauelemente für den Mittelfrequenzbereich
1. Aufl. 1993, 126 S.
ISBN 3-86073-174-2
(vergriffen)

ABISEA Band 10
Skudelny, H.-Ch.
Stromrichtertechnik
4. Aufl. 1997, 259 S.
ISBN 3-86073-189-0

ABISEA Band 11
Skudelny, H.-Ch.
Elektrische Antriebe
3. Aufl. 1997, 124 S.
ISBN 3-86073-231-5

ABISEA Band 12
Schöpe, Friedhelm
Batterie-Management für Nickel-Cadmium Akkumulatoren
1. Aufl. 1994, 148 S.
ISBN 3-86073-232-3
(vergriffen)

ABISEA Band 13
v. d. Weem, Jürgen
Schmalbandige aktive Filter für Schienentriebfahrzeuge am Gleichspannungsfahrdraht
1. Aufl. 1995, 126 S.
ISBN 3-86073-233-1

ABISEA Band 14
Backhaus, Klaus
Spannungseinprägendes Direktantriebssystem mit schnelllaufender geschalteter Reluktanzmaschine
1. Aufl. 1995, 146 S.
ISBN 3-86073-234-X
(vergriffen)

ABISEA Band 15
Reinold, Harry
Optimierung dreiphasiger Pulsdauermodulationsverfahren
1. Aufl. 1996, 107 S.
ISBN 3-86073-235-8

ABISEA Band 16
Köpken, Hans-Georg
Regelverfahren für Parallelschwingkreisumrichter
1. Aufl. 1996, 125 S.
ISBN 3-86073-236-6

ABISEA Band 17
Mauracher, Peter
Modellbildung und Verbundoptimierung bei Elektrostraßenfahrzeugen
1. Aufl. 1996, 192 S.
ISBN 3-86073-237-4

ABISEA Band 18
Protiwa, Franz-Ferdinand
Vergleich dreiphasiger Resonanz-Wechselrichter in Simulation und Messung
1. Aufl. 1997, 178 S.
ISBN 3-86073-238-2

ABISEA Band 19
Brockmeyer, Ansgar
Dimensionierungswerkzeug für magnetische Bauelemente in Stromrichteranwendungen
1. Aufl. 1997, 175 S.
ISBN 3-86073-239-0

Aachener Beiträge des ISEA

ABISEA Band 20
Apeldoorn, Oscar
Simulationsgestützte Bewertung von Steuerverfahren für netzgeführte Stromrichter mit verringerter Netzrückwirkung
1. Aufl. 1997, 134 S.
ISBN 3-86073-680-9

ABISEA Band 21
Lohner, Andreas
Batteriemanagement für verschlossene Blei-Batterien am Beispiel von Unterbrechungsfreien Stromversorgungen
1. Aufl. 1998, 126 S.
ISBN 3-86073-681-7

ABISEA Band 22
Reinert, Jürgen
Optimierung der Betriebseigenschaften von Antrieben mit geschalteter Reluktanzmaschine
1. Aufl. 1998, 153 S.
ISBN 3-86073-682-5

ABISEA Band 23
Nagel, Andreas
Leitungsgebundene Störungen in der Leistungselektronik: Entstehung, Ausbreitung und Filterung
1. Aufl. 1999, 140 S.
ISBN 3-86073-683-3

ABISEA Band 24
Menne, Marcus
Drehschwingungen im Antriebsstrang von Elektrostraßenfahrzeugen - Analyse und aktive Dämpfung
1. Aufl. 2001, 169 S.
ISBN 3-86073-684-1

ABISEA Band 25
von Bloh, Jochen
Multilevel-Umrichter zum Einsatz in Mittelspannungs-Gleichspannungs-Übertragungen
1. Aufl. 2001, 137 S.
ISBN 3-86073-685-X

ABISEA Band 26
Karden, Eckhard
Using low-frequency impedance spectroscopy for characterization, monitoring, and modeling of industrial batteries
1. Aufl. 2002, 137 S.
ISBN 3-8265-9766-4

ABISEA Band 27
Karipidis, Claus-Ulrich
A Versatile DSP/ FPGA Structure optimized for Rapid Prototyping and Digital Real-Time Simulation of Power Electronic and Electrical Drive Systems
1. Aufl. 2001, 164 S.
ISBN 3-8265-9738-9

ABISEA Band 28
Kahlen, Klemens
Regelungsstrategien für permanentmagnetische Direktantriebe mit mehreren Freiheitsgraden
1. Aufl. 2002, 154 S.
ISBN 3-8322-1222-1

ABISEA Band 29
Inderka, Robert B.
Direkte Drehmomentregelung Geschalteter Reluktanzantriebe
1. Aufl. 2003, 182 S.
ISBN 3-8322-1175-6

ABISEA Band 30
Schröder, Stefan
Circuit-Simulation Models of High-Power Devices Based on Semiconductor Physics
1. Aufl. 2003, 123 S.
ISBN 3-8322-1250-7

ABISEA Band 31
Buller, Stephan
Impedance-Based Simulation Models for Energy Storage Devices in Advanced Automotive Power Systems
1. Aufl. 2003, 138 S.
ISBN 3-8322-1225-6

ABISEA Band 32
Schönknecht, Andreas
Topologien und Regelungsstrategien für das induktive Erwärmen mit hohen Frequenz-Leistungsprodukten
1. Aufl. 2004, 157 S.
ISBN 3-8322-2408-4

ABISEA Band 33
Tolle, Tobias
Konvertertopologien für ein aufwandsarmes, zweistufiges Schaltnetzteil zum Laden von Batterien aus dem Netz
1. Aufl. 2004, 148 S.
ISBN 3-8322-2676-1

ABISEA Band 34
Götting, Gunther
Dynamische Antriebsregelung von Elektrostraßenfahrzeugen unter Berücksichtigung eines schwingungsfähigen Antriebsstrangs
1. Aufl. 2004, 157 S.
ISBN 3-8322-2804-7

ABISEA Band 35
Dieckerhoff, Sibylle
Transformatorlose Stromrichterschaltungen für Bahnfahrzeuge am 16 2/3Hz Netz
1. Aufl. 2004, 147 S.
ISBN 3-8322-3094-7

ABISEA Band 36
Hu, Jing
Bewertung von DC-DC-Topologien und Optimierung eines DC-DC-Leistungsmoduls für das 42-V-Kfz-Bordnetz
1. Aufl. 2004, 148 S.
ISBN 3-8322-3201-X

ABISEA Band 37
Detjen, Dirk-Oliver
Characterization and Modeling of Si-Si Bonded Hydrophobie Interfaces for Novel High-Power BIMOS Devices
1. Aufl. 2004, 135 S.
ISBN 3-8322-2963-9

ABISEA Band 38
Walter, Jörg
Simulationsbasierte Zuverlässigkeitsanalyse in der modernen Leistungselektronik
1. Aufl. 2004, 121 S.
ISBN 3-8322-3481-0

ABISEA Band 39
Schwarzer, Ulrich
IGBT versus GCT in der Mittelspannungsanwendung - ein experimenteller und simulativer Vergleich
1. Aufl. 2005, 170 S.
ISBN 3-8322-4489-1

ABISEA Band 40
Bartram, Markus
IGBT-Umrichtersysteme für Windkraftanlagen: Analyse der Zyklenbelastung, Modellbildung, Optimierung und Lebensdauervorhersage
1. Aufl. 2006, 185 S.
ISBN 3-8322-5039-5

ABISEA Band 41
Ponnaluri, Srinivas
Generalized Design, Analysis and Control of Grid side converters with integrated UPS or Islanding functionality
1. Aufl. 2006, 163 S.
ISBN 3-8322-5281-9

ABISEA Band 42
Jacobs, Joseph
Multi-Phase Series Resonant DC-to-DC Converters
1. Aufl. 2006, 185 S.
ISBN 3-8322-5532-X

ABISEA Band 43
Linzen, Dirk
Impedance-Based Loss Calculation and Thermal Modeling of Electrochemical Energy Storage Devices for Design Considerations of Automotive Power Systems
1. Aufl. 2006, 185 S.
ISBN 3-8322-5706-3

ABISEA Band 44
Fiedler, Jens
Design of Low-Noise Switched Reluctance Drives
1. Aufl. 2007, 176 S.
ISBN 978-3-8322-5864-1

ABISEA Band 45
Fuengwarodsakul, Nisai
Predictive PWM-based Direct Instantaneous Torque Control for Switched Reluctance Machines
1. Aufl. 2007, 141 S.
ISBN 978-3-8322-6210-5

ABISEA Band 46
Meyer, Christoph
Key Components for Future Offshore DC Grids
1. Aufl. 2007, 187 S.
ISBN 978-3-8322-6571-7

ABISEA Band 47
Fujii, Kansuke
Characterization and Optimization of Soft-Switched Multi-Level Converters for STATCOMs
1. Aufl. 2008, 199 S.
ISBN 978-3-8322-6981-4

ABISEA Band 48
Carstensen, Christian
Eddy Currents in Windings of Switched Reluctance Machines
1. Aufl. 2008, 179 S.
ISBN 978-3-8322-7118-3

ABISEA Band 49
Bohlen, Oliver
Impedance-based battery monitoring
1. Aufl. 2008, 190 S.
ISBN 978-3-8322-7606-5

ABISEA Band 50
Thele, Marc
A contribution to the modelling of the charge acceptance of lead-acid batteries - using frequency and time domain based concepts
1. Aufl. 2008, 165 S.
ISBN 978-3-8322-7659-1

ABISEA Band 51
König, Andreas
High Temperature DC-to-DC Converters for Downhole Applications
1. Aufl. 2009, 154 S.
ISBN 978-3-8322-8489-3

ABISEA Band 52
Dick, Christian Peter
Multi-Resonant Converters as Photovoltaic Module-Integrated Maximum Power Point Tracker
1. Aufl. 2010, 182 S.
ISBN 978-3-8322-9199-0

ABISEA Band 53
Kowal, Julia
Spatially resolved impedance of nonlinear inhomogeneous devices: using the example of lead-acid batteries
1. Aufl. 2010, 203 S.
ISBN 978-3-8322-9483-0

ABISEA Band 54
Roscher, Michael Andreas
Zustandserkennung von LiFeP04-Batterien für Hybrid- und Elektrofahrzeuge
1. Aufl. 2011, 186 S.
ISBN 978-3-8322-9738-1

ABISEA Band 55
Hirschmann, Dirk
Highly Dynamic Piezoelectric Positioning
1. Aufl. 2011, 146 S.
ISBN 978-3-8322-9746-6

ABISEA Band 56
Rigbers, Klaus
Highly Efficient Inverter Architectures for Three-Phase Grid Connection of Photovoltaic Generators
1. Aufl. 2011, 244 S.
ISBN 978-3-8322-9816-9

ABISEA Band 57
Kasper, Knut
Analysis and Control of the Acoustic Behavior of Switched Reluctance Drives
1. Aufl. 2011, 205 S.
ISBN 978-3-8322-9869-2

Aachener Beiträge des ISEA

ABISEA Band 58
Köllensperger, Peter
The Internally Commutated Thyristor - Concept, Design and Application
1. Aufl. 2011, 214 S.
ISBN 978-3-8322-9909-5

ABISEA Band 59
Schoenen, Timo
Einsatz eines DC/DC-Wandlers zur Spannungsanpassung zwischen Antrieb und Energiespeicher in Elektro-und Hybridfahrzeugen
1. Aufl. 2011, 128 S.
ISBN 978-3-8440-0622-3

ABISEA Band 60
Hennen, Martin
Switched Reluctance Direct Drive with Integrated Distributed Inverter
1. Aufl. 2012, 141 S.
ISBN 978-3-8440-0731-2

ABISEA Band 61
van Treek, Daniel
Position Sensorless Torque Control of Switched Reluctance Machines
1. Aufl. 2012, 144 S.
ISBN 978-3-8440-1014-5

ABISEA Band 62
Bragard, Michael
The Integrated Emitter Turn-Off Thyristor. An Innovative MOS-Gated High-Power Device
1. Aufl. 2012, 164 S.
ISBN 978-3-8440-1152-4

ABISEA Band 63
Gerschler, Jochen B.
Ortsaufgelöste Modellbildung von Lithium-Ionen-Systemen unter spezieller Berücksichtigung der Batteriealterung
1. Aufl. 2012, 334 S.
ISBN 978-3-8440-1307-8

ABISEA Band 64
Neuhaus, Christoph R.
Schaltstrategien für Geschaltete Reluktanzantriebe mit kleinem Zwischenkreis
1. Aufl. 2012, 133 S.
ISBN 978-3-8440-1487-7

ABISEA Band 65
Butschen, Thomas
Dual-ICT- A Clever Way to Unite Conduction and Switching Optimized Properties in a Single Wafer
1. Aufl. 2012, 168 S.
ISBN 978-3-8440-1771-7

ABISEA Band 66
Plum, Thomas
Design and Realization of High-Power MOS Turn-Off Thyristors
1. Aufl. 2013, 113 S.
ISBN 978-3-8440-1884-4

ABISEA Band 67
Kiel, Martin
Impedanzspektroskopie an Batterien unter besonderer Berücksichtigung von Batteriesensoren für den Feldeinsatz
1. Aufl. 2013, 226 S.
ISBN 978-3-8440-1973-5

ABISEA Band 68
Brauer, Helge
Schnelldrehender Geschalteter Reluktanzantrieb mit extremem Längendurchmesserverhältnis
1. Aufl. 2013, 192 S.
ISBN 978-3-8440-2345-9

ABISEA Band 69
Thomas, Stephan
A Medium-Voltage Multi-Level DC/DC Converter with High Voltage Transformation Ratio
1. Aufl. 2014, 226 S.
ISBN 978-3-8440-2605-4

ABISEA Band 70
Richter, Sebastian
Digitale Regelung von PWM Wechselrichtern mit niedrigen Trägerfrequenzen
1. Aufl. 2014, 126 S.
ISBN 978-3-8440-2641-2

ABISEA Band 71
Bösing, Matthias
Acoustic Modeling of Electrical Drives - Noise and Vibration Synthesis based on Force Response Superposition
1. Aufl. 2014, 188 S.
ISBN 978-3-8440-2752-5

ABISEA Band 72
Waag, Wladislaw
Adaptive algorithms for monitoring of lithium-ion batteries in electric vehicles
1. Aufl. 2014, 232 S.
ISBN 978-3-8440-2976-5

ABISEA Band 73
Sanders, Tilman
Spatially Resolved Electrical In-Situ Measurement Techniques for Fuel Cells
1. Aufl. 2014, 126 S.
ISBN 978-3-8440-3121-8

ABISEA Band 74
Baumhöfer, Thorsten
Statistische Betrachtung experimenteller Alterungsuntersuchungen an Lithium-Ionen Batterien
1. Aufl. 2015, 157 S.
ISBN 978-3-8440-3423-3

ABISEA Band 75
Andre, Dave
Systematic Characterization of Ageing Factors for High-Energy Lithium-Ion Cells and Approaches for Lifetime Modelling Regarding an Optimized Operating Strategy in Automotive Applications
1. Aufl. 2015, 196 S.
ISBN 978-3-8440-3587-2

ABISEA Band 76
Merei, Ghada
Optimization of off-grid hybrid PV-wind-diesel power supplies with multi-technology battery systems taking into account battery aging
1. Aufl. 2015, 184 S.
ISBN 978-3-8440-4148-4

ABISEA Band 77
Schulte, Dominik
Modellierung und experimentelle Validierung der Alterung von Blei-Säure Batterien durch inhomogene Stromverteilung und Säureschichtung
1. Aufl. 2016, 165 S.
ISBN 978-3-8440-4216-0

ABISEA Band 78
Schenk, Mareike
Simulative Untersuchung der Wicklungsverluste in Geschalteten Reluktanzmaschinen
1. Aufl. 2016, 126 S.
ISBN 978-3-8440-4282-5

ABISEA Band 79
Wang, Yu
Development of Dynamic Models with Spatial Resolution for Electrochemical Energy Converters as Basis for Control and Management Strategies
1. Aufl. 2016, 188 S.
ISBN 978-3-8440-4303-7

ABISEA Band 80
Ecker, Madeleine
Lithium Plating in Lithium-Ion Batteries:
An Experimental and Simulation Approach
1. Aufl. 2016, 154 S.
ISBN 978-3-8440-4525-3

ABISEA Band 81
Zhou, Wei
Modellbasierte Auslegungsmethode von Temperierungssystemen für Hochvolt-Batterien in Personenkraftfahrzeugen
1. Aufl. 2016, 175 S.
ISBN 978-3-8440-4589-5

ABISEA Band 82
Lunz, Benedikt
Deutschlands Stromversorgung im Jahr 2050
Ein szenariobasiertes Verfahren zur vergleichenden Bewertung von Systemvarianten und Flexibilitätsoptionen
1. Aufl. 2016, 187 S.
ISBN 978-3-8440-4627-4

ABISEA Band 83
Hofmann, Andreas G.
Direct Instantaneous Force Control: Key to Low-Noise Switched Reluctance Traction Drives
1. Aufl. 2016, 228 S.
ISBN 978-3-8440-4715-8

ABISEA Band 84
Budde-Meiwes, Heide
Dynamic Charge Acceptance of Lead-Acid Batteries for Micro-Hybrid Automotive Applications
1. Aufl. 2016, 157 S.
ISBN 978-3-8440-4733-2

ABISEA Band 85
Engel, Stefan P.
Thyristor-Based High-Power On-Load Tap Changers Control under Harsh Load Conditions
1. Aufl. 2016, 156 S.
ISBN 978-3-8440-4986-2

ABISEA Band 86
Van Hoek, Hauke
Design and Operation Considerations of Three-Phase Dual Active Bridge Converters for Low-Power Applications with Wide Voltage Ranges
1. Aufl. 2017, 231 S.
ISBN 978-3-8440-5011-0

ABISEA Band 87
Diekhans, Tobias
Wireless Charging of Electric Vehicles - a Pareto-Based Comparison of Power Electronic Topologies
1. Aufl. 2017, 151 S.
ISBN 978-3-8440-5048-6

ABISEA Band 88
Lehner, Susanne
Reliability Assessment of Lithium-Ion Battery Systems with Special Emphasis on Cell Performance Distribution
1. Aufl. 2017, 184 S.
ISBN 978-3-8440-5090-5

ABISEA Band 89
Käbitz, Stefan
Untersuchung der Alterung von Lithium-Ionen-Batterien mittels Elektroanalytik und elektrochemischer Impedanzspektroskopie
1. Aufl. 2016, 258 S.
DOI: 10.18154/RWTH-2016-12094

ABISEA Band 90
Witzenhausen, Heiko
Elektrische Batteriespeichermodelle: Modellbildung, Parameteridentifikation und Modellreduktion
1. Aufl. 2017, 266 S.
DOI: 10.18154/RWTH-2017-03437

ABISEA Band 91
Münnix, Jens
Einfluss von Stromstärke und Zyklentiefe auf graphitische Anoden
1. Aufl. 2017, 171 S.
DOI: 10.18154/RWTH-2017-01915

ABISEA Band 92
Pilatowicz, Grzegorz
Failure Detection and Battery Management Systems of Lead-Acid Batteries for Micro-Hybrid Vehicles
1. Aufl. 2017, 212 S.
DOI: 10.18154/RWTH-2017-09156

ABISEA Band 93
Drillkens, Julia
Aging in Electrochemical Double Layer Capacitors:
An Experimental and Modeling Approach
1. Aufl. 2017, 179 S.
DOI: 10.18154/RWTH-2018-223434

Aachener Beiträge des ISEA

ABISEA Band 94
Magnor, Dirk
Globale Optimierung netzgekoppelter PV-Batteriesysteme unter besonderer Berücksichtigung der Batteriealterung
1. Aufl. 2017, 210 S.
DOI: 10.18154/RWTH-2017-06592

ABISEA Band 95
Iliksu, Merve
Elucidation and Comparison of the Effects of Lithium Salts on Discharge Chemistry of Nonaqueous Li-O_2 Batteries
1. Aufl. 2018, 160 S.
DOI: 10.18154/RWTH-2018-223782

ABISEA Band 96
Schmalstieg, Johannes
Physikalisch-elektrochemische Simulation von Lithium-Ionen-Batterien: Implementierung, Parametrierung und Anwendung
1. Aufl. 2017, 168 S.
DOI: 10.18154/RWTH-2017-04693

ABISEA Band 97
Soltau, Nils
High-Power Medium-Voltage DC-DC Converters: Design, Control and Demonstration
1. Aufl. 2017, 176 S.
DOI: 10.18154/RWTH-2017-04084

ABISEA Band 98
Stieneker, Marco
Analysis of Medium-Voltage Direct-Current Collector Grids in Offshore Wind Parks
1. Aufl. 2017, 144 S.
DOI: 10.18154/RWTH-2017-04667

ABISEA Band 99
Masomtob, Manop
A New Conceptual Design of Battery Cell with an Internal Cooling Channel
1. Aufl. 2017, 167 S.
DOI: 10.18154/RWTH-2018-223281

ABISEA Band 100
Marongiu, Andrea
Performance and Aging Diagnostic on Lithium Iron Phosphate Batteries for Electric Vehicles and Vehicle-to-Grid Strategies
1. Aufl. 2017, 222 S.
DOI: 10.18154/RWTH-2017-09944

ABISEA Band 101
Gitis, Alexander
Flaw detection in the coating process of lithium-ion battery electrodes with acoustic guided waves
1. Aufl. 2017, 109 S.
DOI: 10.18154/RWTH-2017-099519

ABISEA Band 102
Neeb, Christoph
Packaging Technologies for Power Electronics in Automotive Applications
1. Aufl. 2017, 132 S.
DOI: 10.18154/RWTH-2018-224569

ABISEA Band 103
Adler, Felix
A Digital Hardware Platform for Distributed Real-Time Simulation of Power Electronic Systems
1. Aufl. 2017, 156 S.
DOI: 10.18154/RWTH-2017-10761

ABISEA Band 104
Becker, Jan
Flexible Dimensionierung und Optimierung hybrider Lithium-Ionenbatterie-speichersysteme mit verschiedenen Auslegungs-zielen
1. Aufl., 2017, 157 S.
DOI: 10.18154/RWTH-2017-09278

ABISEA Band 105
Warnecke, Alexander J.
Degradation Mechanisms in NMC Based Lithium-Ion Batteries
1. Aufl. 2017, 158 S.
DOI: 10.18154/RWTH-2017-09646

ABISEA Band 106
Taraborrelli, Silvano
Bidirectional Dual Active Bridge Converter using a Tap Changer for Extended Voltage Ranges
1. Aufl. 2017, 94 S.
DOI: 10.18154/RWTH-2018-228242

ABISEA Band 107
Sarriegi, Garikoitz
SiC and GaN Semiconductors: The Future Enablers of Compact and Efficient Converters for Electromobility
1. Aufl. 2017, 106 S.
DOI: 10.18154/RWTH-2018-227548

ABISEA Band 108
Senol, Murat
Drivetrain Integrated Dc-Dc Converters utilizing Zero Sequence Currents
1. Aufl. 2017, 134 S.
DOI: 10.18154/RWTH-2018-226170

ABISEA Band 109
Kojima, Tetsuya
Efficiency Optimized Control of Switched Reluctance Machines
1. Aufl. 2017, 142 S.
DOI: 10.18154/RWTH-2018-226697

ABISEA Band 110
Lewerenz, Meinert
Dissection and Quantitative Description of Aging of Lithium-Ion Batteries Using Non-Destructive Methods Validated by Post-Mortem-Analyses
1. Aufl. 2018, 139 S.
DOI: 10.18154/RWTH-2018-228663

ABISEA Band 111
Büngeler, Johannes
Optimierung der Verfügbarkeit und der Lebensdauer von Traktionsbatterien für den Einsatz in Flurförderfahrzeugen
1. Aufl. 2018, 171 S.
DOI: 10.18154/RWTH-2018-226569

ABISEA Band 112
Wegmann, Raphael
Betriebsstrategien und Potentialbewertung hybrider Batteriespeichersysteme in Elektrofahrzeugen
1. Auflage 2018, 184 S.
DOI: 10.18154/RWTH-2018-228833

ABISEA Band 113
Nordmann, Hannes
Batteriemanagementsysteme unter besonderer Berücksichtigung von Fehlererkennung und Peripherieanalyse
1. Aufl. 2018, 222 S.
DOI: 10.18154/RWTH-2018-228763

ABISEA Band 114
Engelmann, Georges
Reducing Device Stress and Switching Losses Using Active Gate Drivers and Improved Switching Cell Design
1. Aufl. 2018, 195 S.
DOI: 10.18154/RWTH-2018-228973

ABISEA Band 115
Klein-Heßling, Annegret
Active DC-Power Filters for Switched Reluctance Drives during Single-Pulse Operation
1. Aufl. 2018, 166 S.
DOI: 10.18154/RWTH-2018-231030

ABISEA Band 116
Burkhart, Bernhard
Switched Reluctance Generator for Range Extender Applications - Design, Control and Evaluation
1. Aufl. 2018, 194 S.
DOI: 10.18154/RWTH-2019-00025

ABISEA Band 117
Biskoping, Matthias
Discrete Modeling and Control of a versatile Power Electronic Test Bench with Special Focus on Central Photovoltaic Inverter Testing
1. Aufl. 2018, 236 S.
DOI: 10.18154/RWTH-2019-03346

ABISEA Band 118
Schubert, Michael
High-Precision Torque Control of Inverter-Fed Induction Machines with Instantaneous Phase Voltage Sensing
1. Aufl. 2019, 221 S.
DOI: 10.18154/RWTH-2018-231364

ABISEA Band 119
Van der Broeck, Christoph
Methodology for Thermal Modeling, Monitoring and Control of Power Electronic Modules
1. Aufl. 2019, 290 S.
DOI: 10.18154/RWTH-2019-01370

ABISEA Band 120
Hust, Friedrich Emanuel
Physico-chemically motivated parameterization and modelling of real-time capable lithium-ion battery models – a case study on the Tesla Model S battery
1. Aufl. 2019, 203 S.
DOI: 10.18154/RWTH-2019-00249

ABISEA Band 121
Ralev, Iliya
Accurate Torque Control of Position Sensorless Switched Reluctance Drives
1. Aufl. 2019, 154 S.
DOI: 10.18154/RWTH-2019-03071

ABISEA Band 122
Ayeng'o, Sarah Paul
Optimization of number of PV cells connected in series for a direct-coupled PV system with lead-acid and lithium-ion batteries
1. Aufl. 2019, 114 S.
DOI: 10.18154/RWTH-2019-01843

ABISEA Band 123
Koschik, Stefan Andreas
Permanenterregte Synchronmaschinen mit verteilter Einzelzahnsteuerung - Regelkonzepte und Betriebsstrategien für hochintegrierte Antriebssysteme
1. Aufl. 2019, 158 S.
DOI: 10.18154/RWTH-2019-03446

ABISEA Band 124
Farmann, Alexander
A comparative study of reduced-order equivalent circuit models for state-of-available-power prediction of lithium-ion batteries in electric vehicles
1. Aufl. 2019, 214 S.
DOI: 10.18154/RWTH-2019-04700

ABISEA Band 125
Mareev, Ivan
Analyse und Bewertung von batteriegetriebenen, oberleitungsversorgten und brennstoffzellengetriebenen Lastkraftwagen für den Einsatz im Güterfernverkehr in Deutschland
1. Aufl. 2019, 158 S.
DOI: 10.18154/RWTH-2019-04698

ABISEA Band 126
Qi, Fang
Online Model-predictive Thermal Management of Inverter-fed Electrical Machines
1. Aufl. 2019, 154 S.
DOI: 10.18154/RWTH-2019-08304

ABISEA Band 127
Kairies, Kai-Philipp
Auswirkungen dezentraler Solarstromspeicher auf Netzbetreiber und Energieversorger
1. Aufl. 2019, 140 S.
DOI: 10.18154/RWTH-2019-06706

Aachener Beiträge des ISEA

ABISEA Band 128
Fleischer, Michael
Traction control for Railway Vehicles
1. Aufl. 2019, 162 S.
DOI: 10.18154/RWTH-2019-10570

ABISEA Band 129
Teuber, Moritz
Lifetime Assessment and Degradation Mechanisms in Electric Double-Layer Capacitors
1. Aufl. 2019, 150 S.
DOI: 10.18154/RWTH-2019-10071

ABISEA Band 130
Bußar, Christian
Investigation of Optimal Transformation Pathways towards 2050 for the Successful Implementation of a Sustainable Reduction of Carbon Emissions from Power Generation
1. Aufl. 2019, 204 S.
DOI: 10.18154/RWTH-2019-09975

ABISEA Band 131
Wienhausen, Arne Hendrik
High Integration of Power Electronic Converters enabled by 3D Printing
1. Aufl. 2019, 146 S.
DOI: 10.18154/RWTH-2019-08746

ABISEA Band 132
Kwiecien, Monika
Electrochemical Impedance Spectroscopy on Lead-Acid Cells during Aging
1. Aufl. 2019, 138 S.
DOI: 10.18154/RWTH-2019-09480

ABISEA Band 133
Titiz, Furkan Kaan
A Three-phase Low-voltage Grid-connected Current Source Inverter
1. Aufl. 2019, 128 S.
DOI: 10.18154/RWTH-2020-00458

ABISEA Band 134
Wünsch, Martin
Separation der Kathoden-alterung in Lithium-Ionen-Batteriezellen mittels elektrochemischer Impedanzspektroskopie
1. Aufl. 2019, 177 S.
DOI: 10.18154/RWTH-2019-11017

ABISEA Band 135
Badeda, Julia
Modeling and Steering of Multi-Use Operation with Uninterruptible Power Supply Systems - utilizing the example of lead-acid batteries
1. Aufl. 2020, 282 S.
DOI: 10.18154/RWTH-2020-05456

ABISEA Band 136
Kleinsteinberg, Björn
Energy Efficiency Increase of a Vanadium Redox Flow Battery with a Power-Based Model
1. Aufl. 2020, 163 S.
DOI: 10.18154/RWTH-2020-06092

ABISEA Band 137
Cai, Zhuang
Optimization of dimension and operation strategy for a wind-battery energy system in German electricity market under consideration of battery ageing process
1. Aufl. 2020, 144 S.
DOI: 10.18154/RWTH-2020-06525

ABISEA Band 138
Sabet, Pouyan Shafiei
Analysis of Predominant Processes in Electrochemical Impedance Spectra and Investigation of Aging Processes of Lithium-Ion Batteries with Layered Oxide Cathodes and Graphitic Anodes
1. Aufl. 2020, 136 S.
DOI: 10.18154/RWTH-2020-07683

ABISEA Band 139
Angenendt, Georg
Operation, Optimization and Additional Market Participation of Households with PV Battery Storage System and Power-to-Heat Application
1. Aufl. 2020, 221 S.
DOI: 10.18154/RWTH-2020-05200

ABISEA Band 140
Oberdieck, Karl Friedrich
Measurement and Mitigation of Electromagnetic Emissions of Propulsion Inverters for Electric Vehicles
1. Aufl. 2020, 181 S.
DOI: 10.18154/RWTH-2020-09215

ABISEA Band 141
Bubert, Andreas Martin
Optimierung des elektrischen Antriebsstrangs von Elektrofahrzeugen mit Betrachtung parasitärer Ströme innerhalb der elektrischen Maschine
1. Aufl. 2020, 215 S.
DOI: 10.18154/RWTH-2020-09556

ABISEA Band 142
Fleischer, Christian Georg
Model-Driven Software Development and Verification Solutions for Safety Critical Battery Management Systems
1. Aufl. 2021, 356 S.
DOI: 10.18154/RWTH-2021-00436

ABISEA Band 143
Arzberger, Arno
Thermografische Methoden zur zerstörungsfreien Messung der anisotropen Wärmeleitfähigkeit von Lithium-Ionen Zellen
1. Aufl. 2020, 131 S.
DOI: 10.18154/RWTH-2021-00479

ABISEA Band 144
Lange, Tobias
Oberwellenbasierte Modellierung, Regelung und Auslegung von Permanentmagnet- und Reluktanz-Synchronmaschinen
1. Aufl. 2020, S.
DOI: 10.18154/RWTH-2021-02537

ABISEA Band 145
Weiss, Claude
Fault Tolerant Switched Reluctance Machines with Distributed Inverters – Modeling and Control
1. Aufl. 2020, S.
DOI: 10.18154/RWTH-2021-02327

ABISEA Band 146
Huck, Moritz
Modelling the Transient Behaviour of Lead-Acid Batteries: Electrochemical Impedance of Adsorbed Species
1. Aufl. 2020, 151 S.
DOI: 10.18154/RWTH-2020-08362

ABISEA Band 147
Willenberg, Lisa
Volumenausdehnung und ihre Auswirkungen auf die Alterung einer zylindrischen Lithium-Ionen-Batterie
1. Aufl. 2020, S.
DOI: 10.18154/RWTH-2021-01906

ABISEA Band 148
Rogge, Matthias
Electrification of Public Transport Bus Fleets with Battery Electric Busses
1. Aufl. 2020, 161 S.
DOI: 10.18154/RWTH-2021-02146

ABISEA Band 149
Münderlein, Jeanette
Numerische Methodik zur Auslegung eines Hybriden Speichersystems mit Multinutzen“
1. Aufl. 2020, 221 S.
DOI: 10.18154/RWTH-2021-00867

ABISEA Band 150
Merten, Michael
Participation of Battery Storage Systems in the Secondary Control Reserve Market
1. Aufl. 2020, 187 S.
DOI: 10.18154/RWTH-2021-01029

ABISEA Band 151
Ge, Lefei
Performance Enhancement of Switched Reluctance Machines for High-speed Back-up Generators
1. Aufl. 2020, 152 S.
DOI: 10.18154/RWTH-2020-11546

ABISEA Band 152
Neubert, Markus
Modeling, Synthesis and Operation of Multiport-Active Bridge Converters
1. Aufl. 2020, 227 S.
DOI: 10.18154/RWTH-2020-10814

ABISEA Band 153
Schülting, Philipp
Optimierte Auslegung von hochintegrierten und bidirektionalen Onboard GaN-Ladegeräten
1. Aufl. 2020, 158 S.
DOI: 10.18154/RWTH-2020-09771

ABISEA Band 154
Sewergin, Alexander
Design Challenges and Solutions for the Practical Application of SiC Power Moduls – Exemplified by an Automotive DC-DC Converter. 1. Aufl. 2021, 154 S.
DOI: 10.18154/RWTH-2021-04498

ABISEA Band 155
Stippich, Alexander
Exploiting the Full Potential of Silicon Carbide Devices via Optimized Highly Integrated Power Modules
1. Aufl. 2021, 188 S.
DOI: 10.18154/RWTH-2021-08122

ABISEA Band 156
Gottschlich, Jan
Hilfsspannungsversorgungskonzepte für Mittelspannungs-DC/DC-Wandler
1. Aufl. 2021, 178 S.
DOI: 10.18154/RWTH-2021-11881

ABISEA Band 157
Hollstegge, Philipp
Injektion raumzeigerzerlegter Stromharmonischer zur Minderung tonaler Geräuschanteile in asymmetrisch sechsphasigen Permanentmagnetsynchronmaschinen
1. Aufl. 2021, 191 S.
DOI: 10.18154/RWTH-2021-11040

ABISEA Band 158
Grau, Vivien
Development of a Test Bench to Investigate the Impact of Steep Voltage Slopes on the Lifetime of Insulation Systems for Coil Windings
1. Aufl. 2021, 182 S.
DOI: 10.18154/RWTH-2021-09577

ABISEA Band 159
Ringbeck, Florian
Optimized Charging of Lithium-Ion Batteries with Physico-Chemical Models
1. Aufl. 2021, 174 S.
DOI: 10.18154/RWTH-2021-11038

ABISEA Band 160
Bank, Thomas
Performance and Aging Analysis of High-Power Lithium Titanate Oxide Cells for Low-Voltage Vehicle Applications
1. Aufl. 2021, 148 S.
DOI: 10.18154/RWTH-2021-10369

Aachener Beiträge des ISEA

ABISEA Band 161
Aupperle, Felix
Realizing High-Performance Silicon-Based Lithium-Ion Batteries
1. Aufl. 2022, 138 S.
DOI: 10.18154/RWTH-2022-05155

ABISEA Band 162
Schröer, Philipp A.
Entwicklung einer adaptiven Leistungsprognosefunktion für Starterbatterien mit Lithium-Titanat-Oxid-Anode als Grundlage zur sicheren Energieversorgung im Fahrzeug
1. Aufl. 2021, 187 S.
DOI: 10.18154/RWTH-2021-10819

ABISEA Band 163
Dechent, Philipp
Simulation and Real-Life assessment of cell-to-cell variation of ageing lithium-ion batteries
1. Aufl. 2022, 149 S.
DOI: 10.18154/RWTH-2022-09298

ABISEA Band 164
Li, Weihan
Battery Digital Twin with Physics-Based Modeling, Battery Data and Machine Learning
1. Aufl. 2022, 234 S.
DOI: 10.18154/RWTH-2022-02292

ABISEA Band 165
Thien, Tjark G. C.
Optimaler Betrieb von stationären Hybrid-Batterie-speichern am Beispiel des Projekts M5BAT
1. Aufl. 2022, 172 S.
DOI: 10.18154/RWTH-2022-00997

ABISEA Band 166
Lüdecke, Christoph
Compensating Asymmetries of Parallel-Connected SiC MOSFETs Using Intelligent Gate Drivers
1. Aufl. 2022, 166 S.
DOI: 10.18154/RWTH-2022-09587

ABISEA Band 167
Rahe, Christiane
Untersuchung von Batterieelektroden mit optischen Verfahren
1. Aufl. 2022, 214 S.
DOI: 10.18154/RWTH-2022-08794

ABISEA Band 168
Weber, Felix Martin
Stability of lithium electrolyte interphase enabling rechargeable lithium-metal batteries
1. Aufl. 2023, 168 S.
DOI: 10.18154/RWTH-2023-03565

ABISEA Band 169
Henn, Jochen
Gate Driver Integrated Closed-Loop Control for Electromagnetic Emissions and Switching Losses of Wide Bandgap Power Electronic Converters
1. Aufl. 2023, 169 S.
DOI: 10.18154/RWTH-2023-07726

ABISEA Band 170
Quabeck, Stefan
Modeling of Parasitic Currents and Fault Detection in Electrical Traction Drives
1. Aufl. 2023, 133 S.
DOI: 10.18154/RWTH-2023-10920

ABISEA Band 171
Hecht, Christopher
Usage overview, prediction, and siting optimization for electric vehicles public charging infrastructure with machine learning and big data methods
1. Aufl. 2023, 185 S.
DOI: 10.18154/RWTH-2024-01156

ABISEA Band 172
Kuipers, Matthias L. U.
Development of a Virtual Cell Design Tool for Objective Comparisons between State-of-the-Art Battery Cells and Next Generation Technologies
1. Aufl. 2023, 203 S.
DOI: 10.18154/RWTH-2023-11897

ABISEA Band 173
Brieske, Daniel Martin
Anwendungsbezogene Modellierung und Zustandsbestimmung von Lithium-Schwefel-Batterien
1. Aufl. 2023, 146 S.
DOI: 10.18154/RWTH-2023-10905

ABISEA Band 174
Teichert, Philipp
Einfluss der Degradation von nickelreichen $Li[Ni_xMn_yCo_z]O_2$ (NMC) Elektroden (mit $x \geq 0.6$) auf Vollzellalterung von Lithium-Ionen-Zellen
1. Aufl. 2023, 159 S.
DOI: 10.18154/RWTH-2024-01059

ABISEA Band 175
Kühnle, Hannes Sebastian
Optical and electrochemical investigations of fundamental lithium metal deposition processes on lithium surfaces
1. Aufl. 2023, 218S.
DOI: 10.18154/RWTH-2024-05806

ABISEA Band 176
Epp, Alexander
Multiphysical Models and Optimization for Conceptual Design of High-Voltage Battery Systems
1. Aufl. 2024, 256 S.
DOI: 10.18154/RWTH-2024-00430

ABISEA Band 177
Figgener, Jan
Data-driven battery aging analysis of home storage systems based on high-resolution field measurements
1. Aufl. 2024, 208 S.
DOI: 10.18154/RWTH-2024-10709

ABISEA Band 178
Meishner, Fabian
Untersuchung eines direktnetzgekoppelten stationären LTO-Speichersystems in einem 750 V DC Stadtbahnnetz
1. Aufl. 2024, 116 S.
DOI: 10.18154/RWTH-2024-06358

ABISEA Band 179
Frambach, Tobias
Anwendungsgerechte Dimensionierung und Betriebsstrategien von 48 V Plug-In-Hybridfahrzeugen
1. Aufl. 2024, 154 S.
DOI: 10.18154/RWTH-2024-03411

ABISEA Band 180
Goldbeck, Rafael
Model-Based Control of Three-Phase Dual-Active Bridge Converters for Dynamic Operation and Adaptive Compensation of Parameter Deviations
1. Aufl. 2024, 194 S.
DOI: 10.18154/RWTH-2025-00288

ABISEA Band 181
Götz, Georg Tobias
Bidirectional DC-to-DC Converter with Integrated Switched Reluctance Generator
1. Aufl. 2024, 192 S.
DOI: 10.18154/RWTH-2024-03854

ABISEA Band 182
Harries, Martin
Aktive Reduzierung der Vibrationen von Permanentmagnet-Synchronmaschinen durch adaptive Regler
1. Aufl. 2024, 144 S.
DOI: 10.18154/RWTH-2025-00626

ABISEA Band 183
Börner, Martin Florian
Ein prozessbasiertes Modell zur Berechnung der Kosten von Lithium-Ionen-Batteriezellen
1. Aufl. 2024, 163 S.
DOI: 10.18154/RWTH-2024-07853

ABISEA Band 184
Bihn, Stephan
Automatic Parameterisation of Electrical Equivalent Circuit Models for Virtual Battery Cell Design
1. Aufl. 2024, 226 S.
DOI: 10.18154/RWTH-2024-10636

ABISEA Band 185
Xu, Huihui
Thermal Modeling and Control of an Oil-Cooled Permanent Magnet Synchronous Machine: Initialization, Nonlinearity, and Controllability
1. Aufl. 2025, 156 S.
10.18154/RWTH-2025-01683

ABISEA Band 186
Fritz, Niklas
Generalized Control Methodology for Modular DC-DC Converters
1. Aufl. 2025, S.
DOI: 10.18154/RWTH-

ABISEA Band 187
Kalker, Sven
Toward Robust Monitoring of Power Electronic Devices: Challenges and Efficient Solutions
1. Aufl. 2025, S.
DOI: 10.18154/RWTH-

ABISEA Band 188
Wasylowski, David
Accelerating Battery Cell Design, Manufacturing, and Testing through Ultrasound Imaging
1. Aufl. 2025, 116 S.
DOI: 10.18154/RWTH-2025-00940

ABISEA Band 189
Steininger, Valentin
Aging analysis of lithium-ion batteries with field data
1. Aufl. 2025, 136 S.
DOI: 10.18154/RWTH-2025-00625

ABISEA Band 190
Jacqué, Kevin
Analyse der Belastungsprofile, der Alterung und der Wirtschaft-lichkeit eines Batteriespeichers im Primärregelleistungsmarkt aus realen Feldmessdaten
1. Aufl. 2025, S.
DOI: 10.18154/RWTH-

Energy storage systems, particularly lithium-ion batteries (LIBs), are highly promising for applications such as electrical vehicles. Therefore, improving the cycle life, energy density, and safety of LIBs is of high importance. Graphite (Gr) is a state-of-the-art negative electrode active material; however, its low theoretical capacity (372 mAh/g) limits its usage in high-energy battery applications. Silicon (Si) is a promising anode active material, with high theoretical capacity (3590 mAh/g) and high abundance. However, Si undergoes a significant volume change (~200–400%) upon charge and discharge of the battery. This volume change of Si particles leads to mechanical instability of the anode film, loss of contact with the current collector, unstable solid electrolyte interphase (SEI), irreversible capacity loss, and a short cycle life. Different strategies are employed to improve the performance of Si-based anodes, such as developing Si/Gr electrodes, where the synergistic effect of Gr and Si active materials results in reducing the volume change and increasing the theoretical capacity. The use of suitable polymeric binders that accommodate the volume changes of Si particles can significantly enhance the electrochemical performance of LIBs.
In this work, Si/Gr anodes were developed and different electrode formulations were systematically investigated using a dual polymeric binder system. Pristine and post-mortem morphology measurements, as well as electrochemical characterization of Si/Gr electrodes were performed. Moreover, the implementation of green and environmentally friendly natural polymeric binders was studied in the optimized Si/Gr electrodes.

ISSN 1437-675X